

NASA TECHNICAL MEMORANDUM 100655

**INSTABILITY-RELATED DELAMINATION
GROWTH OF EMBEDDED AND EDGE
DELAMINATIONS**

John D. Whitcomb

August 1988

(NASA-TM-100655) INSTABILITY-RELATED
DELAMINATION GROWTH OF EMBEDDED AND EDGE
DELAMINATIONS Ph.D. Thesis - Virginia
Polytechnic Inst. and State Univ. (NASA)
199 p

N90-23494

Unclas
0287645
CSCL 11D G3/24



National Aeronautics and
Space Administration

Langley Research Center
Hampton, Virginia 23665

1000

1000

1000

INSTABILITY-RELATED DELAMINATION GROWTH OF EMBEDDED AND EDGE DELAMINATIONS

by

John D. Whitcomb

ABSTRACT

Compressive loads can cause local buckling in composite laminates that have a near surface delamination. This buckling causes load redistribution and secondary loads, which in turn cause interlaminar stresses and delamination growth. The goal of this research effort was to enhance the understanding of this instability-related delamination growth in laminates containing either an embedded or an edge delamination.

There were three primary tasks: 1) development of a geometrically nonlinear finite element analysis named NONLIN3D; 2) performance of a parametric analytical study to determine the effects of strain, delamination shape, and delamination size on the distribution of the strain-energy release rate components along the delamination front; and 3) performance of a combined experimental and analytical study of instability-related delamination growth (IRDG). Two material systems (AS4/PEEK and IM7/8551-7) and two stacking sequences (0/90/90/0)₆ and (90/0/0/90)₆ were examined. The laminates were fabricated with Kapton inserts between the fourth and fifth plies from the top surface to give an initial delamination.

The analysis predicted a large variation of G_I and G_{II} along the delamination front. The G_{III} component was always small. The location of maximum G_I and G_{II} depended on the delamination shape and applied strain. In general, the strain-energy release rates were small except in a small region. Hence,

delamination growth was expected to occur over only a small portion of the delamination front. Experiments corroborated this prediction. The laminate stacking sequence had a large effect on the shape of the deformed region, the direction of delamination growth, and the strain at which delamination growth occurred. These effects were predicted by the analysis. The G_I component appeared to govern initial delamination growth in the IM7/8551-7 laminates. Matrix ply cracking generally accompanied delamination growth. In some cases fiber microbuckling also occurred shortly after delamination growth occurred.

TABLE OF CONTENTS

	Page
NOMENCLATURE	1
CHAPTER	
1. INTRODUCTION	3
1.1 Survey of the State of the Art	5
1.1.1 Through-Width Delamination	5
1.1.2 Embedded Delamination	7
1.2 Scope of Investigation	9
2. FINITE ELEMENT ANALYSIS	13
2.1 Governing Nonlinear Equations	14
2.2 Finite Element Approximation	16
2.3 Numerical Integration	20
2.4 Vectorized Implementation	22
2.4.1 Subroutine B0BL3D	25
2.4.2 Subroutine ESTIF3D	40
2.4.3 Execution Times	44
2.5 Eigenvalue Analysis of Stiffness Matrix	45
2.6 Substructuring	46
2.7 Contact Analysis	48
2.8 Strain-Energy Release Rate Calculation	52
2.9 Material Properties	56
3. FINITE ELEMENT MODELING	59
3.1 Mesh Generation	59
3.2 Finite Element Models	62
4. EVALUATION OF NONLIN3D	69
4.1 Analysis of Transversely Loaded Plate	69
4.2 Failure of 8-Node Element	71
4.3 Check of Mesh Refinement	72
4.4 Determination of Allowable Residual	81
4.5 Verification of Substructuring	83

5. PARAMETRIC ANALYSIS OF HOMOGENEOUS QUASI-ISOTROPIC LAMINATES	85
5.1 Deformation and Strain-Energy Release Rates For an Embedded Delamination	85
5.2 Interpretation of Deformation and Load Transfer	94
5.2.1 Comparison of Behaviors for the Through-Width and the Embedded Delamination	94
5.2.2 Mechanics of IRDG for the Embedded Delamination	98
5.3 Comparison of Full 3D, Thin-Film 3D, and Plate Analyses For an Embedded Delamination	108
5.4 Effect of Contact Constraints	110
5.5 Strain-Energy Release Rates For an Edge Delamination	119
6. EXPERIMENTAL PROCEDURE	124
6.1 Specimen Configurations	124
6.2 Measurement of Damage	134
7. COMPARISON OF ANALYTICAL AND EXPERIMENTAL RESULTS	137
7.1 Check Cases	137
7.2 Qualitative Study of AS4/PEEK Laminates	138
7.3 Quantitative Study of IM7/8551-7 Laminates	154
8. SUMMARY and RECOMMENDATIONS	182
9. REFERENCES	186
APPENDIX: Shape Functions for 8- and 20- Node Elements	192

NOMENCLATURE

a_i, b_i, c_i, d_i	Labels for nodes used in G calculation
a, b	Semi-axes of elliptical delamination in x- and y- directions, respectively
C_{ij}	Constitutive coefficients
E_{11}, E_{22}, E_{33}	Young's moduli for orthotropic material
F^α	Nodal forces
$G_I, G_{II},$ G_{III}, G_T	Mode I, mode II, mode III, and total strain-energy release rates
G_{12}, G_{23}, G_{13}	Shear moduli for orthotropic material
h	Thickness of sublaminate
H	Thickness of base laminate
J	Jacobian matrix
$K^{\alpha\beta}$	Coefficients in tangential stiffness matrix
N^m	Shape function for node m
NG	Number of Gaussian quadrature points
NS	Number of shape functions
P	Transverse load
q^α	Nodal displacements
S	Perimeter coordinate
u,v,w	Displacements in x-, y-, and z-directions
U	Strain energy
V	Volume
w_0	Transverse displacement in center of plate
W	Width of finite element model. Also used to designate Gaussian quadrature weighting coefficients.

NOMENCLATURE, concluded

x, y, z	Rectangular Cartesian coordinates
Δa	Increment in delamination length
δ_i	Local coordinates in parent element, $i=1,3$
ϵ_j	Strains
$\nu_{12}, \nu_{23}, \nu_{13}$	Poisson's ratios for orthotropic material
Π	Total potential energy
σ_i	Stresses

Subscripts and Superscripts

- $i, j = 1, 6$ except as noted
 $\alpha, \beta = 1$, number of nodal displacements
 $\theta = 1$, number of Gaussian quadrature points

Chapter 1

INTRODUCTION

In recent years there has been an increasing interest in the application of advanced composite materials to structures. These materials exhibit high specific strength and stiffness. Through the choice of fiber/matrix systems and lamination stacking sequences, there are great opportunities to tailor the material stiffness and thermal expansion coefficients in various directions to meet specific design needs. Some are very resistant to corrosive environments. There are also advantages in fabrication of certain structures, in which the "part count" can be drastically reduced by using composites. The list of desirable characteristics is long.

Unfortunately, there are also potential problems associated with the use of composite materials. One of the primary problems is lack of experience. New material systems are being introduced on a regular basis. Even most of the "older" material systems are only a few years old. Application of composites to strength critical structures has been very limited.

There are also new modes of failure, such as delamination, fiber breakage, and intralaminar cracking. These materials may be very strong in certain directions, but they can also be surprisingly weak (compared to metals) in other directions. The use of high strength, low strain to failure fibers severely reduces plastic deformation. Whereas a metallic structure can experience local yielding to reduce stress concentrations, a composite structure can do little readjusting to reduce locally high stresses without local failure.

To expedite the process of safe application of composites to strength critical structures, much research has been aimed at developing appropriate stress analyses. This is not to say that metal structures do not require sophisticated stress analyses. But, for the same level of geometric and loading complexity, composites are much more demanding of the analyst than are metals.

There are basically two types of stress analyses which must be performed. The

first consists of analysing a problem in which the failure is well documented and understood. The analyst's task is simply to quantify the magnitude of certain parameters which are known to control the failure mode. For many situations it is not clear what governs failure. Since it is not possible to model all aspects of the configuration, approximations must be made. This is the second type of stress analysis problem.

The problem addressed by this thesis is of the second type. Failure of a laminated composite material under compression loads is a very complicated process. Besides all of the failure modes commonly observed under tensile loads, there are additional failure modes related to instability. There is the possibility of fiber microbuckling, lamina buckling, and global buckling of the entire laminate. Usually, the concern is that some initial damage or defect will precipitate the operation of one of these instability-related mechanisms. The initial defect may be quite simple: perhaps a disbond between two lamina. Initial damage can be due to high stresses during service or impact damage. Impact damage is a particularly messy situation for the analyst. It is impossible to model all of the fiber breaks, delaminations, and lamina cracks. The task is to make approximations which make the analysis tractable without losing any of the essential elements of the problem. Learning to identify the essence of a complicated problem involves dissection of the original problem into independent, less complicated problems that exhibit one or two failure mechanisms. These less complicated problems are then carefully analyzed to determine the basic behavior. Hopefully, certain mechanisms can be identified as unlikely or at least unimportant. Then potential interactions of the mechanisms would be considered.

Presently, there is no consensus as to what are the critical mechanisms of compression failure. Likely, different modes are critical under different situations. Also, more understanding of the basic mechanisms of compression failure is needed. This thesis will examine the failure mode instability-related delamination growth; that is, delamination growth which is caused by localized buckling of

a delaminated group of lamina. This buckling causes load redistribution and secondary loads, which in turn cause interlaminar stresses and delamination growth. The next several sections will survey the literature and describe the scope of this investigation.

1.1 Survey of the State of the Art

Most of the research on instability-related delamination growth (IRDG) has used one of two configurations: the through-width delamination or the embedded delamination. These are shown in Fig. 1.1 . When a critical compressive strain level is reached, the delaminated region buckles. This causes interlaminar stresses along the delamination front, possibly leading to delamination growth. The term “sublaminar” will be used to refer to the buckled group of plies. The term “base laminate” will be used to refer to the unbuckled group of plies. These regions are labeled in Fig. 1.1.

The literature on instability-related delamination growth differs in the choice of configuration, the type of stress analysis, and the method of characterizing the magnitude of the delamination front stresses. Also, some papers are primarily experimental and others concentrate on just the analysis. The literature survey in the next two sections will be organized according to the configuration considered.

1.1.1 Through-Width Delamination

The primary motivation for considering the through-width delamination is that it is less complicated than the embedded delamination. Hence, it provides a convenient vehicle for checking various ideas about modeling.

Kachanov was perhaps the first to analyse the through-width delamination (ref. 1). He developed an approximate nonlinear beam-column analysis for the case of thin-film buckling. The change in strain-energy in the thin film due to delamination was compared with the rupture energy. If sufficient strain-energy was released, the delamination was assumed to grow. Kachanov did not consider

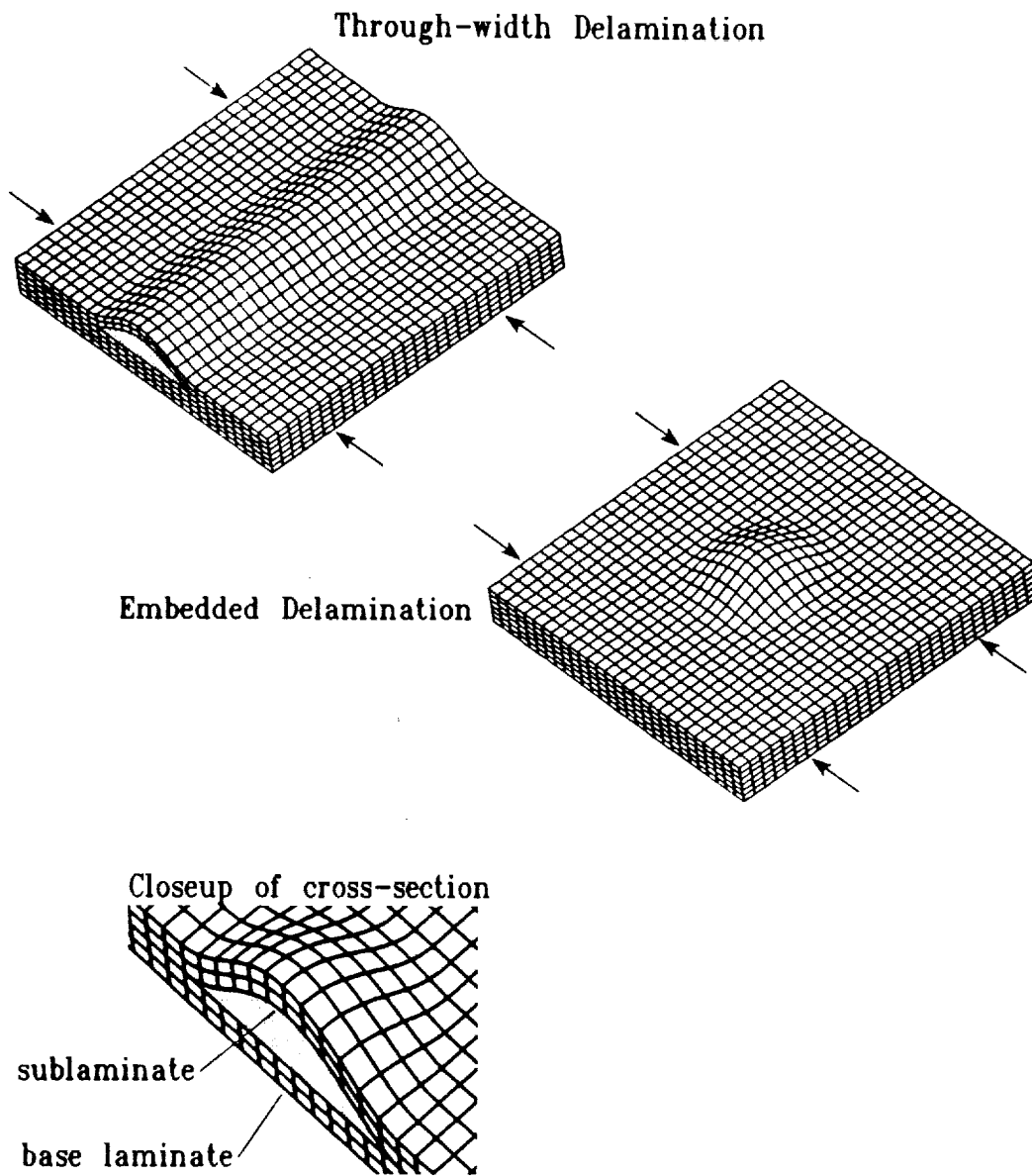


Fig. 1.1 Two configurations which exhibit instability-related delamination growth.

the individual components of strain-energy release rate. Whitcomb (ref. 2,3) developed a geometrically-nonlinear finite element analysis for calculating the mode I and mode II strain-energy release rates (G_I and G_{II}). Linear finite element analysis was later combined with nonlinear beam theory to obtain results for many configurations (ref. 4, 5). This hybrid analysis drastically reduced the computational effort required to perform a parametric study. Chai, et al (ref. 6) developed a beam-column analysis for calculating total strain-energy release rate ($G_T = G_I + G_{II}$). G_T was calculated based on differentiation of the total strain energy. This analysis could handle the case of global bending combined with local buckling. The analysis could also handle multiple delaminations, although no provision was made to prevent interpenetration of the different groups of buckled lamina. Wang (ref. 7) performed a finite element analysis of composites with multiple delaminations. Constraints were included to prevent interpenetration of adjacent lamina groups. However, only the bifurcation buckling problem was studied. Since there was no postbuckling analysis, strain-energy release rates could not be calculated. Ashizawa (ref. 8) also published a beam-column analysis. He calculated G_T based only on the moment at the end of the delamination. Simites, et al used plate analysis to study how local buckling of a delaminated group of lamina affects global stability (ref. 9). In ref. 10 Sallam and Simites presented a plate analysis which can be used to calculate the effects of coupling between bending and stretching on G_T .

Experimental measurements of instability-related delamination growth have been published for both fatigue (ref. 3, 4, 11, 12) and static (ref. 11, 12, 13) loads. No unusual experimental techniques were used, so individual references will not be discussed.

1.1.2 Embedded Delamination

Kachanov (ref. 1) was also perhaps the first to analyse the embedded delamination. He presented a thin-film analysis for a circular delamination in a plate subjected to uniform radial loads. Prediction of delamination growth was

based on the change in strain energy in the buckled thin film versus the rupture energy. The individual modes of strain-energy release rate were not considered. Konishi and Johnston (ref. 14) assumed a trigonometric form for the transverse displacements of a rectangular delamination with an initial imperfection. The moments along the delamination boundary were estimated by differentiation of the assumed displacement function. Results from this analysis were used to design specimens for a study of delamination growth under fatigue loads. However, no analytical results were presented. Also, experimental results were not compared with the analytical model. Chai (ref. 15) developed a Rayleigh-Ritz analysis for the postbuckling of an embedded elliptical delamination. The buckled group of lamina was assumed to be very thin compared to the rest of the laminate. The entire laminate was assumed to be isotropic. The total strain-energy release was obtained by differentiation of the strain-energy with respect to the lengths of the axes of the ellipse. This procedure gave an average measure of the strain-energy release rate along the boundary. The analysis was later modified to be able to analyse orthotropic laminates (ref. 16). Webster (ref. 17) developed a Rayleigh-Ritz analysis for determining bifurcation buckling of a circular delamination. He used Ashton and Whitney's technique (ref. 18) to account for bending-extension coupling of unsymmetric sublaminates. Shivakumar and Whitcomb also presented a bifurcation buckling analysis (ref. 19). They used both finite element and Rayleigh-Ritz plate analyses. Orthotropic, elliptical sublaminates with various orientations relative to the load direction were considered. Since postbuckling was not considered, there was not the possibility of a strain-energy release rate calculation in either ref. 17 or 19. Whitcomb and Shivakumar (ref. 20) presented a technique for calculating the distribution of strain-energy release rate along the delamination front from plate analysis results. Although this technique is general, only results for isotropic laminates were presented. Yin (ref. 21) developed a plate analysis for calculating total strain-energy release rate for axisymmetric loading of an isotropic plate with a circular delamination. Fei and Yin (ref. 22) developed a similar analysis for axisymmetric bending of an isotropic plate.

All of the preceding analyses are for quasi-static loading. Bottega (ref. 23) developed a dynamic plate analysis for estimating the effects of dynamic loading on delamination growth. Only axisymmetric configurations were considered.

A variety of experimental programs have observed growth of embedded delaminations. Konishi and Johnston (ref. 14) used Kapton implants to create delaminations of a known size. They performed both static and fatigue tests. Rhodes, et al (ref. 24) observed that impact of compression panels could lead to delamination, followed by local buckling and delamination growth. Byers (ref. 25) and Porter (ref. 26) studied the growth of delaminations which originated either due to impact or an implant. Ramkumar (ref. 11) also performed tests on laminates with implants. Chai et al (ref. 27) combined high-speed photography and shadow moire to study dynamic growth of delaminations due to combined impact and compression.

1.2 Scope of Investigation

The literature survey showed that there has been no detailed analysis of any truly three-dimensional (3D) configuration which exhibits instability-related delamination growth. Even the approximate analyses that have been performed have examined only a very limited range of parameters. None of the analyses have been capable of calculating the individual modes of strain-energy release rate. The goal of this investigation is to enhance the understanding of instability-related delamination growth through detailed stress analysis supplemented by experiments.

There are two facets of the analytical study: development of a suitable stress analysis and using it to calculate strain-energy release rates.

Geometrically nonlinear 3D analysis is required to perform the detailed analysis. In particular, finite element analysis will be used. Such analyses are inherently expensive. However, geometrically nonlinear 3D analysis has become more practical since the introduction of supercomputers, which have processing capabilities

in the neighborhood of 200 million floating point operations per second. To fully exploit the capabilities of a supercomputer requires tailoring of one's program to fit the architecture of the computer. Programs written for ordinary mainframe computers are not generally suitable for supercomputer usage. Hence, one of the tasks in this study was to develop a finite element program which exploits a supercomputer architecture. This program is named NONLIN3D. The development and verification of NONLIN3D will be discussed.

There are several aspects to the use of NONLIN3D. Even with the use of supercomputers and special purpose programs, efficient modeling must be used. This means avoiding excessive mesh refinement and using nonlinear analysis only where it is necessary. Also, tasks like mesh generation can become intractable unless approached properly. These aspects of the use of NONLIN3D will be discussed.

NONLIN3D was used to perform a parametric study of two 3D configurations which exhibit instability-related delamination growth. In particular, the embedded delamination (Fig. 1.1) and the edge delamination (Fig. 1.2) will be examined. A few results will be presented for the through-width delamination, which is basically two-dimensional. The parameters studied include strain, delamination size, and delamination shape. Also, the effect of stacking sequence was studied. Delamination growth behavior was predicted based on the calculated strain-energy release rates.

Another use of NONLIN3D was to determine how accurate plate analysis is for calculating total strain-energy release rates. Plate analysis is potentially attractive because it is inherently much less expensive than 3D analysis. Results from the literature were used for the plate analysis. (No plate analysis was performed as part of this study.)

Some preliminary experiments were performed on a configuration which does not buckle, but does exhibit geometric nonlinearity. This configuration was used to

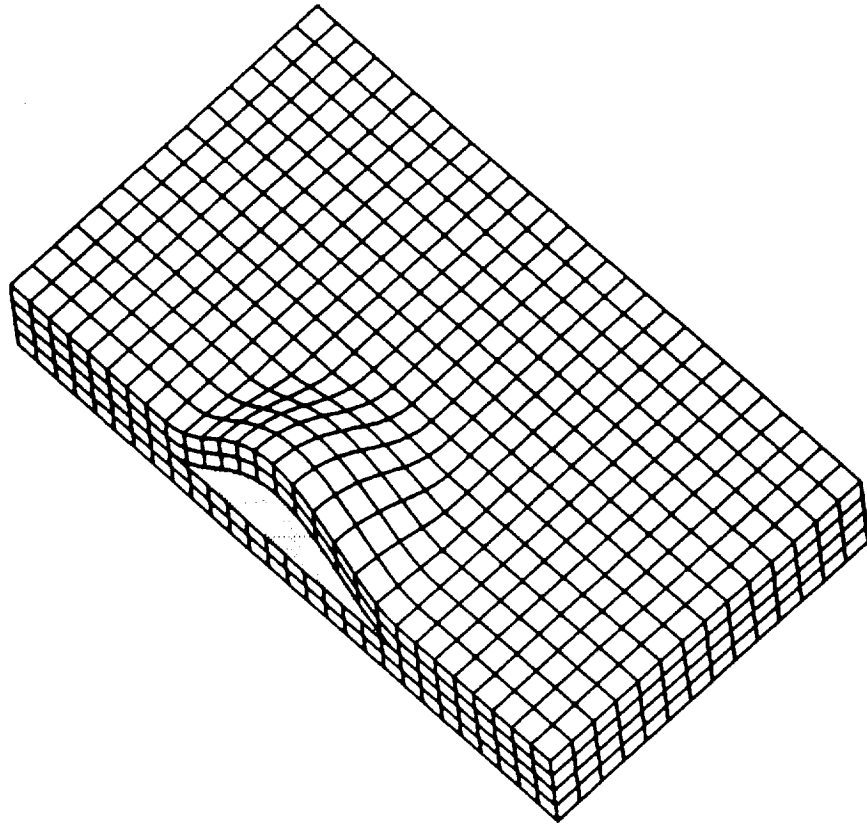


Fig. 1.2 Laminate with postbuckled edge delamination.

check the degree of agreement one might expect between analysis and experiment for relatively simple configurations.

Experiments were performed to determine whether instability-related delamination growth could be predicted using strain-energy release rate parameters. Laminates with embedded and edge delaminations were tested. The deformation and growth of the buckled region were monitored during the tests. Also, X-rays and light microscopy were used to determine the extent of delamination and other types of damage. Predicted and observed behaviors are compared.

The following chapters will begin with a discussion of NONLIN3D. Then the results of a parametric analysis of *homogeneous quasi-isotropic laminates* with either an embedded or edge delamination will be presented. Then the experimental procedure will be discussed. Finally the results of a combined analytical and experimental parametric study will be presented.

Chapter 2

FINITE ELEMENT ANALYSIS

This chapter describes the theoretical aspects of the finite element analysis program NONLIN3D. This program was developed as part of this thesis effort to perform the stress analyses presented in later chapters. There were two primary reasons for developing a new program rather than using a commercially available one. The first reason is related to the size of the computational task. Nonlinear 3D analyses generally require large computer resources, both in terms of memory and number of computations. Supercomputers, such as the CDC VPS-32 and the CRAY-2, are well suited for the task. To exploit the power of such machines requires special programming techniques. Unless a program is written specifically for a supercomputer, the program will usually not perform well. NONLIN3D was written to exploit the capabilities of the VPS-32, which was the supercomputer available for this work. The second reason for developing a new program was to permit tailoring of the source code to suit the needs of this particular research effort. This tailoring involved all aspects of the analysis, including ease of input and output, simple techniques for specifying boundary conditions, and automated strain-energy release rate calculations.

The following topics will be covered in this chapter:

2.1 Governing Nonlinear Equations

2.2 Finite Element Approximation

2.3 Numerical Integration

2.4 Vectorized Implementation

2.5 Eigenvalue Analysis of Stiffness Matrix

2.6 Substructuring

2.7 Contact Analysis

2.8 Strain-Energy Release Rate Calculation

2.9 Material Properties

2.1 Governing Nonlinear Equations

This subsection discusses the derivation of the equilibrium equations and the expressions for the internally generated nodal forces and the tangent stiffness matrix. Also, the strain-displacement relations are discussed.

The total potential energy Π is given by

$$\Pi = \frac{1}{2} \int C_{ij} \epsilon_i \epsilon_j dV - F^\alpha q^\alpha \quad (2.1.1)$$

where the integral term is the strain energy and the second term is the potential energy of the applied loads. The terms C_{ij} and ϵ_i are terms in the constitutive matrix and the strains, respectively. The terms F^α and q^α are the generalized forces and displacements, respectively. The adjective "generalized" is used to indicate that F^α and q^α need not be nodal forces and displacements in the usual sense. For example, in traditional Rayleigh-Ritz analyses, the q^α are simply unknown coefficients in the series expansion for the displacements. However, in this discussion the F^α and q^α will always refer to the nodal forces and displacements in the x -, y -, and z -directions. The system is assumed to be conservative; hence, the equilibrium state is obtained by minimizing Π , which is accomplished by setting the first partial derivatives with respect to the unknowns equal to zero.

$$\frac{\partial \Pi}{\partial q^\alpha} = \int C_{ij} \epsilon_i \frac{\partial \epsilon_j}{\partial q^\alpha} dV - F^\alpha = 0 \quad (2.1.2)$$

Equation 2.1.2 is nonlinear because of the nonlinear strain-displacement rela-

tions. The integral in eqn. 2.1.2 gives the magnitude of the internally generated nodal forces corresponding to the current displacements. Until a converged solution is obtained, the internally generated forces do not equal the externally applied forces. The differences in the forces, referred to as residuals, equal $\frac{\partial \Pi}{\partial q^\alpha}$. The Newton-Raphson procedure that was used to solve eqn. 2.1.2 requires the partial derivatives of the residuals with respect to the unknowns. These partial derivatives of the residuals are the coefficients in the tangential stiffness matrix K and are given by eqn. 2.1.3.

$$K^{\alpha\beta} = \frac{\partial^2 \Pi}{\partial q^\alpha \partial q^\beta} = \int C_{ij} \frac{\partial \varepsilon_i}{\partial q^\alpha} \frac{\partial \varepsilon_j}{\partial q^\beta} dV + \int C_{ij} \frac{\partial^2 \varepsilon_i}{\partial q^\alpha \partial q^\beta} dV \quad (2.1.3)$$

The first integral gives the terms for the sum of the linear and large displacement matrices. The second integral gives the terms in the geometric stiffness matrix. If the strains are equal to zero, the matrix obtained using the first integral and the nonlinear strain-displacement relations is identical to the matrix obtained by simply updating the coordinates and using the linear strain-displacement relations. If the strains are not equal to zero, there is a difference. This was verified numerically for 2D elements.

A Lagrangian formulation was used in NONLIN3D. For infinitesimal strain the nonlinear strain displacement relations are (ref. 28)

$$\begin{aligned} \varepsilon_1 &= u_x + 1/2(u_x u_x + v_x v_x + w_x w_x) \\ \varepsilon_2 &= v_y + 1/2(u_y u_y + v_y v_y + w_y w_y) \\ \varepsilon_3 &= w_z + 1/2(u_z u_z + v_z v_z + w_z w_z) \\ \varepsilon_4 &= u_y + v_x + (u_x u_y + v_x v_y + w_x w_y) \\ \varepsilon_5 &= v_z + w_y + (u_z u_y + v_z v_y + w_z w_y) \\ \varepsilon_6 &= u_z + w_x + (u_z u_x + v_z v_x + w_z w_x) \end{aligned} \quad (2.1.4)$$

where u , v , and w are displacements in the x -, y -, and z -directions, and the subscripts x , y , and z indicate partial differentiation (e.g. $u_y = \frac{\partial u}{\partial y}$). The nodal values of u , v , and w are the unknowns referred to earlier as q^α . Note that ε_4 , ε_5 , and ε_6 are engineering shear strains. Since a Lagrangian formulation is used, the strains are based on the original configuration. For example, ε_1 is the axial strain of a line which was originally (i.e., before deformation) parallel to the x -axis. *Although this line could be oriented parallel to the y -axis after deformation, the axial strain is still ε_1 (not ε_2).*

The material coefficients, C_{ij} , were assumed to couple normal and shear strains in the xy plane only; hence, $C_{5j} = 0$ for $j = 1, 2, 3, 4$, and 6 and $C_{6j} = 0$ for $j = 1$ through 5 . This corresponds to an orthotropic material which has one material axis parallel to the z direction. In expanded form, the stresses are given by

$$[\sigma_i] = \begin{bmatrix} C_{11} & C_{12} & C_{13} & C_{14} & 0 & 0 \\ C_{12} & C_{22} & C_{23} & C_{24} & 0 & 0 \\ C_{13} & C_{23} & C_{33} & C_{34} & 0 & 0 \\ C_{14} & C_{24} & C_{34} & C_{44} & 0 & 0 \\ 0 & 0 & 0 & 0 & C_{55} & 0 \\ 0 & 0 & 0 & 0 & 0 & C_{66} \end{bmatrix} \begin{bmatrix} \varepsilon_1 \\ \varepsilon_2 \\ \varepsilon_3 \\ \varepsilon_4 \\ \varepsilon_5 \\ \varepsilon_6 \end{bmatrix} \quad (2.1.5)$$

2.2 Finite Element Approximation

Equations 2.1.1 through 2.1.5 are general equations which can be used with any procedure based on minimization of total potential energy. In the finite element method, the body is divided into subregions referred to as elements. Within an element, the displacements u , v , and w are approximated by interpolation functions N^m and nodal values of the displacements, u^m , v^m , and w^m .

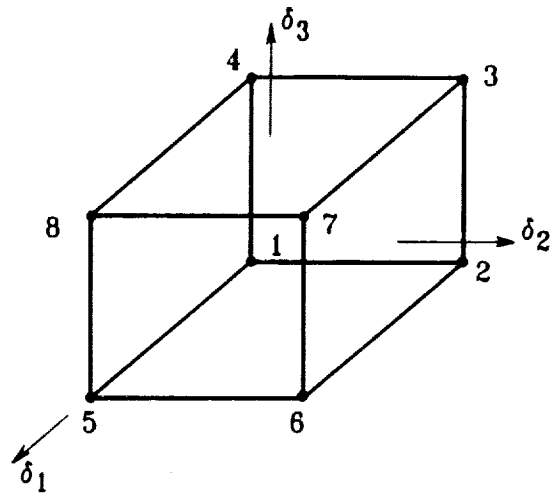
$$\begin{aligned} u &= N^m u^m \\ v &= N^m v^m \\ w &= N^m w^m \end{aligned} \quad \begin{aligned} &\text{where } m = 1, NS \\ &(NS = \text{number of shape functions}) \end{aligned} \quad (2.2.1)$$

The shape functions for 8- and 20-node elements are given in the appendix. Fig. 2.2.1 shows schematics of the two elements.

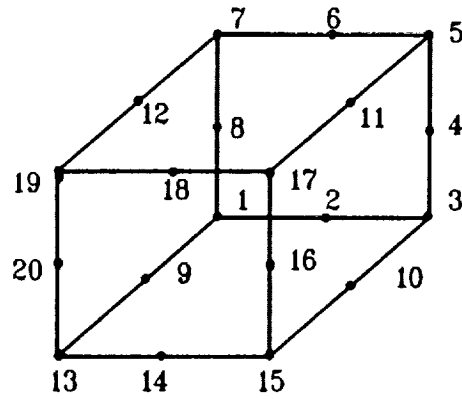
Since an isoparametric formulation was used, the element geometry is approximated using the same interpolation functions and the nodal coordinates, x^m , y^m , and z^m .

$$\begin{aligned}
 x &= N^m x^m \\
 y &= N^m y^m \\
 z &= N^m z^m
 \end{aligned}
 \tag{2.2.2}$$

Calculation of the tangential stiffness matrix (eqn. 2.1.3) requires the first and second partial derivatives of the strains ϵ_i (eqn. 2.1.4) with respect to the nodal displacements u^m , v^m , and w^m . Since the nodal values are independent of the coordinates, the partial derivatives with respect to coordinate directions take the form $\frac{\partial u}{\partial x} = \frac{\partial N^m}{\partial x} u^m$. Also, the nodal displacements are independent. Hence, $\frac{\partial u^m}{\partial u^n} = \delta_{mn}$ and $\frac{\partial u^m}{\partial v^n} = 0$, where δ_{mn} is the Kronecker delta. Equation 2.2.3 gives the expressions for the derivatives of the strains.



(a) 8-node element



(b) 20-node element

Fig. 2.2.1 Schematics of 8- and 20-node elements.

$$[B] = \begin{bmatrix} \frac{\partial \varepsilon_1}{\partial u^m} & \frac{\partial \varepsilon_1}{\partial v^m} & \frac{\partial \varepsilon_1}{\partial w^m} \\ \frac{\partial \varepsilon_2}{\partial u^m} & \frac{\partial \varepsilon_2}{\partial v^m} & \frac{\partial \varepsilon_2}{\partial w^m} \\ \frac{\partial \varepsilon_3}{\partial u^m} & \frac{\partial \varepsilon_3}{\partial v^m} & \frac{\partial \varepsilon_3}{\partial w^m} \\ \frac{\partial \varepsilon_4}{\partial u^m} & \frac{\partial \varepsilon_4}{\partial v^m} & \frac{\partial \varepsilon_4}{\partial w^m} \\ \frac{\partial \varepsilon_5}{\partial u^m} & \frac{\partial \varepsilon_5}{\partial v^m} & \frac{\partial \varepsilon_5}{\partial w^m} \\ \frac{\partial \varepsilon_6}{\partial u^m} & \frac{\partial \varepsilon_6}{\partial v^m} & \frac{\partial \varepsilon_6}{\partial w^m} \end{bmatrix} = \begin{bmatrix} N_x^m + u_x N_x^m & v_x N^m & w_x N_x^m \\ u_y N_y^m & N_y^m + v_y N_y^m & w_y N_y^m \\ u_z N_z^m & v_z N_z^m & N_z^m + w_z N_z^m \\ N_y^m + u_x N_y^m & N_x^m + v_x N_y^m & w_x N_y^m + N_x^m \\ + u_y N_x^m & + v_y N_x \\ u_y N_z^m + u_x N_y^m & N_x^m + v_y N_z^m & N_y^m + w_y N_z^m \\ + v_z N_y^m & + v_z N_y^m \\ N_x^m + u_x N_z^m & v_x N_z^m + v_z N_x^m & N_x^m + w_x N_z^m \\ + u_y N_x^m & + w_z N_x^m \end{bmatrix} \quad (2.2.3)$$

$$[B] = \begin{bmatrix} B_{11} & B_{12} & B_{13} \\ B_{21} & B_{22} & B_{23} \\ B_{31} & B_{32} & B_{33} \\ B_{41} & B_{42} & B_{43} \\ B_{51} & B_{52} & B_{53} \\ B_{61} & B_{62} & B_{63} \end{bmatrix} \quad (2.2.4)$$

The matrix B is introduced to define the terms B_{ir} , which will be used later to conveniently refer to the derivatives in eqn. 2.2.3. Most of the second partial derivatives are zero. The non-zero ones are given in eqn. 2.2.5. Note that the terms are the same for derivatives with respect to u, v, and w.

$$\begin{aligned}
\frac{\partial^2 \varepsilon_1}{\partial u^m \partial u^n} &= \frac{\partial^2 \varepsilon_1}{\partial v^m \partial v^n} = \frac{\partial^2 \varepsilon_1}{\partial w^m \partial w^n} = N_x^m N_x^n = a_1^{mn} \\
\frac{\partial^2 \varepsilon_2}{\partial u^m \partial u^n} &= \frac{\partial^2 \varepsilon_2}{\partial v^m \partial v^n} = \frac{\partial^2 \varepsilon_2}{\partial w^m \partial w^n} = N_y^m N_y^n = a_2^{mn} \\
\frac{\partial^2 \varepsilon_3}{\partial u^m \partial u^n} &= \frac{\partial^2 \varepsilon_3}{\partial v^m \partial v^n} = \frac{\partial^2 \varepsilon_3}{\partial w^m \partial w^n} = N_z^m N_z^n = a_3^{mn} \\
\frac{\partial^2 \varepsilon_4}{\partial u^m \partial u^n} &= \frac{\partial^2 \varepsilon_4}{\partial v^m \partial v^n} = \frac{\partial^2 \varepsilon_4}{\partial w^m \partial w^n} = N_x^m N_y^n + N_y^m N_x^n = a_4^{mn} \\
\frac{\partial^2 \varepsilon_5}{\partial u^m \partial u^n} &= \frac{\partial^2 \varepsilon_5}{\partial v^m \partial v^n} = \frac{\partial^2 \varepsilon_5}{\partial w^m \partial w^n} = N_y^m N_z^n + N_z^m N_y^n = a_5^{mn} \\
\frac{\partial^2 \varepsilon_6}{\partial u^m \partial u^n} &= \frac{\partial^2 \varepsilon_6}{\partial v^m \partial v^n} = \frac{\partial^2 \varepsilon_6}{\partial w^m \partial w^n} = N_x^m N_z^n + N_z^m N_x^n = a_6^{mn}
\end{aligned} \tag{2.2.5}$$

2.3 Numerical Integration

The integrals in eqns. 2.1.2 and 2.1.3 were evaluated using numerical integration. The integrations become summations as shown in eqns. 2.3.1 and 2.3.2:

$$\frac{\partial \Pi}{\partial q^\alpha} = \sum_{\theta=1}^{NG} (C_{ij} \varepsilon_i \frac{\partial \varepsilon_i}{\partial q^\alpha} |J|W)^\theta - F^\alpha \tag{2.3.1}$$

$$K^{\alpha\beta} = \sum_{\theta=1}^{NG} (C_{ij} \frac{\partial \varepsilon_i}{\partial q^\alpha} \frac{\partial \varepsilon_j}{\partial q^\beta} |J|W)^\theta + \sum_{\theta=1}^{NG} (\sigma_i \frac{\partial^2 \varepsilon_i}{\partial q^\alpha \partial q^\beta} |J|W)^\theta \tag{2.3.2}$$

where

NG = number of quadrature points

$|J|$ = determinant of the Jacobian (required because integrations

are performed using local coordinate system)

W = Gaussian quadrature weighting coefficients

and the superscript θ indicates that the term was evaluated at quadrature

point θ .

The first summation in eqn. 2.3.2 can be expressed in a symmetric form. This form is like that in ref. 29, but the motivation is different. Herein, the symmetry is the valuable characteristic which will be exploited in the vector implementation of the finite element analysis. The material coefficients C_{ij} are replaced by $C_{ij} = Q_{is}Q_{js}$, where $Q_{is} = 0$ for $i < s$. The terms Q_{is} are obtained using Cholesky decomposition. Cholesky decomposition is always possible since the constitutive matrix C_{ij} is symmetric and positive definite. The weighting coefficients W and the determinant of the Jacobian $|J|$ are positive, so the square root of $|J|W$ is real (only the positive square root need be considered). Integration schemes which involve negative weighting coefficients are not considered herein. Hence, the first summation in eqn. 2.3.2 can be written as

$$K_L^{\alpha\beta} = \sum_{\theta=1}^{NG} (T^{s\alpha} T^{s\beta})^{\theta} \quad (2.3.3)$$

and $T^{s\alpha}$ is defined to be

$$T^{s\alpha} = Q_{is} \frac{\partial \epsilon_i}{\partial q^{\alpha}} (|J|W)^{.5} \quad s = 1, NSTR \quad (2.3.4)$$

where $NSTR = \text{number of strains}$

The product is now that of the transpose of a matrix and itself.

For the 8-node element, the terms related to normal strains were evaluated at 8 points (i.e. a $2 \times 2 \times 2$ integration scheme). To improve the performance of the 8-node element in modeling bending deformation, terms related to ϵ_5 and ϵ_6 were evaluated at the centroid only (ref. 3, 30, 31). The other shear strain terms related to ϵ_4 were evaluated with full integration. Both $2 \times 2 \times 2$ and $3 \times 3 \times 3$ integration schemes were considered for the 20-node element. There was not much difference in the behavior of the element for the two integration schemes, so the

$2 \times 2 \times 2$ integration scheme was used for the results presented herein.

2.4 Vectorized Implementation

The three-dimensional finite element program NONLIN3D developed for use in this study was designed to exploit the vector processing capabilities of a supercomputer, the CDC VPS32. The CDC VPS32 is closely related to the CDC CYBER 205. In the context of computation on the VPS32, a vector is simply a list of numbers; it is not a vector in the usual mathematical sense, wherein a vector has magnitude and direction. The architecture of the VPS32 is such that long vectors can be manipulated (i.e., multiplied, added, etc.) more than an order of magnitude faster than the individual terms could be manipulated separately. Ref. (32,33) gives some quantitative information on the processing speed. Processing speed is often expressed in terms of millions of floating point operations per second (MFLOPS). Actually, the speed is not the same for different operations. For example, multiplication is performed considerably faster than division. The following rates are applicable for multiplication and addition. For scalar operations, the processing speed is approximately 3-5 million MFLOPS. For very long vectors, the speed is 100-200 MFLOPS. Short vectors are not processed nearly so fast. However, a vector length of 110 to 160 will result in a rate of 50-100 MFLOPS. Obviously, it is highly advantageous to manipulate long vectors rather than scalars or short vectors.

To *vectorize* a program simply means to implement the mathematical algorithms in such a way that long lists of numbers are manipulated rather than individual numbers. There is usually no unique vectorization of a particular task. There is considerable room for ingenuity. In fact, successful vectorization of a task generally requires discarding of procedures familiar to the scalar programmer (for example, those procedures in familiar textbooks) and taking a fresh look at what has to be accomplished.

There are three subroutines which perform essentially all of the computation

intensive work in NONLIN3D. These are BOBL3D, ESTIF3D, and the equation solver. The subroutine BOBL3D calculates strains, stresses, and element forces. The subroutine ESTIF3D calculates element stiffness matrices. The equation solver will not be discussed, since vectorized versions of banded (ref. 34) and profile (a vectorized version of that in ref. 35) equation solvers are already available.

Reference 36 describes a vectorized procedure for calculating element stiffness matrices for linear high-order elements, which require a large number of quadrature points. The primary technique in ref. 36 was to manipulate the values of a parameter at all the quadrature points simultaneously, rather than individually. This resulted in vectors of length equal to NG (the number of quadrature points) and, at times, $NG * NS$, where NS = number of shape functions. At one stage of the stiffness matrix calculation in ref. 36 even larger vectors were manipulated, but the longer vectors were obtained at the expense of significant replication of vectors and fairly complicated logic. Reference 37 describes a technique which results in long vector lengths for low order elements, but it has the same drawbacks mentioned above for the technique in ref. 36. Also, the technique in ref. 37 has very large memory requirements. Techniques were developed in the current study which result in fairly long vector lengths without much replication, complexity, or memory requirements. Also many of the techniques used can be extended to process multiple elements at the same time, thereby increasing vector lengths. Simultaneous multiple element processing was not attempted for two reasons: 1) time constraints and 2) the expected reduction in total computation costs did not appear to justify further optimization of the routines.

To expedite the discussion of BOBL3D and ESTIF3D, special notation will be introduced. Also, simple vector programming methods are discussed. Vectors are given abbreviated names. A bar under a name indicates that it is the name of a vector. When vectors are separated by the symbol " * ", vector multiplication is implied. For example,

$$\underline{A} * \underline{B} = \underline{C} \quad (2.4.1)$$

is equivalent to $A_i \bar{B}_i = C_i$, with no sum on i . The vectors may also be stacked, for example,

$$\begin{bmatrix} \underline{A} \\ \underline{B} \\ \underline{C} \end{bmatrix} * \begin{bmatrix} \underline{D} \\ \underline{E} \\ \underline{F} \end{bmatrix} = \begin{bmatrix} \underline{A} * \underline{D} \\ \underline{B} * \underline{E} \\ \underline{C} * \underline{F} \end{bmatrix} \quad (2.4.2)$$

In all cases, vector multiplication refers to term by term multiplication without any summation. A dot “.” will be used to denote an inner product. A VPS32 special function is used to perform the inner products as a single vector operation.

It is very convenient to manipulate vectors just like scalars. For example, suppose we need the determinant of ten 2 x 2 matrices. In vector form, we would write the matrices as follows

$$\begin{bmatrix} \underline{A} & \underline{B} \\ \underline{C} & \underline{D} \end{bmatrix} \quad (2.4.3)$$

In eqn. 2.4.3 all 10 values of a coefficient are grouped in a single vector. Hence, the length of each vector in the matrix is 10. The 10 determinants are obtained using two vector multiplications and one vector subtraction

$$\text{the ten determinants} = \underline{A} * \underline{D} - \underline{C} * \underline{B} \quad (2.4.4)$$

Using scalar methods there would have been 20 scalar multiplications and 10 scalar subtractions.

Often it is desirable to perform replication of a scalar or vector in order to reduce the number of subsequent vector operations. For example, suppose we

need 20 copies of the vector \underline{a} stacked contiguously in the vector \underline{D} . Consider \underline{D} to consist of 20 subvectors \underline{d}^i , each of which have the same length as \underline{a} .

The first step is to assign values to \underline{d}^1 ; that is, set $\underline{d}^1 = \underline{a}$. Then assign $\underline{d}^2 = \underline{a}$.

$$\text{then assign } \begin{bmatrix} \underline{d}^3 \\ \underline{d}^4 \end{bmatrix} = \begin{bmatrix} \underline{d}^1 \\ \underline{d}^2 \end{bmatrix}$$

$$\text{Then assign } \begin{bmatrix} \underline{d}^5 \\ \underline{d}^6 \\ \underline{d}^7 \\ \underline{d}^8 \end{bmatrix} = \begin{bmatrix} \underline{d}^1 \\ \underline{d}^2 \\ \underline{d}^3 \\ \underline{d}^4 \end{bmatrix}$$

$$\text{Then assign } \begin{bmatrix} \underline{d}^9 \\ \underline{d}^{10} \\ \underline{d}^{11} \\ \underline{d}^{12} \\ \underline{d}^{13} \\ \underline{d}^{14} \\ \underline{d}^{15} \\ \underline{d}^{16} \end{bmatrix} = \begin{bmatrix} \underline{d}^1 \\ \underline{d}^2 \\ \underline{d}^3 \\ \underline{d}^4 \\ \underline{d}^5 \\ \underline{d}^6 \\ \underline{d}^7 \\ \underline{d}^8 \end{bmatrix}$$

$$\text{Finally assign } \begin{bmatrix} \underline{d}^{17} \\ \underline{d}^{18} \\ \underline{d}^{19} \\ \underline{d}^{20} \end{bmatrix} = \begin{bmatrix} \underline{d}^1 \\ \underline{d}^2 \\ \underline{d}^3 \\ \underline{d}^4 \end{bmatrix}$$

By using this technique the number of vector assignments is reduced from 20 to just 6.

The next two subsections describe the two routines B0BL3D and ESTIF3D.

2.4.1 Subroutine B0BL3D

Figure 2.4.1.1 shows a flowchart for B0BL3D. There are 8 primary tasks performed by this routine. The first task is to calculate local derivatives of the global coordinates at each of the quadrature points. The shape functions

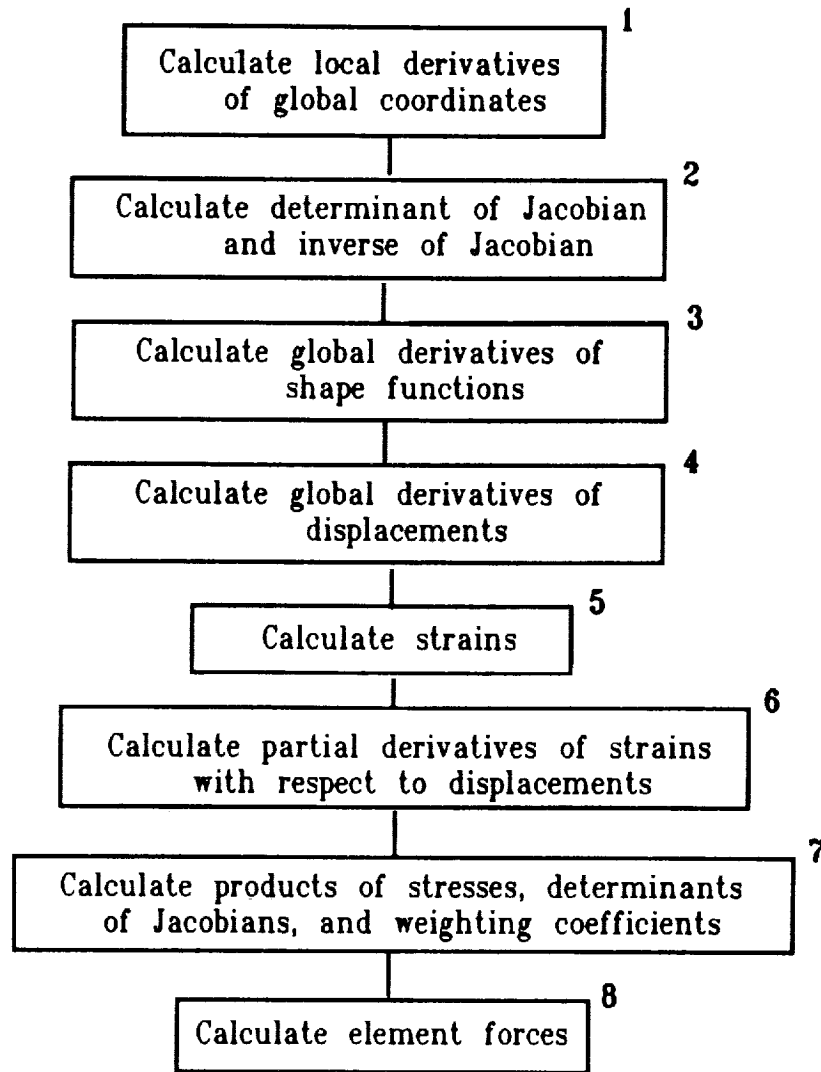


Fig. 2.4.1.1 Flowchart for subroutine BOBL3D.

are expressed in terms of local coordinates δ_r (see appendix), but derivatives with respect to global coordinates are required. The first step towards obtaining these derivatives is to calculate the local derivatives of the global coordinates, $\frac{\partial x}{\partial \delta_r}$, $\frac{\partial y}{\partial \delta_r}$, and $\frac{\partial z}{\partial \delta_r}$. Since an isoparametric formulation is used, the geometry is approximated with the same shape functions as the displacements. For example, $x = N^m x^m$ where $x^m =$ the x coordinate of the m^{th} node. Hence,

$$\frac{\partial x}{\partial \delta_r} = \frac{\partial(N^m x^m)}{\partial \delta_r} = \frac{\partial N^m}{\partial \delta_r} x^m \quad (2.4.1.1)$$

There are NS shape functions to be differentiated at NG quadrature points. For a single element type, the $\frac{\partial N^m}{\partial \delta_r}$ are invariant, so they are calculated only once and stored in DL in the following order.

$$\underline{DL} = \begin{bmatrix} \frac{\partial N}{\partial \delta_1} \\ \frac{\partial N}{\partial \delta_2} \\ \frac{\partial N}{\partial \delta_3} \end{bmatrix} \quad \text{where } \underline{N} = \begin{bmatrix} N^1 \\ N^2 \\ N^3 \\ \vdots \\ N^{NS} \end{bmatrix} \quad (2.4.1.2)$$

and $\underline{N}^m =$ the m^{th} shape function evaluated at each of the NG quadrature points. Note that \underline{N}^m has a length of NG. (The length of DL is 3 * NS * NG.)

The nodal coordinates for an element are stored in vectors X, Y, and Z. Each nodal coordinate is replicated NG times. The ordering is as follows for the vector X.

$$\underline{X} = \begin{bmatrix} x^1 \\ x^1 \\ \vdots \\ x^1 \\ x^2 \\ x^2 \\ \vdots \\ x^2 \\ \text{etc.} \end{bmatrix} \quad (2.4.1.3)$$

Note that the vector \underline{X} has a length of $NS * NG$. The vectors \underline{Y} and \underline{Z} are ordered the same way. The vectors \underline{X} , \underline{Y} , and \underline{Z} are stacked and replicated once to obtain a long vector \underline{XXYYZZ} . This stacking and replication reduces the number of vector multiplications required in the next step. The organization of \underline{XXYYZZ} is given by eqn. 2.4.1.4.

$$\underline{XXYYZZ} = \begin{bmatrix} \underline{X} \\ \underline{Y} \\ \underline{Z} \\ \underline{X} \\ \underline{Y} \\ \underline{Z} \end{bmatrix} \quad (2.4.1.4)$$

The vector \underline{XXYYZZ} is of length $6 * NS * NG$.

The derivatives of the global coordinates are obtained in two steps. First, three vector multiplications between \underline{DL} and parts of \underline{XXYYZZ} are performed and the results are stacked in \underline{D} , as shown in eqn. 2.4.1.5.

$$\underline{D} = \begin{bmatrix} \underline{DL} * \begin{bmatrix} \underline{X} \\ \underline{Y} \\ \underline{Z} \end{bmatrix} \\ \underline{DL} * \begin{bmatrix} \underline{Y} \\ \underline{Z} \\ \underline{X} \end{bmatrix} \\ \underline{DL} * \begin{bmatrix} \underline{Z} \\ \underline{X} \\ \underline{Y} \end{bmatrix} \end{bmatrix} \quad (2.4.1.5)$$

The length of \underline{D} is $9 * NS * NG$.

As indicated in eqn. 2.4.1.1, there are NS terms to be summed for each of the nine partial derivatives. After the summations, there will be NG values of each partial derivative. The vector \underline{D} in eqn. 2.4.1.5 is organized such that there are nine subvectors, each of length $NS * NG$. Recursive addition is used on each subvector to sum the appropriate terms. The vector product of $\frac{\partial N}{\partial \delta_1}$ (which is part of \underline{DL}) and \underline{X} will be used to illustrate the recursive addition. The number of nodes, NS, will be assumed to be 8. This product constitutes the first subvector in eqn. 2.4.1.5. The vector product of $\frac{\partial N}{\partial \delta_1}$ and \underline{X} creates a vector which consists of the subvectors \underline{d}_i (see eqn. 2.4.1.6).

$$\frac{\partial N}{\partial \delta_1} * \underline{X} = \begin{bmatrix} \underline{d}^1 \\ \underline{d}^2 \\ \underline{d}^3 \\ \underline{d}^4 \\ \underline{d}^5 \\ \underline{d}^6 \\ \underline{d}^7 \\ \underline{d}^8 \end{bmatrix} \quad (2.4.1.6)$$

where \underline{d}^m = the contribution from shape function m. The length of each \underline{d}^m is NG.

For example, $\underline{d}^2 = \frac{\partial N^2}{\partial \delta_1} * x^2$ evaluated at each of the NG quadrature points.

Now three recursive additions are performed to add up the \underline{d}^m .

$$\begin{bmatrix} \underline{d}_1 \\ \underline{d}_2 \\ \underline{d}_3 \\ \underline{d}_4 \end{bmatrix} = \begin{bmatrix} \underline{d}_1 \\ \underline{d}_2 \\ \underline{d}_3 \\ \underline{d}_4 \end{bmatrix} + \begin{bmatrix} \underline{d}_5 \\ \underline{d}_6 \\ \underline{d}_7 \\ \underline{d}_8 \end{bmatrix} \quad (2.4.1.7)$$

then

$$\begin{bmatrix} \underline{d}_1 \\ \underline{d}_2 \end{bmatrix} = \begin{bmatrix} \underline{d}_1 \\ \underline{d}_2 \end{bmatrix} + \begin{bmatrix} \underline{d}_3 \\ \underline{d}_4 \end{bmatrix} \quad (2.4.1.8)$$

finally, $\underline{d}_1 = \underline{d}_1 + \underline{d}_2$

The vector \underline{d}_1 now contains $\frac{\partial x}{\partial \delta_1}$ evaluated at NG quadrature points. The other eight derivatives ($\frac{\partial x}{\partial \delta_2}, \frac{\partial x}{\partial \delta_3}, \frac{\partial y}{\partial \delta_1}$, etc.) are obtained in a similar fashion. For example, the derivative $\frac{\partial y}{\partial \delta_2}$ is obtained by replacing δ_1 with δ_2 and \underline{X} with \underline{Y} in eqn. 2.4.1.6.

The second task in BOBL3D is the calculation of the determinant and inverse of the Jacobian at each of the quadrature points. The Jacobian consists of derivatives of the global coordinates with respect to the local coordinates. The scalar form is shown in eqn. 2.4.1.9.

$$J = \begin{bmatrix} \frac{\partial x}{\partial \delta_1} & \frac{\partial y}{\partial \delta_1} & \frac{\partial z}{\partial \delta_1} \\ \frac{\partial x}{\partial \delta_2} & \frac{\partial y}{\partial \delta_2} & \frac{\partial z}{\partial \delta_2} \\ \frac{\partial x}{\partial \delta_3} & \frac{\partial y}{\partial \delta_3} & \frac{\partial z}{\partial \delta_3} \end{bmatrix} \quad (2.4.1.9)$$

In the vector implementation, the entries in J are vectors (the vectors which were calculated in task 1). For example, J_{11} is a vector consisting of $\frac{\partial x}{\partial \delta_1}$ evaluated at NG points. The inversion and determinant are performed explicitly in terms of these vectors. The result is an inverse which has entries which are vectors of length NG and a determinant vector of length NG.

Next the global derivatives of the shape functions are calculated at each quadrature point (task 3, Fig. 2.4.1.1). These derivatives are calculated by multiplying the local derivatives by the inverse of the Jacobian. The scalar form is shown in eqn. 2.4.1.10.

$$\begin{bmatrix} \frac{\partial N^m}{\partial x} \\ \frac{\partial N^m}{\partial y} \\ \frac{\partial N^m}{\partial z} \end{bmatrix} = \begin{bmatrix} IJ_{11} & IJ_{12} & IJ_{13} \\ IJ_{21} & IJ_{22} & IJ_{23} \\ IJ_{31} & IJ_{32} & IJ_{33} \end{bmatrix} \begin{bmatrix} \frac{\partial N^m}{\partial \delta_1} \\ \frac{\partial N^m}{\partial \delta_2} \\ \frac{\partial N^m}{\partial \delta_3} \end{bmatrix} \quad (2.4.1.10)$$

where the matrix IJ is the inverse of J.

In the vector implementation, the entries in eqn. 2.4.1.10 are replaced by vectors of length NG. For example, the NG values of $\frac{\partial N^2}{\partial x}$ are obtained as follows

$$\frac{\partial N^2}{\partial x} = IJ_{11} * \frac{\partial N^2}{\partial \delta_1} + IJ_{12} * \frac{\partial N^2}{\partial \delta_2} + IJ_{13} * \frac{\partial N^2}{\partial \delta_3} \quad (2.4.1.11)$$

where IJ_{ij} = the i, j vector term in the inverse Jacobian matrix, calculated in task 2, and N^2 is defined in eqn. 2.4.1.2.

The nine global derivatives of the displacements ($\frac{\partial u}{\partial x}$, $\frac{\partial u}{\partial y}$, ..., etc.) with respect to the global coordinates can now be calculated (task 4). A typical term is:

$$\frac{\partial u}{\partial x} = u_x = \frac{\partial N^m}{\partial x} * u^m \quad (2.4.1.12)$$

For convenience, a subscript is used to indicate the variable of differentiation. For example, $u_x = \frac{\partial u}{\partial x}$ and $u_z = \frac{\partial u}{\partial z}$.

This is exactly the same form as in eqn. 2.4.1.1. The local derivative $\frac{\partial}{\partial \delta_r}$, has been replaced by the global derivative $\frac{\partial}{\partial x}$, and the nodal coordinates, x^m , have been replaced by nodal displacements, u^m . Consequently, the same vector

procedure that was used earlier to calculate local derivatives of coordinates is now used to calculate global derivatives of displacements. A vector \underline{DG} is assembled from the global derivatives of the shape functions.

$$\underline{DG} = \begin{bmatrix} \underline{N}_x \\ \underline{N}_y \\ \underline{N}_z \end{bmatrix} \quad (2.4.1.13)$$

where \underline{N} is defined in eqn. 2.4.1.2. The subscript indicates the variable of differentiation. Note that the length of the vector \underline{DG} is $3 * \text{NG} * \text{NS}$.

Equation 2.4.1.13 is simply a “global derivative” version of eqn. 2.4.1.2. Also, a displacement vector \underline{uuvw} is assembled.

$$\underline{uuvw} = \begin{bmatrix} \underline{u} \\ \underline{v} \\ \underline{w} \\ \underline{u} \\ \underline{v} \\ \underline{w} \end{bmatrix} \quad (2.4.1.14)$$

The organization of \underline{u} , \underline{v} , and \underline{w} are identical to \underline{x} , \underline{y} , and \underline{z} respectively. For example, in eqn. 2.4.1.3 replace x^1, x^2, \dots by u^1, u^2, \dots . Now the vector procedure used earlier can be used by simply replacing \underline{DL} by \underline{DG} and \underline{xyyzz} by \underline{uuvw} . Two copies of the shape function derivatives, N_x , N_y , and N_z , are stored in \underline{DSXYZ} (eqn. 2.4.1.15).

$$\underline{DSXYZ} = \begin{bmatrix} \underline{DG} \\ \underline{DG} \end{bmatrix} \quad (2.4.1.15)$$

The vector \underline{DSXYZ} is of length of $6 * \text{NG} * \text{NS}$.

Task 5 is to calculate strains. The strains are calculated using eqn. 2.1.4,

except that the scalar variables are replaced by vectors of length NG. Thus, the value of a strain component is calculated at all integration points simultaneously. For example,

$$\underline{\varepsilon}_x = \underline{u}_x + \frac{1}{2}(\underline{u}_x * \underline{u}_x + \underline{v}_x * \underline{v}_x + \underline{w}_x * \underline{w}_x) \quad (2.4.1.16)$$

This is possible because the global derivatives of the displacements (calculated in task 4) are organized such that for each displacement derivative, all NG values are contiguous in memory. The strains are stored in the vector $\underline{\varepsilon}$ in the following order.

$$\underline{\varepsilon} = \begin{bmatrix} \underline{\varepsilon}_1 \\ \underline{\varepsilon}_2 \\ \underline{\varepsilon}_3 \\ \underline{\varepsilon}_4 \\ \underline{\varepsilon}_5 \\ \underline{\varepsilon}_6 \end{bmatrix} \quad (2.4.1.17)$$

where the length of each $\underline{\varepsilon}_i$ is NG.

Task 6 is to calculate the partial derivatives of the strains with respect to the displacements. The scalar form of these derivatives is shown in eqn. 2.2.3. These involve derivatives of the shape functions (for example, N_x^m) and products of the derivatives of the shape functions and displacements (for example, $u_x N^m$). There are 27 products. To reduce the number of vector operations in forming the products, stacks of vectors are manipulated, as described next.

The displacement derivatives calculated in task 4 are replicated (for a total of NS copies of each derivative) and stacked in the vector \underline{DD} .

$$\underline{DD} = \begin{bmatrix} \underline{Ru_x} \\ \underline{Rv_y} \\ \underline{Rw_z} \\ \underline{Rv_x} \\ \underline{Rw_y} \\ \underline{Ru_z} \\ \underline{Rw_x} \\ \underline{Ru_y} \\ \underline{Rv_z} \end{bmatrix} \quad \underline{Ru_x} = \begin{bmatrix} \underline{u_x} \\ \underline{u_x} \\ \vdots \\ \vdots \\ \underline{u_x} \end{bmatrix} \quad \text{--- NS copies} \quad (2.4.1.18)$$

similarly for other subvectors in DD

Note that the displacement derivative vectors $\underline{u_x}$, $\underline{v_y}$, etc. are replicated NS times. Hence, the vector DD is of length 9 * NS * NG. This is in preparation for multiplication with the shape function derivatives, since, for example, the length of $\underline{u_x}$ is NG but the length of N_y is NG * NS. To expedite the discussion of the use of these replicated vectors, the use of the prefix "R" will be used to denote replication. The required products are calculated by performing vector multiplications of parts of DD with parts of DSXYZ. These products are stored in a vector BLV.

$$\underline{BLV} = \left[\begin{array}{l} \left[\begin{array}{l} \underline{Ru_x} \\ \underline{Rv_y} \\ \underline{Rw_z} \end{array} \right] * \left[\begin{array}{l} \underline{N_x} \\ \underline{N_y} \\ \underline{N_z} \end{array} \right] \\ \left[\begin{array}{l} \underline{Rv_x} \\ \underline{Rw_y} \\ \underline{Ru_z} \end{array} \right] * \left[\begin{array}{l} \underline{N_x} \\ \underline{N_y} \\ \underline{N_z} \end{array} \right] \\ \left[\begin{array}{l} \underline{Rv_y} \\ \underline{Rw_z} \\ \underline{Rv_x} \\ \underline{Rw_y} \\ \underline{Ru_z} \\ \underline{Rw_x} \end{array} \right] * \left[\begin{array}{l} \underline{N_x} \\ \underline{N_y} \\ \underline{N_z} \\ \underline{N_x} \\ \underline{N_y} \\ \underline{N_z} \end{array} \right] \\ \left[\begin{array}{l} \underline{Rw_z} \\ \underline{Rv_x} \\ \underline{Rw_y} \\ \underline{Ru_z} \\ \underline{Rw_x} \end{array} \right] * \left[\begin{array}{l} \underline{N_x} \\ \underline{N_y} \\ \underline{N_z} \\ \underline{N_x} \\ \underline{N_y} \\ \underline{N_z} \end{array} \right] \\ \underline{Rv_y} * \underline{N_z} \\ \left[\begin{array}{l} \underline{Rw_x} \\ \underline{Ru_y} \\ \underline{Rv_z} \end{array} \right] * \left[\begin{array}{l} \underline{N_x} \\ \underline{N_y} \\ \underline{N_z} \end{array} \right] \\ \underline{Ru_x} * \underline{N_y} \\ \left[\begin{array}{l} \underline{Ru_y} \\ \underline{Rv_z} \end{array} \right] * \left[\begin{array}{l} \underline{N_x} \\ \underline{N_y} \end{array} \right] \\ \underline{Ru_x} * \underline{N_z} \\ \underline{Rv_z} * \underline{N_x} \end{array} \right] \quad (2.4.1.19)$$

Note that only 9 vector products are required to form the 27*NS+NG products in BLV.

Now it is a simple matter to form a vector of the 18 strain derivatives by adding vectors stored in DG and BLV.

$$\begin{array}{l}
 \underline{B}_{11} \\
 \underline{B}_{21} \\
 \underline{B}_{31} \\
 \underline{B}_{41} \\
 \underline{B}_{51} \\
 \underline{B}_{61} \\
 \underline{B}_{12} \\
 \underline{B}_{22} \\
 \underline{B}_{32} \\
 \underline{B}_{42} \\
 \underline{B}_{52} \\
 \underline{B}_{62} \\
 \underline{B}_{13} \\
 \underline{B}_{23} \\
 \underline{B}_{33} \\
 \underline{B}_{43} \\
 \underline{B}_{53} \\
 \underline{B}_{63}
 \end{array}
 =
 \begin{array}{l}
 \underline{N}_x + \underline{u}_x \underline{N}_x \\
 \underline{u}_y \underline{N}_y \\
 \underline{u}_z \underline{N}_z \\
 \underline{N}_y + \underline{u}_x \underline{N}_y + \underline{u}_y \underline{N}_x \\
 \underline{u}_z \underline{N}_y + \underline{u}_y \underline{N}_z \\
 \underline{N}_z + \underline{u}_z \underline{N}_x + \underline{u}_x \underline{N}_z \\
 \underline{v}_x \underline{N}_x \\
 \underline{N}_y + \underline{v}_y \underline{N}_y \\
 \underline{v}_z \underline{N}_z \\
 \underline{N}_x + \underline{v}_y \underline{N}_x + \underline{v}_x \underline{N}_y \\
 \underline{N}_z + \underline{v}_y \underline{N}_z + \underline{v}_z \underline{N}_y \\
 \underline{v}_x \underline{N}_z + \underline{v}_z \underline{N}_x \\
 \underline{w}_x \underline{N}_x \\
 \underline{w}_y \underline{N}_y \\
 \underline{N}_z + \underline{w}_z \underline{N}_z \\
 \underline{w}_y \underline{N}_x + \underline{w}_x \underline{N}_y \\
 \underline{N}_y + \underline{w}_z \underline{N}_y + \underline{w}_y \underline{N}_z \\
 \underline{N}_x + \underline{w}_x \underline{N}_z + \underline{w}_z \underline{N}_x
 \end{array}
 \tag{2.4.1.20}$$

where the \underline{B}_{i_j} are vector versions of the B_{i_j} shown in eqn. 2.2.4. The length of

each is $NS \cdot NG$. Since the \underline{B}_{ij} are formed using vector operations, the organization of each \underline{B}_{ij} in terms of the NS shape function contributions and NG quadrature point values is the same as for \underline{N} , described in eqn. 2.4.1.2. For example,

$$\underline{B}_{11} = \begin{bmatrix} \underline{B}_{11}^1 \\ \underline{B}_{11}^2 \\ \underline{B}_{11}^3 \\ \vdots \\ \vdots \\ \vdots \\ \vdots \\ \underline{B}_{11}^{NS} \end{bmatrix} \quad \text{and the length of each subvector } \underline{B}_{11}^m \text{ is } NG \quad (2.4.1.21)$$

Task 7 is to calculate the product of the stresses, determinant of the Jacobian, $|J|$, and weighting coefficient W . The first step is to assemble a vector containing copies of $|J| \cdot W$ evaluated at the NG quadrature points.

$$\underline{DDJJWW} = \begin{bmatrix} \underline{DJW} \\ \underline{DJW} \\ \underline{DJW} \\ \vdots \\ \vdots \\ \vdots \\ \underline{DJW} \end{bmatrix} \quad \text{--- --- } NSTR \text{ replicates of } \underline{DJW} \quad (2.4.1.22)$$

where $\underline{DJW} = |J| \cdot W$ evaluated at NG quadrature points and $NSTR =$ number of strains ($NSTR = 6$ for 3D analysis)

The vectors of the strains ε_i are stacked in memory, (see eqn. 2.4.1.17) so that only a single vector multiplication of the stacked strains and \underline{DDJJWW} is

required to obtain the scaled strains $\hat{\underline{\epsilon}}$.

$$\hat{\underline{\epsilon}} = \begin{bmatrix} \hat{\epsilon}_1 \\ \hat{\epsilon}_2 \\ \hat{\epsilon}_3 \\ \hat{\epsilon}_4 \\ \hat{\epsilon}_5 \\ \hat{\epsilon}_6 \end{bmatrix} = \underline{DDJJWW} * \begin{bmatrix} \epsilon_1 \\ \epsilon_2 \\ \epsilon_3 \\ \epsilon_4 \\ \epsilon_5 \\ \epsilon_6 \end{bmatrix} \quad (2.4.1.23)$$

The scaled stresses are obtained by linear combination of the scaled strains.

$$\hat{\sigma}_i = C_{ij} \hat{\epsilon}_j \quad (2.4.1.24)$$

This is analogous to the unscaled, scalar stresses in eqn. 2.1.5. For efficiency later, the $\hat{\sigma}_i$ are stacked contiguously in $\hat{\underline{\sigma}}$ in a form which is exactly analogous to the stacking of $\underline{\epsilon}_i$ in eqn. 2.4.1.17.

The final task in BOBL3D is to calculate the element forces R^α corresponding to the current stress state. The element forces are calculated using a vectorized version of the summation in eqn. 2.3.1. For clarity in the following discussion, the displacements q^α are separated into u, v, and w, the displacements in the x-, y-, and z-directions. The vector form of the strain derivatives in eqn. 2.3.1 are in the large vector \underline{B} (see eqn. 2.4.1.20).

The vector implementation of the summation in eqn. 2.3.1 will be illustrated by describing the calculation of the x-direction forces next. The first step in calculating the x-direction forces is to evaluate the products in eqn. 2.3.1 at all NG quadrature points and for all NS nodes. Recall that values of the triple product $(\sigma_i |J|W)^\theta$ are already available in the vector $\hat{\underline{\sigma}}$. At each quadrature point each stress must be multiplied by NS values related to each derivative of the strains. To reduce the number of vector multiplications, the weighted stresses are replicated and stored as follows.

where $\underline{R\hat{\sigma}}_i$ is a replicated form of $\hat{\sigma}_i$

$$\underline{R\hat{\sigma}} = \begin{bmatrix} \underline{R\hat{\sigma}}_1 \\ \underline{R\hat{\sigma}}_2 \\ \underline{R\hat{\sigma}}_3 \\ \underline{R\hat{\sigma}}_4 \\ \underline{R\hat{\sigma}}_5 \\ \underline{R\hat{\sigma}}_6 \end{bmatrix} \quad \text{For example,} \quad (2.4.1.25)$$

$$\underline{R\hat{\sigma}}_1 = \begin{bmatrix} \hat{\sigma}_1 \\ \hat{\sigma}_1 \\ \vdots \\ \hat{\sigma}_1 \end{bmatrix} \quad \text{--- NS copies of } \hat{\sigma}_1$$

The length of $\underline{R\hat{\sigma}}$ is $6 * NS * NG$

Now all the products for the x-direction can be formed with a single vector multiplication (eqn. 2.4.1.26).

$$\underline{f} = \begin{bmatrix} \underline{f}_1 \\ \underline{f}_2 \\ \underline{f}_3 \\ \underline{f}_4 \\ \underline{f}_5 \\ \underline{f}_6 \end{bmatrix} = \begin{bmatrix} \underline{B}_{11} \\ \underline{B}_{21} \\ \underline{B}_{31} \\ \underline{B}_{41} \\ \underline{B}_{51} \\ \underline{B}_{61} \end{bmatrix} * \begin{bmatrix} \hat{\sigma}_1 \\ \hat{\sigma}_2 \\ \hat{\sigma}_3 \\ \hat{\sigma}_4 \\ \hat{\sigma}_5 \\ \hat{\sigma}_6 \end{bmatrix} \quad (2.4.1.26)$$

Now recursive addition is used to sum the \underline{f}_i , as follows.

$$\begin{bmatrix} \underline{f}_1 \\ \underline{f}_2 \\ \underline{f}_3 \end{bmatrix} = \begin{bmatrix} \underline{f}_1 \\ \underline{f}_2 \\ \underline{f}_3 \end{bmatrix} + \begin{bmatrix} \underline{f}_4 \\ \underline{f}_5 \\ \underline{f}_6 \end{bmatrix} \quad (2.4.1.27)$$

then $\underline{f}_1 = \underline{f}_1 + \underline{f}_2 + \underline{f}_3$.

The content of \underline{f}_1 is now

$$\underline{f}_1 = \begin{bmatrix} \text{NG terms to be summed to obtain } F_x^1 \\ \text{NG terms to be summed to obtain } F_x^2 \\ \vdots \\ \text{NG terms to be summed to obtain } F_x^{NS} \end{bmatrix} \quad (2.4.1.28)$$

where $F_x^m = x$ -direction force at node m .

The summations required to obtain the F_x^m from the terms in \underline{f}_1 are performed using a VPS32 special function which is optimized for summing contiguous numbers in storage locations. The y - and z -direction nodal forces are obtained in a similar manner.

2.4.2 Subroutine ESTIF3D

The routine ESTIF3D is used to calculate the tangential stiffness matrix, which consists of the large displacement matrix, K_L and the geometric (or initial stress) matrix (eqn. 2.3.2). The large displacement matrix involves derivatives of the strains (which are in \underline{B}_{ij}), the Cholesky factors Q_{is} for the constitutive matrix ($C_{ij} = Q_{is}Q_{js}$), and the square root of the products $|J|W$. From eqn. 2.3.3, we see that for each term $(K_L)^{\alpha\beta}$, there are NG inner products to be evaluated. For example,

$$K_L^{13} = \sum_{\theta=1}^{NG} (T^{s1}T^{s3})^\theta \quad s = 1, NSTR \quad (2.4.2.1)$$

The vector \underline{T} is formed which contains the T^{sm} at the NG quadrature points and is organized such that all NG inner products for a particular stiffness matrix term can be performed at once. The first step in forming the vector \underline{T} is to perform a vector version of the product $Q_{is} * \frac{\partial \epsilon_i}{\partial q^\alpha}$. The strain derivatives are available in the vectors \underline{B}_{ij} . Since the Cholesky factor terms Q_{is} are scalars, the resultant product vectors \underline{P}_{ij} are simply linear combinations of the vectors \underline{B}_{ij} .

$$\underline{P}_{ij} = Q_{ti}\underline{B}_{tj} \quad (2.4.2.2)$$

The organization of the product vectors \underline{P}_{ij} is the same as for \underline{B}_{ij} (in terms of contributions for NS nodes and NG quadrature points). Also, the \underline{P}_{ij} are

stacked contiguously in memory as \underline{P} just like the \underline{B}_i in \underline{B} (see eqn. 2.4.1.20). Now the vector is reordered so that terms which will be summed are contiguous. The reordering is performed using a special VPS32 function referred to as Q8VGATHR. Equation 2.4.2.3 gives the order of \underline{T} , which is the reordered version of \underline{P} .

$$\underline{T} = \begin{bmatrix} \underline{T}_x^1 \\ \text{---} \\ \underline{T}_y^1 \\ \text{---} \\ \underline{T}_z^1 \\ \text{---} \\ \cdot \\ \cdot \\ \cdot \\ \text{---} \\ \underline{T}_x^{NS} \\ \text{---} \\ \underline{T}_y^{NS} \\ \text{---} \\ \underline{T}_z^{NS} \end{bmatrix} = \begin{bmatrix} \left. \begin{array}{l} \underline{P}_{11}^1 \\ \underline{P}_{21}^1 \\ \underline{P}_{31}^1 \\ \underline{P}_{41}^1 \\ \underline{P}_{51}^1 \\ \underline{P}_{61}^1 \end{array} \right\} = \underline{T}_x^1 \\ \text{---} \\ \left. \begin{array}{l} \underline{P}_{12}^1 \\ \underline{P}_{22}^1 \\ \underline{P}_{32}^1 \\ \underline{P}_{42}^1 \\ \underline{P}_{52}^1 \\ \underline{P}_{62}^1 \end{array} \right\} = \underline{T}_y^1 \\ \text{---} \\ \left. \begin{array}{l} \underline{P}_{13}^1 \\ \underline{P}_{23}^1 \\ \underline{P}_{33}^1 \\ \underline{P}_{43}^1 \\ \underline{P}_{53}^1 \\ \underline{P}_{63}^1 \end{array} \right\} = \underline{T}_z^1 \\ \text{---} \\ \text{similarly for} \\ \text{shape functions} \\ \text{2 through NS} \end{bmatrix} \quad (2.4.2.3)$$

In \underline{T} , the \underline{P}_{11}^m vectors are placed according to the shape function with which the term is associated. The same is the case for other \underline{P}_{ij}^m vectors. Recall that in \underline{P}_{ij} , all NS \underline{P}_{11}^m vectors were stacked together. The subvectors \underline{T}_x^m , T_y^m , and T_z^m are introduced here for convenience later. These subvectors are stored contiguously in eqn. 2.4.2.3 for convenience later in determining pointers for the inner products. The length of each subvector is 6 * NG. The subscripts x, y, and z indicate that these subvectors contain terms related to the x-, y-, and z-directions, respectively.

The terms in \underline{T} must be multiplied by the square root of the determinants and weights (i.e. $\sqrt{|J|W}$ terms) to obtain \hat{T} . To reduce the number of vector multiplications, the square root of \underline{DJW} (which has a length of NG) was calculated and then replicated to obtain the vector \underline{SDJW} which has a length of 3 * NS * NSTR * NG. Then only a single vector multiplication is required to form the vector \hat{T} .

$$\hat{T} = \underline{T} * \underline{SDJW} \quad (2.4.2.4)$$

The terms in K_L are simply the inner products involving the subvectors \underline{T}_x^m , \underline{T}_y^m , and \underline{T}_z^m .

For example, the term in K_L related to the first shape function and the x-direction and the fourth shape function and the y-direction is

$$\hat{T}_x^1 \cdot \hat{T}_y^4 \quad (2.4.2.5)$$

The inner products (indicated by the " . ") were performed by a VPS-32 special function.

The geometric stiffness matrix involves much less manipulation than K_L . The terms $C_{ij}\sigma_j|J|W$ are already available in the vector $\hat{\sigma}$. Equation 2.2.5 gives the scalar form of the second partial derivatives of the strains. Note that the

derivatives are independent of the direction of the displacements variable. Hence, the three nonzero stiffness terms associated with each coordinate direction for each combination of shape functions are the same. These derivatives consist of products of the derivatives of the shape functions with respect to the global coordinates, which are stored in the vector DSXYZ. For a particular shape function, the NG values of each second partial derivative is calculated by performing vector multiplications and additions with the appropriate subvectors (of length NG) in DSXYZ. The second partial derivatives are stored contiguously in memory, so each stiffness term is calculated with a single inner product of the stress vector $\hat{\sigma}$ and the second partial derivatives.

$$k^{mn} = \begin{bmatrix} \underline{a}_1^{mn} \\ \underline{a}_2^{mn} \\ \underline{a}_3^{mn} \\ \underline{a}_4^{mn} \\ \underline{a}_5^{mn} \\ \underline{a}_6^{mn} \end{bmatrix} \cdot \hat{\sigma} \quad (2.4.2.6)$$

$$\text{where } \underline{a}_i^{mn} = \frac{\partial^2 \epsilon_i}{\partial u^m \partial u^n} = \frac{\partial^2 \epsilon_i}{\partial v^m \partial v^n} = \frac{\partial^2 \epsilon_i}{\partial w^m \partial w^n}.$$

The k^{mn} are assembled in the element stiffness matrix as follows.

$$\begin{bmatrix} k^{11} & 0 & 0 & k^{12} & 0 & 0 & \dots \\ 0 & k^{11} & 0 & 0 & k^{12} & 0 & \dots \\ 0 & 0 & k^{11} & 0 & 0 & k^{12} & \dots \\ k^{12} & 0 & 0 & k^{22} & 0 & 0 & \dots \\ 0 & k^{12} & 0 & 0 & k^{22} & 0 & \dots \\ 0 & 0 & k^{12} & 0 & 0 & k^{22} & \dots \\ \vdots & \vdots & \vdots & \vdots & \vdots & \vdots & \ddots \end{bmatrix} \quad (2.4.2.7)$$

2.4.3 Execution Times

This section discusses the results of several CPU "time trials" which quantify the advantages of using vector algorithms on the VPS32. The following discussion is for the 20-node element and a $2 \times 2 \times 2$ integration scheme, except as noted.

One of the programs available in the Fatigue and Fracture Branch at NASA Langley Research Center used a non-vectorized algorithm to calculate the linear element stiffness matrix for the 20-node element. This algorithm took .33 second of CPU to calculate the linear element stiffness matrix for one element. A vector version of this program took only .014 second of CPU for the same calculation. The program NONLIN3D was tailored for geometrically nonlinear analysis. No provision is provided (as of this writing) for calculating just the linear stiffness matrix. So a comparable timing is not available for NONLIN3D. However, the total time for NONLIN3D to obtain 1) the tangential stiffness matrix (which includes both the large displacement stiffness matrix and the geometric stiffness matrix), 2) the element strains and stresses, and 3) the element forces was only .015 second per element. Since these three calculations involve many more terms than the linear stiffness matrix, the algorithms developed for NONLIN3D can be considered to be very well vectorized.

Timings were also obtained for NONLIN3D for a $3 \times 3 \times 3$ scheme. For the three tasks listed in the previous paragraph, the total time was .0215 CPU second per element. This is only 40 percent more time than for the $2 \times 2 \times 2$ scheme. For a scalar code, the time per element would have increased by more than a factor of three, since there are 27 quadrature points for the $3 \times 3 \times 3$ scheme instead of the 8 for the 2×2 scheme. The reason that the time increased by only 40 percent is that the more refined integration scheme has longer vector lengths, but the number of vector operations is unchanged.

2.5 Eigenvalue Analysis of the Element Stiffness Matrices

The finite element stiffness matrix should permit rigid body translation and rotation of the element without inducing any strain-energy. Further, there should be strain-energy whenever the element is deformed. For displacement formulated finite elements which are integrated with exact numerical integration, there is usually no problem. However, at times it is desirable to use a lower order of numerical integration in order to improve the performance of an element in modeling bending deformation (ref. 3, 30, 31) or simply to reduce the number of computations required to form the element stiffness matrix. Whenever a reduced order of numerical integration is used, there is the possibility of introducing zero-energy deformation modes; that is, the element can deform in certain modes without the expenditure of any work.

A convenient method of detecting zero-energy deformation modes is to perform an eigenvalue analysis on the element stiffness matrix. The eigenvalue analysis is described next. The following discussion is based in large part on ref. 38.

The eigenvalue problem has the general form

$$K\delta = \lambda\delta \quad (2.5.1)$$

The solution of eqn. 2.5.1 yields "n" eigenvalues and eigenvectors, where n = the number of degrees of freedom (DOF) in the element. For example, the 20-node 3D element has 60 DOF, so $n = 60$. For a 3D element there should be 6 rigid body modes ... 3 translations and 3 rotations. An excess of 6 rigid body modes indicates the presence of spurious zero-energy deformation modes. Less than 6 rigid body modes indicates that strain is associated even with rigid body motion. The eigenvalue corresponding to each rigid body mode should equal zero. This is apparent when eqn. 2.5.1 is pre-multiplied by the transpose of δ .

$$\delta^T K \delta = \delta^T \lambda \delta \quad (2.5.2)$$

The left side of the equation is simply twice the strain energy in the element when it undergoes the displacements δ . For rigid body motion the energy should be zero. The right hand side of the equation is zero only if all the displacements are zero (which is the trivial solution) or if $\lambda = 0$.

Early check-out runs of NONLIN3D used the reduced integration 8-node element to analyse a very simple configuration. The stiffness matrix was found to be singular, which indicted that the zero-energy deformation modes might be causing problems. Eigenvalue analyses of the element stiffness matrix showed that there is one zero-energy deformation mode for each shear strain treated with reduced integration. The cause for this can be seen readily by considering a set of displacements which causes a shear strain ϵ_5 which varies linearly in the x-direction, does not vary with y or z, and is zero at the centroid. If only the centroidal value of the strain is sampled, the strain will be determined to be zero and there will be no energy associated with the deformation. For many problems the boundary conditions are such that the spurious zero-energy deformation modes do not cause any major problems. Section 4.2 discusses the results of an attempt to use the reduced integration 8-node element for analysis of a postbuckled sublaminar.

2.6 Substructuring

The program NONLIN3D was designed to perform analysis by substructures. A brief description of the substructuring technique is given here. More details can be found in ref. 39. In addition to reducing computer memory requirements, substructuring allows the structure to be modeled as a combination of linear and nonlinear components. For the configurations studied herein (figure 1.1 and 1.2), linear analysis is appropriate everywhere except the majority of the postbuckled region. By substructuring into linear and nonlinear regions, expensive iterative

solution is needed for only a fraction of the equations.

In this study, two substructures were used: one linear and one nonlinear. The substructuring procedure begins by obtaining a reduced stiffness matrix and load vector for the linear region. The reduced stiffness matrix can be treated as the stiffness matrix for just another type of element. Because of the large number of nodes, this element will be referred to as a superelement. The stiffness matrix and load vector are "reduced" in the sense that only the nodes shared by the two substructures (the interface nodes) are included.

The technique used for calculating the reduced stiffness coefficients utilized the formal definition of a stiffness coefficient: a stiffness coefficient is related to the restraint forces required to maintain unit displacement at one degree of freedom (DOF) and zero displacement at the remainder of the element DOF. Suppose there are to be n DOF in the superelement. These n DOF are restrained. One of these DOF is specified to have a unit displacement (and there are no other loads) and the governing equations are solved. The restraint forces at all n DOF constitute one column of the reduced stiffness matrix. This procedure is repeated for all n DOF. The reduced load vector is obtained in a similar fashion. All n DOF in the superelement are still restrained. However, now the specified loads for the linear region are applied. The reduced load vector is equal to the negative of the restraint forces at the restrained nodes.

Once the superelement stiffness matrix and load vector are calculated, the analysis proceeds to the nonlinear substructure. Whenever the nonlinear stiffness matrix and load vector are formed, the interaction with the linear substructure is included by simply adding the superelement stiffness matrix and load vector. When the internally generated nodal forces are calculated to determine residuals, the contribution of the linear substructure consists of the product of the superelement stiffness matrix and the superelement nodal displacements.

For the configuration analyzed, the delamination front is within the linear

substructure. Hence, further work is required even after obtaining a converged solution for the nonlinear substructure. After obtaining a converged solution, the displacements for the interface nodes are known. These displacements fully account for the effect of the nonlinear substructure on the linear substructure. That is, the displacements in the linear substructure can be determined as though there was no other substructure, except that the magnitudes of the displacements at the interface nodes are specified. To reduce the computer resource requirements, it is usually advantageous to obtain multiple solutions for the nonlinear substructure and then obtain multiple solutions for the linear substructure.

2.7 Contact Analysis

For certain combinations of delamination size and strain level, closure occurs over part of the delamination front. Unless constraints are imposed, the delamination faces will overlap in the analysis. When contact constraints are added, there are two types of geometric nonlinearity: that due to significant rotations and that due to the unknown contact area. Since the contact area affects the global response and vice versa, the iterative loop includes two inner iterative loops for obtaining either the effects of significant rotation or the contact area. Because of the selected substructuring, there are two substructures in which contact can occur. But, as mentioned in section 2.6, one of the substructures was treated with linear analysis. Strictly speaking, there is not a linear substructure now. However, an "engineering" (as opposed to a purist) approach was taken in implementing the contact analysis. If only a small fraction of the original interpenetration is permitted, then most of the effect of imposing full contact constraints will be seen. Also, because of the nature of the problem, large interpenetration cannot occur in the "linear" substructure if large interpenetration is prevented in the nonlinear substructure. Hence, the approach taken was to perform nonlinear analysis on the buckled region only.

There was also an approximation made in how the constraints were imposed.

Fig. 2.7.1 will be used to explain this approximation. The figure shows a disk resting on a base. Constraints are imposed to prevent the disk from overlapping the base. Ideally the constraints would be imposed such that the constraint force on the disk is provided by the node it contacts on the base. A free-body diagram would look like Fig. 2.7.1b. In NONLIN3D the constraint force on the disk is supplied externally, so the free-body diagram looks like that in Fig. 2.7.1c. Obviously there is some error due to using an external force, but the amount of error and its importance depends on the individual problem.

Unfortunately, for the postbuckled sublaminates, the computational effort would have been too large to perform a more rigorous analysis to determine the amount of error. However, since the base laminate has a $w=0$ boundary condition on the plane $z=0$, the effect of applying an external force rather than reacting the contact force on the base laminate is probably small.

The flow chart in Fig. 2.7.2 outlines the procedure used to perform the contact analysis. In the flowchart the term *nonlinear solution* refers to solving the governing equilibrium equations (eqns. 2.1.2) with the current set of contact constraints. The first step is to check for w displacements which would cause overlap. Since the w displacements of the base laminate are so small, it is sufficient to search for nodes with negative w displacements. If there are none, the current solution is correct. For each node with a negative w , a constraint and a load are imposed such that the node will have $w=0$. Next, a nonlinear solution is obtained for the current contact constraints and applied load. Then the signs of the contact forces are checked. Any node with a tensile constraint force must have the constraint released. If there are no tensile restraint forces, the current solution is correct. After releasing all tensile constraints, another nonlinear solution is obtained. Now the loop begins again with checking for negative w .

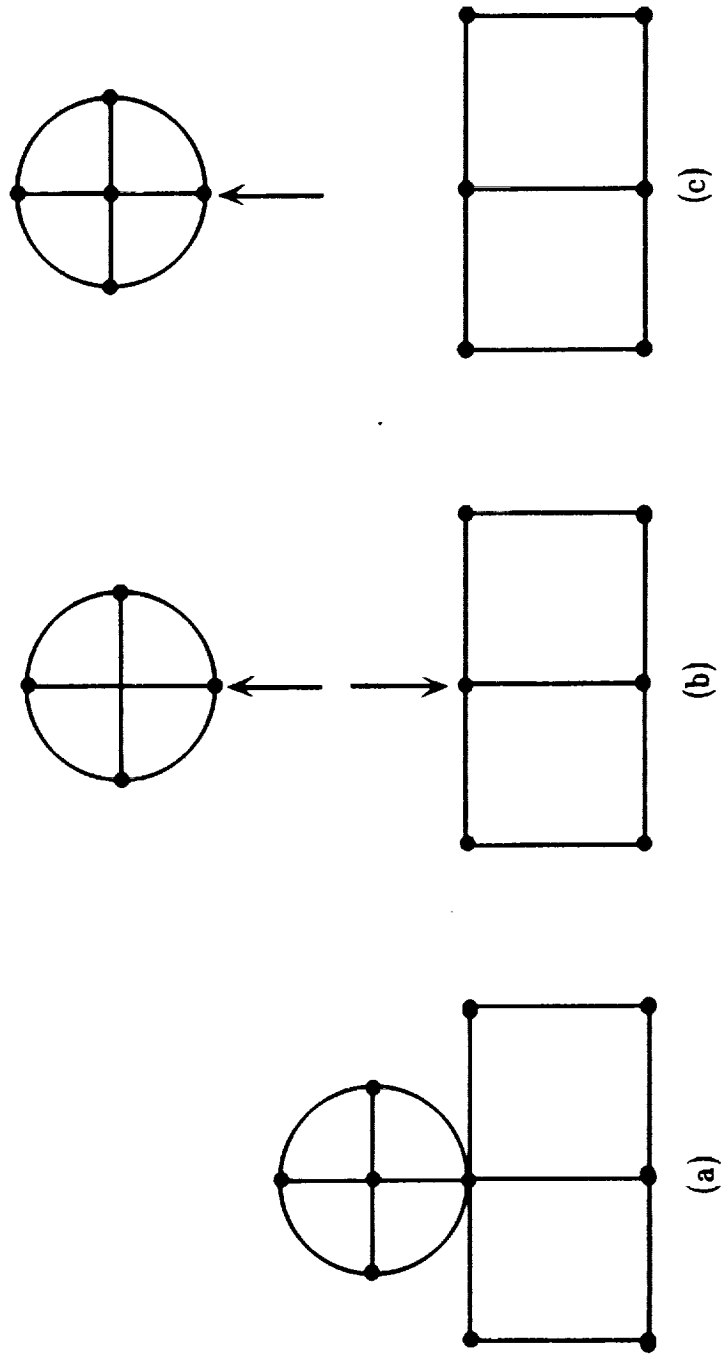


Fig. 2.7.1 Schematic of contact problem consisting of disk resting on base.

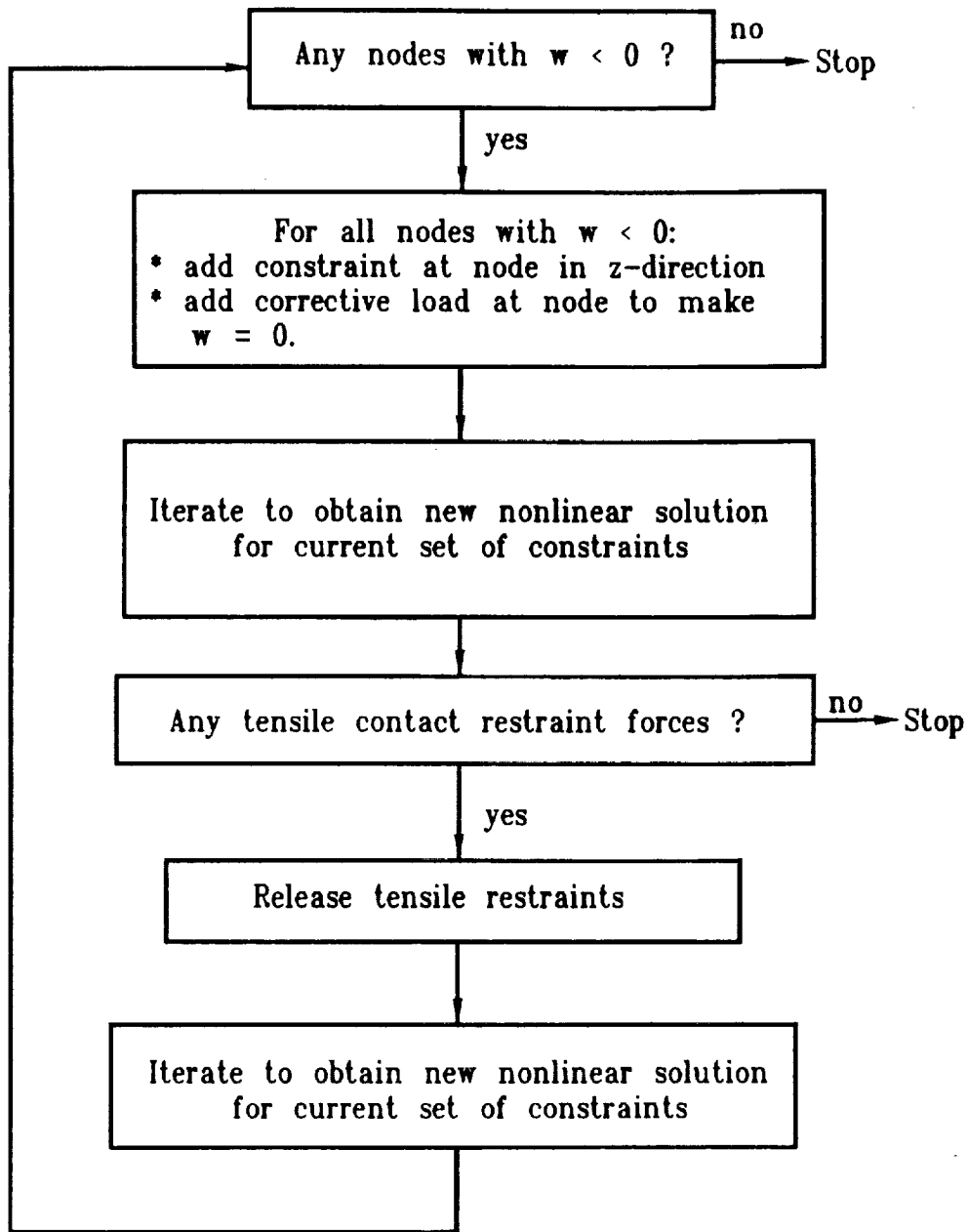


Fig. 2.7.2 Flowchart for contact analysis.

2.8 Strain-Energy Release Rate Calculation

The well-known virtual crack closure technique (ref. 40) served as the basis of the strain-energy release rate calculation. This procedure determines G_I , G_{II} , and G_{III} from the energy required to close the delamination over a short distance, Δa . The closure energy involves products of delamination front nodal forces and relative displacements behind the delamination front. The delamination front nodal forces can be determined by actually closing the delamination over Δa . Another technique, which requires only a single solution, assumes that the current delamination front nodal forces are the same as they would be if the delamination length was reduced by Δa . The single solution method was used herein.

The strain-energy release rate calculation will be illustrated for the 20-node element, since this element was used for all of the parametric analysis. Figure 2.8.1 shows a schematic of the delamination front region. The nodes of interest for the strain-energy release rate calculations are indicated by the filled circles. Because it is not appropriate to close the delamination over part of an element, there are four sets of nodes (indicated by the letters a , b , c , and d) which are used to calculate the closure energies. The relative displacements are obtained by subtracting the displacements at nodes a'_i and b'_i from the displacements at nodes a_i and b_i , respectively. The forces are equal to the nodal forces transmitted across the delamination plane at nodes c_i and d_i . These forces are obtained by evaluating the integral $\int C_{ij}\epsilon_i \frac{\partial \epsilon_i}{\partial q^a} dV$ for all elements which are connected to nodes c_i or d_i and whose centroids lie above the delamination plane. There are two sets of energy products. One of the sets of energy products consists of the relative displacements for nodes a_i and a'_i multiplied by the forces for nodes c_i . The other set of energy products consists of the relative displacements for nodes b_i and b'_i multiplied by the forces for nodes d_i . The energies equal 1/2 of these products.

Strain-energy release rate is a measure of energy per unit area. Hence, the energy products must be normalized by the appropriate areas. Unfortunately, there is not a simple exact way to determine the appropriate areas. The primary

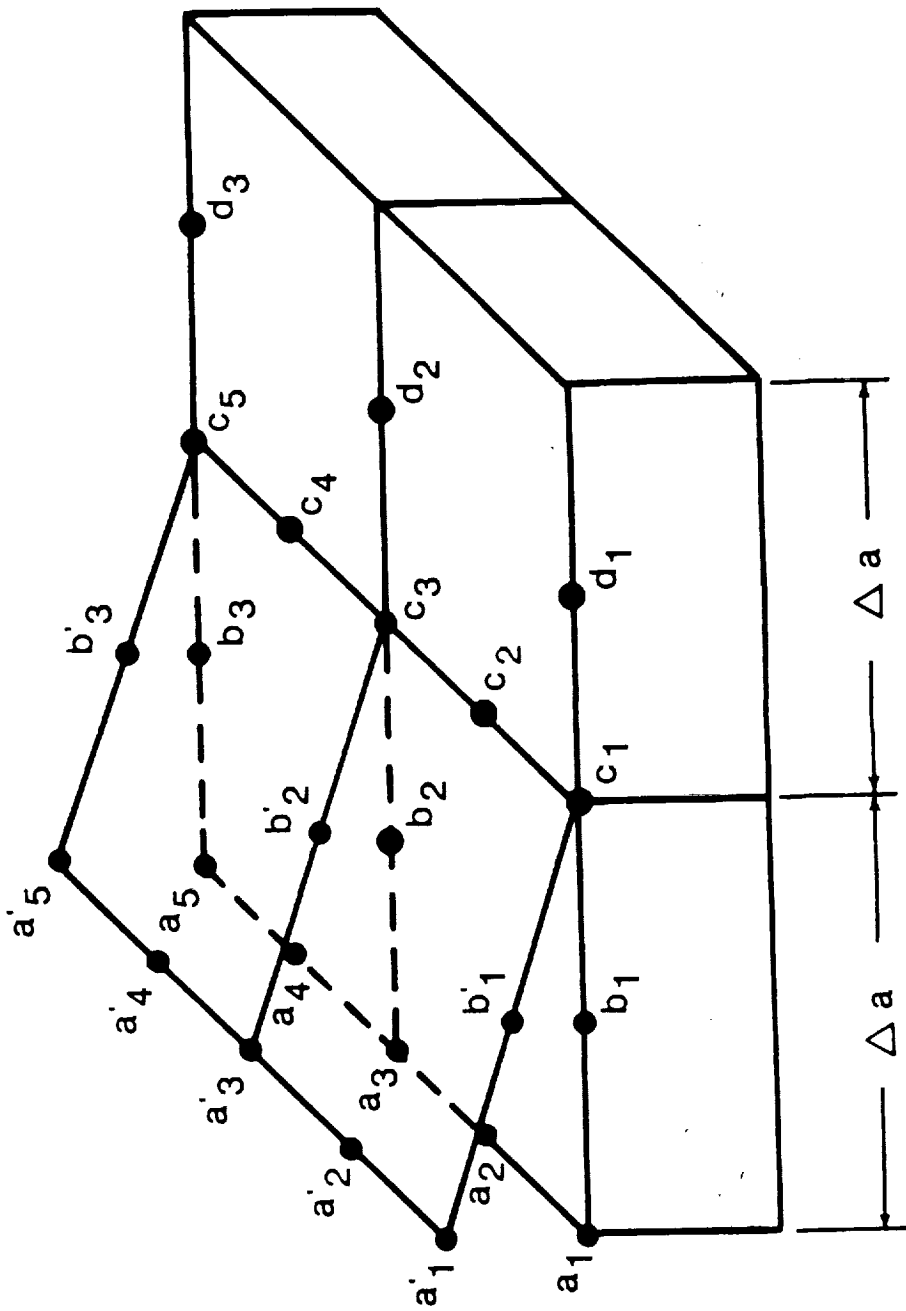


Fig. 2.8.1 Schematic of the delamination front region.

complication is that the midside nodes and corner nodes are “weighted” differently by the assumed element shape functions. The result is that, even if the strain-energy release rates are actually constant along the delamination front, there would be much larger energy products for the midside nodes than for the corner nodes. For example, in figure 2.8.1 the energy products associated with nodes c_2 and c_4 would be much larger than for that associated with nodes c_1 and c_3 . An approximate solution to this dilemma is as follows. The strain-energy release rate is not calculated for locations like c_2 and c_4 along the delamination front. Instead, the energy products associated with those locations are split evenly between the adjacent nodes. For example, the energy associated with location c_3 along the delamination front becomes

$$\bar{E} = \bar{E}_{a_3 a'_3 c_3} + \bar{E}_{b_2 b'_2 d_2} + \frac{1}{2} [\bar{E}_{a_2 a'_2 c_2} + \bar{E}_{a_4 a'_4 c_4}] \quad (2.8.1)$$

where \bar{E} denotes the energy products associated with G_I , G_{II} , and G_{III} and the subscripts indicate the nodes involved. The area is approximated by the product of Δa times the distance between the midside nodes on either side of the corner node being considered. For example, the area for node c_3 is Δa times the distance from node c_2 to node c_4 .

If the delamination front is not parallel to one of the coordinate axes, it is preferable to add a coordinate transformation to the procedure outlined above. In particular, a local coordinate system is defined for each node along the physical delamination front (i.e., the nodes c_i). Figure 2.8.2 shows a schematic of a delamination plane and the global (xy) and local ($x'y'$) coordinate systems. This local coordinate system has one axis tangent to the delamination front, one axis normal to the delamination front, and one axis normal to the delamination plane. For all the cases considered z and z' were parallel. The transformed nodal forces $F_{x'}$, $F_{y'}$, and $F_{z'}$, are

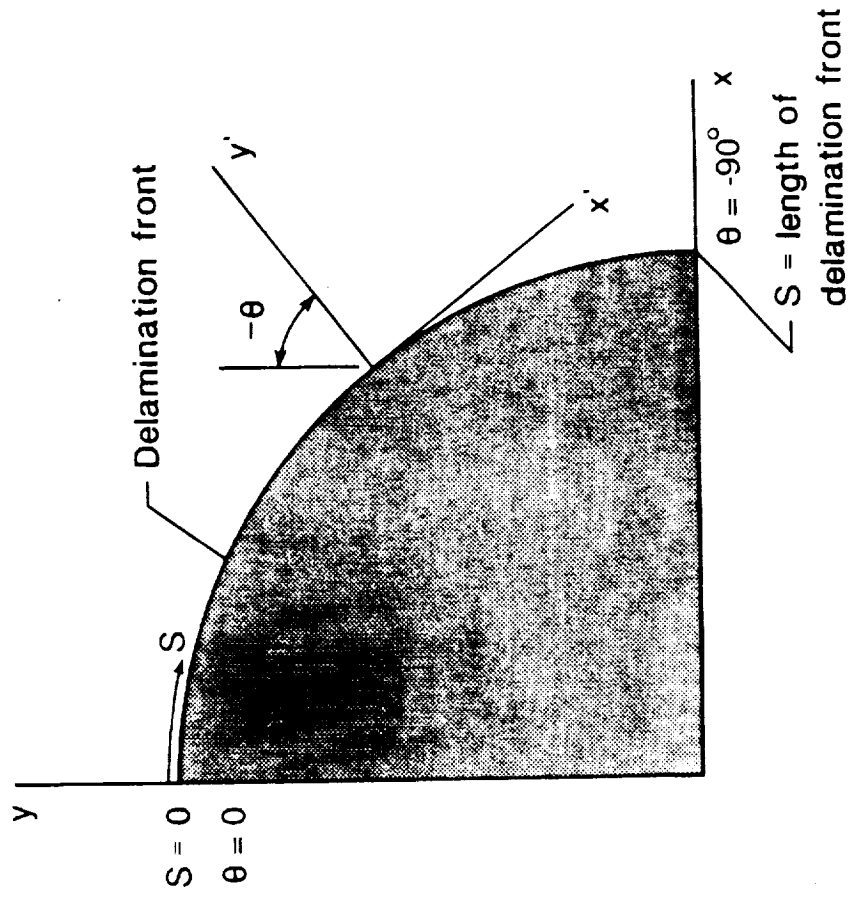


Fig. 2.8.2 Global and local coordinate systems and perimeter coordinate S .

$$\begin{aligned}
F_{x'} &= F_x \cos \theta + F_y \sin \theta \\
F_{y'} &= -F_x \sin \theta + F_y \cos \theta \\
F_{z'} &= F_z
\end{aligned}
\tag{2.8.2}$$

The relative displacements are transformed similarly. The transformed forces and relative displacements are then used to calculate the energy products. Figure 2.8.2 also defines the perimeter coordinate "S", which is the distance along the delamination front measured from the *y*-axis.

The procedure just outlined was implemented in two slightly different ways for the results presented here. The difference was in the way the nodal forces were calculated. Initially in the study, the nonlinear strain-displacement relations were used to calculate the nodal forces from the nodal displacements in the linear region. This is inconsistent, but if the region assumed to be linear is "exactly linear", it would make no difference. The results for the mesh convergence study were obtained using this procedure. All of the other results were obtained by using the linear strain-displacement relations to calculate the nodal forces from the nodal displacements in the linear region. Because the linear region is not exactly linear, there is a difference in the results obtained using the two methods. The configuration used for the mesh convergence study was also used in the parametric study, so results appear for that configuration using both methods. The second method is recommended by the author.

2.9 Material Properties

Several kinds of materials were used in this study. Some of the specimens involved Al or steel. Also, two graphite composite systems were examined: AS4/PEEK and IM7/8551-7. The material properties used are given in Table 1. For the two metals, the usual assumed properties were used. The assumed properties for the PEEK were actually some that are typical for graphite/epoxy (ref. 41). Since only a qualitative analysis of PEEK was performed, these

Table 1 Material Properties

	<u>Generic Graphite/Epoxy*</u>	<u>IM7/8551-7**</u>
E_{11}	13.4E10 Pa	16.2E10 Pa
E_{22}	1.02E10 Pa	.814E10 Pa
E_{33}	1.02E10 Pa	.814E10 Pa
ν_{12}	.3	.22
ν_{23}	.49	.22
ν_{13}	.3	.22
G_{12}	.552E10 Pa	.648E10 Pa
G_{23}	.343E10 Pa	.648E10 Pa
G_{13}	.552E10 Pa	.648E10 Pa

* ref. 41

** unpublished data generated by the University of Wyoming under NASA grant NAG1-674, which began in July, 1986.

properties were probably sufficiently accurate. The properties for the IM7/8551-7 were based on unpublished data generated by the University of Wyoming under NASA grant NAG1-674, which began in July, 1986. This grant determined the inplane properties, E_{11} , E_{22} , G_{12} , and ν_{12} . Because of a lack of other data, the remaining 3D properties were assumed.

In addition to the materials mentioned above, a fictitious material was used. For the initial parametric study, the goal was to examine the effect of strain level and geometric parameters on G_I , G_{II} , and G_{III} . Material properties were desired which would have minimal effect on the distribution of the strain-energy release rates. For quasi-isotropic laminates the in-plane stiffness is independent of direction. But even for quasi-isotropic laminates the flexural stiffness varies with direction. Hence, even if the postbuckled region consisted of a quasi-isotropic group of plies, one would expect variations in the strain-energy release rate along the delamination front which are due solely to the variation in flexural stiffness. Also, the properties of the interface plies (i.e., those plies on either side of the delamination) would be expected to at least affect the percentages of G_I , and G_{II} , and G_{III} .

The simplified material properties chosen for this study are those for a "homogeneous quasi-isotropic laminate" throughout the entire specimen (buckled and unbuckled regions). These properties \bar{C}_{ij} are obtained as follows:

$$\bar{C}_{ij} = \frac{1}{8} \sum_{\ell=1}^8 (C_{ij})^{\ell} \quad (2.9.1)$$

where $(C_{ij})^{\ell}$ are the constitutive properties for the ℓ^{th} ply in the 8-ply quasi-isotropic laminate $(\pm 45/0/90)_s$. With these properties throughout, there are obviously no stacking sequence effects and no variation of material properties with orientation.

Chapter 3
FINITE ELEMENT MODELING

This chapter describes the technique used for mesh generation and discusses typical finite element models.

3.1 Mesh Generation

Figure 3.1.1 outlines the procedure used for generating most of the meshes. This procedure is based on the procedure in ref. 42. A two-dimensional model is swept through a 90° arc to generate a cylindrical 3D mesh. The outer part of the cylindrical mesh is then transformed to obtain a square boundary. Then an elliptical transformation is applied to obtain an elliptical delamination front. If the ellipse is longer in the y -direction than in the x -direction (i.e., $b > a$), the conformal transformation is

$$\begin{aligned}x' &= x \\y' &= y \sqrt{1 + \frac{b^2 - a^2}{x^2 + y^2}} \\z' &= z\end{aligned}\tag{3.1.1}$$

If $a > b$, the transformation is the same except that x and y are interchanged. To avoid a singularity in eqn. (3.1.1), nodes at zero radius were shifted to lie on an arc of very small radius, i.e. about 10^{-9} m.

The transformation in eqn. 3.1.1 maintains the orthogonality of lines which were orthogonal in the modified cylindrical mesh (Fig. 3.1.1c). This orthogonality at the delamination front simplifies the pairing of nodal forces and relative displacements in the strain-energy release rate calculation.

A peculiarity of the transformation in eqn. 3.1.1 is the unusually close spacing of the elements close to the delamination front on the long axis of the ellipse (Fig. 3.1.2b). Also note what appears to be a triangular element

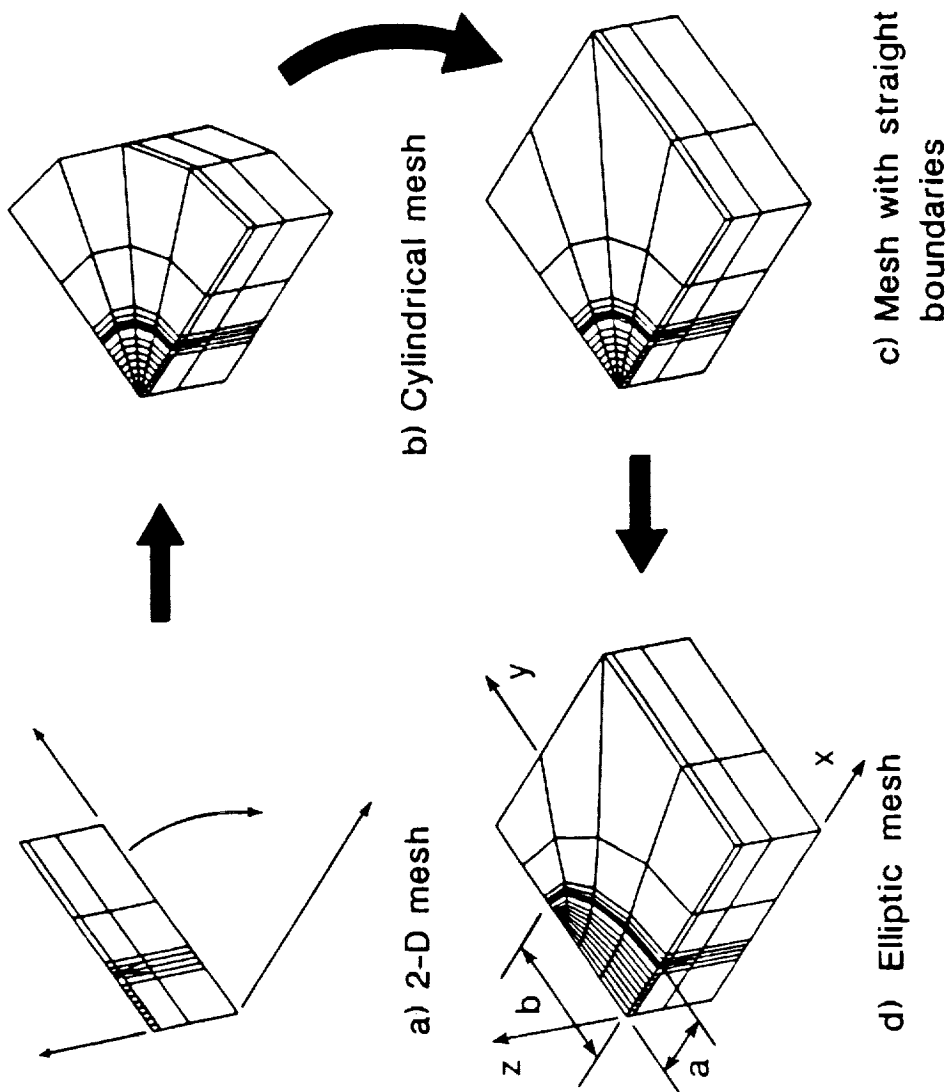


Fig. 3.1.1 Procedure for generating three-dimensional finite element models.

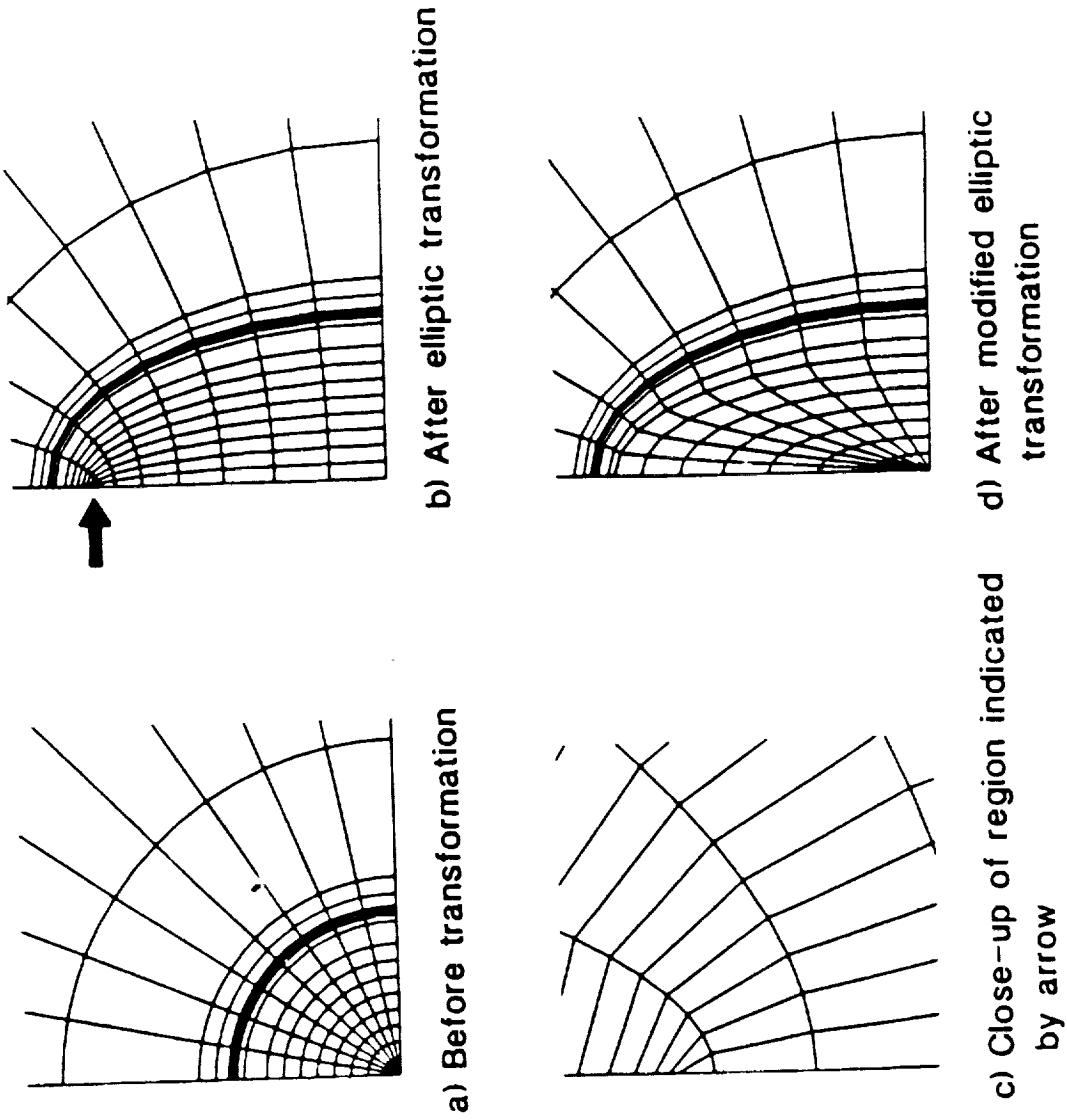


Fig. 3.1.2 Transformed meshes using elliptic transformation of ref. 42 and the modified transformation.

in Fig. 3.1.2c . This element has two sides which are essentially colinear. A modified transformation which results in more even mesh refinement is obtained by introducing a scale factor for the "stretching"

$$y' = y \left(\sqrt{1 + \frac{b^2 - a^2}{x^2 + y^2}} F - F + 1 \right)$$

$$\text{where } F = \frac{\sqrt{x^2 + y^2}}{r} \text{ for } r \geq \sqrt{x^2 + y^2} \quad (3.1.2)$$

$$\text{and } F = 1 \text{ for } r \leq \sqrt{x^2 + y^2}$$

By choosing the parameter r a little less than the radius of the delamination front in the cylindrical mesh, orthogonality is maintained in the neighborhood of the delamination front during the elliptical transformation.

After the elliptical transformation the midside nodes are no longer at the middle of an element edge. Therefore, the coordinates of the midside nodes are recalculated as the average of the coordinates of the adjacent corner nodes.

In section 5.3 results are presented for a square and a rectangular delaminated region. For the square delamination circular arcs in a mesh like 3.1.1c were *stretched* to form the side of a square. A typical mesh is shown in Fig. 3.1.3. For a rectangular delamination the coordinates were magnified in one direction to elongate the delaminated region. The transformations for the square and rectangular delaminations are not conformal. Hence, the orthogonality of the lines which are orthogonal in Fig. 3.1.1c was not preserved in the model in Fig. 3.1.3. This probably reduced the accuracy of the modeling.

3.2 Finite Element Models

In the course of this investigation the following configurations were examined:

- 1) a laminate with an embedded delamination, 2) a laminate with an edge

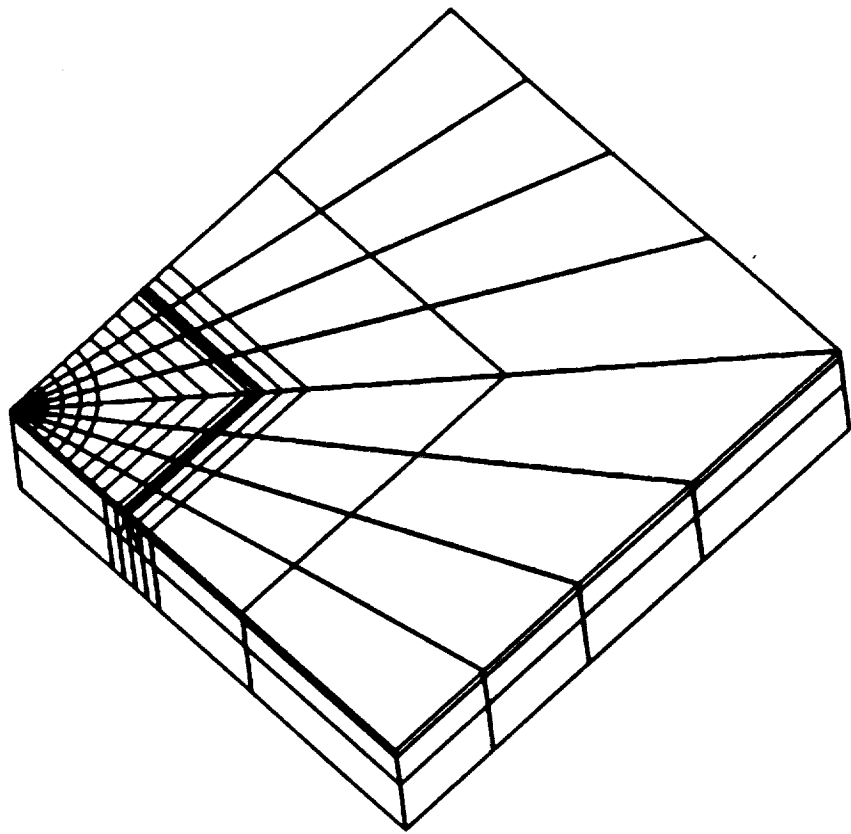


Fig. 3.1.3 Mesh used for analysis of the square delamination.

delamination, and 3) a laminate with a through-width delamination. The loading was in-plane compression except for the transversely loaded circular delamination. The finite element models for these configurations are discussed in this section.

Figure 3.2.1 shows a typical finite element model for a laminate with an embedded delamination. The elements are 20-node isoparametric hexahedra. Because of symmetry it is sufficient to model only one fourth of the specimen and impose the constraints $u = 0$ on $x = 0$ and $v = 0$ on $y = 0$. There is also a constraint $w = 0$ on $z = 0$. This constraint was imposed to remove global bending from the analysis. In reality, there might be global bending (particularly if the buckled region is thick), but the amount of global bending would depend on the region modeled and the boundary conditions at the external boundaries. Imposition of $w = 0$ on $z = 0$ simply removes overall specimen size and external boundary conditions as parameters to be considered in this study. The constraint on w represents a laminate which is well constrained globally. Of course, one could also view the imposition $w = 0$ on $z = 0$ as an indication of symmetry about the $z = 0$ plane. This implies the presence of two delaminations.

Along the boundary $x = W$, all u displacements are specified to equal $W\epsilon_0$, where ϵ_0 is the specified compressive axial strain. To initiate transverse deflections, a transverse load was applied at the center of the delaminated region. After a converged solution was obtained, the load was removed, and solutions were obtained with only compression loading.

Figure 3.2.2 shows a typical model after division into substructures. Most of the postbuckled region is included in the nonlinear substructure. The distance between the delamination front and the beginning of the nonlinear substructure was ℓ . In all cases, ℓ was approximately equal to the sublaminar thickness h .

The edge delamination models were similar to the embedded delamination models. Because the plane $y = 0$ is now a free surface, the constraint $v = 0$ on $y = 0$ used for the embedded delamination was not used for the edge delamination.

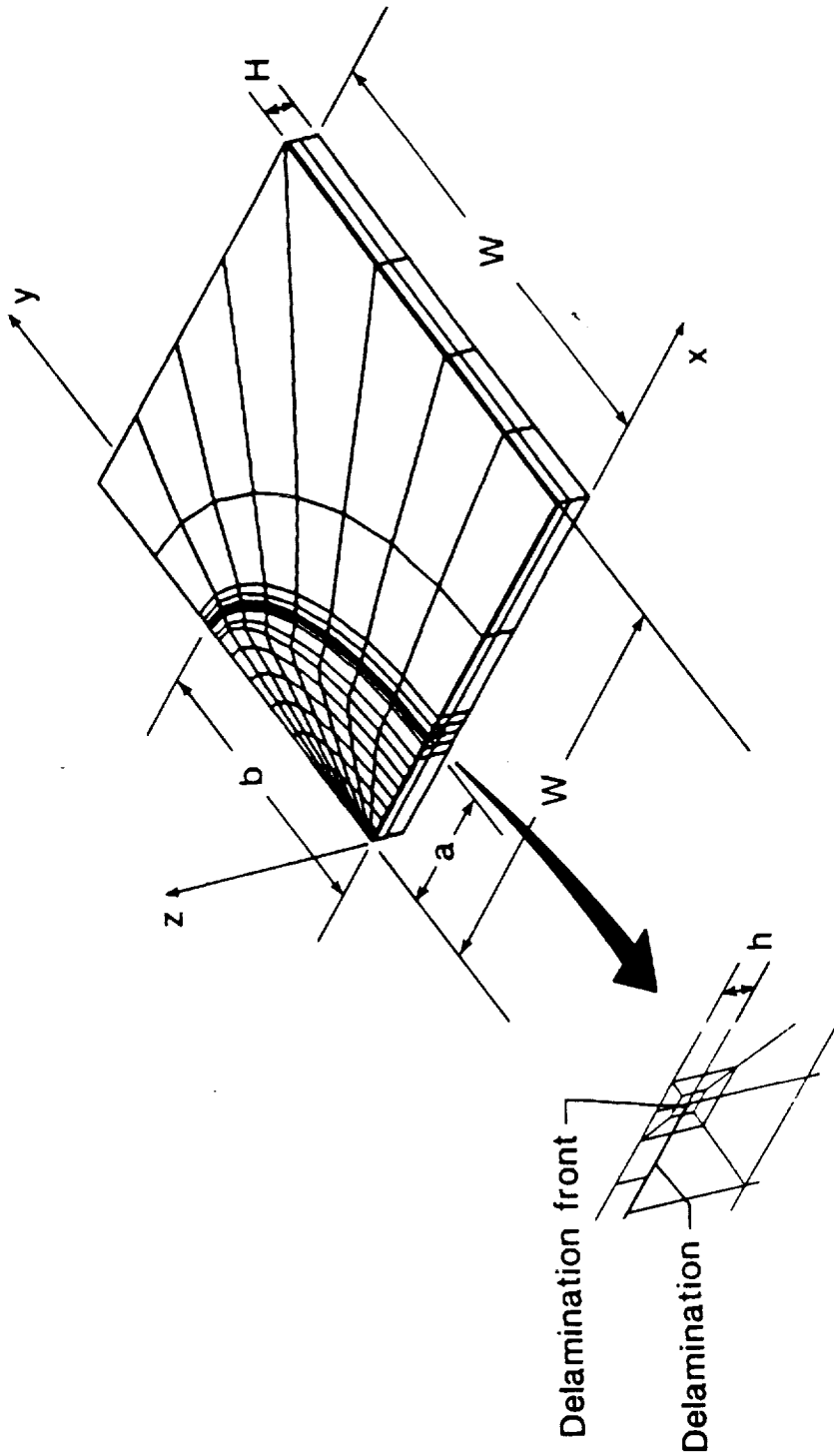


Fig. 3.2.1 Typical finite element model.

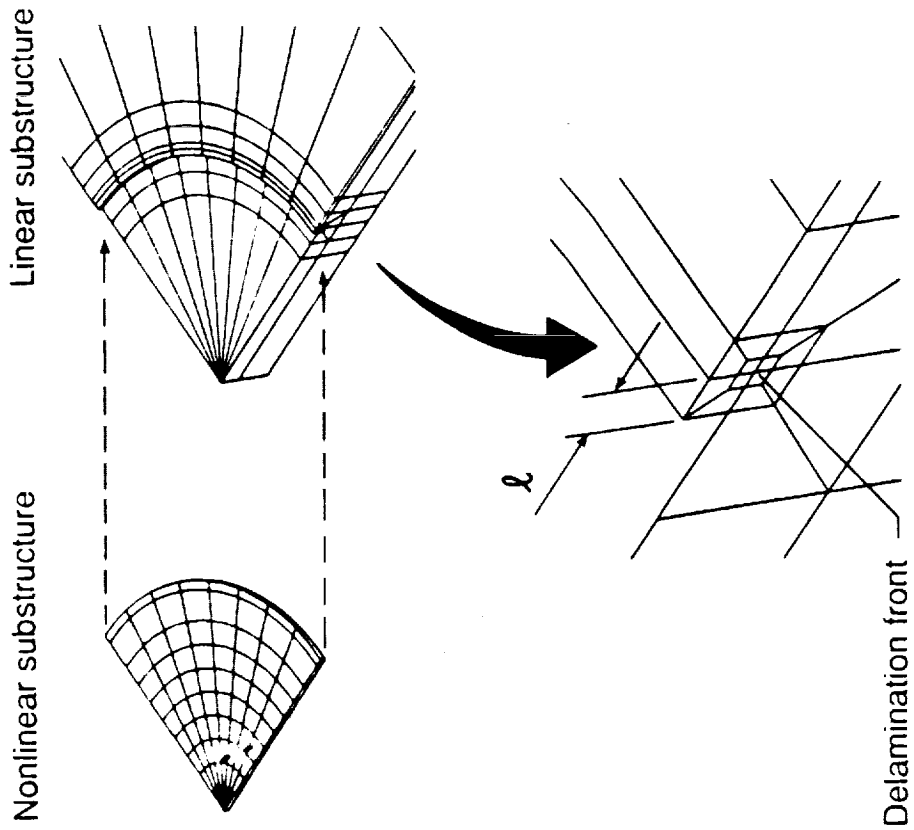


Fig. 3.2.2 Typical division of model into substructures.

The model for a laminate with a through-width delamination (Fig. 3.2.3) had exactly the same boundary conditions as the model for a laminate with an embedded delamination, except an additional constraint $v = 0$ on $y = W$ was imposed to cause a plane strain response.

A transversely loaded laminate with a circular delamination was analyzed to help verify NONLIN3D. The model for this configuration was like that in Fig. 3.2.1, except the delaminated region was circular and a transverse load (i.e a load in the z-direction) was applied at $(x,y,z)=(0,0,H+h)$.

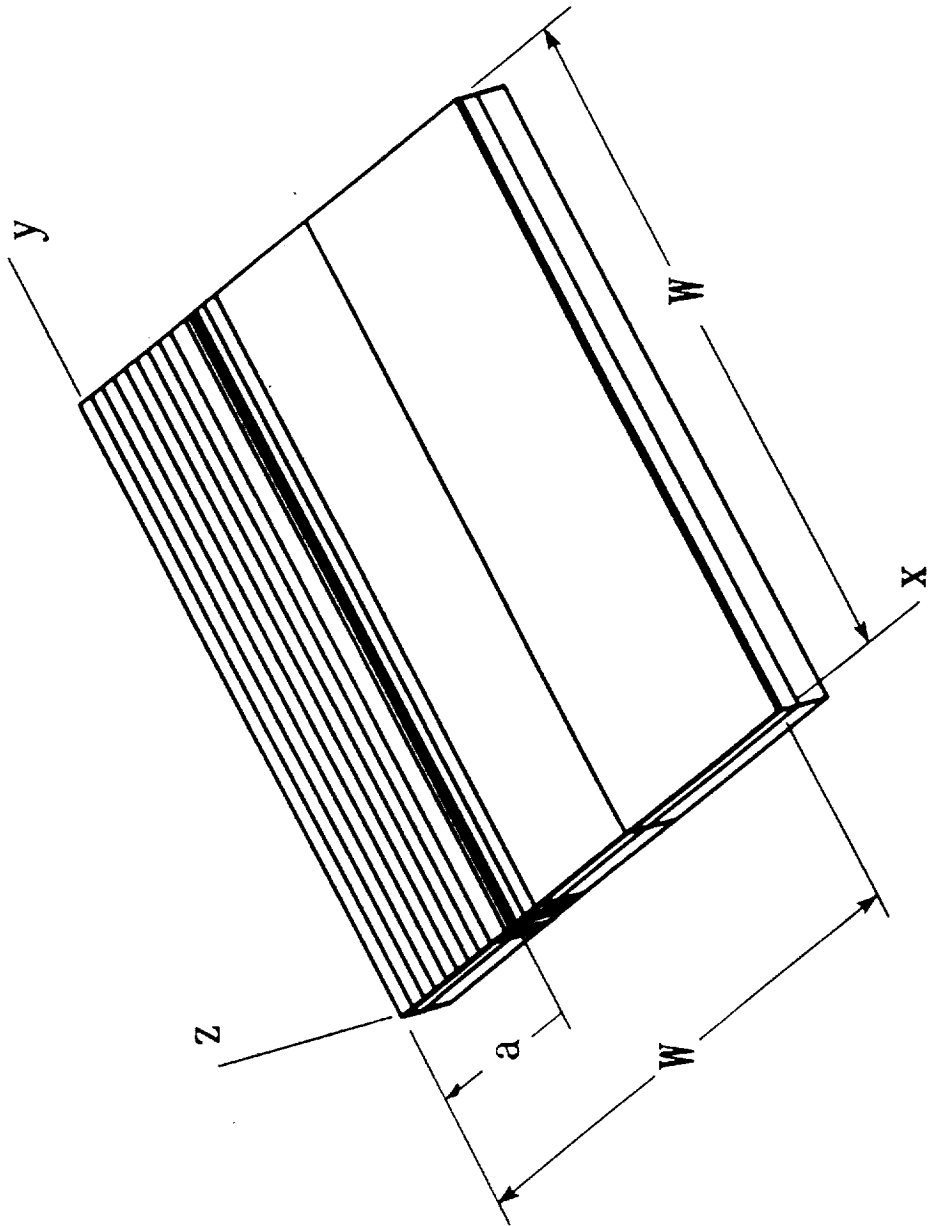


Fig. 3.2.3 Through-width delamination model.

Chapter 4
EVALUATION of NONLIN3D

A variety of checks were made to verify the reliability of the finite element program NONLIN3D and the models used with the program. Some of these checks are presented in the following subsections.

4.1 Analysis of Transversely Loaded Plate

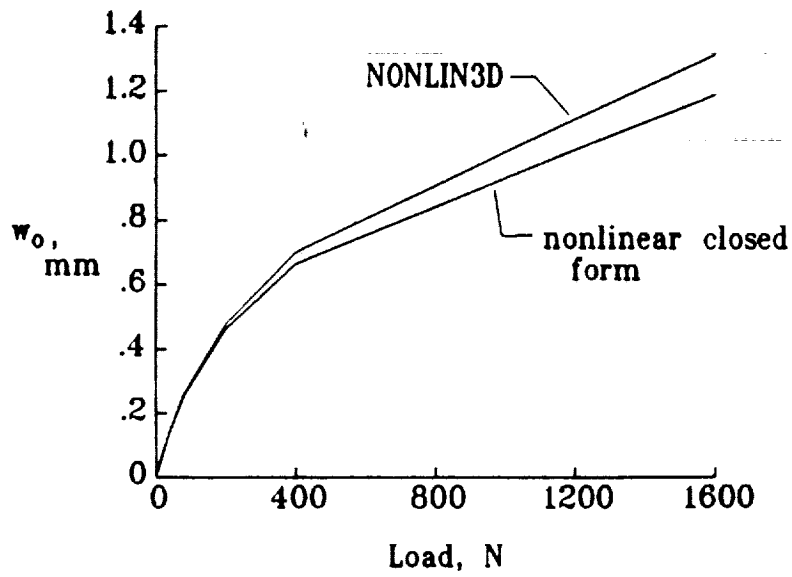
A closed form solution for a circular isotropic plate subjected to a central point load is given in ref. 43. This solution is exact for linear deflections and approximate for large deflections. The equation for the central deflection w_o is

$$\frac{w_o}{h} + .443 \left(\frac{w_o}{h} \right)^3 = .217 \frac{Pa^2}{Eh^4} \quad (4.1.1)$$

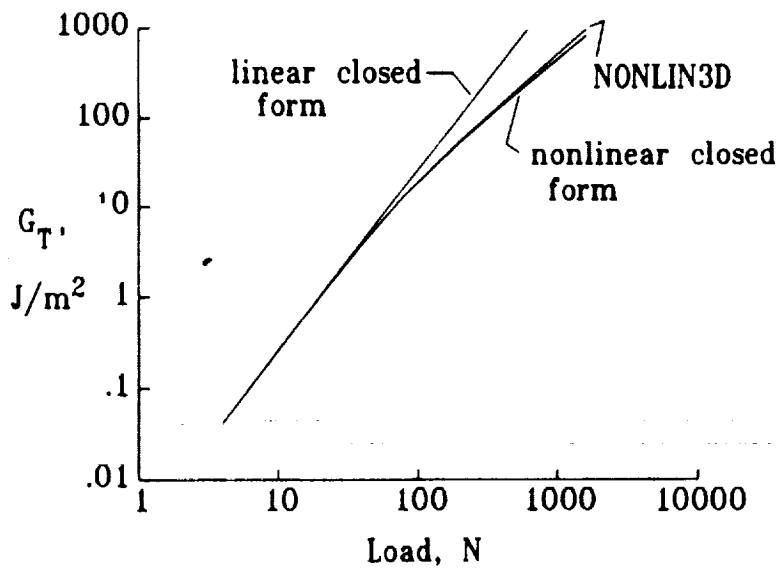
Finite element analyses were performed using a mesh similar to that in Fig.3.2.1, but with a circular debond. The thickness and radius of the debonded region were .4 mm and 15 mm, respectively. The Young's modulus was 207 GPa and the Poisson's ratio was .3 .

Figure 4.1.1a compares the deflection at the center obtained from the closed form solution and NONLIN3D. The agreement between the two analyses is excellent in the linear and the initial nonlinear region. There is a 10 percent difference in the deflections at the highest load level considered. This is not surprising, since the closed form analysis is not exact for large deflections.

The closed form solution in ref. 43 can be used to calculate the total strain energy release rate. Because the configuration is axisymmetric, G_T is constant around the boundary. The strain-energy release rate is $-(\partial U / \partial a) / (2\pi a)$. The strain energy U can be calculated as the work done by the applied load (since all of the work is stored as strain-energy).



(a) Deflection



(b) Total strain-energy release rate

Fig. 4.1.1 Analysis of a transversely loaded plate with a circular delamination.

$$U = \int P dw_0 \quad (4.1.2)$$

Equation 4.1.2 yields

$$U = 2.30 \frac{w_o^2 E h^3}{a^2} + .510 \frac{w_o^4 E h}{a^2} \quad (4.1.3)$$

An expression for G_T is obtained by differentiating eqn. 4.1.3 with respect to a and dividing by the circumference.

$$G_T = \frac{E h w_o^2}{2\pi a^4} \left[\frac{h^2}{.217} + 1.02 w_o^2 \right] \quad (4.1.4)$$

Figure 4.1.1b shows G_T vs. load. Results are shown for the linear closed-form solution (eqn. 4.1.4 without the fourth order w_o term), the nonlinear closed-form solution (eqn. 4.1.4), and NONLIN3D. The results are plotted with log-log axes because of the wide range of the parameters. In the linear range all three solutions agree very well. Even after nonlinear effects become important, the nonlinear closed-form solution and NONLIN3D still agree very well.

These comparisons indicate that NONLIN3D does account for geometric nonlinearity and that the strain-energy release rate calculation technique is valid.

4.2 Failure of 8-Node Element

Initially, the 8-node element with reduced integration was to be used for the stress analyses. As pointed out earlier, it was known that the element could exhibit spurious zero-energy modes. However, initial tests with the element seemed to show good performance. The critical test involved analysis of a postbuckled sublaminant, since this is the focus problem for this thesis. For simplicity only the sublaminant was modeled and constraints were applied to the lower surface to simulate a very stiff base laminate. As mentioned in the analysis chapter,

postbuckling was initiated by applying both in-plane compression and transverse loads. After obtaining a converged solution, the transverse load was removed. Then the desired solutions could be obtained. For this particular test of the 8-node element, the transverse load was removed in steps. (In all the other cases presented in this thesis, the transverse load was removed all at once, not in steps.)

Fig. 4.2.1 shows the deformed meshes for the four load cases. Converged solutions were obtained for all four load cases. For the first three cases, the deformed shape is quite smooth. All spurious oscillations are very small. When the last of the transverse load was removed, the deformed shape shows clearly that the zero energy modes are no longer subdued. A close-up of the central part of the plate for the case $P=0$ is shown in Fig. 4.2.2. These results show that the contribution of spurious zero-energy deformation modes depends on both the displacement constraints applied on the boundaries and the load system. Because of this behavior, it was decided that this element is not reliable. Hence, the 20-node element was used exclusively for the strain-energy release rate analyses.

4.3 Check of Mesh Refinement

Several configurations were analyzed as part of this study. Consequently, it was neither practical nor warranted to perform a convergence study for all cases. Instead, a systematic convergence study was performed for a single configuration. Mesh refinements for other configurations were selected based on the results of the convergence study.

The configuration selected for the convergence study had a circular delamination with a radius of 15 mm. The sublaminates thickness h was .4 mm and the base laminate thickness H was 4 mm. The overall laminate width W was 50 mm. The material properties were those for the homogeneous quasi-isotropic laminate described earlier. Figure 4.3.1 shows the extremes of refinement used for the 2D meshes. The elements in the coarse mesh were subdivided to obtain the refined mesh. Note that for the coarse mesh, only two elements are used to model most of

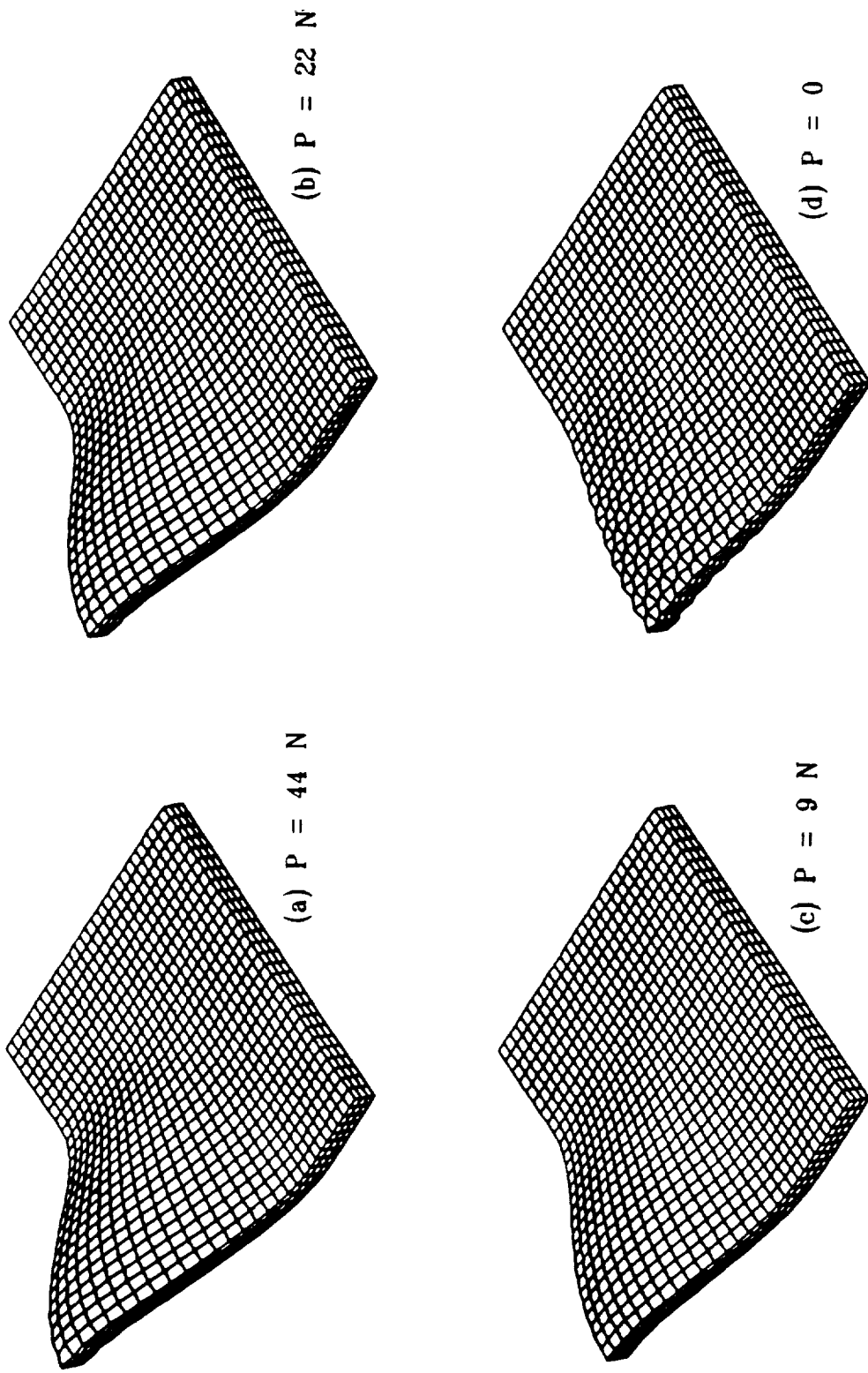


Fig. 4.2.1 Postbuckled meshes using 8-node element. (strain = -.0045)

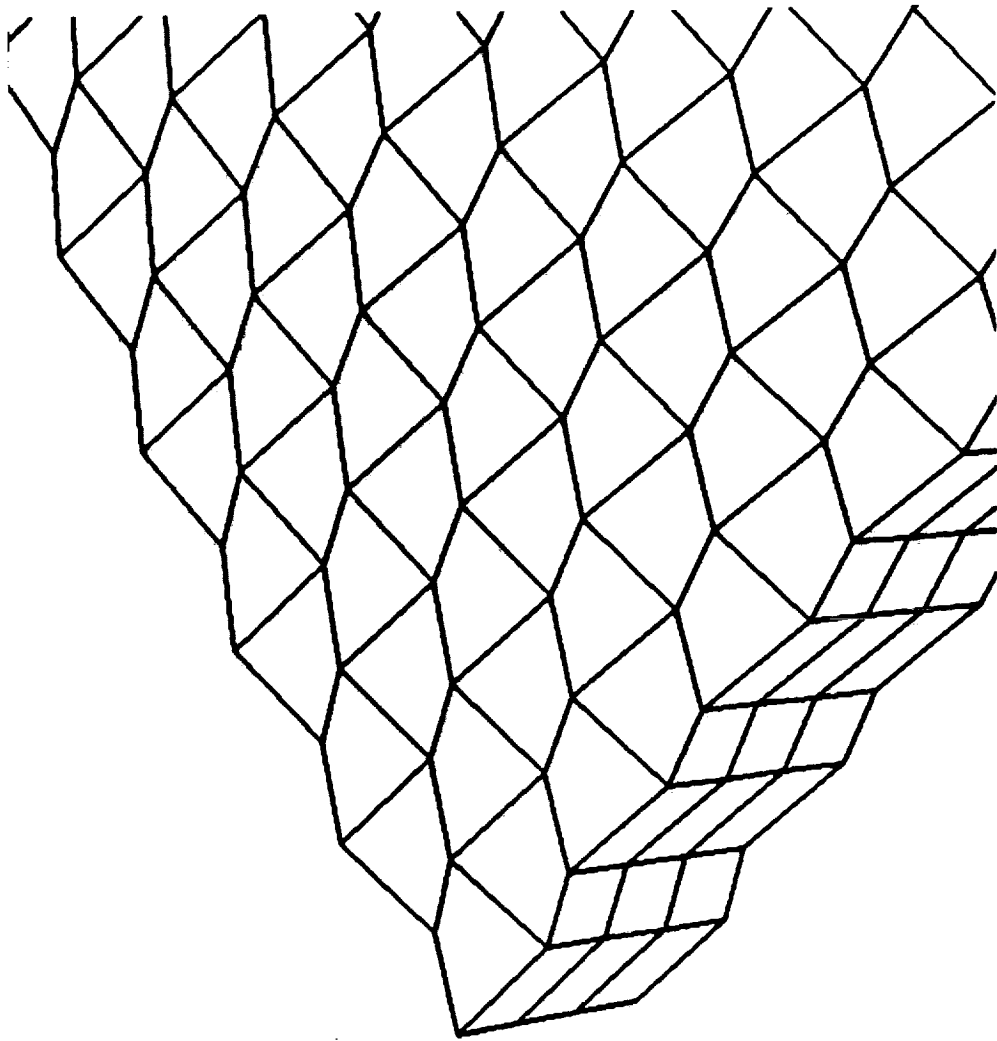
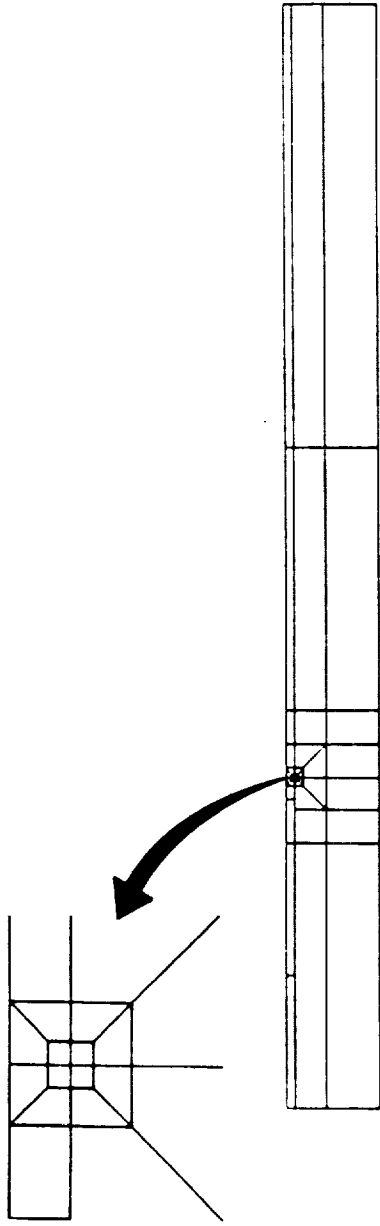
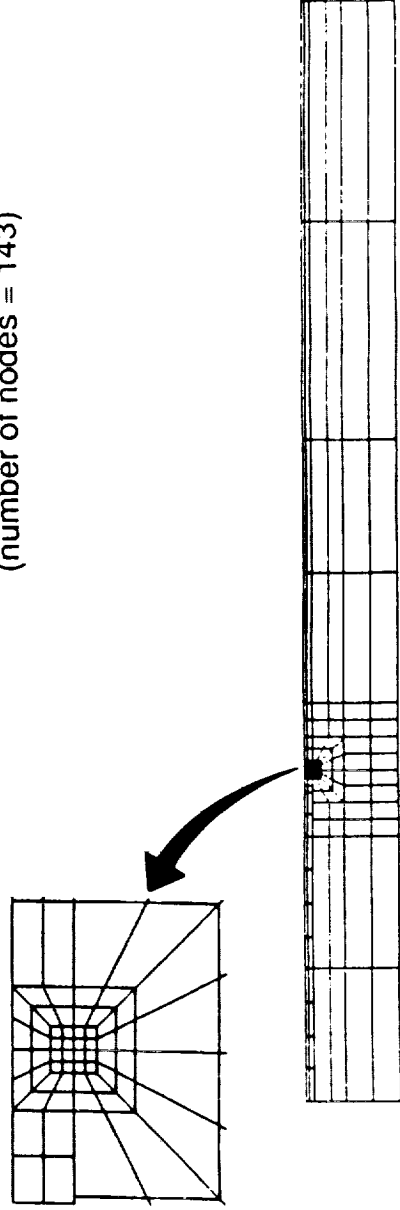


Fig. 4.2.2 Closeup of postbuckled mesh ($P = 0$).



a) Coarse 2-D model
(number of nodes = 143)



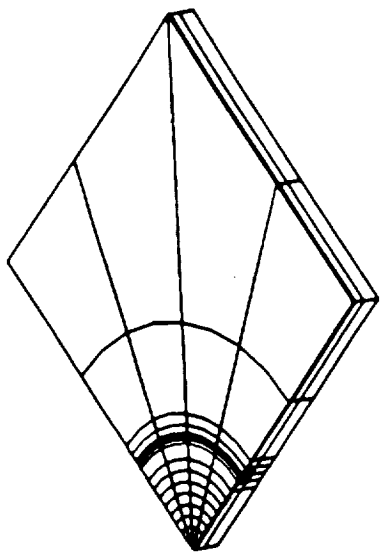
b) Refined 2-D model
(number of nodes = 533)

Fig. 4.3.1 Range of two-dimensional mesh refinement for convergence study.

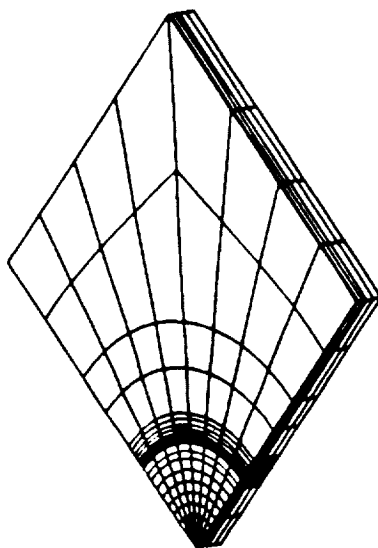
the buckled region. As described earlier, the 2D meshes were swept through a 90° arc to generate the 3D meshes. Figure 4.3.2 shows four of the meshes generated. As shown in the figure, the number of slices of elements was also varied. Models with 4 and 8 slices are shown. A 12-slice model was also used. Information on all of the models used in the convergence study are given in Table 2. As shown by the figures and the table, a fairly wide range of refinement was examined.

Since strain-energy release rates were of primary importance, variations in G_I , G_{II} , and G_{III} were used to determine the adequacy of the mesh refinement. Figure 4.3.3 shows the distribution of G_I and G_{II} along the delamination front for three strain levels and four models (models 1,3,4, and 6). Only symbols are shown for the crudest mesh, model 3. These meshes bracket the entire range of refinement in Table 2. The mode III component G_{III} was negligible for all cases. Of interest here are the differences in the results obtained using the various meshes. Except for model 3, which only had 4 slices of elements, the results from all of the models are essentially equal. Even a coarse 4-slice model gives the correct trends. Apparently, a fairly crude model is sufficient to calculate G_I and G_{II} . Models with 8 slices were selected for the parametric analyses in Chapter 5, which will discuss the significance of the magnitude and the distribution of G_I and G_{II} .

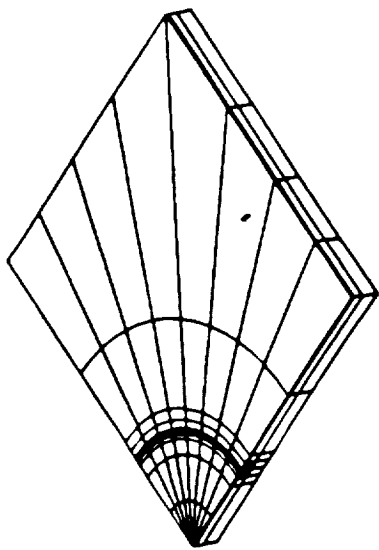
The preceding convergence study was for a homogeneous quasi-isotropic laminate, which is a fictitious material. Chapter 7 presents strain-energy rates for actual laminates. Because a minimum of one element was required through the thickness of each lamina, the 2D mesh used to generate the 3D mesh had more nodes than the homogeneous laminate required. Unfortunately, the required computational effort prevented a systematic convergence study. In fact, to keep the computational effort manageable, the number of slices in the models was limited to just four (instead of the 8 slices used for the homogeneous quasi-isotropic laminates). Fig. 4.3.4 shows one of the models. Based on the convergence study presented for a homogeneous laminate, one might estimate that the four slice models for actual laminates underestimate the maximum G_I and G_{II} by about 15-20



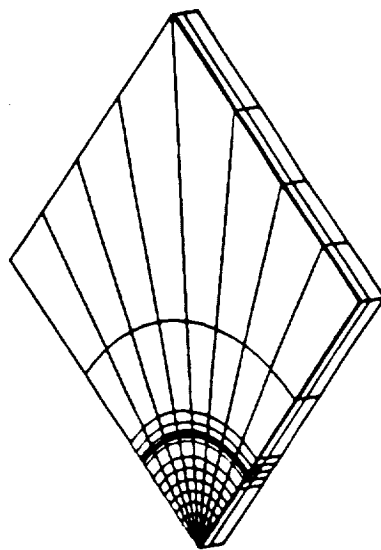
b) Model 3



d) Model 6



a) Model 1



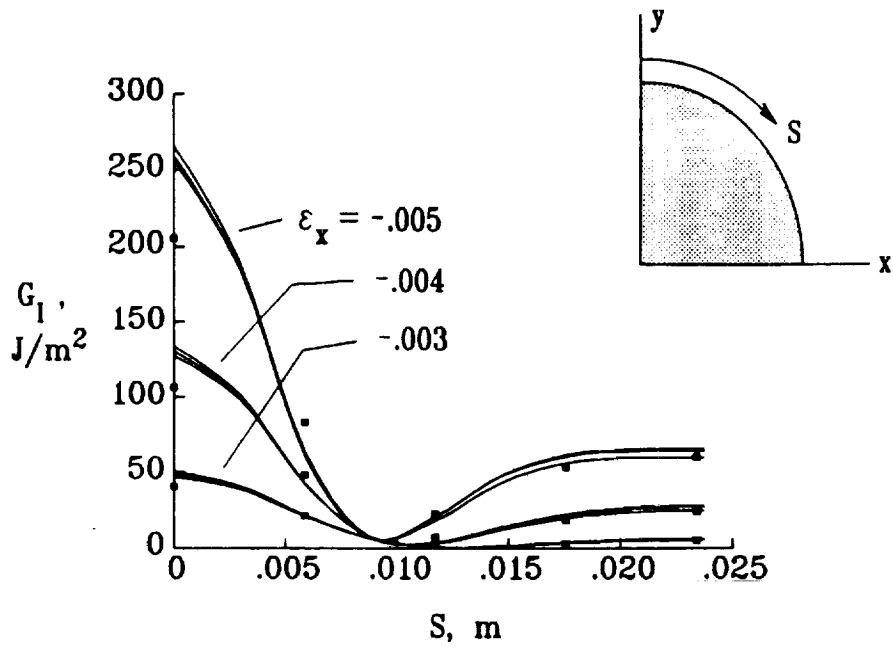
c) Model 4

Fig. 4.3.2 Several of the three-dimensional meshes used in the convergence study.

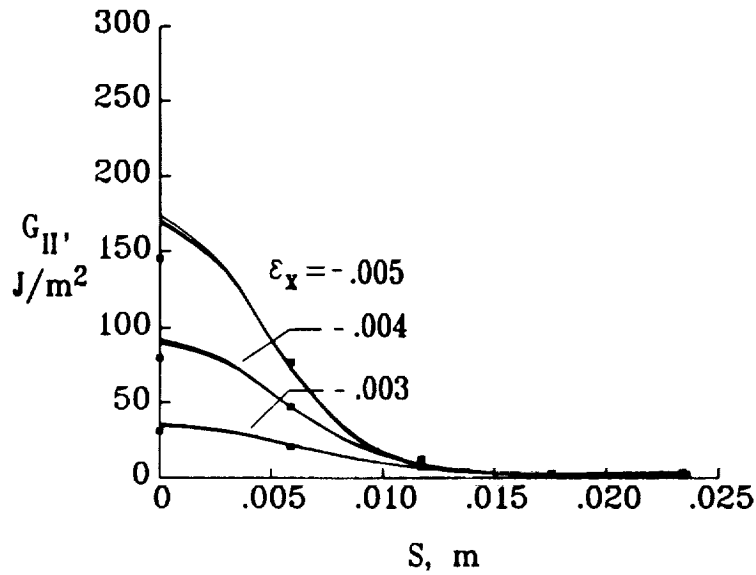
TABLE 2 Statistics on models used in convergence study

Model	Number of nodes/Number of elements					
	2D MODEL	3D MODEL	SUBSTRUCTURE 1	SUBSTRUCTURE 2	#OF SLICES	
1	143/36	1719/288	1475/256	287/32		8
2	153/38	1841/304	1475/256	409/48		8
3	173/42	1129/168	799/128	353/40		4
4	173/42	2085/336	1475/256	653/80		8
5	173/42	3041/504	2151/384	953/120		12
6	533/152	6325/1216	5173/1024	1221/192		8

Notes: Substructures 1 and 2 are linear and nonlinear, respectively.



(a) Mode I



(b) Mode II

Fig. 4.3.3 Strain-energy release rates calculated using different meshes. The symbols indicate the results for model 3.

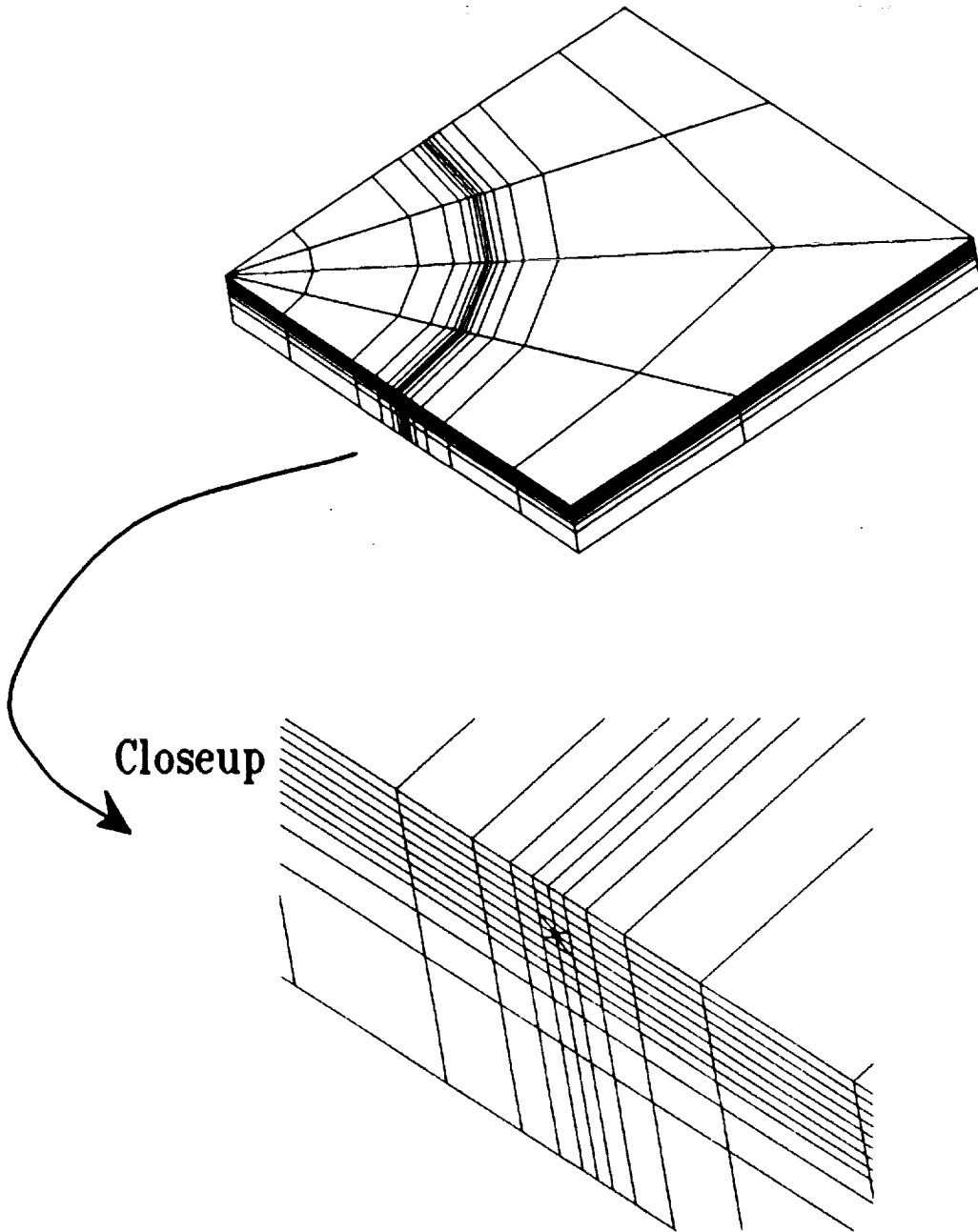


Fig. 4.3.4 Typical finite element mesh used for analysis of actual laminates.

percent.

4.4 Determination of Allowable Residual

NONLIN3D solves the governing nonlinear equations using a modified Newton-Raphson solution procedure. During each iteration the internally generated forces are compared with the externally applied loads. The differences are the residuals. If all of the residuals are identically zero, the governing equations are exactly satisfied. Of course, in practice exact agreement is seldom obtained. Iteration could continue until the algorithm's best approximation of zero is obtained. The size of this "numerical" zero will depend on the computer and variable type specifications (i.e. single or double precision) in the program. However, negligible residuals are in general orders of magnitude larger than a numerical zero.

To determine what is a negligible residual, three residual tolerances were considered: 1000., 1., and .0001 Newtons. A laminate with a 30×60 mm delamination was analyzed for five strain levels. The range of strains was such that the maximum lateral deflection for the buckled region varied from about .6 to 2.2 times the thickness of the buckled region. The tolerance of 1000 Newtons gave erroneous results. The other two tolerances gave virtually identical results except for the lowest strain level ($\epsilon_x = -.001$), for which there were differences of about 6 percent. Figure 4.4.1 shows G_I and G_{II} for $\epsilon_x = -.001$ (i.e., the worst case). Results for the other strains are not shown, since the differences are very small.

Based on these results, a tolerance of .0001 Newton was selected for all the analyses. Probably a somewhat larger residual could have been tolerated. However, the residuals tend to decrease quite rapidly during the iterations, so there is little to be gained (in terms of reduced cost) by trying to specify the largest acceptable residual. Also, a larger tolerance might give poor results for some cases in which the loads are small.

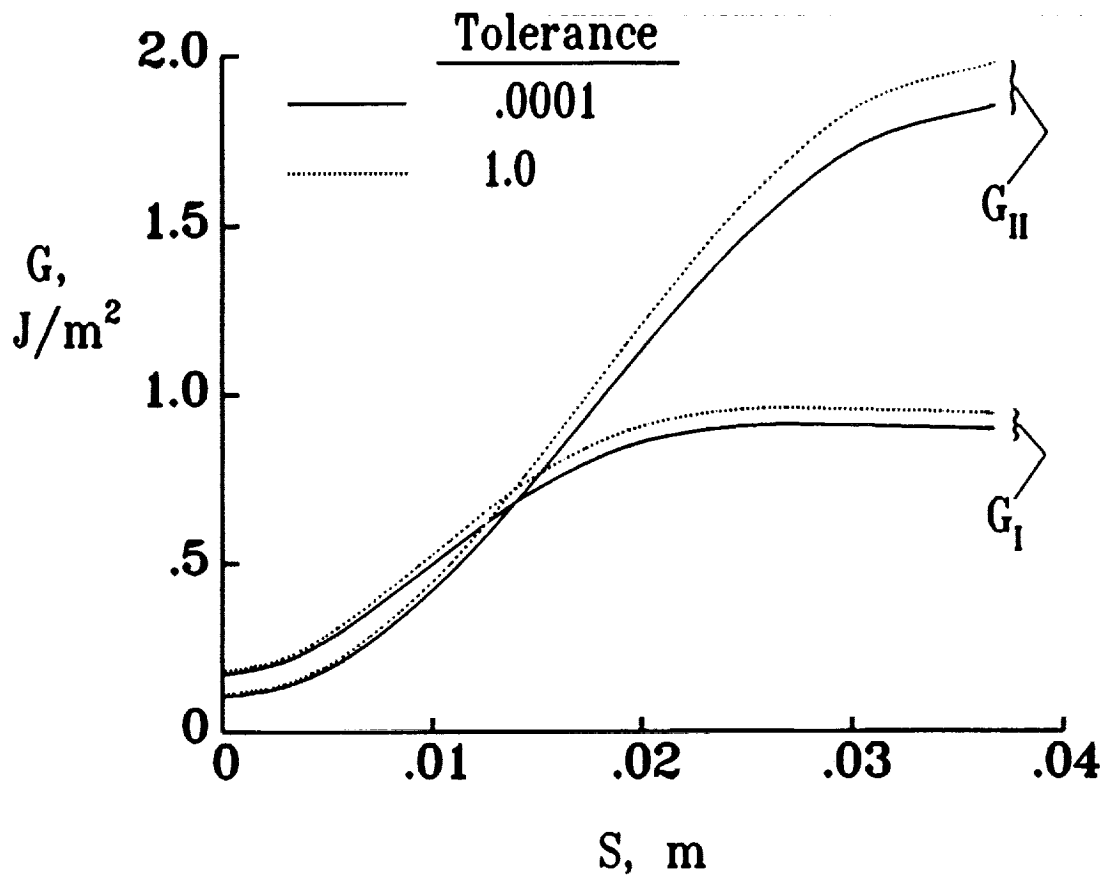


Fig. 4.4.1 Effect of specified residual tolerance on G_I and G_{II} . Applied strain = $-.001$.

4.5 Verification of Substructuring

The configuration used for the convergence study was also used to verify the validity of the substructuring. Model 3 was analyzed with and without substructuring. The calculated G_I and G_{II} distributions from these analyses are shown in Fig. 4.5.1. The small difference in the results verifies the substructuring technique.

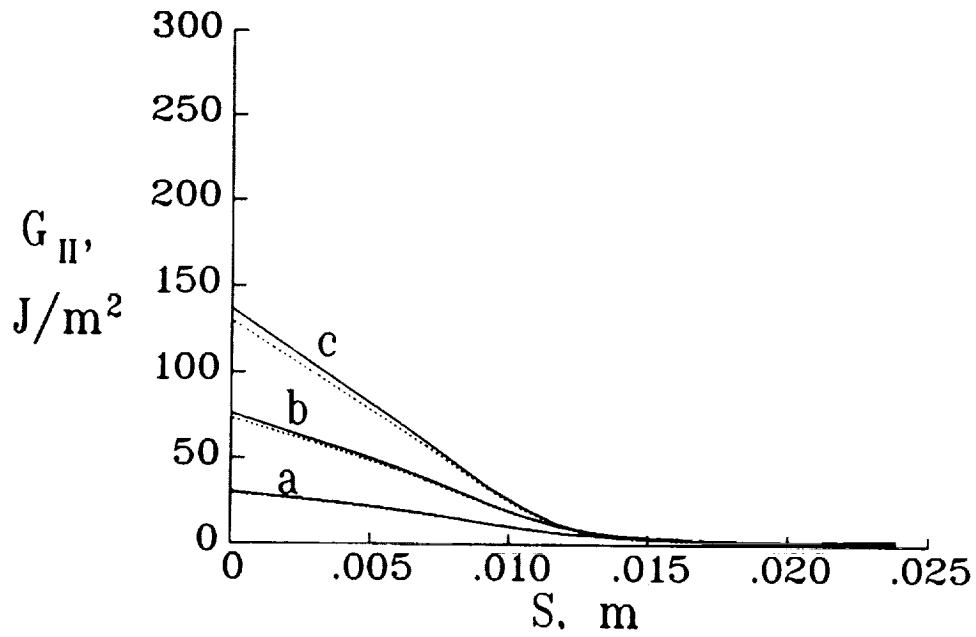
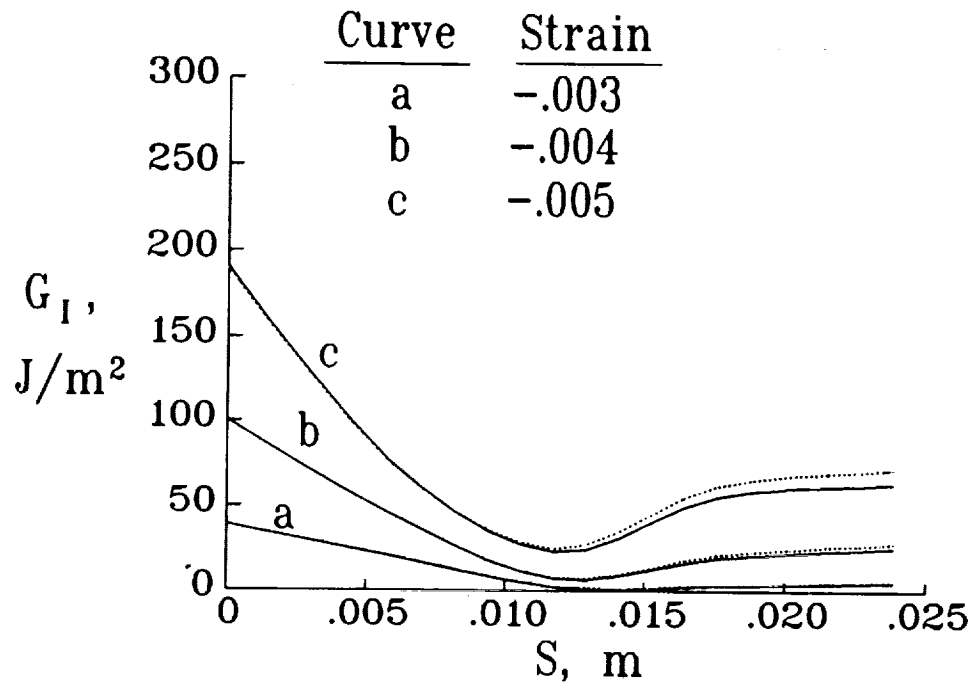


Fig. 4.5.1 Effect of substructuring on calculated G_I and G_{II} distributions. The solid curves are for analysis with substructures. The dashed curves are for analysis without substructures.

PARAMETRIC ANALYSIS OF HOMOGENEOUS QUASI-ISOTROPIC LAMINATES

This chapter will discuss the results of a parametric study of homogeneous quasi-isotropic laminates containing a postbuckled embedded or edge delamination. This fictitious homogeneous laminate was selected so that the effects of strain level and various geometric parameters on deformation and strain-energy release rate could be examined without the additional complications due to stacking sequence effects.

The following sections begin with a parametric study on the effect of strain level, delamination shape, and delamination size on deformation and the distribution of G_I , G_{II} , G_{III} and G_T along the delamination front.

5.1 Deformation and Strain-Energy Release Rates For an Embedded Delamination

The parameters considered were strain level, delamination shape, and delamination size.

Fig. 5.1.1 shows lateral displacement in the middle of the delaminated region vs. axial strain for two circular and two elliptical delaminations. The dimensions of the delaminations are shown on the figure. Before buckling the lateral deflection is essentially zero. When the buckling load is exceeded, the displacement increases rapidly at first with increased strain. Then the rate of increase in displacement decreases. Obviously, the response is quite nonlinear.

Fig. 5.1.2 shows plots of deformed finite element meshes for a circular and an elliptical delamination. The displacements have been multiplied by 10 to improve visualization. The deformed shape is relatively simple except near the delamination front. For both cases the delamination front is open near the intersection of the delamination front with the $x=0$ plane. However, for the circular delamination, the delamination faces actually overlap near the $y=0$ plane.

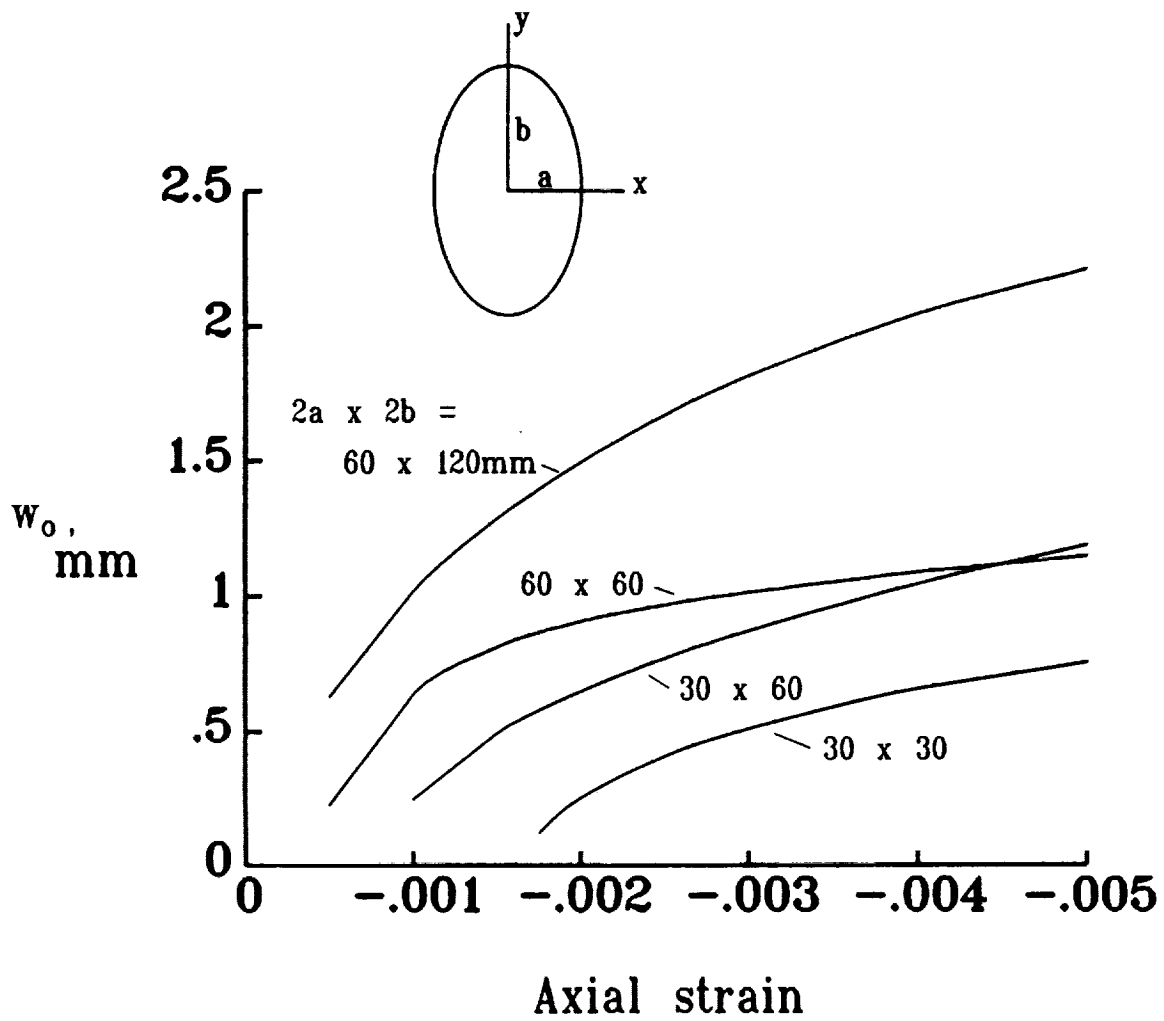


Fig. 5.1.1 Peak transverse displacement vs. axial strain for four delamination sizes.

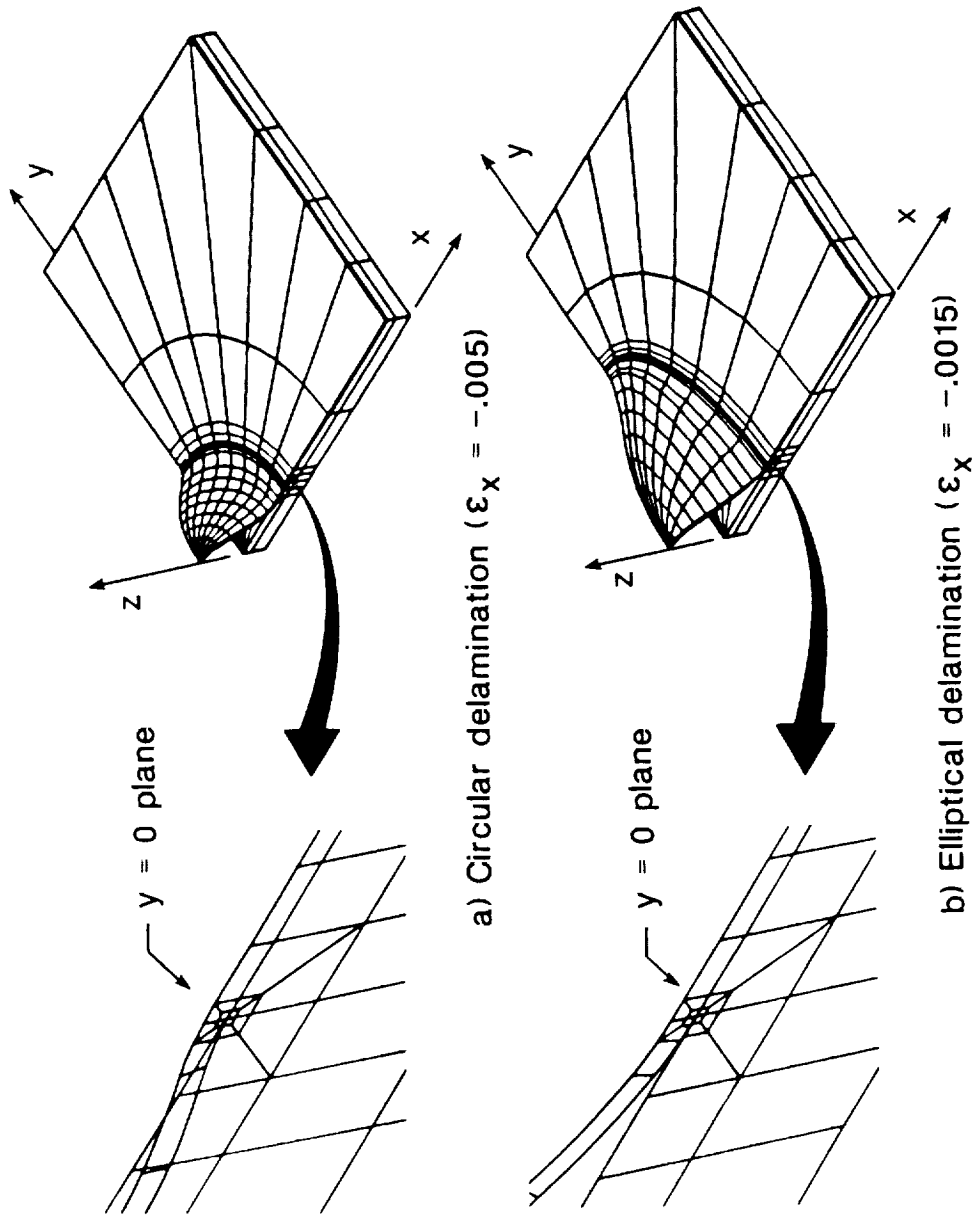
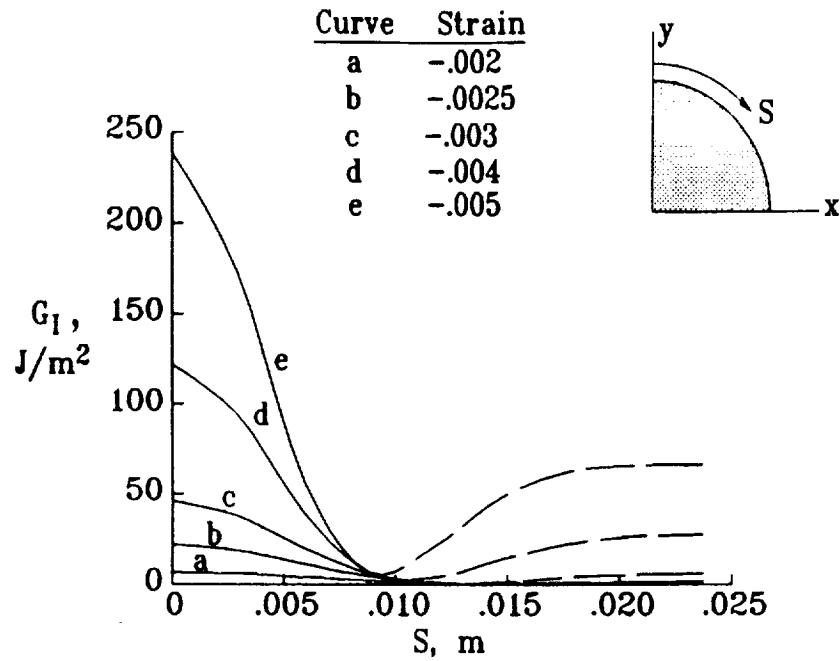


Fig. 5.1.2 Deformed finite element meshes. Displacements scaled by 10 for (a) and 20 for (b).

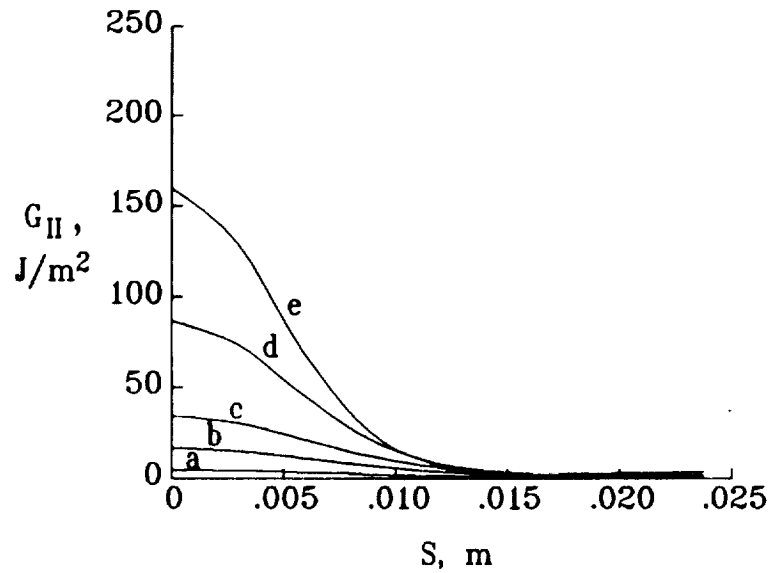
Even at strains smaller and larger than that shown, the circular delamination exhibited closing. For the elliptical delamination “small” strains result in opening along the entire length. At larger strains (not shown), the elliptical delamination also exhibited closure. Strictly speaking, constraints should be added to prevent overlapping of the delamination faces. However, including constraints to prevent overlapping further complicates an already complicated stress analysis problem. Consequently, no contact constraints were added for any of the results presented in this section. Section 5.4 presents a few results which illustrate the effect of including contact constraints. In the results that follow, dashed lines will be used for the G_I and G_{II} distribution curves in regions where overlap occurred.

Figure 5.1.3 shows the G_I and G_{II} distributions for a circular delamination for five strain levels. This is the same configuration used for the convergence study in section 4.3. G_{III} was essentially zero for this and all other cases considered in this study. In general, one would not necessarily expect G_{III} to be zero. The strain-energy release rates are plotted in Fig. 5.1.3 using the perimeter coordinate S . This coordinate is zero where the delamination front meets the y -axis and is maximum where the delamination front meets the x -axis. Both G_I and G_{II} show large variations along the front and are maximum at $S = 0$. There is overlapping of the delamination surfaces over a large portion of the front, as indicated in figure 5.1.3a. Although G_I is larger than G_{II} for the five strain levels, the difference is not large; this is definitely a mixed mode situation. Since both G_I and G_{II} are largest at $S = 0$, one would expect delamination growth to occur preferentially perpendicular to the load direction, i.e. in the y -direction.

Since a circular delamination is expected to become elongated perpendicular to the load direction, a 30x60 mm elliptical delamination was analyzed. Fig. 5.1.4 shows the distribution of G_I , G_{II} , and G_T for this elliptical delamination. There is a large variation of both G_I and G_{II} along the front. Note that the location of the G_I peak shifts slightly with strain level. In contrast to the circular delamination, the peak values of G_I and G_{II} occur at different locations. Also, the peak value

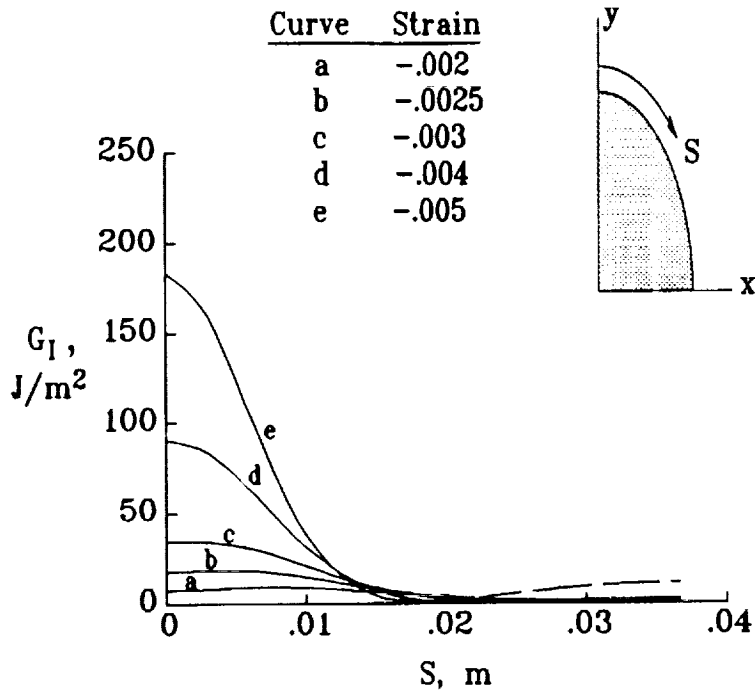


(a) Mode I

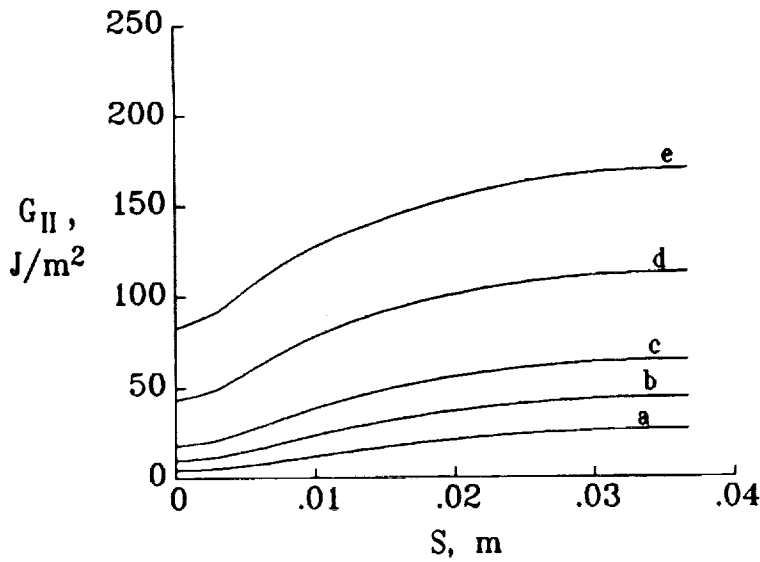


(b) Mode II

Fig. 5.1.3 Strain-energy release rate distributions for a circular delamination.
(diameter = 30mm)

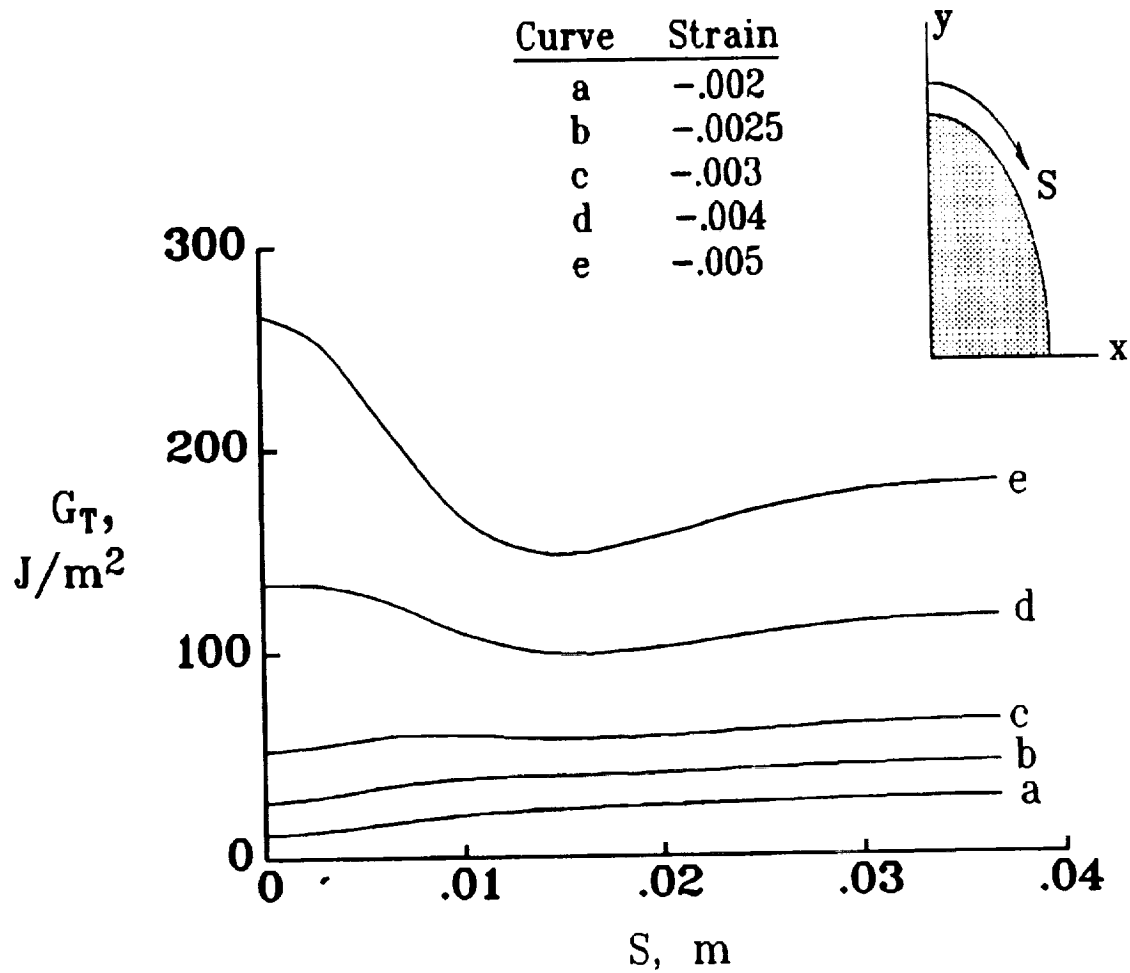


(a) Mode I



(b) Mode II

Fig. 5.1.4 Strain-energy release rate distributions for an elliptical delamination.
 $(2a \times 2b = 30 \times 60mm)$



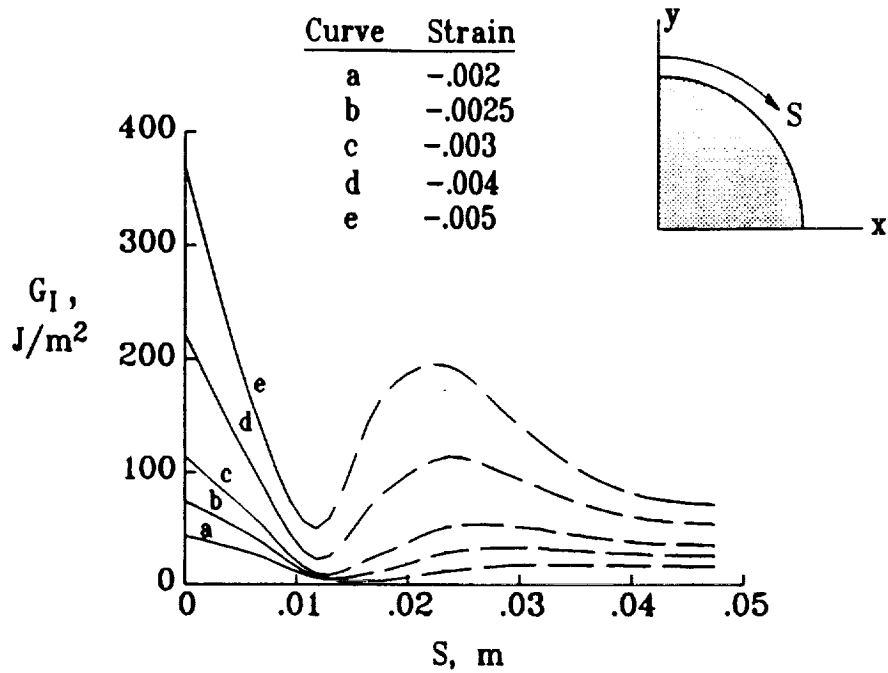
(c) Total strain-energy release rate

Fig. 5.1.4, Concluded.

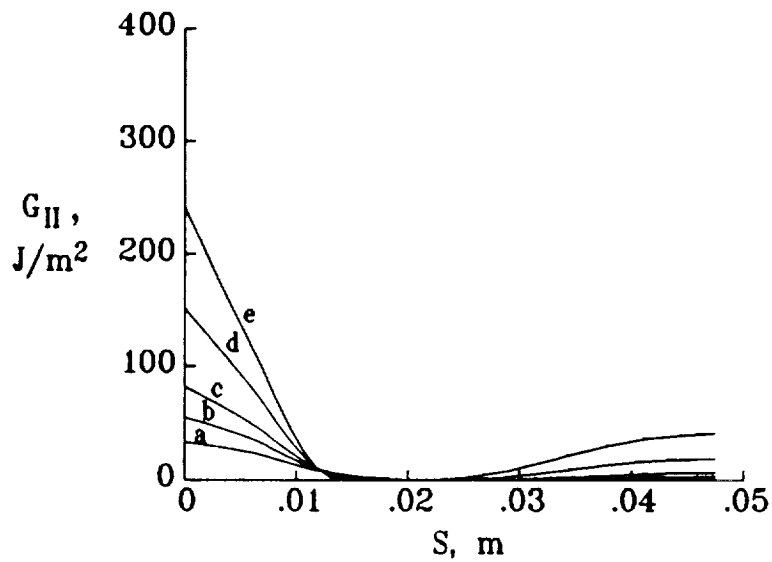
of G_{II} is larger than the peak value of G_I except for the case $\epsilon_x = -.005$. The total strain-energy release rate (Fig. 5.1.4c) varies significantly along the front for the larger strains, but for the smaller strains the magnitude is almost constant. Depending on one's choice of growth criterion, very different predictions of even the direction of growth are possible. A criterion based only on G_I would predict growth perpendicular or nearly perpendicular to the load direction for all of the strain levels. A criterion based only on G_{II} would predict growth parallel to the load direction. For the smaller strains, a criterion based on total strain-energy release rate would predict almost uniform growth along the delamination front.

Fig. 5.1.5 shows G_I and G_{II} for a 60x60 mm delamination. Comparison of Figs. 5.1.3 and 5.1.5 show the effect of delamination size on G_I and G_{II} for two circular delaminations. Both delaminations were subjected to the same strain levels. Figs. 5.1.3a and 5.1.5a show that the larger delamination is closed (actually over-lapping) for more of the delamination front. Also, note that the distribution in the overlapping region is more complicated for the larger delamination. This is because the strains for the larger delamination are larger multiples of the bifurcation buckling strain. This conclusion was verified by subjecting the smaller delamination to higher strains. (These results are not presented in this dissertation.) The larger delamination has a much larger G_I for the region near $S = 0$. Figs. 5.1.3b and 5.1.5b show that G_{II} is also larger for the larger delamination near $S = 0$. Hence, one might expect unstable extension of the delamination once it begins to grow. However, based on the calculated strain-energy release rates, a circular delamination is not expected to grow self-similarly into a larger circular delamination. It should become elliptical.

Figures 5.1.3 and 5.1.4 show results for 30x30 and 30x60 mm delaminations. Comparison of Figs. 5.1.3 and 5.1.4 shows that except for the lowest strains, the smaller (circular) delamination actually has a larger G_I . Hence, the growth rate based on G_I is expected to be larger for the smaller delamination. As pointed out earlier, the distributions of G_{II} for circular and elliptical delaminations are quite



(a) Mode I



(b) Mode II

Fig. 5.1.5 Strain-energy release rate distributions for a circular delamination. (diameter = 60mm)

different. Even the location of maximum G_{II} is different. The peak values of G_{II} for the two delaminations are similar. Hence, based on G_{II} the growth rate should be about the same for both delaminations, but the direction of growth would be different.

5.2 Interpretation of Deformation and Load Transfer

Section 5.1 presented some numerical results for strain-energy release rates. Several trends were observed and discussed. The purpose of this section is to present an intuitive explanation of the process by which load is redistributed and secondary loads created which lead to instability-related delamination growth (IRDG).

The mechanics of IRDG for the through-width delamination have been described previously in refs. 3, 4, 5. The mechanics of IRDG for the embedded delamination will be *derived* here. Both axisymmetric and uniaxial loading of the embedded delamination will be considered (even though axisymmetric loading is not considered elsewhere in this thesis). The approach will be to present first G_I and G_{II} results which illustrate the different behaviors of several configurations which exhibit IRDG. Then mechanics arguments will be offered to explain the different behaviors.

5.2.1 Comparison of Behaviors for the Through-Width and the Embedded Delamination

Four cases were analyzed: the through-width delamination, the axisymmetrically loaded embedded circular delamination, the uniaxially loaded embedded circular delamination, and the uniaxially loaded embedded elliptical delamination. In all cases the thicknesses H and h were 4 and .4 mm, respectively. The through-width delamination was 30mm long. The circular delaminations were 30mm in diameter. The elliptical delamination was elongated along the y -axis and had dimensions of 30x60mm. The same strain range was used for all the cases.

Figures 5.2.1.1 and 5.2.1.2 show the effect of strain level on G_I and G_{II} for the through-width delamination and the embedded delamination. The mode III component is not shown because it was essentially zero for all the cases considered. In general, one would not necessarily expect G_{III} to be zero. Both uniaxial and axisymmetric loads were considered for the embedded delamination. For the uniaxially loaded embedded delamination, both a circular and an elliptical delamination were analyzed. Figs. 5.2.1.1c, 5.2.1.1d, 5.2.1.2c, and 5.2.1.2d show the variation with strain level at two points along the delamination front of the uniaxially loaded embedded delamination: at $\theta = 0^\circ$ and $\theta = -90^\circ$. See Fig. 2.8.2 for the definition of θ .

The variation of G_I with strain level is dramatically different for the four cases. For the through-width delamination G_I increases very rapidly after buckling occurs (Fig. 5.2.1.1a). After reaching a peak, G_I decreases. For the axisymmetric case, G_I increases monotonically. Also, the magnitude of G_I in Fig. 5.2.1.1b is much larger than in Fig. 5.2.1.1a.

Fig. 5.2.1.1c shows the variation of G_I at $\theta = -90^\circ$ for a uniaxially loaded embedded delamination. Only the results for the elliptical delamination are shown here, since G_I was zero at $\theta = -90^\circ$ for all strain levels for the circular delamination. The shape of the curve for the elliptical delamination is similar to that for the through-width delamination (Fig. 5.2.1.1a), but the magnitude is less. At $\theta = 0^\circ$, G_I is shown for both the circular and elliptical delaminations (Fig. 5.2.1.1d). Note that the magnitude of G_I is much larger than in Figs. 5.2.1.1a-5.2.1.1c. Also, G_I increases rapidly and monotonically with applied strain.

Fig. 5.2.1.2 shows the G_{II} variations with strain level. In all cases G_{II} increased monotonically with strain. G_{II} is of the same order of magnitude for all the cases except for the uniaxially loaded circular delamination at $\theta = -90^\circ$ (Fig. 5.2.1.2c). This contrasts with the very wide range of magnitudes in Fig. 5.2.1.1 for G_I .

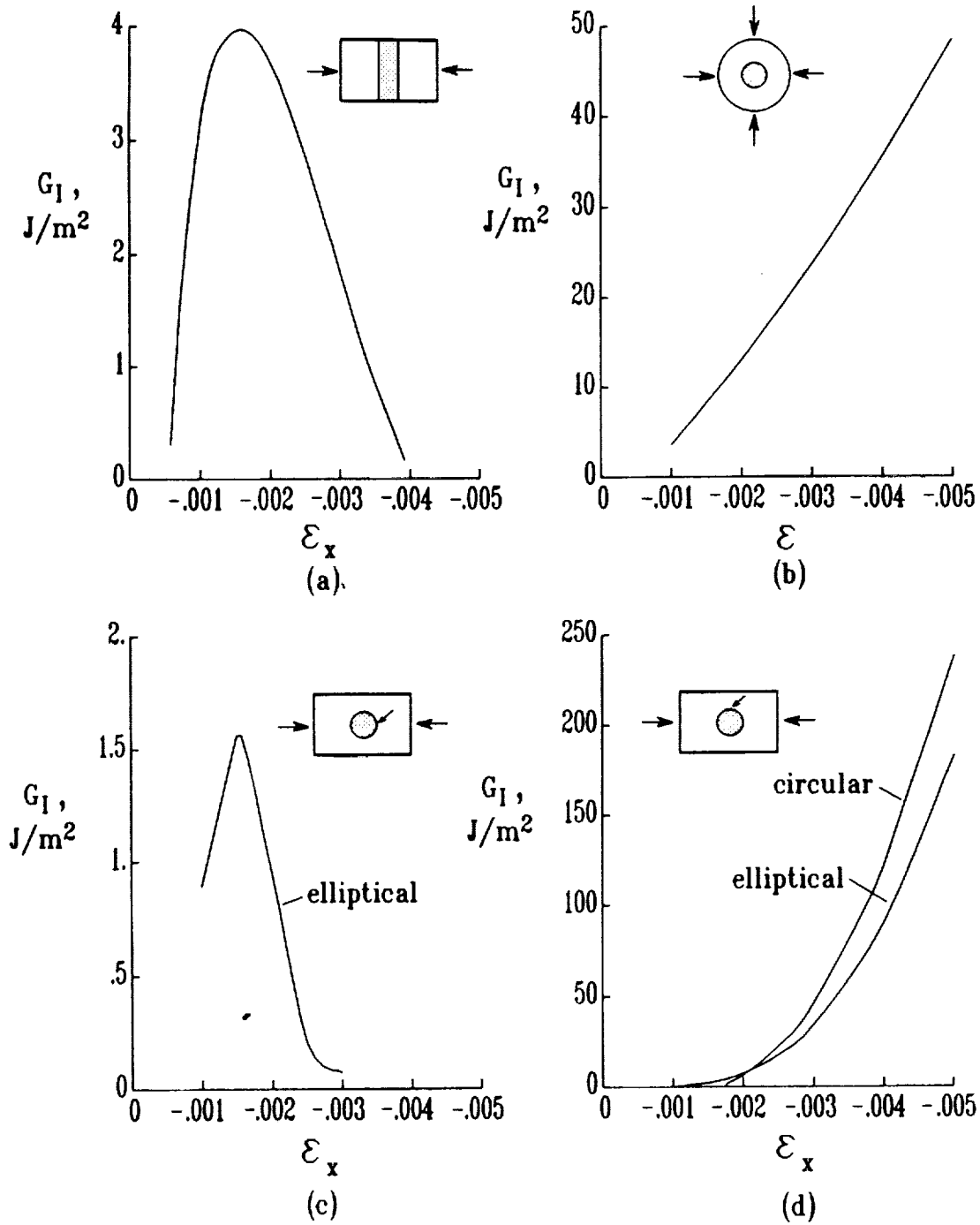


Fig. 5.2.1.1 Effect of strain level on G_I . (a) Through-width delamination, (b) Embedded delamination with axisymmetric load, (c) Embedded delamination with load at $\theta = -90$, and (d) Embedded delamination with uniaxial load at $\theta = 0$.

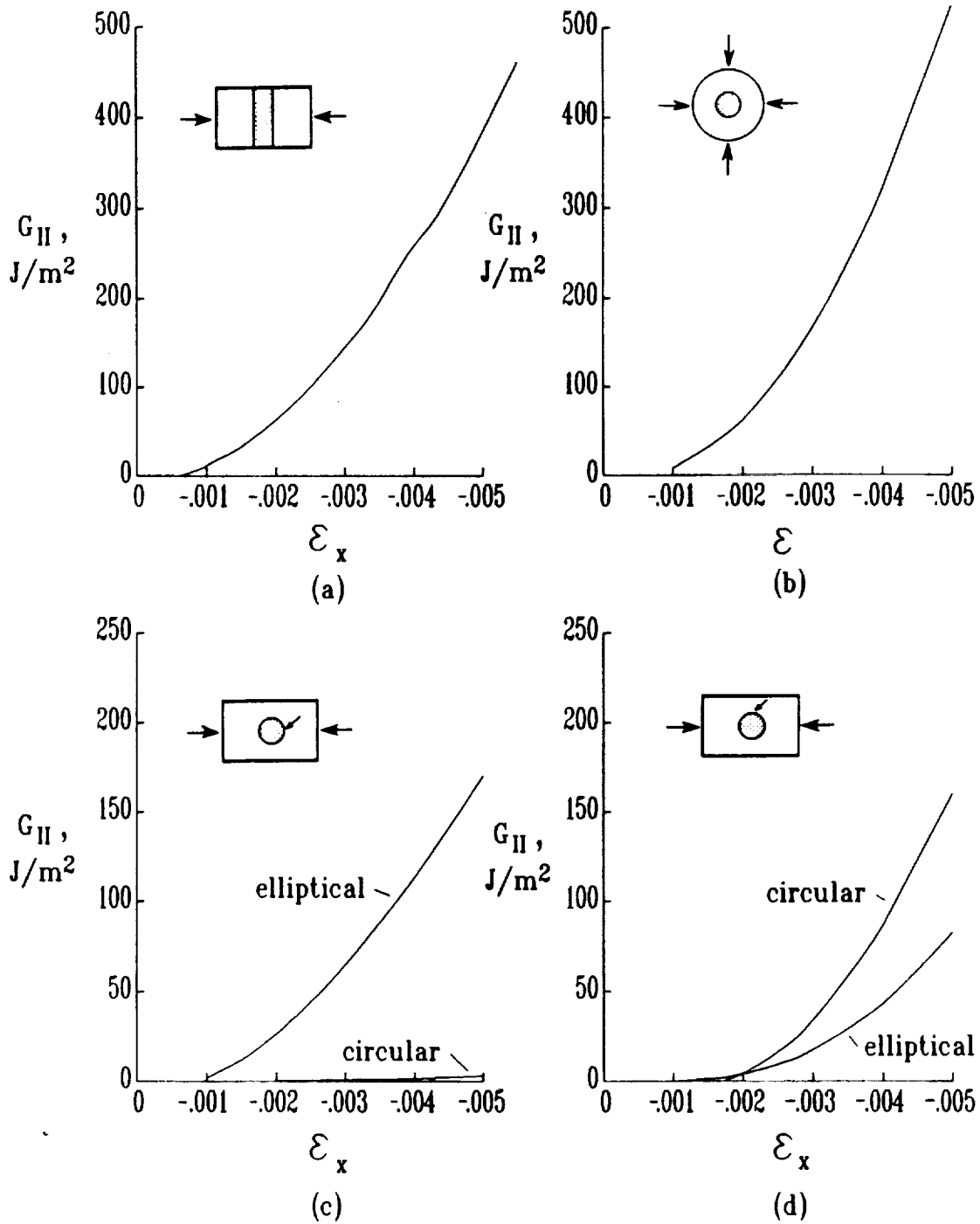


Fig. 5.2.1.2 Effect of strain level on G_{II} . (a) Through-width delamination, (b) Embedded delamination with axisymmetric load, (c) Embedded delamination with uniaxial load at $\theta = -90$, and (d) Embedded delamination with uniaxial load at $\theta = 0$.

Even though the strain-energy release rates in all the cases illustrated in Figs. 5.2.1.1 and 5.2.1.2 are a result of local buckling, the variety of behavior suggests that there must be variations in the mechanism by which local buckling causes strain-energy release rates. The next section will attempt to explain these mechanisms.

5.2.2 Mechanics of IRDG for the Embedded Delamination

In highly simplified anthropomorphic terms, a strip of the buckled region which is parallel to the load direction (strip A in Fig. 5.2.2.1) wants to buckle outward. A strip of the buckled region which is perpendicular to the load direction (strip B in Fig. 5.2.2.1) has no desire to deform outward; it is pushed out by strip A. Strip A is analogous to the through-width case. The constraint provided by strip B reduces G_I for strip A. Conversely, strip A causes high G_I at the ends of strip B when strip A pushes strip B outward. Of course, the buckled region is not comprised of strips, but this simplified interpretation helps explain the behavior observed. The following paragraphs present a more rigorous and detailed discussion of the mechanics of instability-related delamination growth (IRDG).

The through-width delamination will be discussed first. After describing the mechanics for the through-width delamination, its close relationship with the embedded delamination with axisymmetric loads will be discussed. Next, tractions will be applied to the through-width delamination configuration which transform it into a uniaxially loaded embedded delamination. The required tractions should give some feel for why the behaviors differ for the embedded delamination and the through-width delamination under uniaxial loads.

The discussion of the through-width delamination can be expedited by first transforming this geometrically nonlinear problem into a linear one with nonlinearly related loads (ref. 4). Fig. 5.2.2.2a shows a schematic of a laminate with a postbuckled through-width delamination. In Fig. 5.2.2.2b the buckled region is replaced by the loads P_D and M , the axial load and moment, respectively, in the

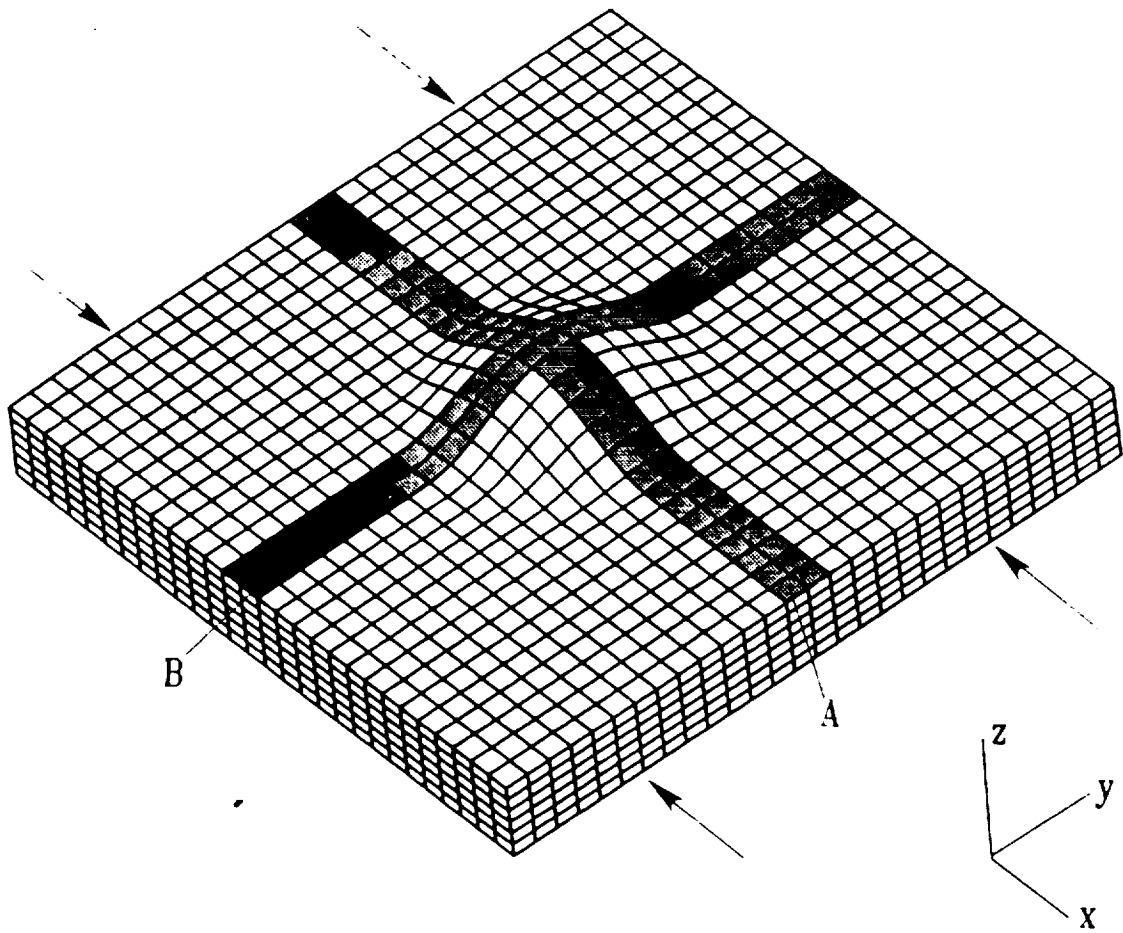


Fig. 5.2.2.1 Strips of sublaminates aligned perpendicular and parallel to the load direction.

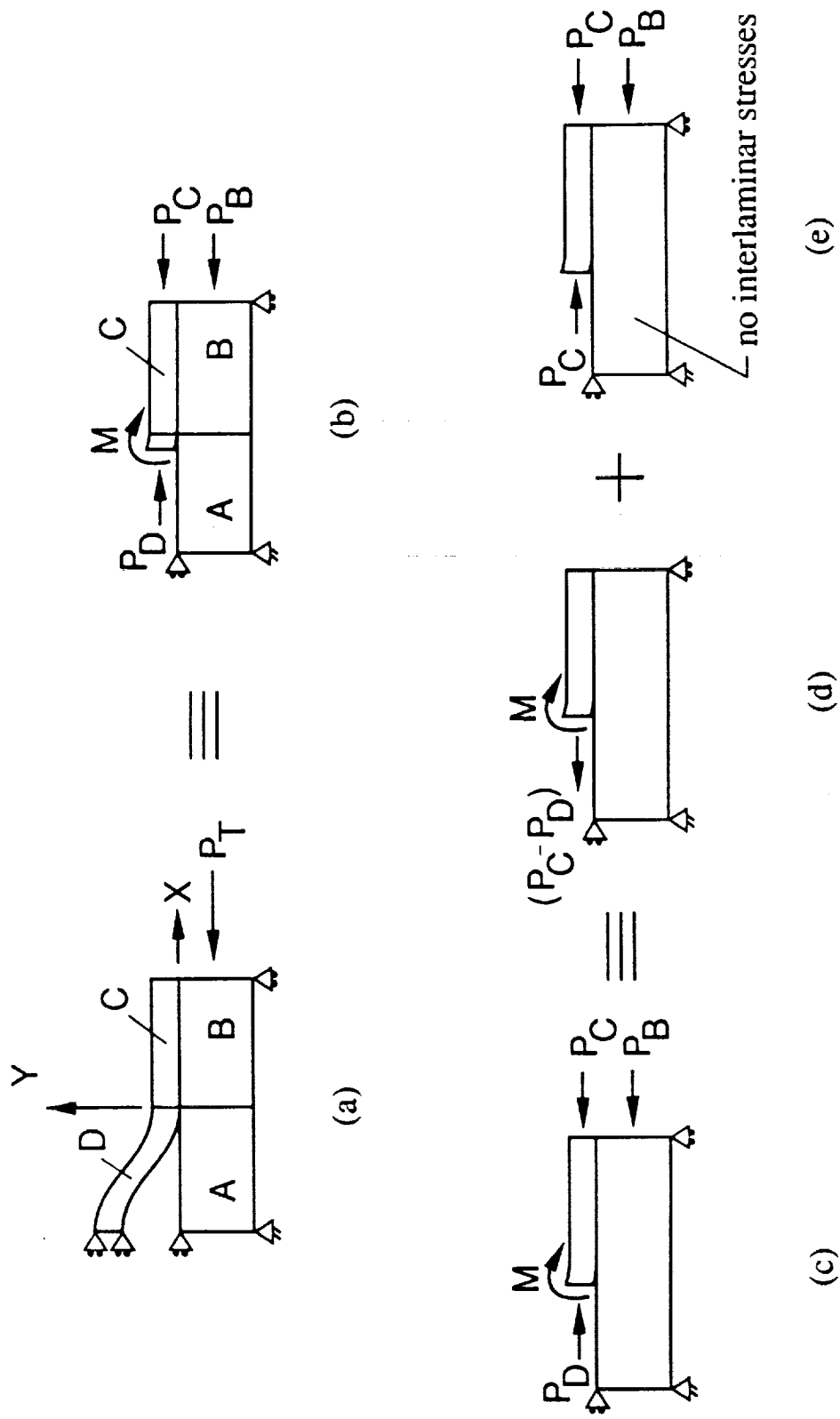


Fig. 5.2.2.2 Nonlinear configuration (a) transformed into linear configuration (d) with two nonlinearly related loads ($P_C - P_D$) and M .

buckled region where it is cut. The total applied load P_T is equal to $P_B + P_C$. The load system in Fig. 5.2.2.2c, (which is the same as Fig. 5.2.2.2b) can be divided into the two load systems shown in Figs. 5.2.2.2d and 5.2.2.2e. Because P_C and P_B are calculated using rule of mixtures, the load system in Fig. 5.2.2.2e causes a uniform axial strain state and no interlaminar stresses. Accordingly, for strain-energy release rate calculation, the configuration in Fig. 5.2.2.2d is equivalent to the original configuration (Fig. 5.2.2.2a). The moment M opens the delamination, contributing to G_I . It also contributes to some G_{II} (ref. 4). Also, the load $(P_C - P_D)$ contributes to G_{II} . In addition, because of the offset of the line of action of $P_C - P_D$ relative to the delamination, this force creates a moment which tends to close the delamination and reduce the G_I component caused by M . The result of the competing mechanisms are strain-energy release rate variations like that in Fig. 5a and 5.2.1.2a. The mode I strain-energy release rate first increases very rapidly with increasing strain and then decreases to zero. The mode II strain-energy release rate increases monotonically with applied load, since both M and $(P_C - P_D)$ contribute to G_{II} .

The axisymmetrically loaded circular delamination is very similar to the through-width delamination. In fact, the schematics in Fig. 5.2.2.2 are applicable if the forces are replaced by forces per unit length. The load in a column, P_D , is essentially constant after the applied strain is increased beyond the buckling strain, but the load in an axisymmetrically loaded plate continues to increase significantly after buckling. The load P_C increases linearly with the applied load. Hence, $(P_C - P_D)$ is large for the through-width delamination but is relatively small for the axisymmetric case. As a result, there is little attenuation of the effects of M by $(P_C - P_D)$ for the axisymmetric case. Consequently, G_I is much larger for the axisymmetric case (Compare Figs. 5.2.1.1a and 5.2.1.1b).

Now the uniaxially loaded embedded delamination will be considered. Figs. 5.2.2.3-5.2.2.6 illustrate the transformation of a through-width delamination (Fig. 5.2.2.3) into an embedded delamination (Fig. 5.2.2.6). The letters A through

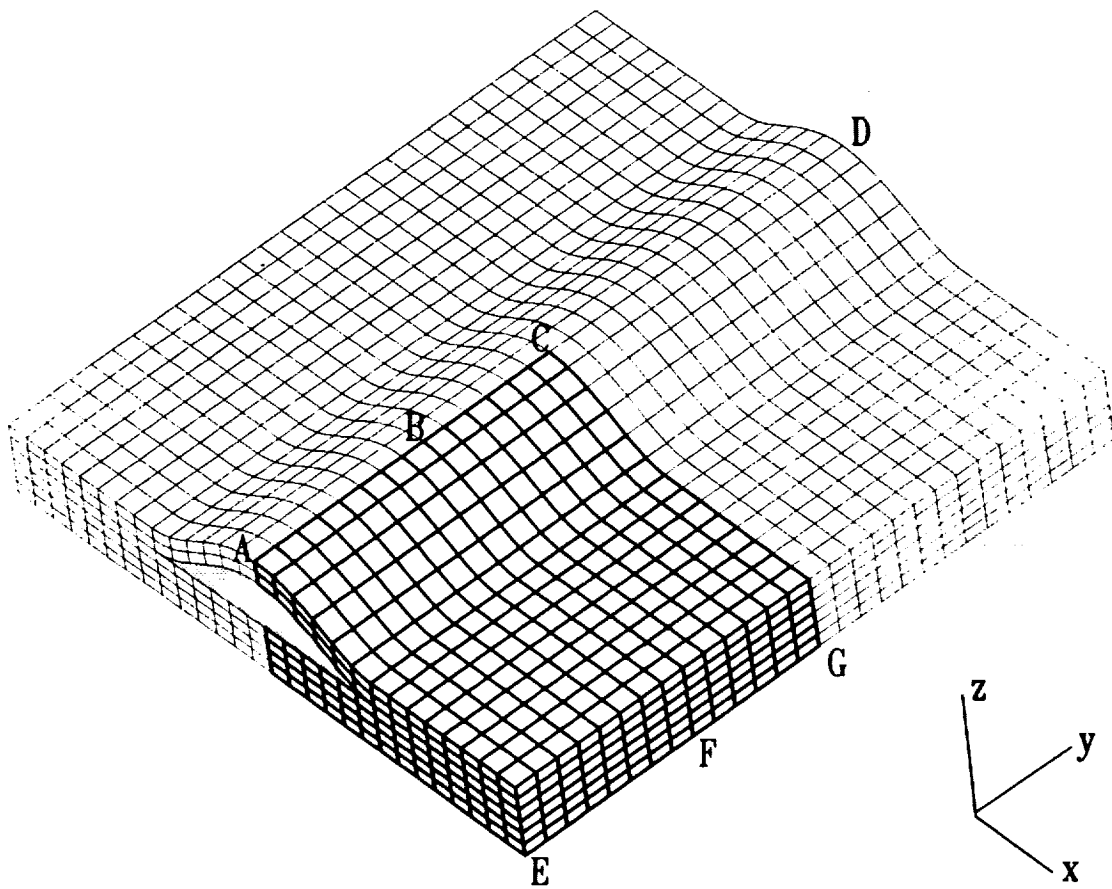


Fig. 5.2.2.3 Schematic for transformation of through-width delamination into an embedded delamination.

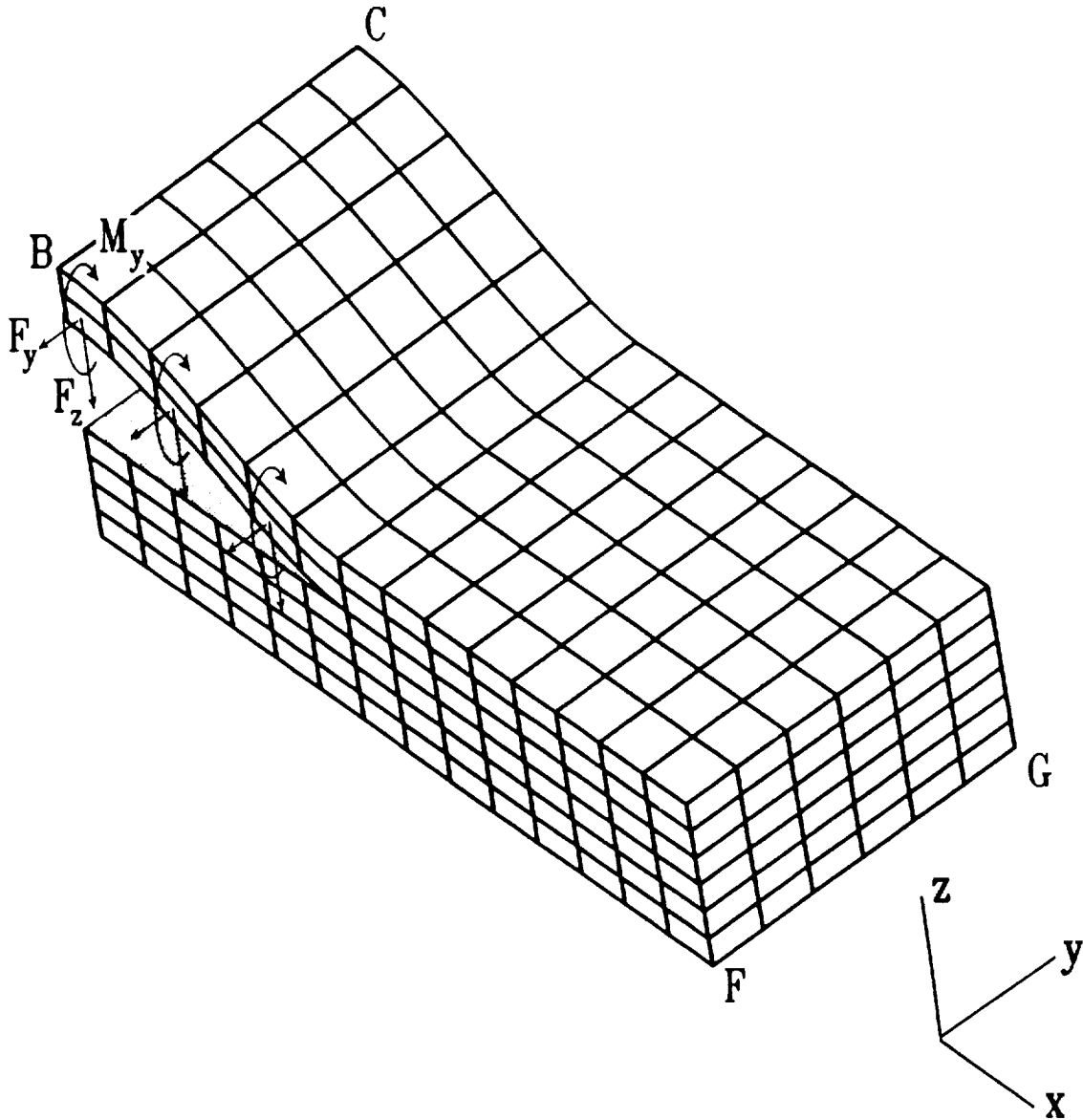


Fig. 5.2.2.4 Slice of laminate showing tractions required to perform transformation by closing buckled part of boundary BF.

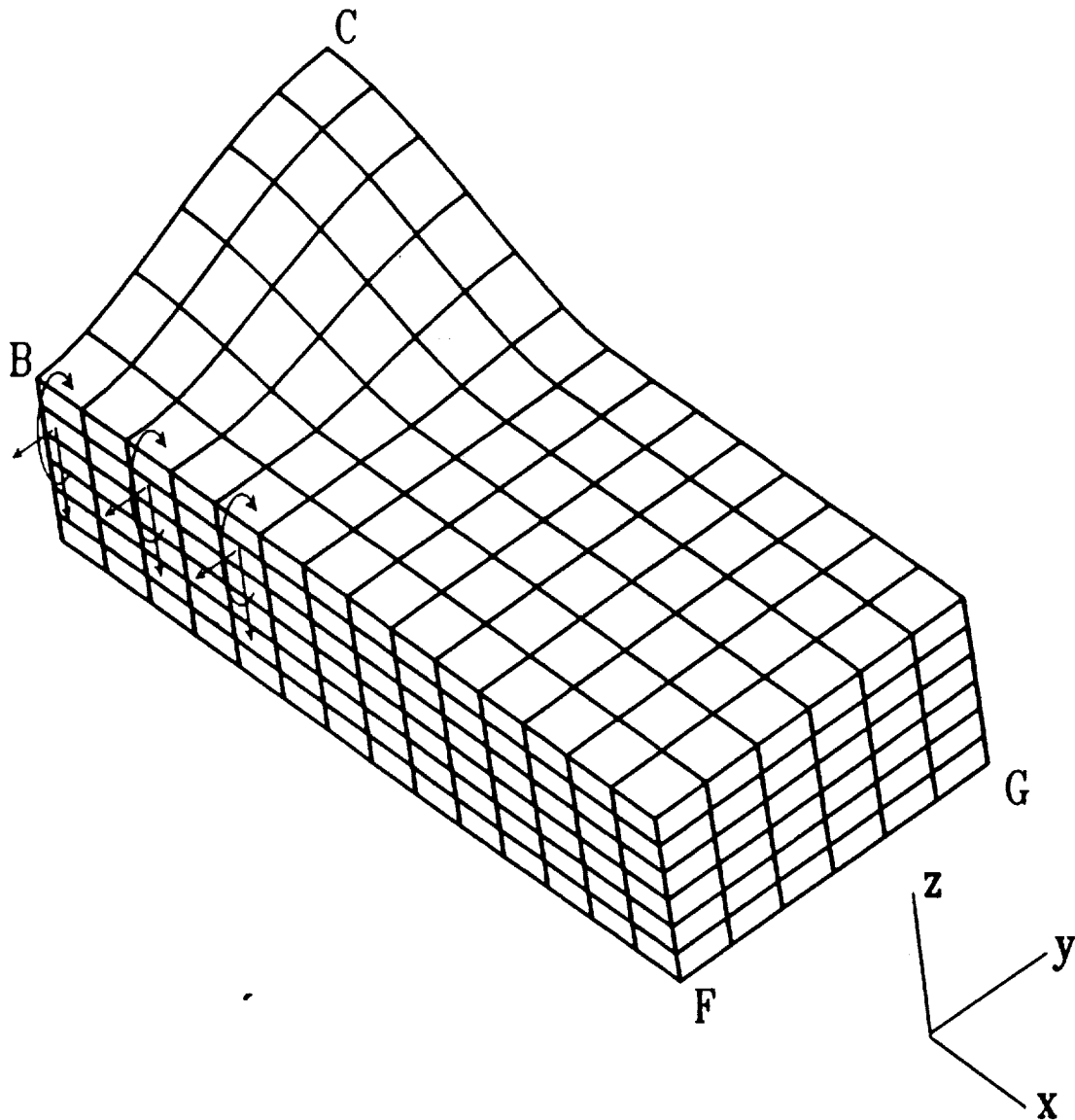


Fig. 5.2.2.5 Slice of laminate after tractions have closed boundary.

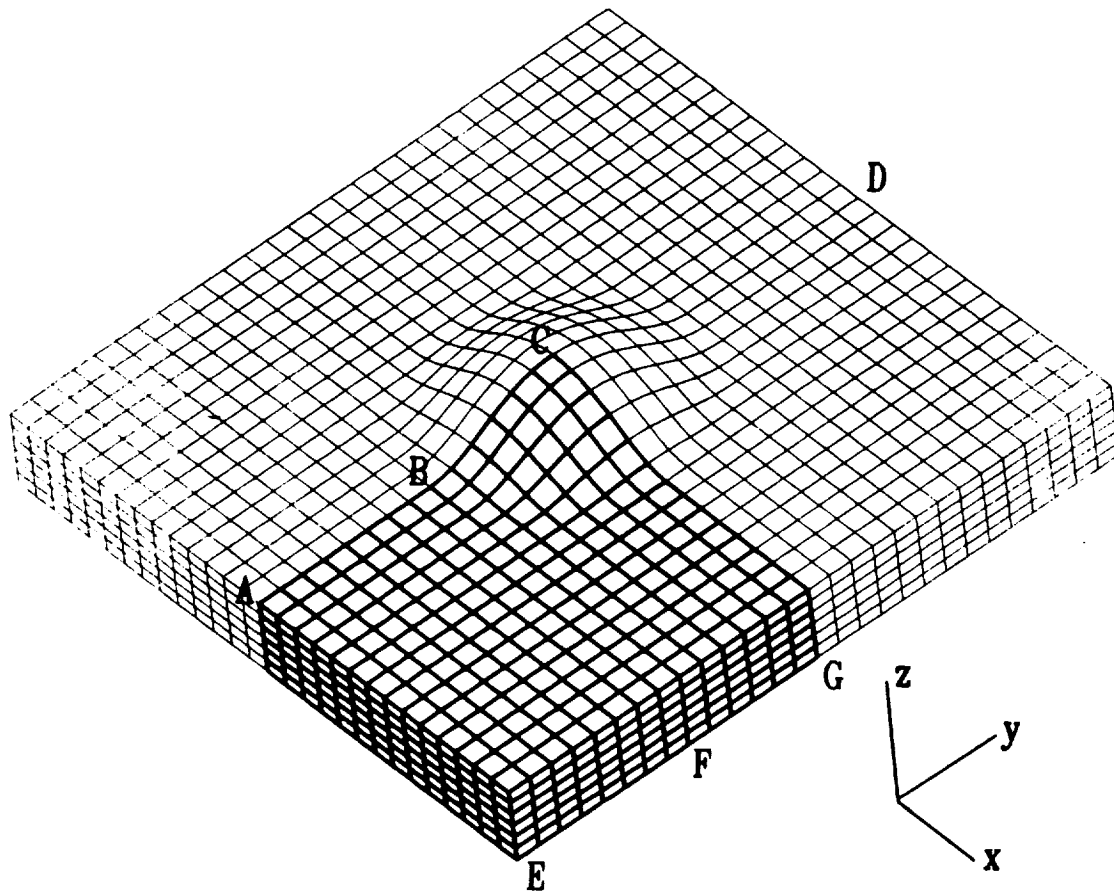


Fig. 5.2.2.6 Entire laminate after transformation to embedded delamination.

G are added to aid the discussion. They are not related to the letters in Fig. 5.2.2.2. To expedite the discussion, the embedded delamination will be assumed to be rectangular. Traction is required to close the buckled part of region AEFB. These will only be non-zero near the new delamination front and are, in fact, the interlaminar stresses.

Fig. 5.2.2.4 shows a slice removed from the laminate. The figure shows the forces required to close the buckled part of the boundary BF. These forces are generated when the region AEFB is closed. These forces indicate some of the interaction of regions AEFB with BFGC. There are in-plane forces F_y , transverse forces F_z , and a moment M_y . Fig. 5.2.2.5 shows the same slice after the forces have closed the buckled part of BF.

The moment M_y would operate in the direction indicated in Fig. 5.2.2.4 based on the curvature in Fig. 5.2.2.5. Likewise, the transverse force, F_z , would be expected to act downward to help close the delamination front. The force, F_y , is a result of two things: transverse deflection and Poisson's ratio. When transverse deflection occurs, the length of a line from A to D (Fig. 5.2.2.6) increases, hence the buckled region must be stretched in the y-direction. When the laminate is compressed in the x-direction, it expands in the y-direction due to Poisson's effect. If the base laminate has a larger Poisson's ratio than the sublaminates, then a force F_y is required to enforce compatibility when the buckled part of BF is closed. The sign of F_y due to Poisson's ratio would depend on the relative magnitudes of the Poisson's ratios. Differences in Poisson's ratio were not considered in this study.

The magnitude of F_y should be related to the in-plane stiffness in the y-direction. The magnitude of M_y should be related to the flexural stiffness in the y-direction. The effect of material properties on F_z is not as straight-forward, so no prediction will be offered.

The dimensions of the embedded delamination should affect the forces and moment. For the same transverse deflection, the curvature in the y-direction is

less for a larger dimension b , so M_y should decrease with increasing b . Also, the strain in the y -direction due to the increased length A-D (Fig. 5.2.2.6) would be less for larger b . Hence, for the same transverse deflection F_y should decrease with increasing b .

The moment M_y should contribute primarily to G_I , but it also contributes to G_{II} . The force F_y should contribute to G_{II} and reduce G_I . The reduction is due to the offset between the delamination plane and the middle of the sublaminates. This offset causes a moment relative to the delamination plane which is opposite to M_y . Based on the large G_I in Fig. 5.2.1.1d, the opening effects of M_y must dominate the closing effects of F_y .

The original configuration with a through-width delamination (Fig. 5.2.2.3) had some distribution of G_I and G_{II} along $x = a$. The application of the forces F_y , F_z , and the moment M_y changes the load flow significantly. Closing the ends of the through-width delamination (area AEFB) contributes a compressive component of interlaminar stresses along the front $x = a$, thus reducing G_I . In fact, because of this reduction, G_I was zero for all strain levels at $\theta = -90^\circ$ for the circular delamination under uniaxial loads. For the elliptical delamination, the magnitude of G_I at $\theta = -90^\circ$ was less than for the through-width delamination for the same reason (Fig. 5.2.1.1a and 5.2.1.1c).

Based on the preceding discussion, one would expect the behavior of a through-width delamination and the uniaxially loaded embedded delamination to have some similarity, but probably more differences. Fig. 5.2.1.1 illustrates this very well. For an embedded delamination highly elongated perpendicular to the load direction, one would expect the behavior to be like that for the through-width delamination. No highly elongated delaminations were examined in this study, but even the 1:2 aspect ratio ellipse has a G_I variation at $\theta = -90^\circ$ (Fig. 5.2.1.1c) which is very similar to that for a through-width delamination (Fig. 5.2.1.1a). But this similarity has little importance for this case, since the G_I was very much larger at $\theta = 0^\circ$ (Fig. 5.2.1.1d).

5.3 Comparison of Full 3D, Thin-film 3D, and Thin-film Plate Analyses

For an Embedded Delamination

Geometrically nonlinear 3D finite element analysis is inherently very expensive. Hence, there is considerable motivation to use simplified and less rigorous (and less expensive) analysis techniques. An obvious approximation is to assume that the base laminate is so much thicker and stiffer than the sublaminates, that the base laminate strains are independent of how the sublaminates deform. For most of the configurations analyzed herein, the base laminate deformation can be expressed in closed form. Because of the base laminate dominance, only the sublaminates need to be analyzed. This is referred to as a thin-film analysis. Boundary conditions consist of displacements prescribed to impose compatibility of the sublaminates with the known base laminate deformations. This thin-film assumption can be used with 3D or with plate analysis.

The thin-film assumption has been used with plate analysis by several researchers, as mentioned in Chapter 1. However, only ref. 21 gives distributions of total strain-energy release rate. This section will compare results for a square and a rectangular delamination from ref. 21 with 3D solutions. The sublaminates are assumed to have an initial waviness of a sinusoidal shape, as given by eqn. 5.3.1.

$$w_{initial} = \frac{.05}{4} \left(1 + \cos \frac{\pi x}{a}\right) \left(1 + \cos \frac{\pi y}{b}\right) \quad mm \quad (5.3.1)$$

The sublaminates and base laminate thicknesses were .51 mm and 5.1 mm, respectively. The entire laminate is assumed to be isotropic with a Young's modulus of 53.3 GPa and a Poisson's ratio of .31. Both full 3D and thin-film 3D results will be presented.

Fig. 5.3.1 shows the distribution of G_T along the delamination front for the square delamination (25.4 x 25.4 mm). Three strain levels were considered. Results are shown for full 3D, thin-film 3D, and thin-film plate analysis. There is good

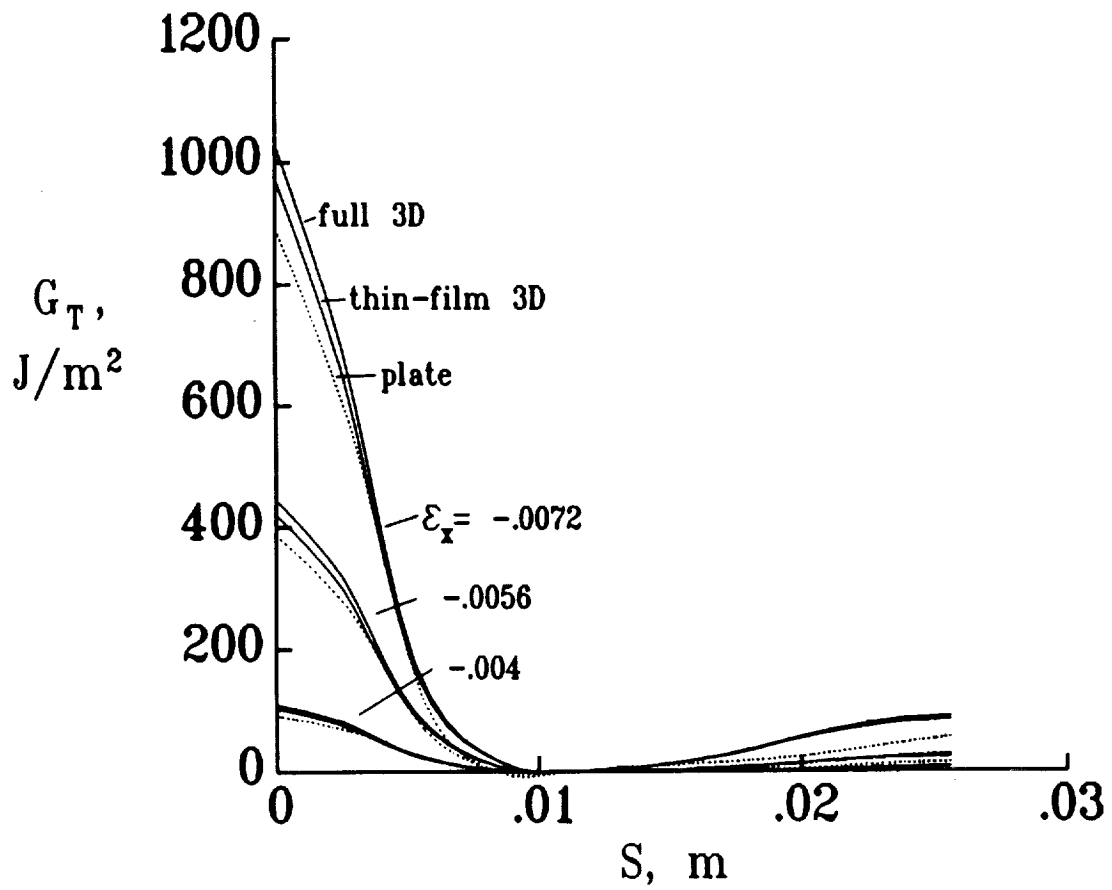


Fig. 5.3.1 Total strain-energy release rate distribution for a square delamination calculated using 3D, thin-film 3D, and plate analysis. ($2a \times 2b = 25.4 \times 25.4 \text{mm}$)

agreement between the three analyses for all three strain levels. Fig. 5.3.2 shows the distribution of G_T along the delamination front for a rectangular delamination (25.4 x 50.8 mm). The agreement between the three analyses is not as good as for the square delamination, but it still is fairly good.

For the cases compared, thin-film plate analysis gave reasonably good predictions of G_T . When one considers the high sensitivity of G_T to parameters such as sublaminar thickness, delamination size, and initial imperfection and the uncertainty of knowing these parameters precisely, the differences between the plate analysis and 3D analysis appear negligible. Of greater importance is the limitation that plate analysis can only calculate G_T , not the components. A hybrid analysis which uses 3D analysis near the crack front and plate analysis elsewhere appears to be a good alternative. Such a technique was used in ref. 4 for the through-width delamination.

The results in Figs. 5.3.1 and 5.3.2 also serve a secondary purpose. Totally different analyses were used to obtain the results in ref. 20 and the 3D results. Also, the method for calculating strain-energy release rates were different. But the agreement is good. Hence, the results give additional validation to both the virtual crack closure technique presented in ref. 20 and to the 3D analysis developed herein.

5.4 Effect of Contact Constraints

Earlier it was shown that for certain combinations of delamination size and strain level, closure occurs over part of the delamination front. Unless constraints are imposed to prevent interpenetration, overlap of the crack faces will occur in an analysis. The results presented in section 5.1 are based on an analysis which allowed interpenetration of the crack faces. This section examines the effects of including contact constraints on the calculated distribution of strain-energy release rates.

The configuration analyzed is a "homogeneous" quasi-isotropic laminate with

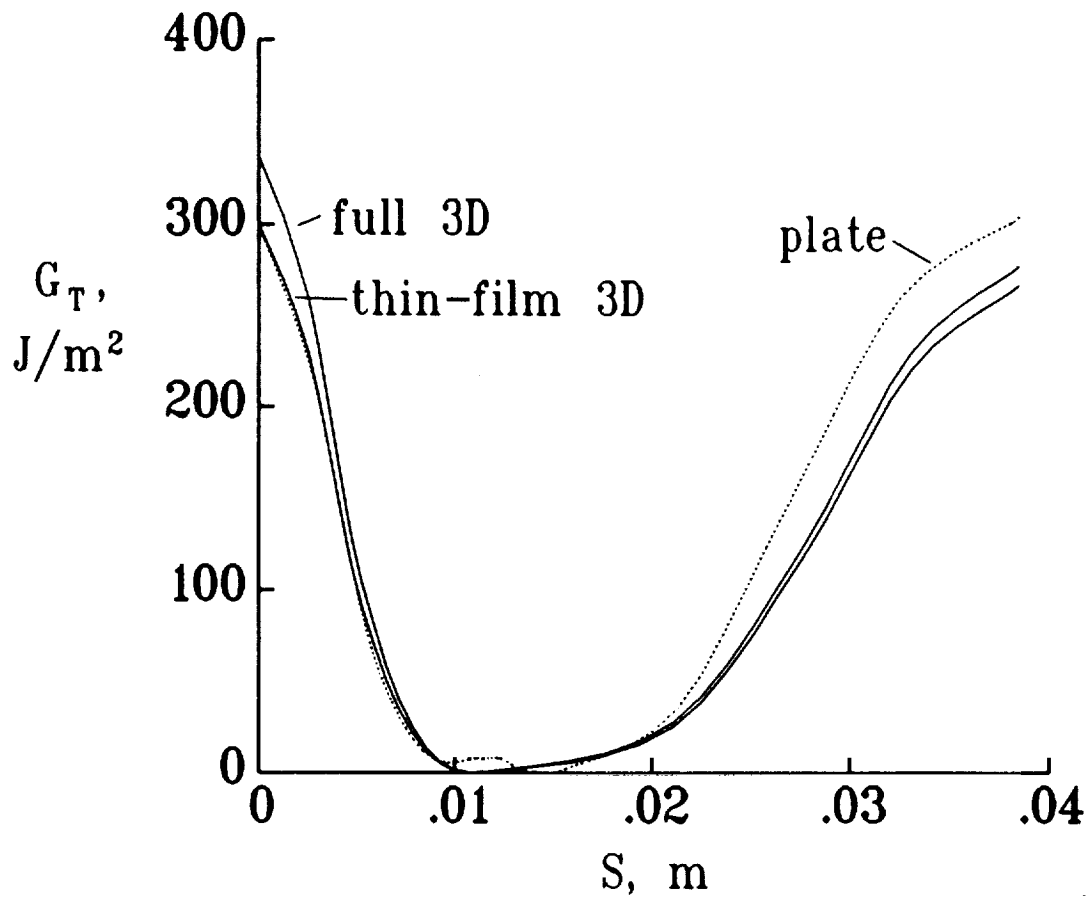


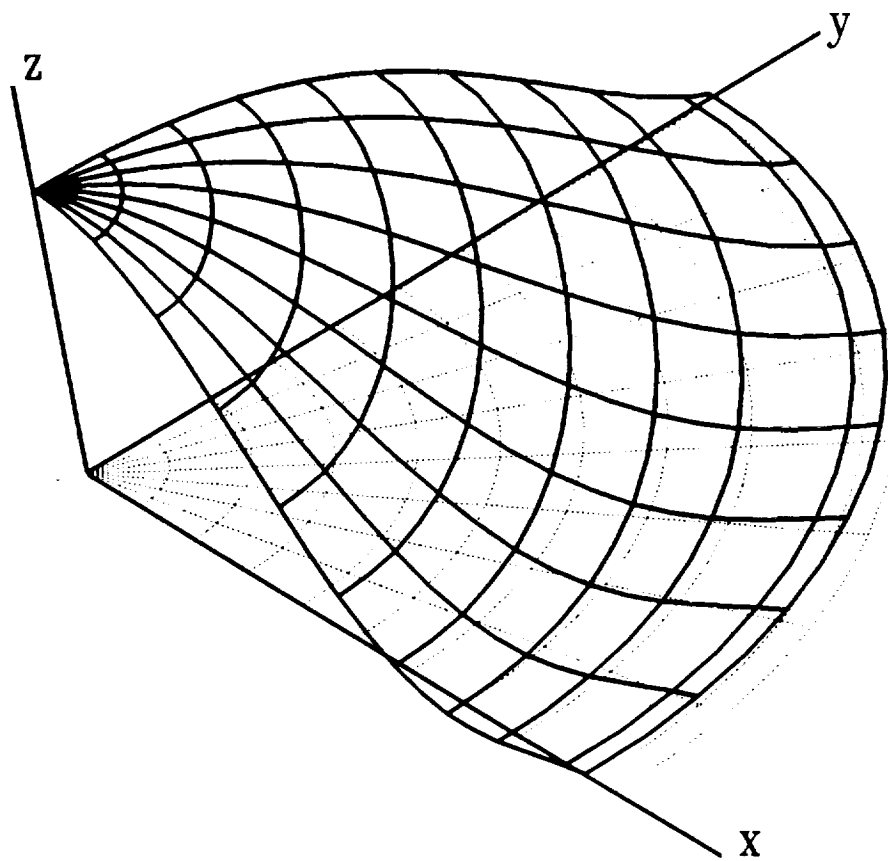
Fig. 5.3.2 Total strain-energy release rate distribution for a rectangular delamination calculated using 3D, thin-film 3D, and plate analysis. ($2a \times 2b = 25.4 \times 50.8mm$) ($\epsilon_x = -.0043$)

a circular delamination ($2a \times 2b = 30 \times 30$ mm). The thickness of the sublaminates is .4 mm and the base laminate is 4.0 mm. For the circular delamination, closure occurred near $\theta = -90^\circ$ for all of the strain levels considered. The amount of closure at 90° relative to the amount of opening elsewhere along the front increased with the ratio of applied strain to the bifurcation buckling strain. Hence, only large strains will be considered here: -.005 and -.02. These are about 3 to 11 times the bifurcation buckling strain. Of course, -.02 strain is unrealistically large for current composites. But larger delaminations or thinner sublaminates can be subjected to strains more than 11 times the buckling strain. The -.02 strain case should simply be considered a case where the applied strain is quite large compared to the buckling strain.

Fig. 5.4.1 and 5.4.2 show the deformation of the sublaminates for the two strains before and after imposing contact constraints. Only the top surface of the sublaminates is plotted. The displacements were scaled up by a factor of 10 and 2.5 for the cases $\epsilon_x = -.005$ and $-.02$, respectively. The interpenetration is much more severe for the larger strain.

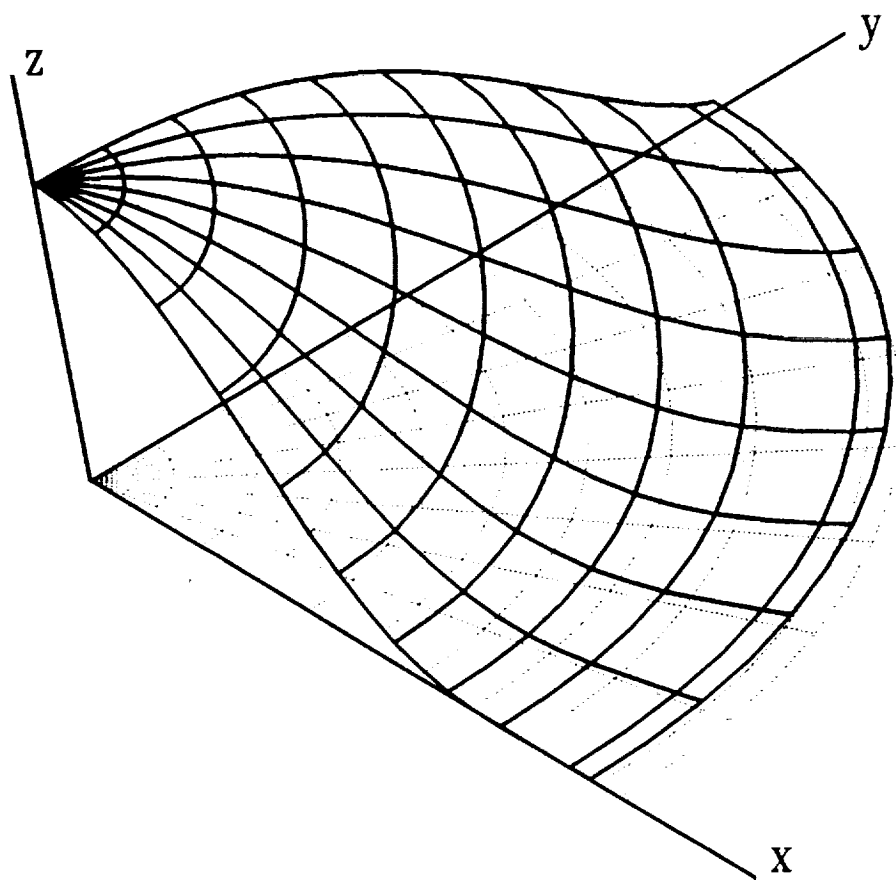
Fig. 5.4.3 shows G_I and G_{II} for a strain of -.005. For comparison, results with and without contact constraints are shown. Because of the approximations mentioned earlier in imposing the constraints, G_I is not computed to be identically zero in the contact region. But it is now negligibly small. In the region where the delamination front is open, G_I is not very sensitive to whether or not contact constraints are imposed. In absolute terms, G_{II} is also not affected much. Fig. 5.4.4 shows G_I and G_{II} for a strain of -.02. Since the overlap (before constraints are imposed) is much greater for the larger strain, one would expect a larger effect on G_I and G_{II} . Comparison of Figs. 5.4.3 and 5.4.4 shows this is the case. But the trends are the same for both strain levels. That is, imposition of the constraints reduces G_I to a negligible magnitude in the contact region and increases G_I in the non-contact region. G_{II} is increased along the entire front.

For a strain level of -.005, little error is incurred by not imposing contact



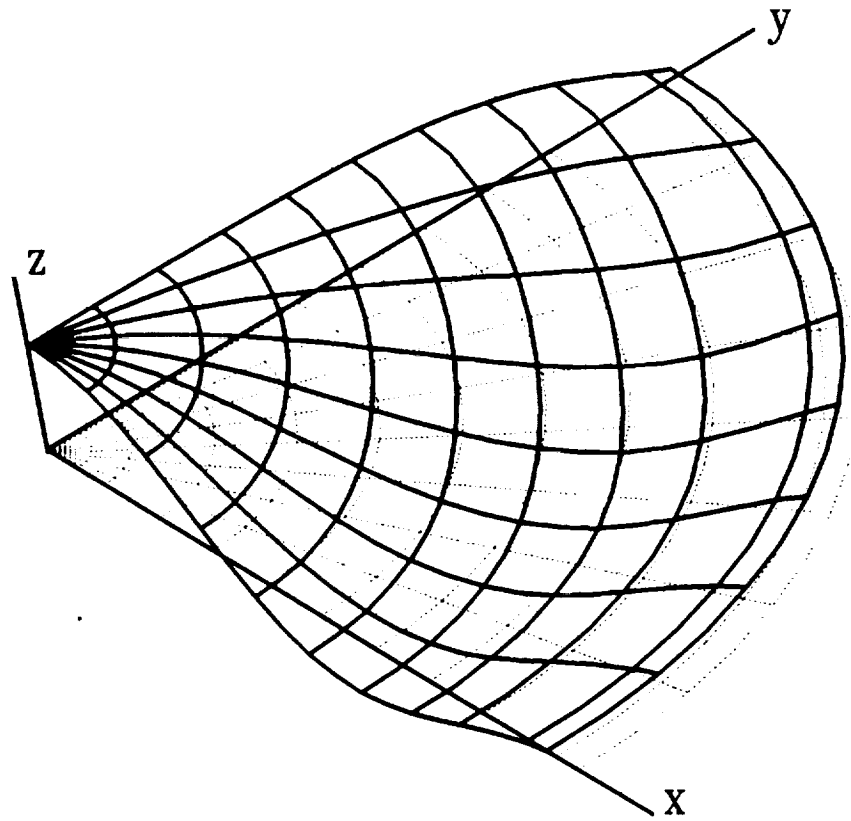
(a) without contact constraints

Fig. 5.4.1 Deformation of top surface of postbuckled sublaminde with and without contact constraints. Displacements multiplied by 10. ($\epsilon_x = -.005$)



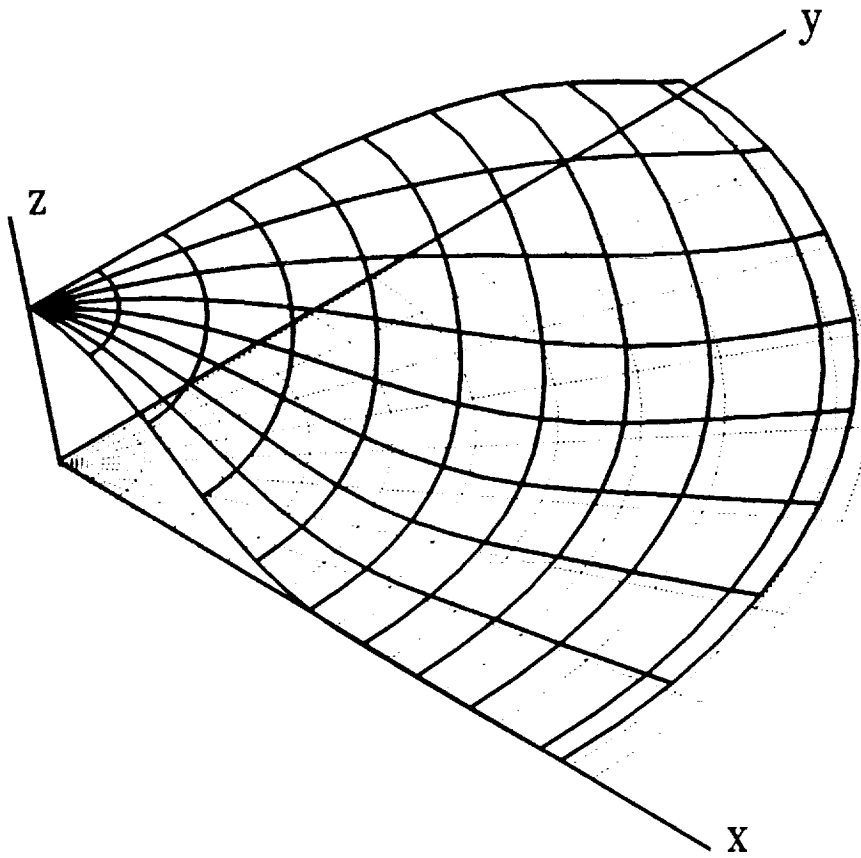
(b) with contact constraints

Fig. 5.4.1, Concluded.



(a) without contact constraints

Fig. 5.4.2 Deformation of top surface of postbuckled sublaminated with and without contact constraints. Displacements multiplied by 2.5. ($\epsilon_x = -.02$)



(b) with contact constraints

Fig. 5.4.2, Concluded.

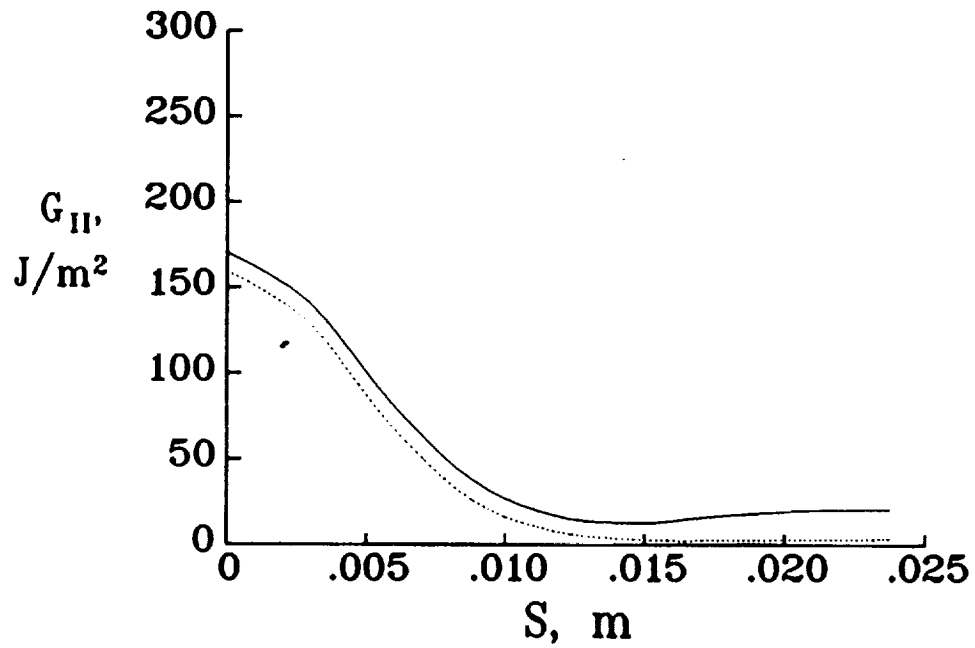
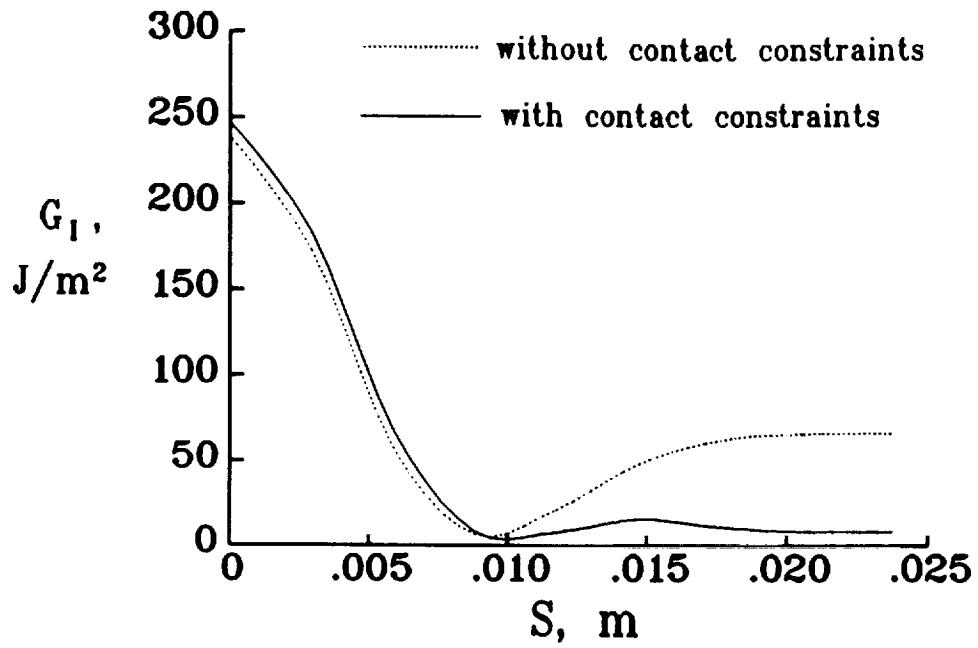


Fig. 5.4.3 Effect of contact constraints on G_I and G_{II} distributions ($\epsilon_x = -.005$).

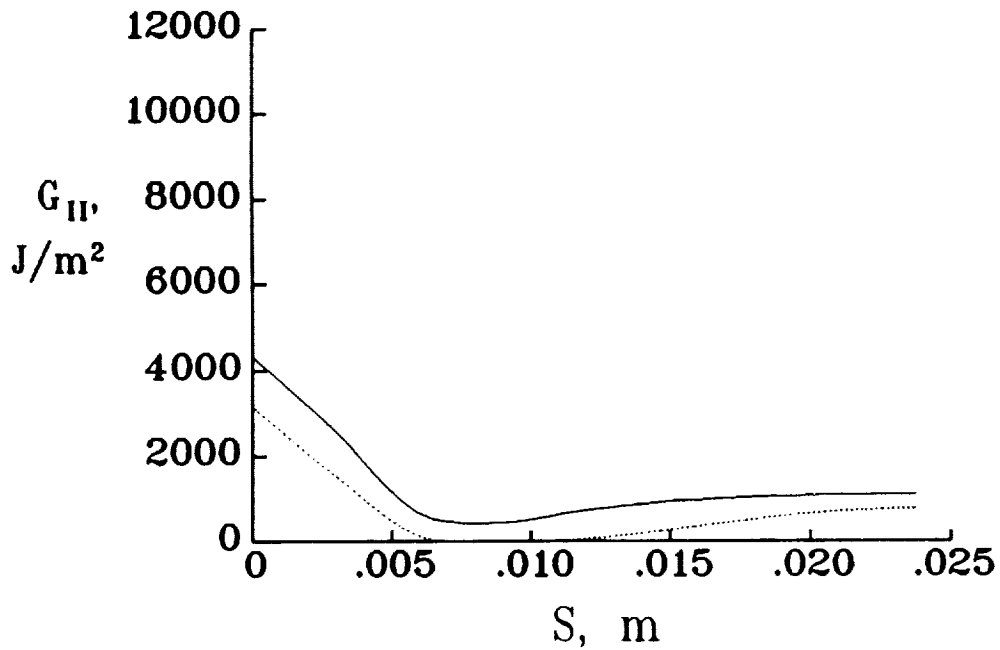
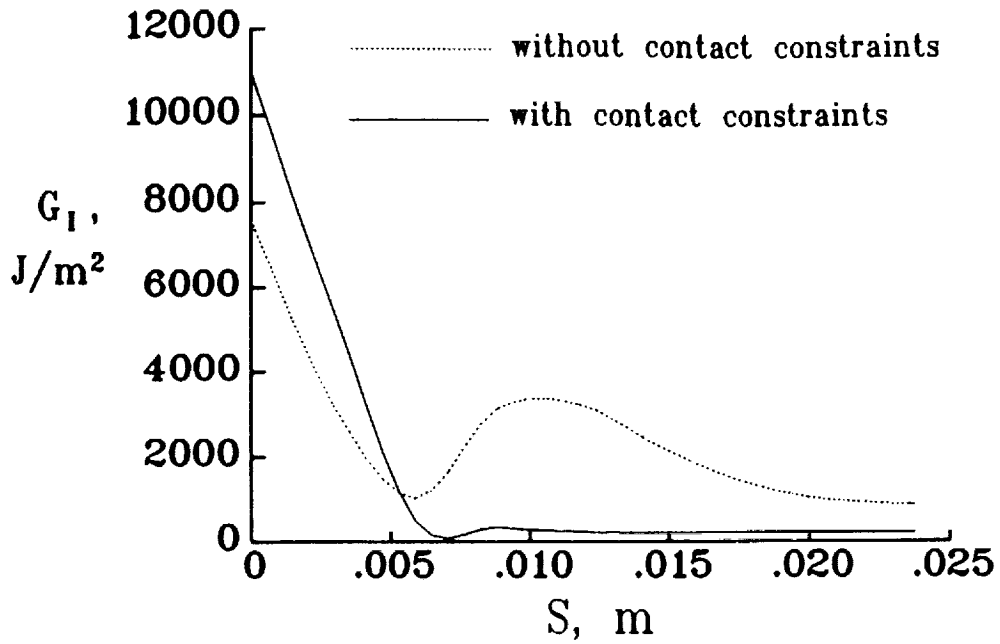


Fig. 5.4.4 Effect of contact constraints on G_I and G_{II} distributions ($\varepsilon_x = -0.02$).

constraints and just recognizing that G_I is zero in the contact region. For a strain of -.02, significant errors occur when contact constraints are not imposed. Since there is a significant computational cost associated with including contact constraints, constraints probably should not be imposed unless the overlap is quite extensive.

5.5 Strain-Energy Release Rates For an Edge Delamination

This section will discuss the results of a limited parametric study of homogeneous quasi-isotropic laminates containing a postbuckled edge delamination. The parameters varied were strain level, delamination shape, and delamination size. The effects of these parameters on deformation and strain-energy release rate were determined.

Figure 5.5.1 shows the variation of G_I , G_{II} , and G_T along the delamination front for a semi-circular edge delamination of radius 15mm. The strain-energy release rates increase rapidly with increased strain. There is a large variation of the strain-energy release rates along the delamination front. The maximum value of G_I is a little larger than the maximum value of G_{II} for each strain level. Note that there is no overlap region for this configuration, in contrast to the response for the circular embedded delamination (see Fig. 5.1.3). The maximum G_I and G_{II} occur at different locations for the edge delamination, which is also different than the circular embedded delamination behavior. In fact, the semi-circular edge delamination behaves somewhat like an elliptical embedded delamination. Fig. 5.1.4 shows that an elliptical embedded delamination exhibits little overlap and has maximum values of G_I and G_{II} at the same locations that the edge delamination has its maximum values. However, G_{II} increased monotonically with perimeter coordinate S for the elliptical embedded delamination. For the edge delamination G_{II} decreases and then increases with S. For the elliptical embedded delamination G_T was almost constant for some strain levels. The G_T is far from constant for any strain level for the edge delamination. The predicted direction of delamination growth depends on the assumed growth criterion, since

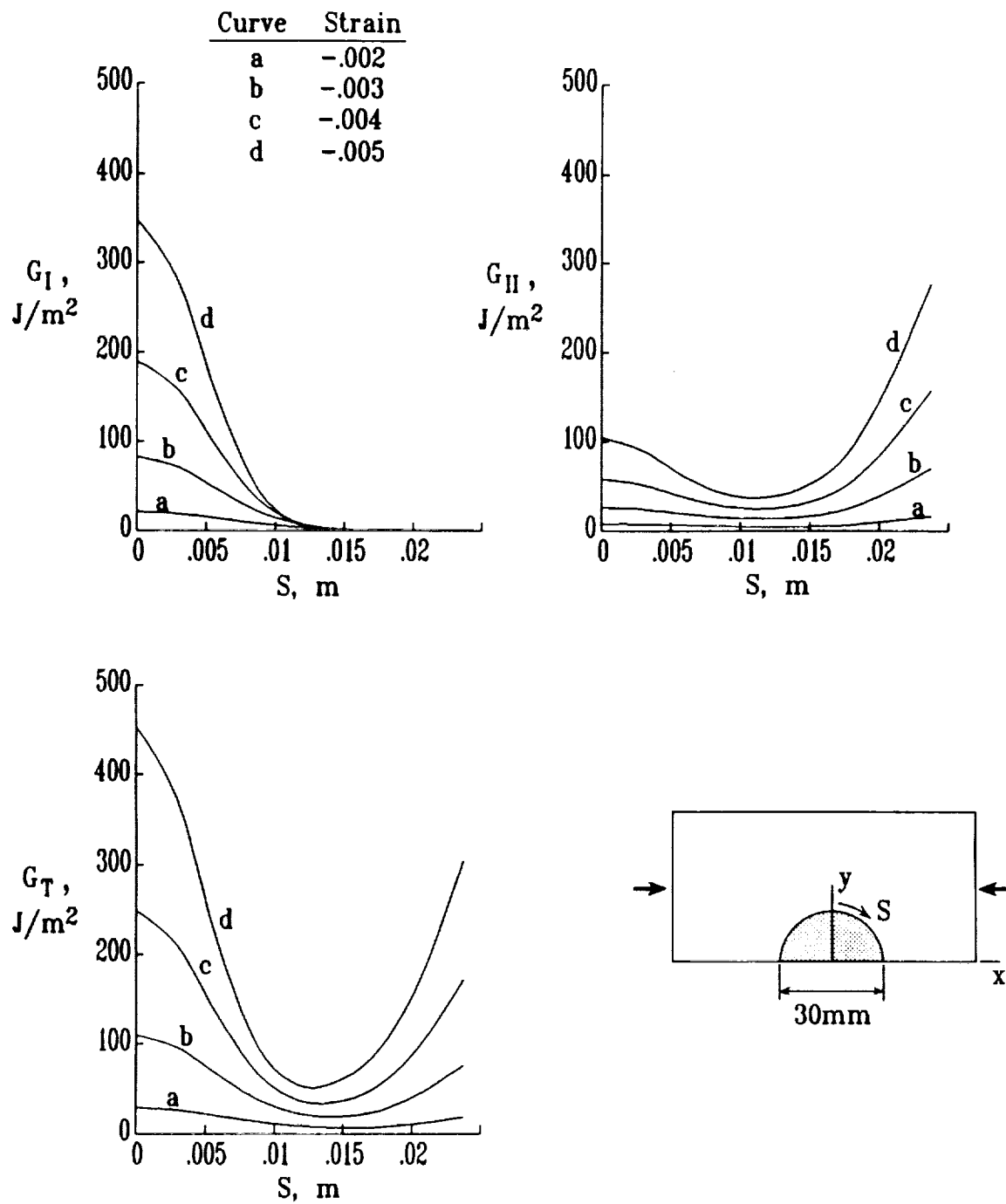


Fig. 5.5.1 Strain-energy release rate distributions for a laminate with a semi-circular edge delamination with a radius of 15mm.

the peak G_I and G_{II} occur at different locations. However, growth should occur preferentially either near the x- or y-axes, and not in between.

Figure 5.5.2 shows the variation of G_I , G_{II} , and G_T along the delamination front for a semi-elliptical edge delamination. The maximum values of G_I and G_{II} still occur at different locations. Now the maximum value of G_{II} is much larger than that for G_I . The predicted direction of growth is still dependent on the assumed growth criterion. However, the semi-elliptical is more likely to grow in the load direction than is the semi-circular delamination.

Figure 5.5.3 shows the variation of G_I , G_{II} , and G_T along the delamination front for a semi-circular edge delamination of radius 30mm. The distributions are similar to the distributions in Fig. 5.5.1 for the smaller semi-circular delamination. The magnitudes of the strain-energy release rates are larger for the larger semi-circular delamination. Note that in Fig. 5.5.3 there is a small amount of overlap, which did not occur for the smaller delamination. This is because the ratio of the applied strain to the buckling strain is larger for the larger delamination.

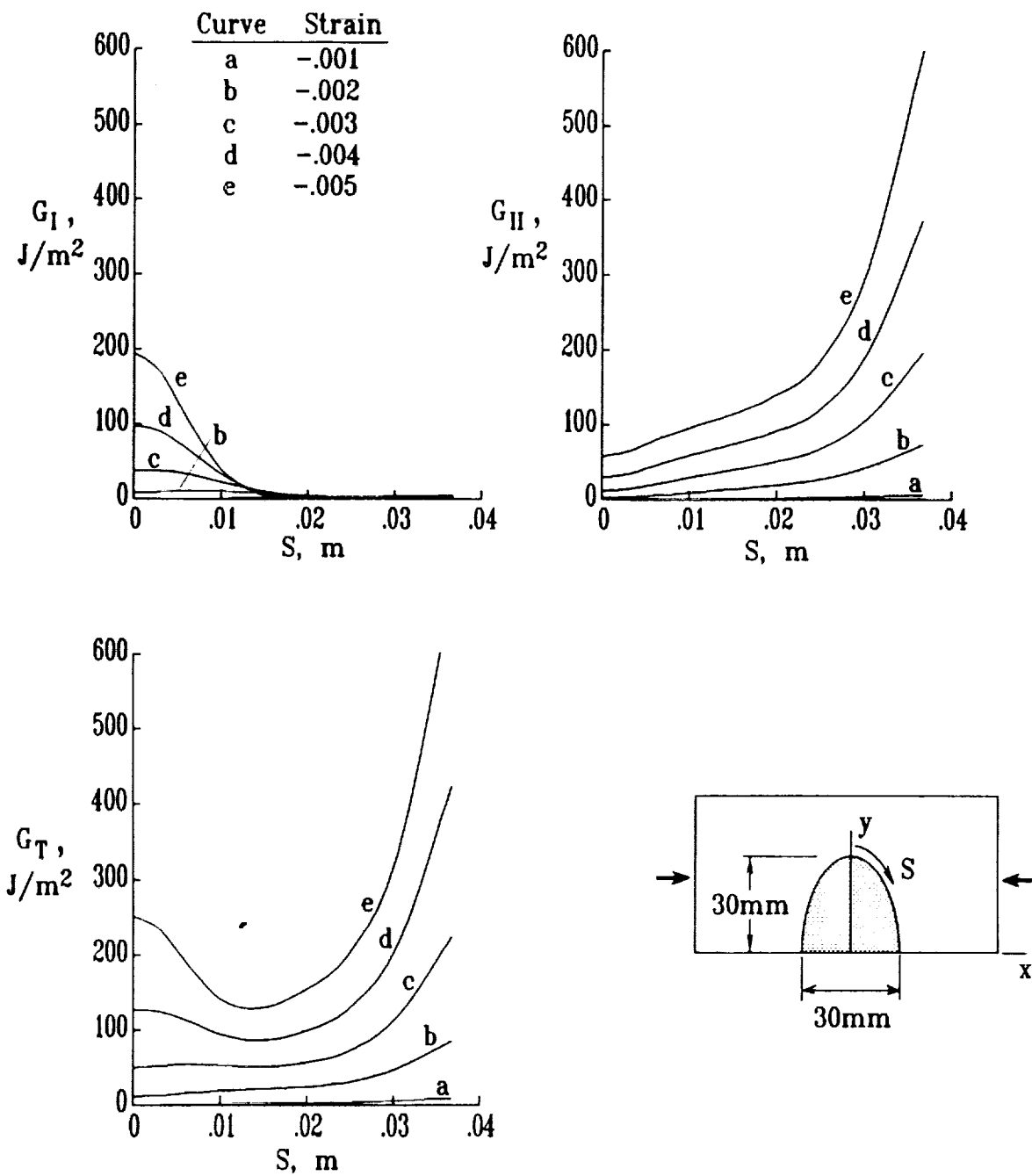


Fig. 5.5.2 Strain-energy release rate distributions for a laminate with a semi-elliptical edge delamination.

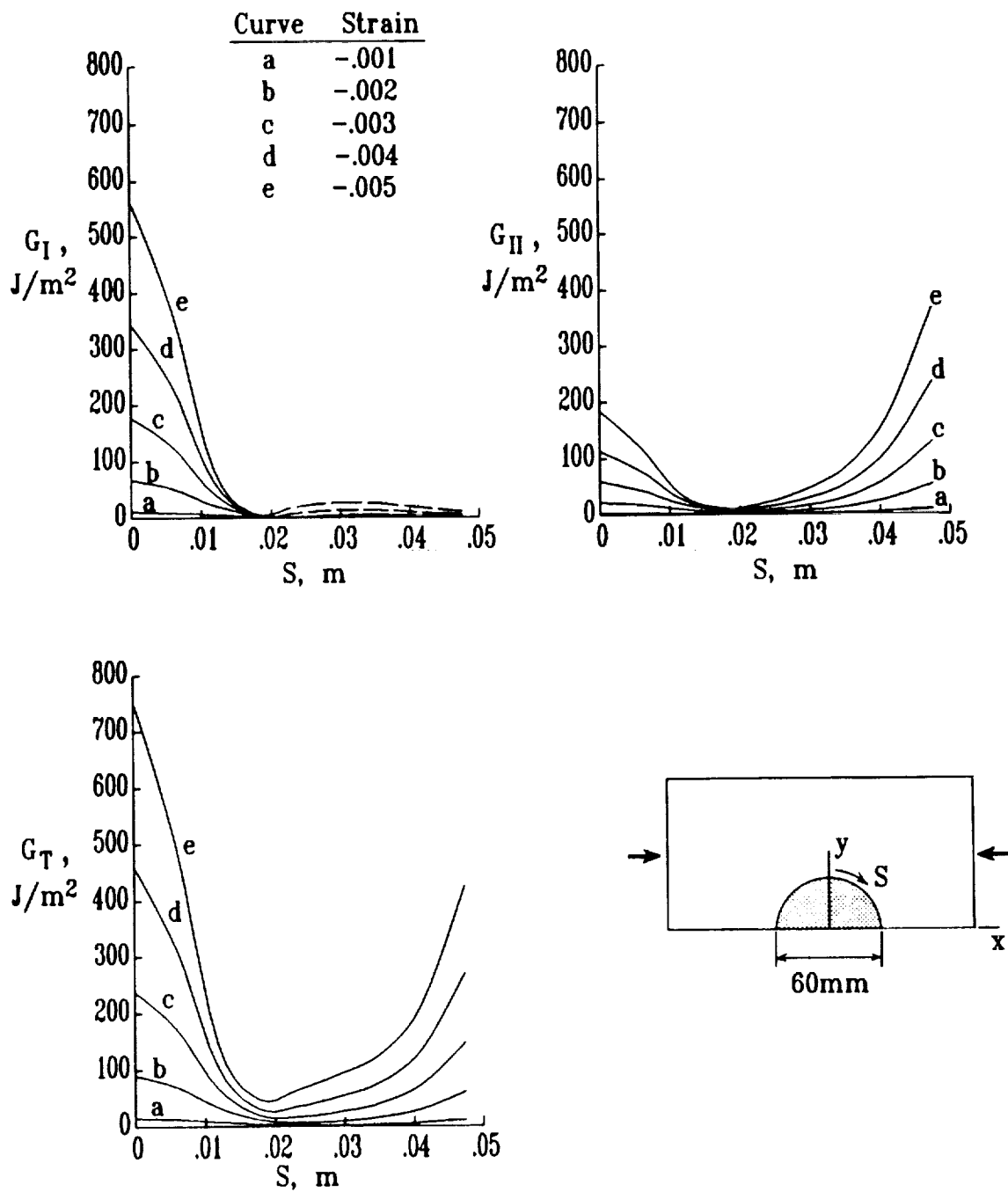


Fig. 5.5.3 Strain-energy release rate distributions for a laminate with a semi-circular edge delamination with a radius of 30mm.

CHAPTER 6

DESCRIPTION of SPECIMENS and EXPERIMENTAL PROCEDURES

This chapter describes the various specimens which were tested and the procedures used to conduct the tests. There are two subsections in this chapter :

1. Specimen configurations and
2. Measurement of deformation and damage.

6.1 Specimen Configurations

There were three basic specimen configurations: the transversely loaded plate, a laminate with an embedded delamination, and a laminate with an edge delamination.

Fig. 6.1.1 shows a schematic of the transversely loaded plate configuration. A thin sheet of steel was bonded to a thick aluminum plate with a room temperature cure adhesive. The aluminum plate had a 50.5mm diameter through-hole. A single transverse load was applied to the center of the steel using a 12.7mm diameter indenter. Fig. 6.1.2 shows the specimen and the test fixture. This set-up is the same as that used in ref. 44. Direct-current differential transformers were used to monitor load point deflections. The purpose of these tests were to obtain load versus deflection. No debond measurements were performed on these specimens.

Several types of specimens with embedded delaminations were fabricated. One of the specimens consisted of spring steel bonded to aluminum. Fig. 6.1.3 shows a schematic of the specimen. This specimen type was tested to provide postbuckling deformation data for a laminate without stacking sequence effects. As indicated in the figure, EA934NA room-temperature cure adhesive was used for bonding. A teflon insert was used to prevent bonding over a circular region, resulting in a simulated delamination.

Another type of specimen with an embedded delamination consisted of a thin AS4/PEEK laminate with a delamination. The stacking sequence was either $(0/90/90/0)_s$ or $(90/0/0/90)_s$. Fig. 6.1.4 shows a photograph of a typical laminate.

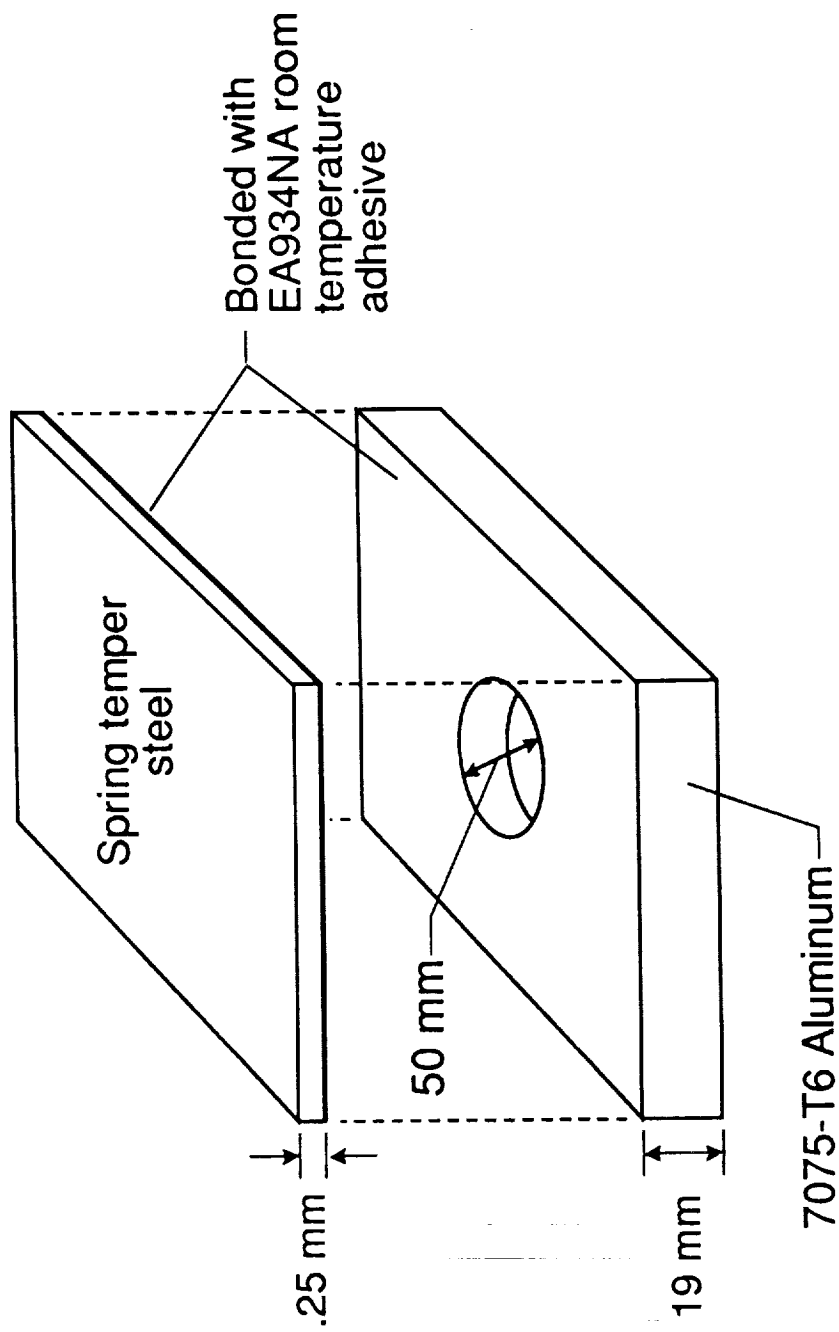


Fig. 6.1.1 Schematic of transversely loaded plate specimen.

ORIGINAL PAGE
BLACK AND WHITE PHOTOGRAPH

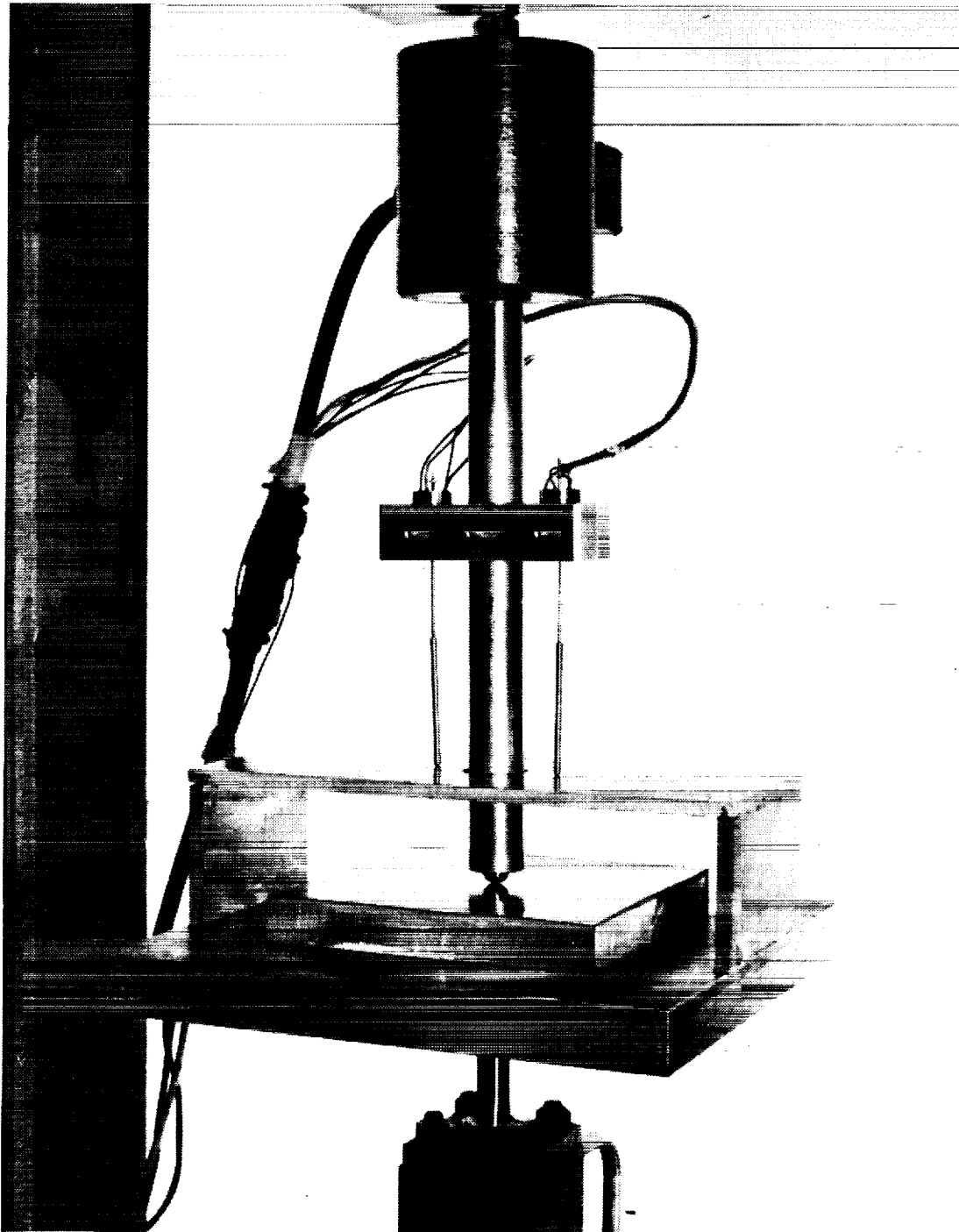


Fig. 6.1.2 Experimental set-up for transversely loaded plate.

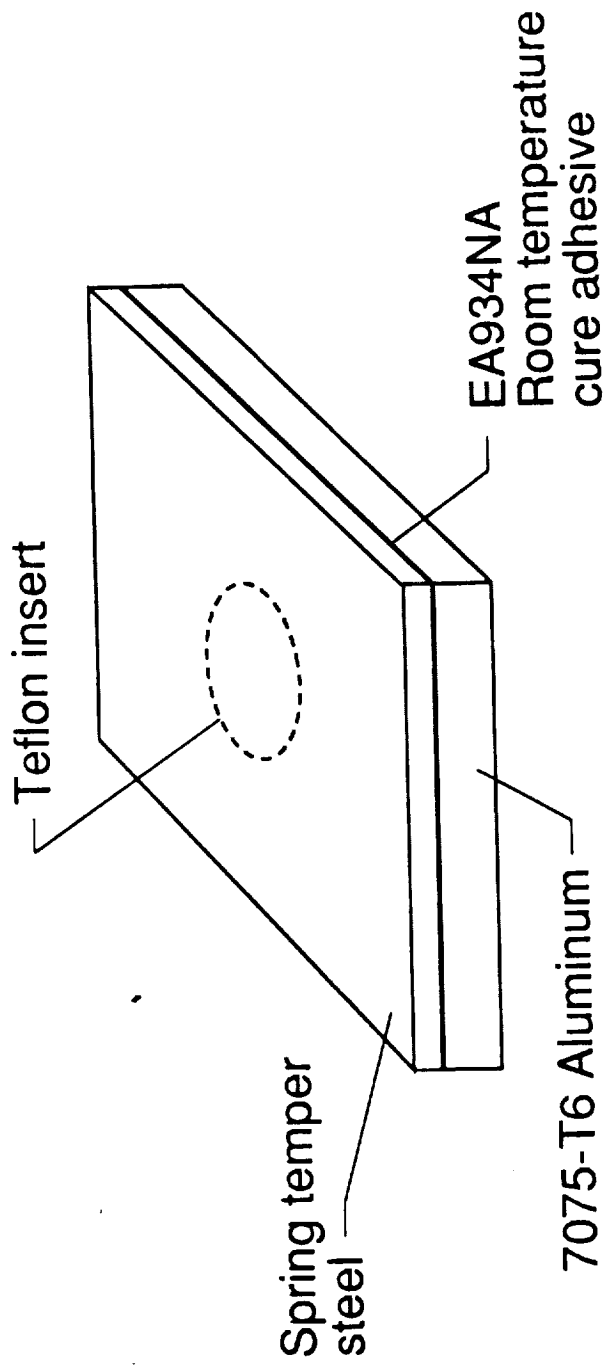


Fig. 6.1.3 Steel/Al specimen with embedded delamination.

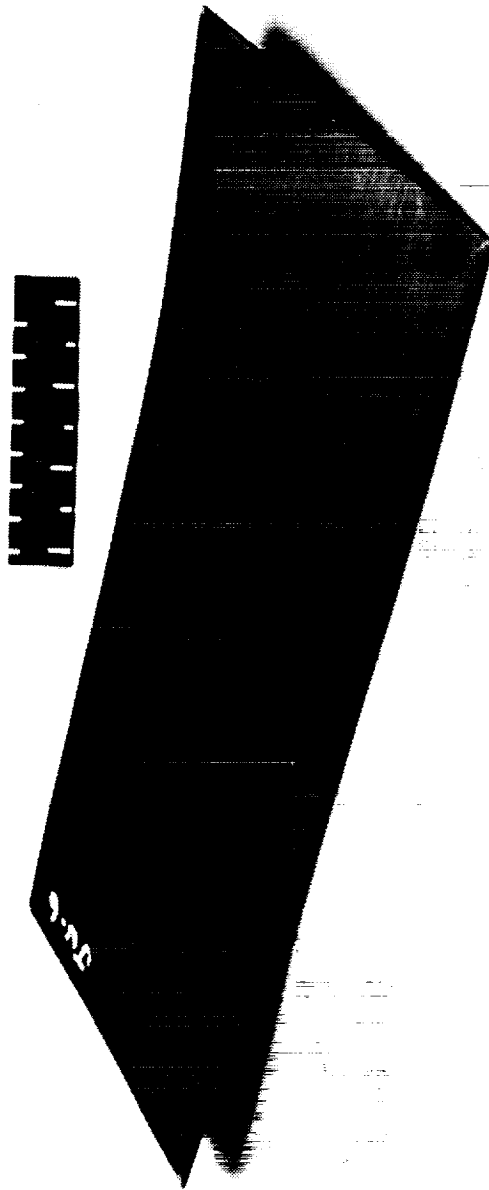


Fig. 6.1.4 AS4/PEEK laminate.

As shown in the figure, the laminates were badly warped. The PEEK laminate was bonded to an aluminum sheet to increase resistance to global buckling. Fig. 6.1.5 shows a schematic of the specimen. A double layer of thin Kapton film (thickness of each layer = .013mm) was used to provide an initial delamination of 30, 40 or 60mm diameter between the fourth and fifth plies. The double layer of Kapton was used because Kapton might bond with the PEEK, but it should not bond to another piece of Kapton. Apparently the high temperature and pressure used in processing the PEEK laminates caused a small amount of bonding. Even a small amount of bonding was sufficient to prevent local buckling of the delamination region prior to global collapse. Hence, a small block of aluminum was bonded to the sublaminates using a low strength bond, as illustrated in Fig. 6.1.6, and small forces were applied by hand to loosen the Kapton bond. Because of this poorly quantified "preconditioning" and the bad warpage problem, the specimens were only used for qualitative measurements of delamination growth.

Twenty-four ply composite specimens with embedded delaminations were fabricated from IM7/8551-7 prepreg. The stacking sequences were $(0/90/90/0)_6$ and $(90/0/0/90)_6$. A double layer of Kapton film was used to provide an initial delamination between the fourth and fifth plies. Delamination sizes were 30, 40, or 60mm. Unlike the PEEK laminates, the Kapton film did not exhibit spurious sticking in these specimens.

Several of the PEEK specimens described above were sliced longitudinally to obtain laminates with semi-circular edge delaminations.

The specimens with embedded or edge delaminations were tested in compression. Steel guide plates were used to prevent global buckling. Most of the tests were conducted using a solid guide plate on one side of the specimen and a plate with a 82mm window on the other side. A few tests were performed using plates with windows on both sides. The guide plates are shown in Fig. 6.1.7. The guide plates were 19mm thick. For specimens with an embedded delamination, the window was centered over the delaminated region. For specimens with an edge

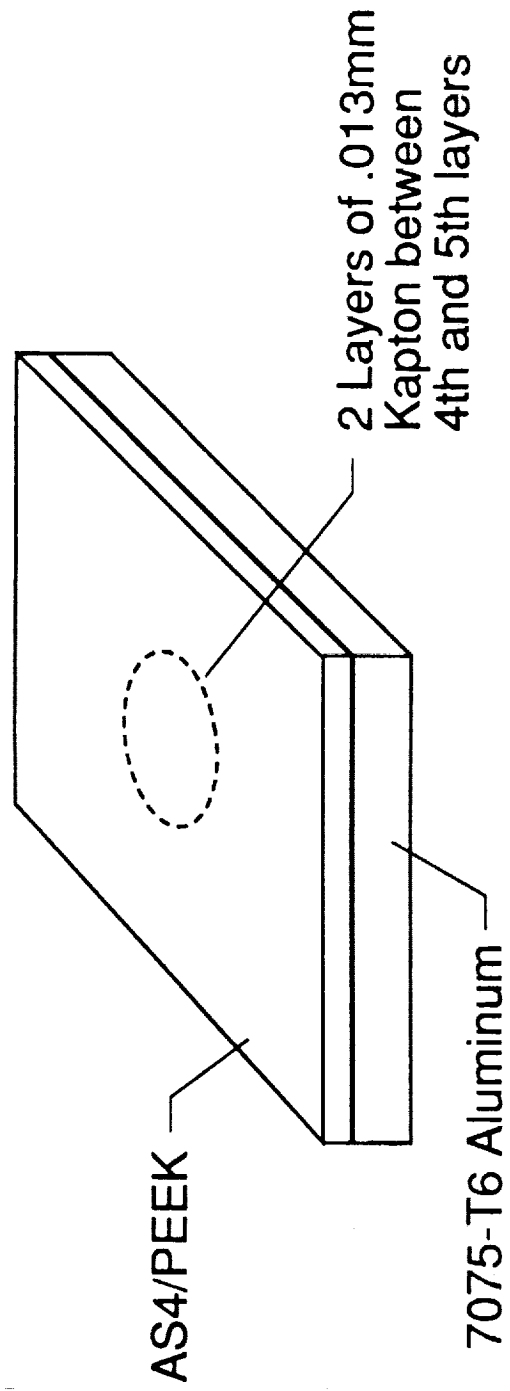


Fig. 6.1.5 AS4/PEEK/AL specimen with embedded delamination.

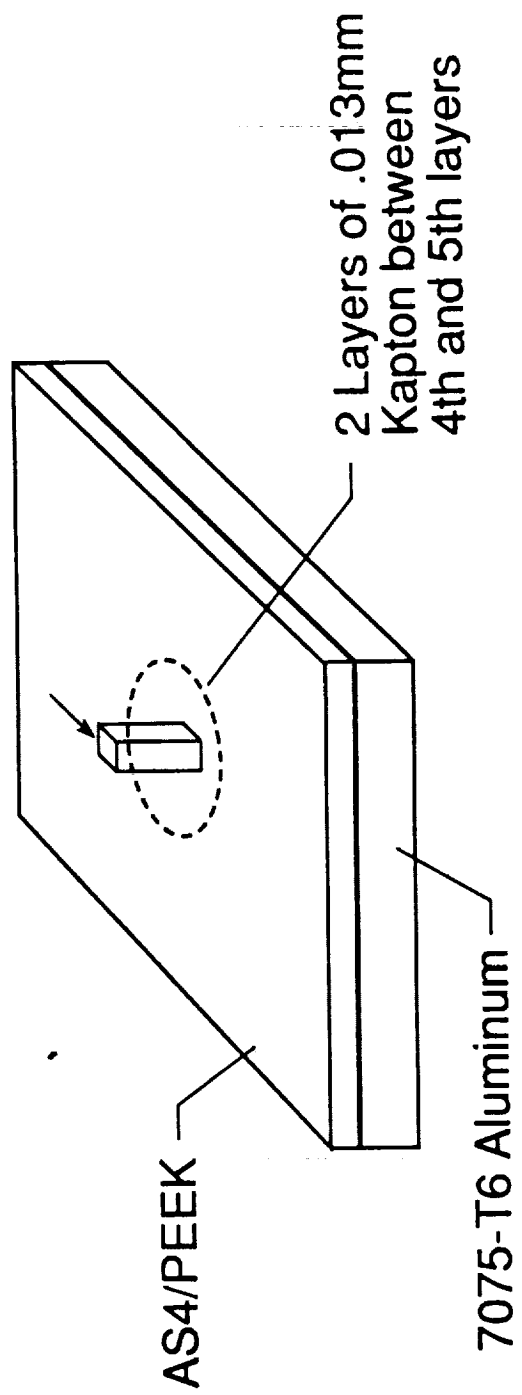
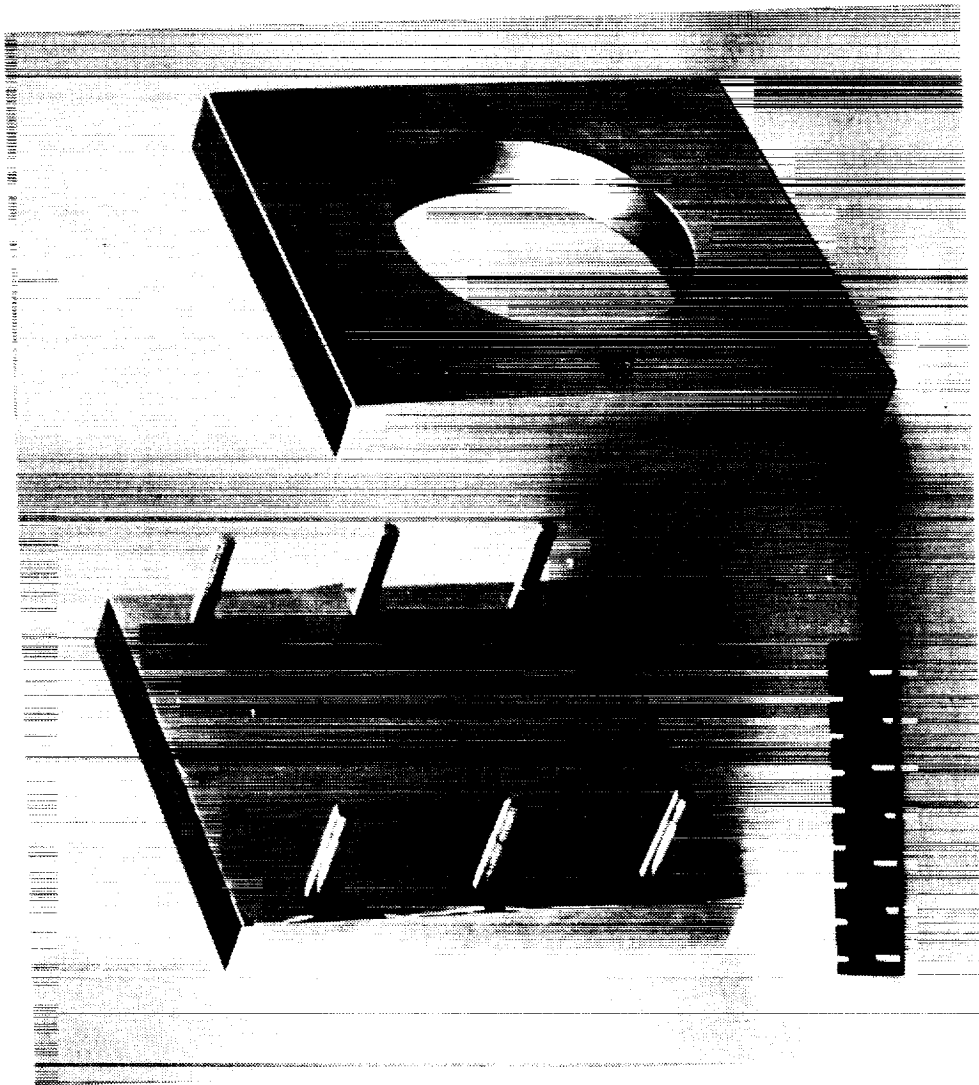


Fig. 6.1.6 Breaking Kapton to Kapton bond with glued on block.

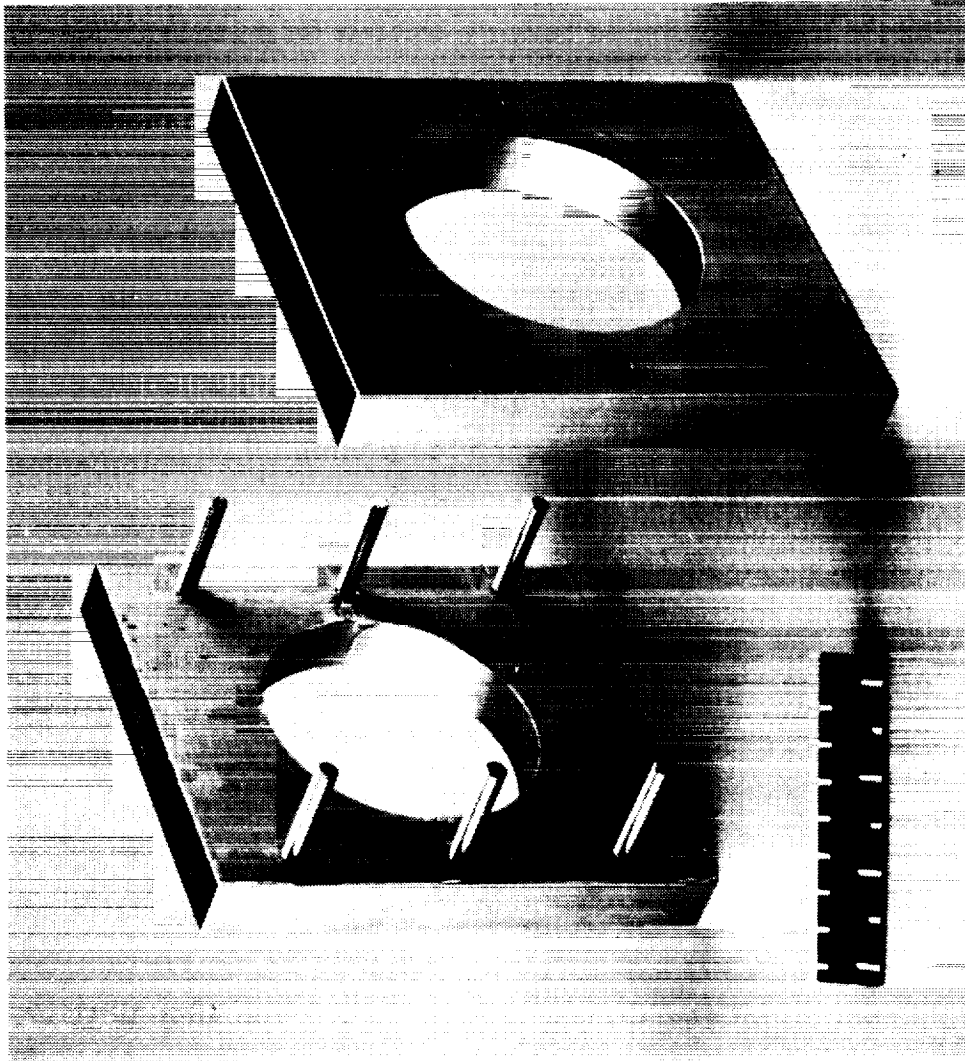
ORIGINAL PAGE
BLACK AND WHITE PHOTOGRAPH



(a) window on one side only

Fig. 6.1.7 Guide plates.

ORIGINAL PAGE
BLACK AND WHITE PHOTOGRAPH



(b) window on both sides

Fig. 6.1.7, Concluded.

delamination, the guide plates were offset to one side to provide extra support.

6.2 Measurement of Damage

Several techniques were used for detecting damage in the compression specimens. Because delamination growth resulted in a larger buckled region, visual inspection during the loading proved to be fairly accurate for detecting when delamination growth initiated. A more refined technique was measurement of the deformed shape of the buckled region. The delamination boundary corresponded to the location where transverse displacements were negligible. The measurements were obtained using the fixture illustrated in Fig. 6.2.1. This fixture is very similar to that described in ref. 45. Basically, the fixture consists of a machinist's vise with three DCDT's. One of the DCDT's measures the transverse deflection of the buckled region and the other two indicate where the transverse deflection is being measured. In some cases, two DCDT's were used to monitor transverse displacements; one DCDT monitored back face displacement and the other monitored front face (i.e. where the buckling occurred) displacement. By subtracting the outputs of the two transducers, a change in thickness could be measured. Essentially all change in thickness would be due to postbuckling displacements. This technique using two DCDT's was less sensitive to artifacts due to slight misalignment of the specimen and the machinist's vise.

Another technique for measuring damage was applying an X-ray opaque dye penetrant and then taking an X-ray. The dye highlighted ply cracks and delaminations. However, if little or no surface damage occurred, the dye penetrant was not able to reach the internal damage area. In those cases, after all testing of those specimens were completed, a small hole was drilled in the center of the specimen. Then, the dye could be applied internally.

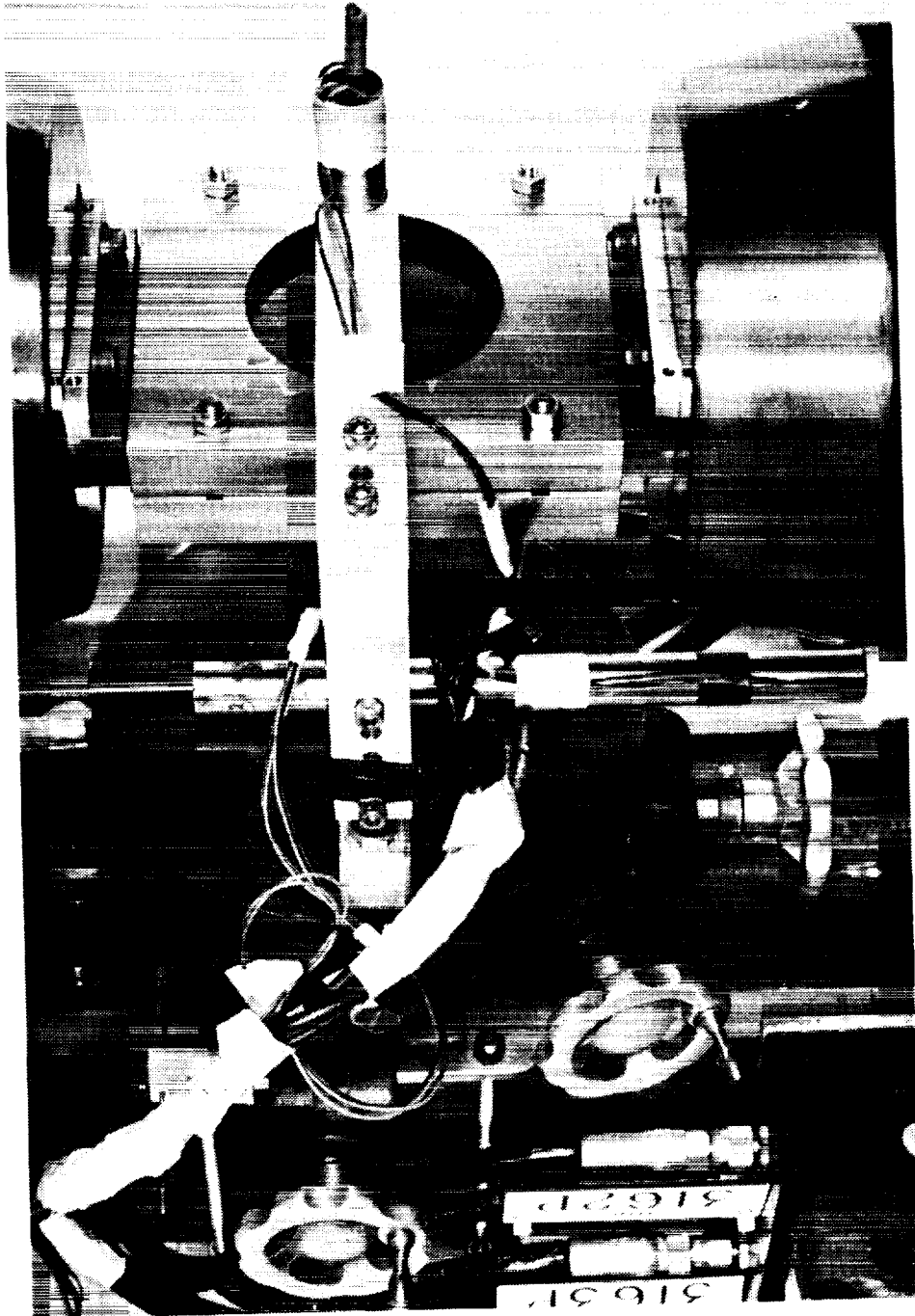


Fig. 6.2.1 Deflection measurement fixture.

Some specimens were sectioned using a diamond saw and polished. The cross sections were examined using light microscopy. This technique was particularly useful for determining the distribution of cracking through the thickness and details of the types of damage.

CHAPTER 7

COMPARISON of ANALYTICAL and EXPERIMENTAL RESULTS

The primary purpose of this chapter is to describe the results of a combined experimental and analytical study of instability-related delamination growth. Specimens were designed based on the trends observed in the analytical study discussed earlier. Based on the analytical study differences in the buckling strain, the shape of the postbuckled region, the strain at which delamination growth would occur, and the direction of growth were expected. The experimental program was conducted to determine whether the expectations based on analysis were correct. Also, it was hoped that a strain-energy release rate parameter would be identified which could be used to quantitatively predict the onset of delamination growth.

Two composite material systems were considered: AS4-PEEK and IM7/8551-7. Because of the processing difficulties described earlier in Chapter 6, only qualitative comparisons of analysis and experiments will be presented for the PEEK specimens.

A secondary purpose of this chapter is to present results for two "check cases": the transversely loaded plate and the steel bonded to aluminum compression specimen. These configurations were examined because they were expected to behave in a fairly predictable fashion. Hence, they provided a good starting point for comparison of analytical and experimental results. These check cases will be presented first, and then the primary study will be discussed.

7.1 Check Cases

Two types of experiments were conducted just to help verify the finite element program NONLIN3D. One of the experiments involved central transverse loading of a circular plate (see Fig. 6.1.2). The other test consisted of spring steel bonded to aluminum and loaded in compression to cause local postbuckling of a delaminated region (see Fig. 6.1.3). The results for these two check cases are described in this section.

Figure 7.1.1 shows experimentally measured load point deflection versus applied load for the transversely loaded plate. Results are shown for two specimens. Each specimen was loaded and unloaded more than once, so there are multiple data for each load level. Also shown are the results from NONLIN3D. The figure shows that NONLIN3D predicts the deflection quite well, even though the response is highly nonlinear.

Figure 7.1.2 shows results from the steel/Al postbuckling tests. This figure shows the deformation of the specimens and the finite element models along the planes $x = 0$ and $y = 0$. The finite element analysis was performed at a slightly different strain level than was present in the test. Ideally, the same strain would have been used for both the analysis and the experiments. However, the deflection increases rapidly with applied strain and even small imperfections can shift the load versus deflection curve. To expedite the comparison of the *shape* of the buckled region with the prediction, the strain for the finite element analysis was chosen so that the peak deflection would be about the same as was observed in the experiment.

Figure 7.1.2 shows the deformation for a specimen with a 60mm diameter delamination. The predicted and observed deformed shape agree quite well. Note that the deformation is much different along the $x = 0$ and $y = 0$ planes. Along the $y = 0$ plane the large deformation is restricted to a much narrower region than along the $x = 0$ plane. This restricted deformation caused the delaminated region to appear elliptical during the test, even though the delamination was known to be circular.

7.2 Qualitative Study of AS4/PEEK Laminates

As described earlier in the experimental procedures section, there were problems with the fabrication of the AS4/PEEK specimens. Consequently, only a qualitative study was performed on this material system. Observations were made of the shape of the buckled region, the location of delamination growth, the direction

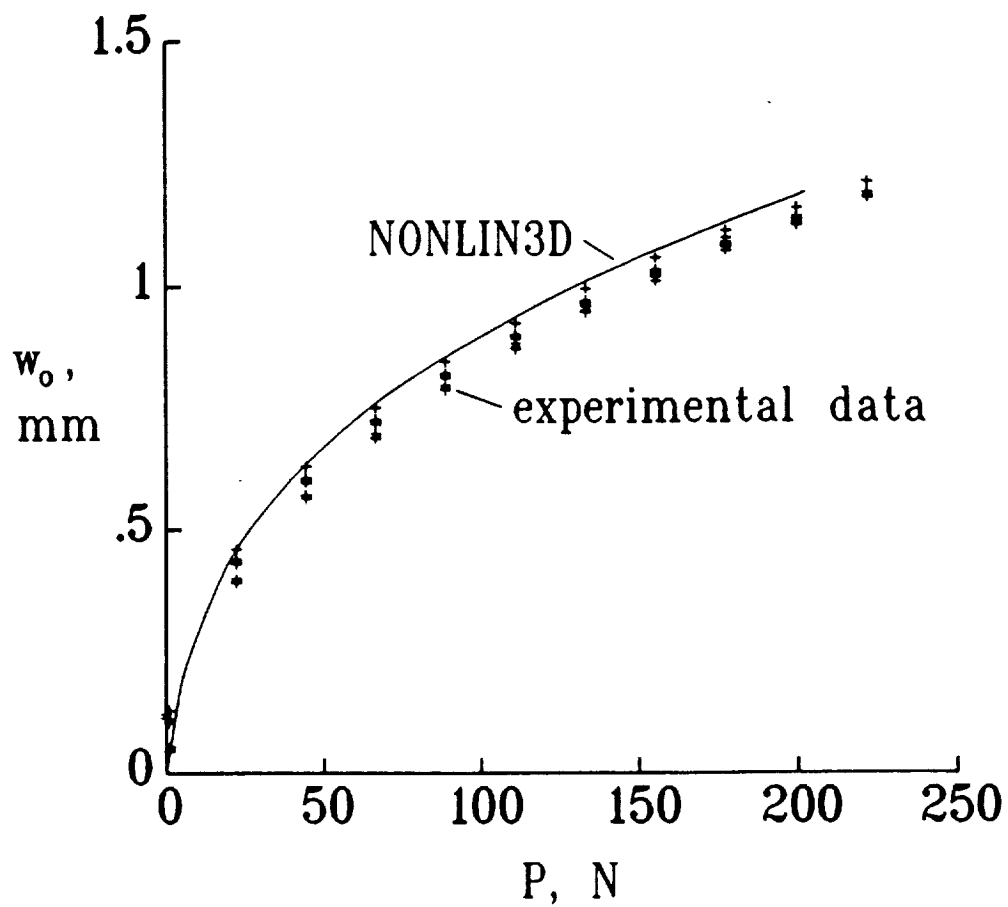
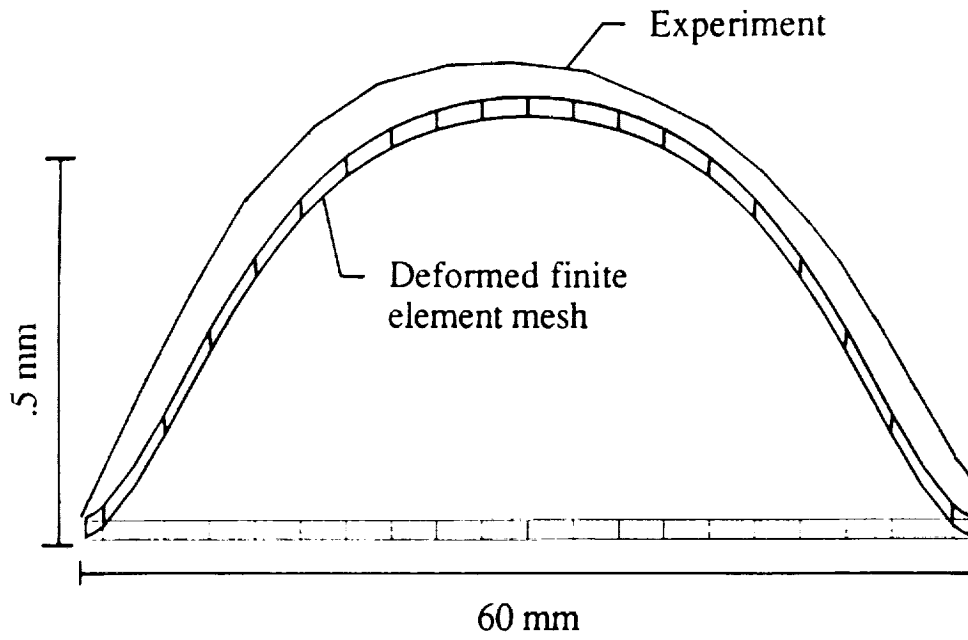
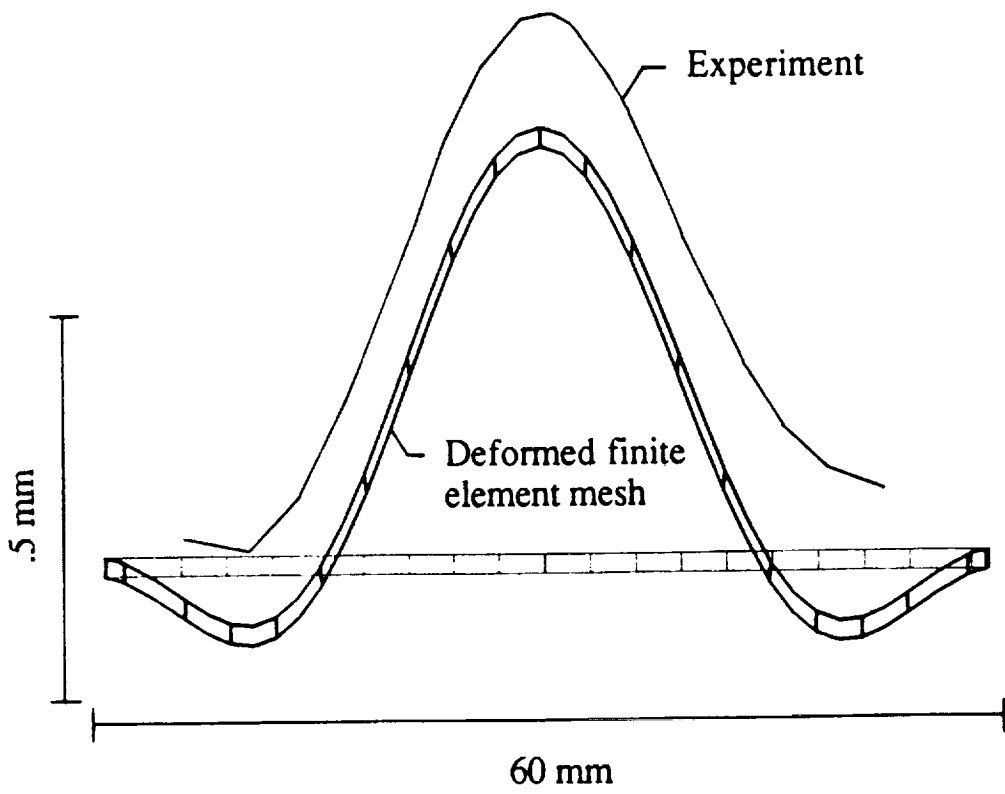


Fig. 7.1.1 Comparison of measured and predicted load point displacement for a transversely loaded circular plate.



(a) $x = 0$ plane

Fig. 7.1.2 Deformation of the $x = 0$ and $y = 0$ planes in a steel/AL specimen with a postbuckled 60mm diameter delamination.



(b) $y = 0$ plane

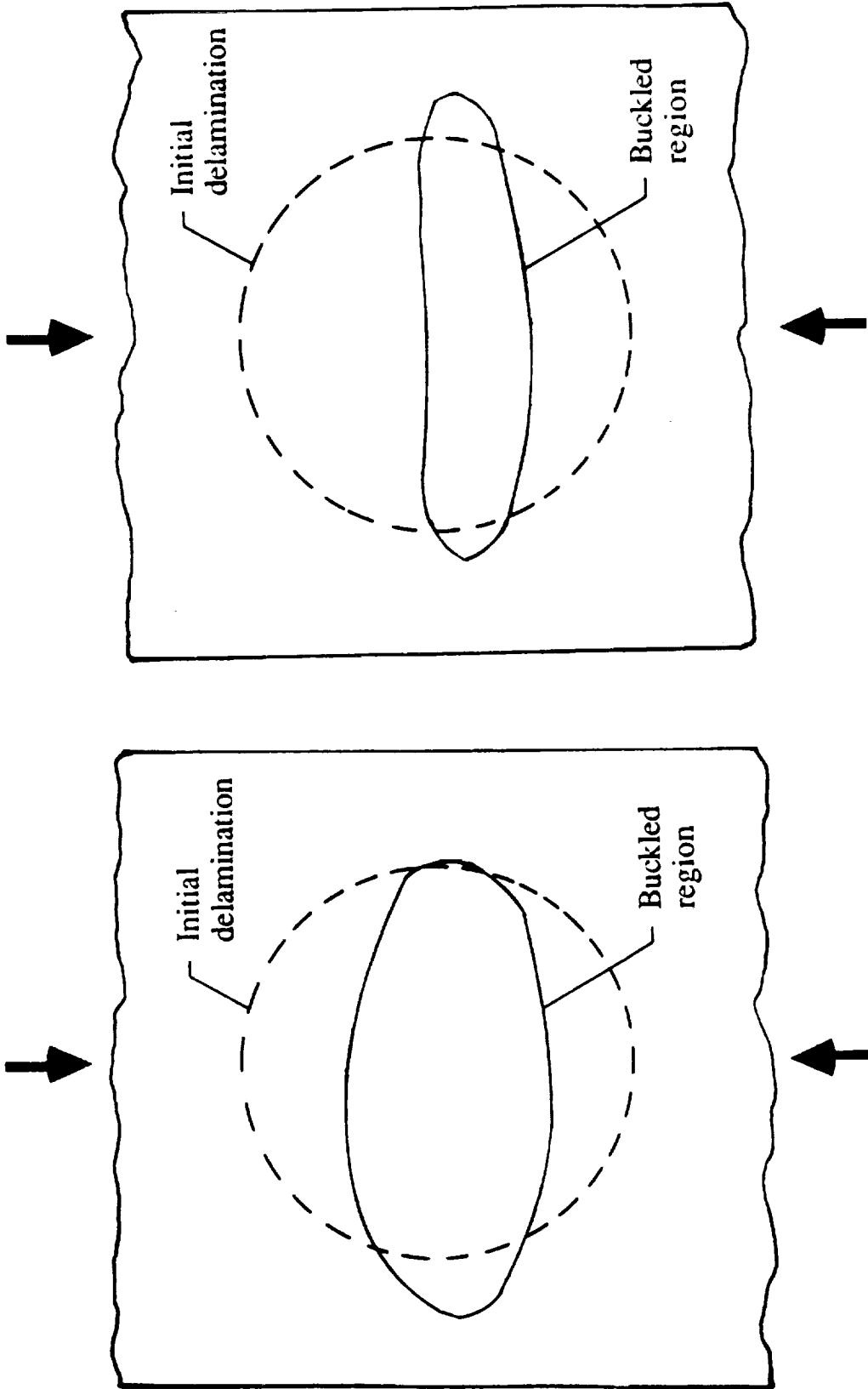
Fig. 7.1.2, Concluded

of growth, and ply cracking. Fatigue loads were used to cause delamination growth in most of the tests because of the high resistance of PEEK to static delamination growth. A few specimens were tested statically. However, effects due to problems with specimen fabrication prevented isolation of fatigue versus static behavior. Laminates with either an embedded or an edge delamination were tested. Two sublaminates stacking sequences for the sublaminates were considered: (0/90/90/0) and (90/0/0/90). The embedded delamination will be discussed first, then the edge delamination.

Fig. 7.2.1 shows sketches of two specimens (which had a 60mm diameter initial delamination). The boundary of the initial delamination is indicated by dashed lines. The region which actually buckled outward is indicated by solid lines. This region was determined by visual inspection. Only part of the delaminated region buckles outward for both sublaminates. Also, the buckled region is much narrower for the (90/0/0/90) sublaminates than for the (0/90/90/0) sublaminates. The same trends were observed for 40mm delaminations.

Finite element analysis was performed before the tests were conducted. In fact, the stacking sequences for the experiments were selected because the analysis predicted that the behaviors of the two laminates should be different. These preliminary analyses were performed for a 30mm delamination. Since problems with fabrication precluded quantitative comparisons, the analyses were not repeated for the actual delamination sizes. Fig. 7.2.2 shows the $y=0$ plane for deformed finite element models for the two stacking sequences. These particular models were for a 30mm delamination, but the trends are independent of delamination size. Note that the analysis prediction agrees with the experiments, i.e. that the buckled region should be narrower for the 90/0/0/90 sublaminates than for the 0/90/90/0 sublaminates.

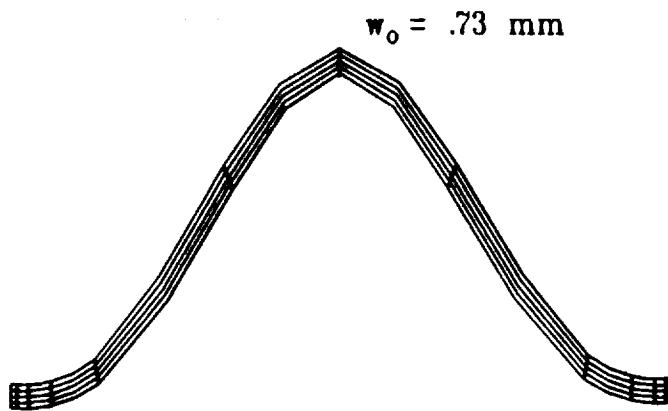
Fig. 7.2.3 shows strain-energy release rate distributions for a 30mm delamination for the two stacking sequences. Both G_I and G_{II} are maximum at $S=0$ and are much less elsewhere. These results suggest that delamination growth



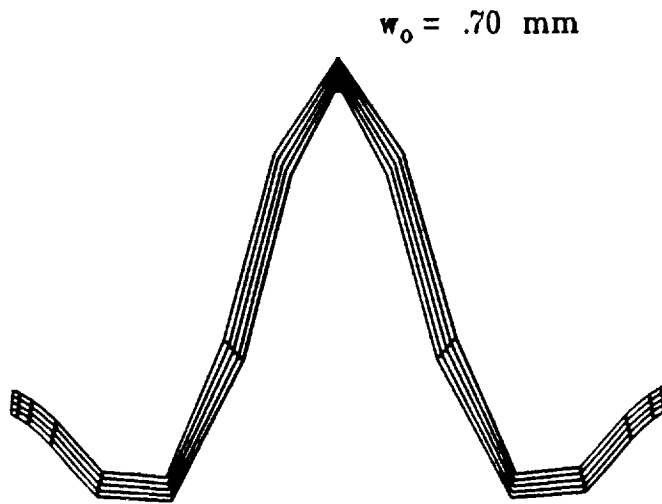
90/0/0/90 Sublaminare

0/90/90/0 Sublaminare

Fig. 7.2.1 Outline of postbuckled region for 60mm delamination in two AS4/PEEK laminates.

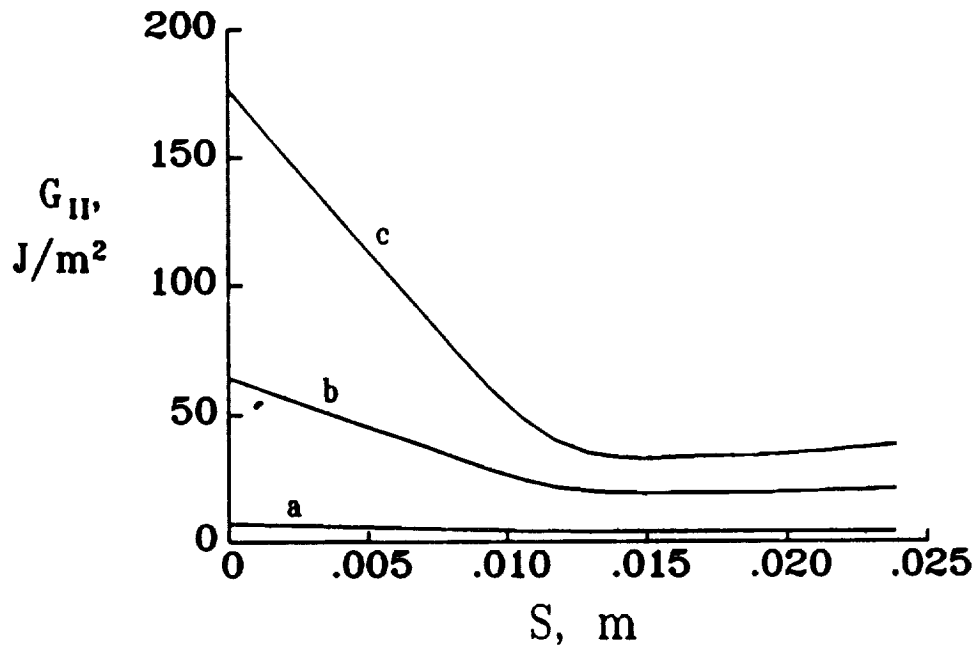
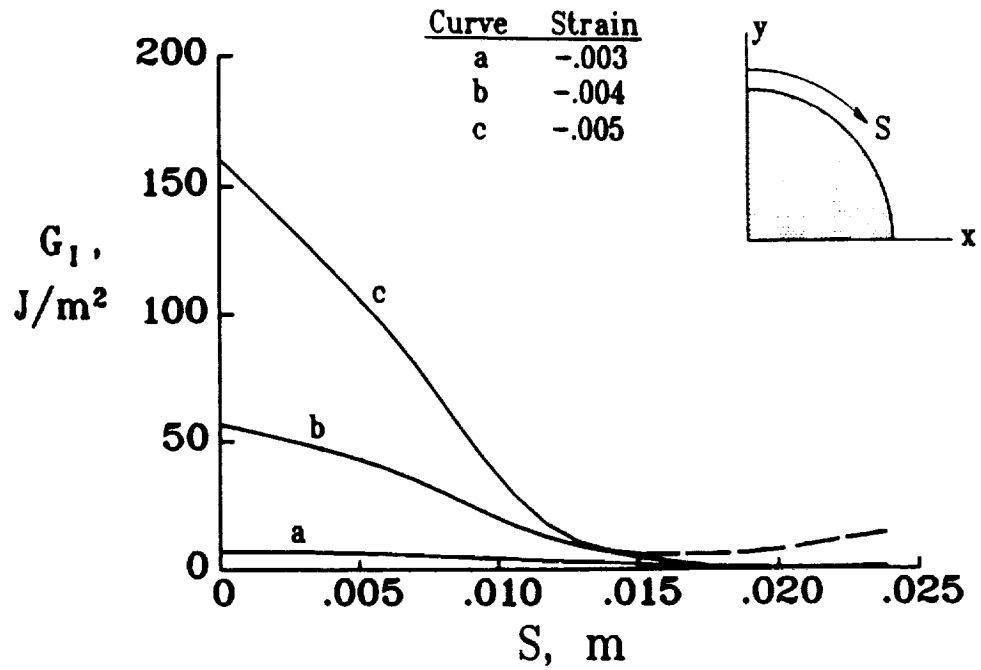


(a) (0/90/90/0) sublaminar



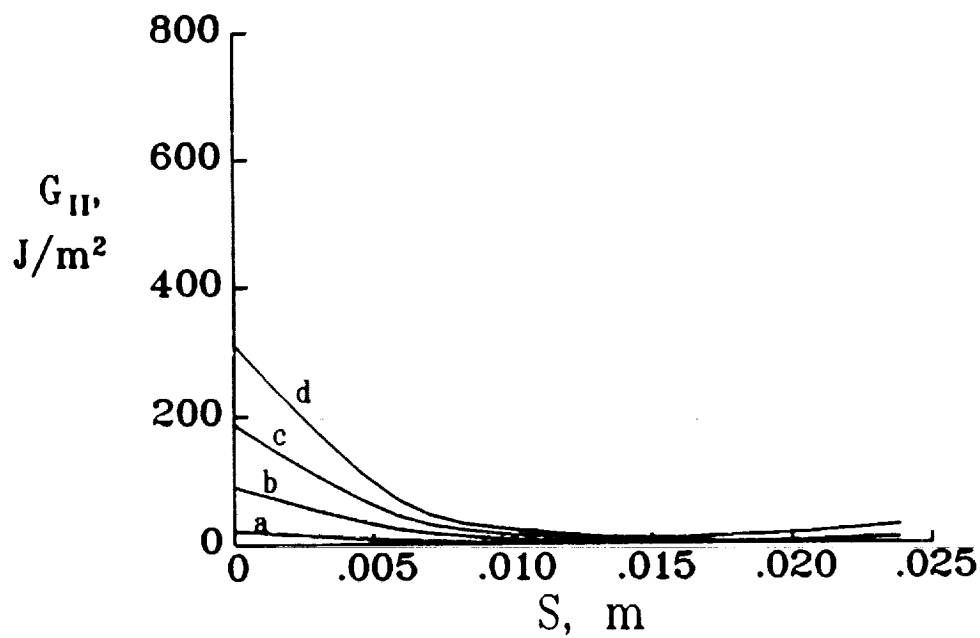
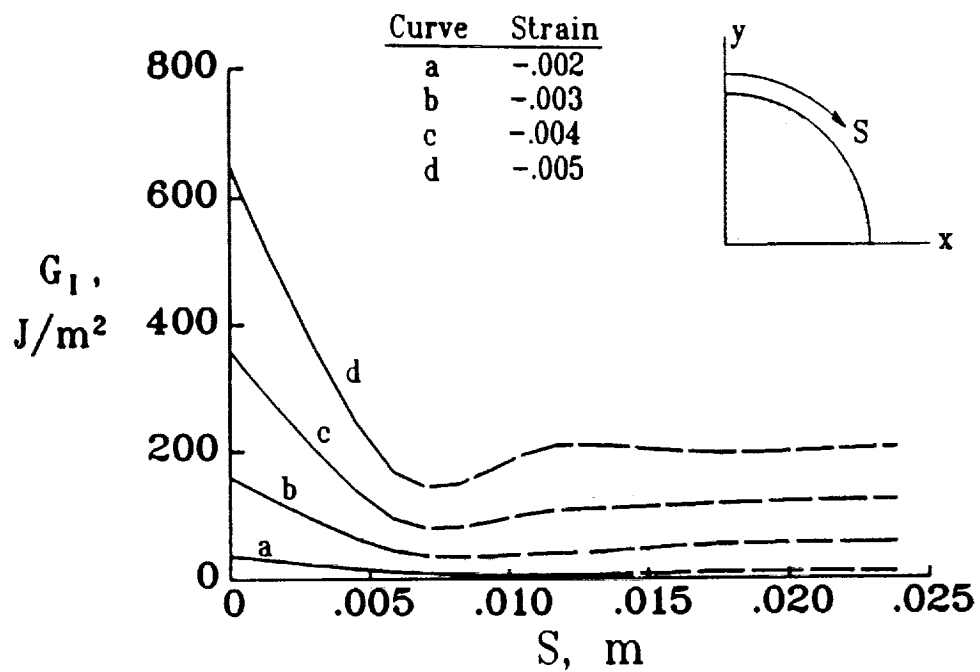
(b) (90/0/0/90) sublaminar

Fig. 7.2.2 Deformation of the $y = 0$ plane for two AS4/PEEK laminates. Diameter of delamination is 30mm.



(a) (0/90/90/0) sublaminates

Fig. 7.2.3 Strain-energy release rate distributions for two AS4/PEEK sublaminates. Delamination diameter is 30mm.



(b) (90/0/0/90) sublaminated

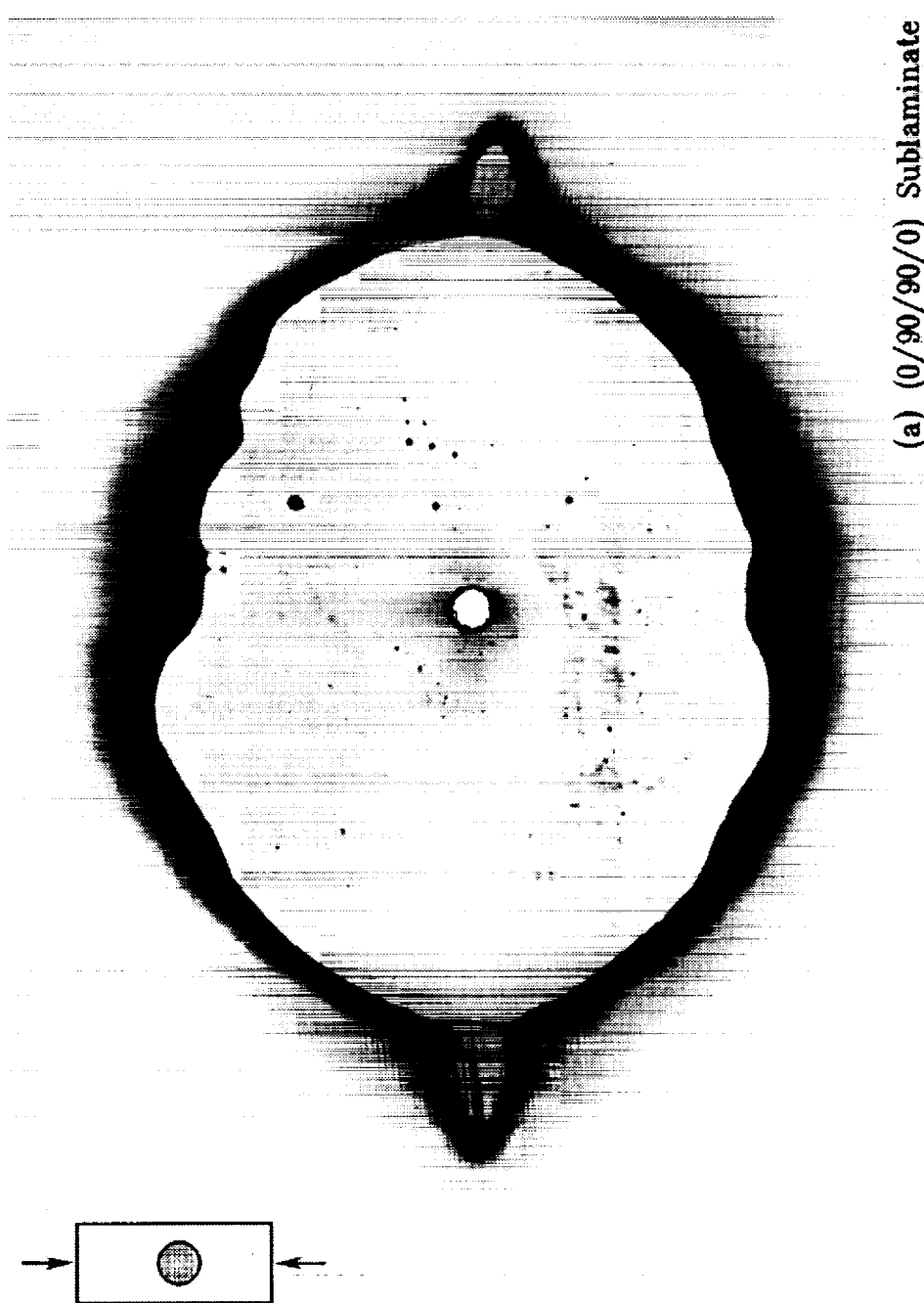
Fig. 7.2.3 Concluded.

should initiate in a small area and should propagate transverse to the load direction. Figure 7.2.4 shows X-rays for the two stacking sequences. The observed initial delamination growth is very localized and the growth is transverse to the load direction. Of course, after a small amount of growth the analytical results in Fig. 7.2.3 are not applicable, since the configuration has changed considerably. The X-rays show matrix cracking, which is apparently caused by the flexure during postbuckling. The delamination growth was usually very rapid. Sometimes there was essentially instantaneous propagation to the guide plates, but not always.

Stacking sequence effects were quite obvious for the edge delamination specimens also. It was difficult to obtain delamination growth for the 30mm diameter delamination for the (0/90/90/0) sublaminates. Except for one case, global failure occurred simultaneously with delamination growth. In the one case that growth could be observed before global failure, only a small amount of growth occurred and approximately the same amount of growth occurred in both the load direction and transverse to the load direction. Fig. 7.2.5 shows an X-ray of a laminate with a 20mm radius initial delamination and a (0/90/90/0) sublaminates. In this case, the dominant delamination growth is definitely in the load direction. Also, whenever catastrophic growth occurred, there was significant delamination growth in the load direction.

Only 30mm delaminations were examined for the (90/0/0/90) sublaminates. The X-ray in Fig. 7.2.6 shows that for this case the delamination growth is definitely transverse to the load direction. Even when extensive delamination growth occurred, it was transverse to the load direction. Matrix cracking was more obvious for the 90/0/0/90 sublaminates (Fig. 7.2.6) than for the 0/90/90/0 sublaminates (Fig. 7.2.5).

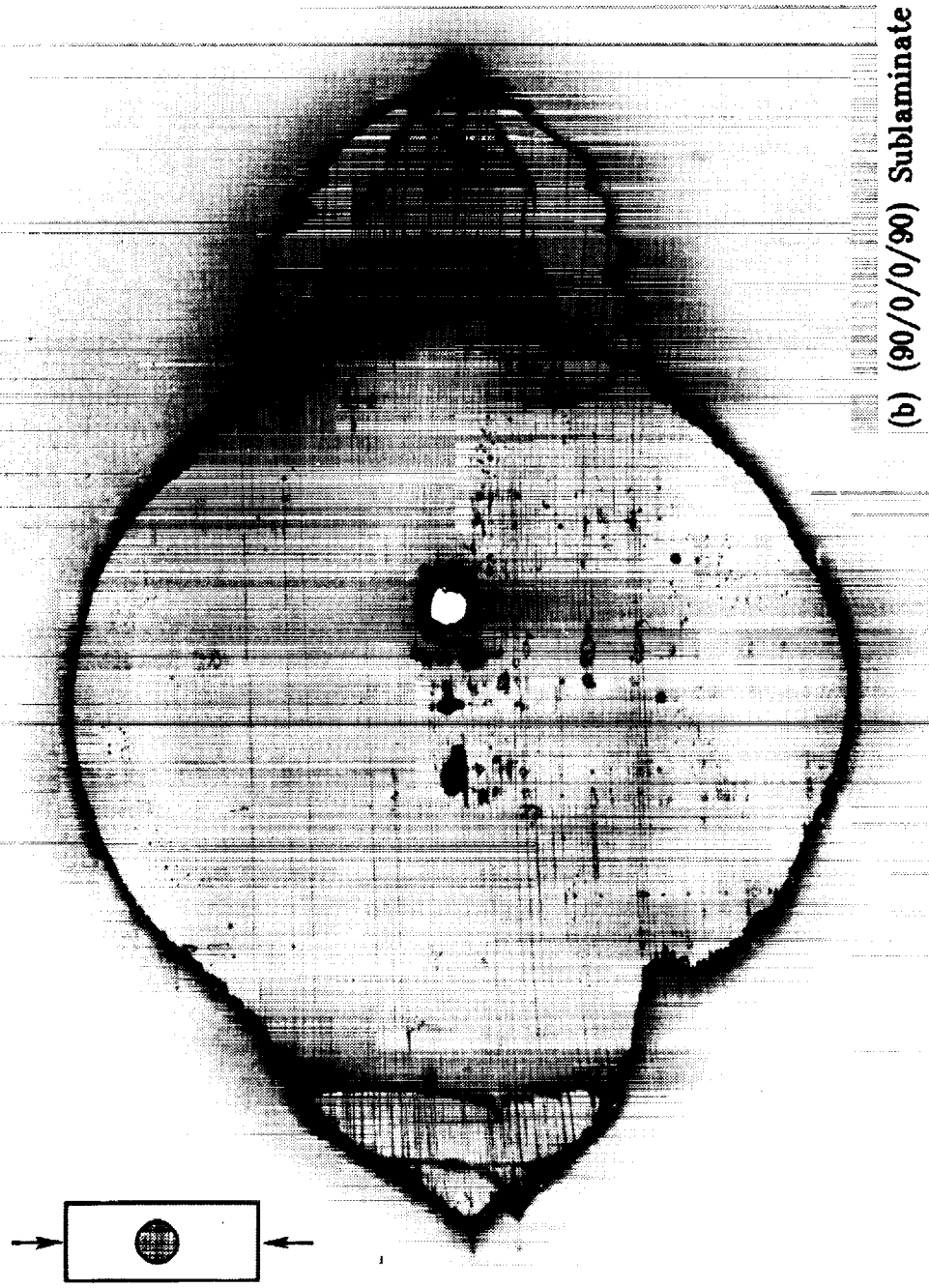
Figures 7.2.7 and 7.2.8 show strain-energy release rate distributions for two specimens with edge delaminations. The analytical results are for approximately the same range of strains that were used in the tests. Results are shown for three strain levels.



(a) (0/90/90/0) Sublamine

Fig. 7.2.4 Radiographs of two peek laminates with 60mm diameter initial delamination.

ORIGINAL PAGE IS
OF POOR QUALITY



(b) (90/0/0/90) Sublaminate

Fig. 7.2.4, Concluded.

ORIGINAL PAGE IS
OF POOR QUALITY

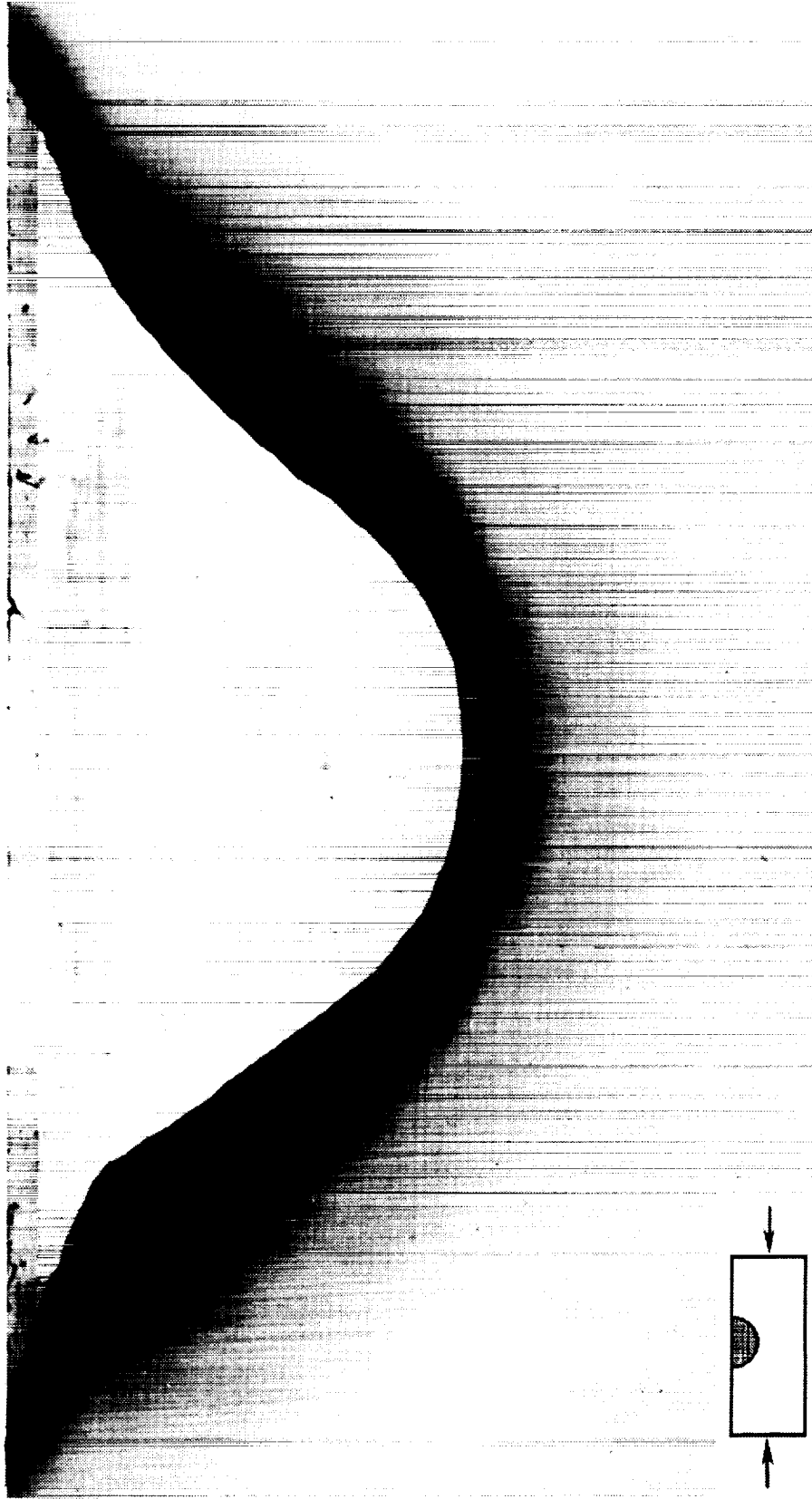


Fig. 7.2.5 Radiograph of PEEK laminate with an initial semi-circular edge delamination of radius 20mm. The sublaminare is (0/90/90/0).

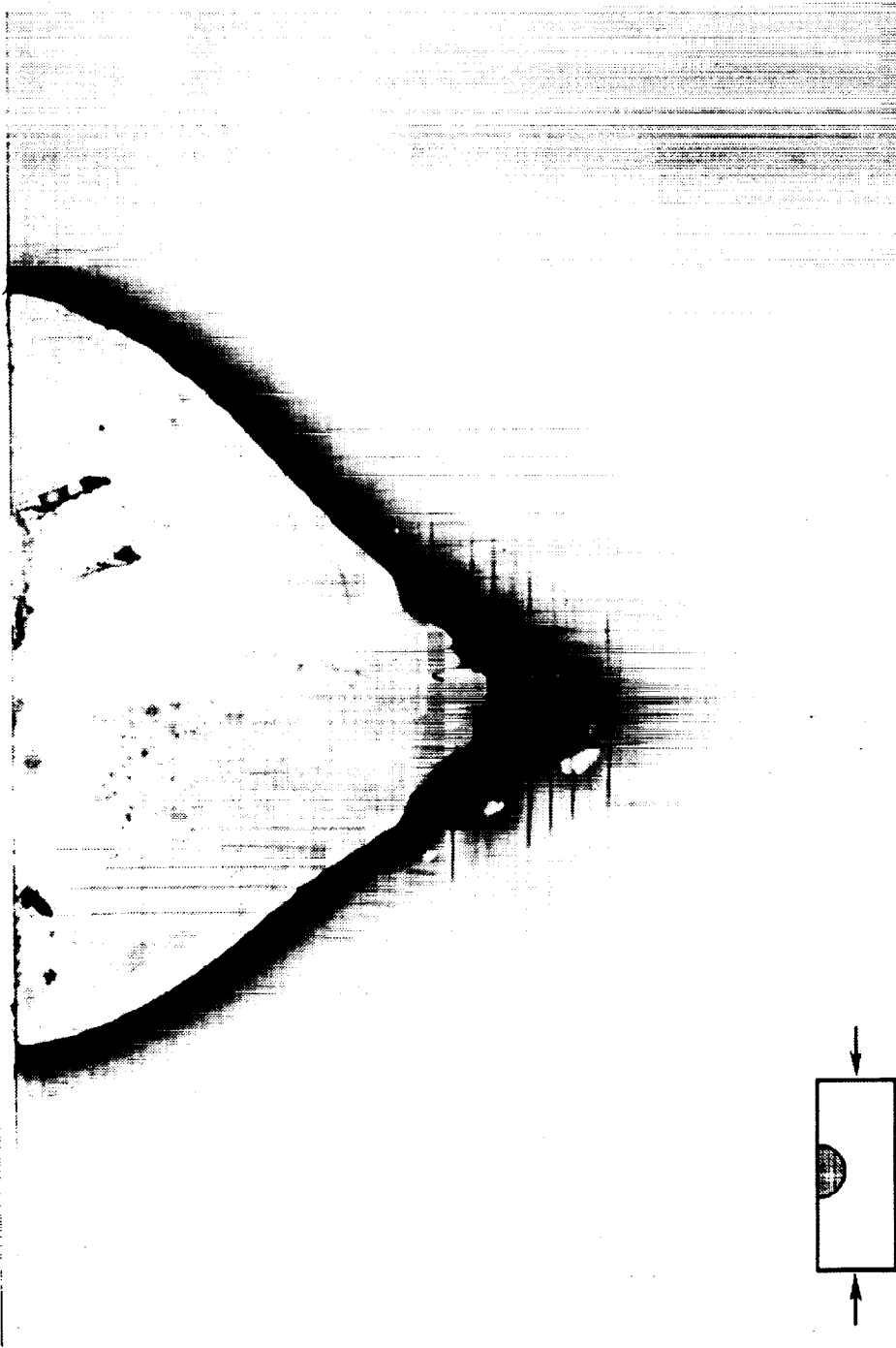


Fig. 7.2.6 Radiograph of PEEK laminate with an initial semi-circular edge delamination of radius 15mm. The sublaminates is (90/0/0/90).

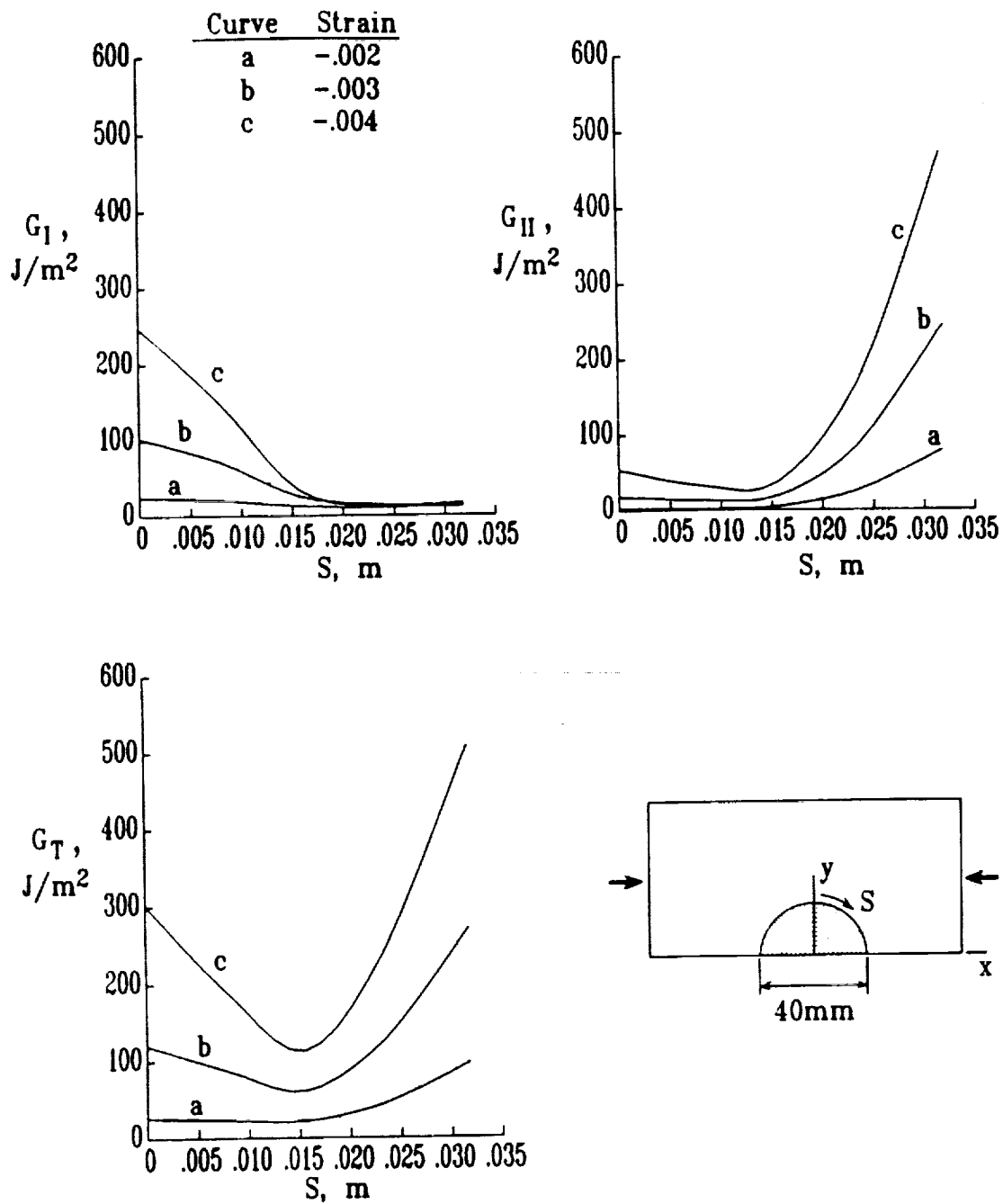


Fig. 7.2.7 Strain-energy release rate distributions for (0/90/90/0) AS4/PEEK sublaminates with a semi-circular edge delamination.

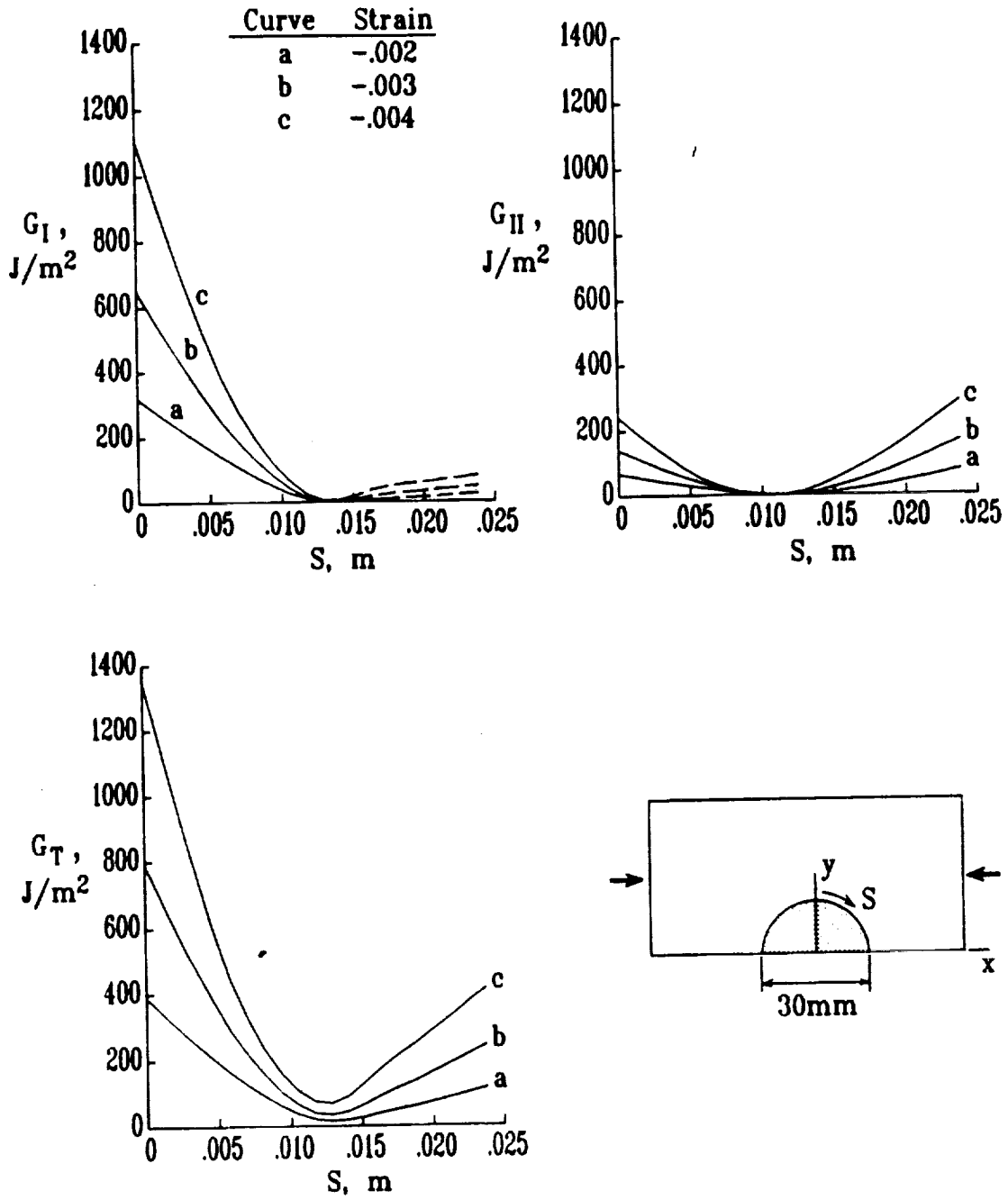


Fig. 7.2.8 Strain-energy release rate distribution for a (90/0/0/90) AS4/PEEK sublaminde with a semi-circular edge delamination.

The strain-energy release rate distributions for a 40mm edge delamination and (0/90/90/0) sublaminates are shown in figure 7.2.7. Based on G_I one would expect growth transverse to the load direction. But based on G_{II} , one would expect growth along the load direction. Without a mixed-mode delamination growth criterion, it is not possible to *predict* the direction of delamination growth. The experiments usually exhibited dominant growth in the load direction. The figure shows that the peak G_{II} is about twice the peak G_I . Hence, it appears that the large magnitude of G_{II} was sufficient to cause dominant growth to occur in the load direction.

The strain-energy release rate distributions for a 30mm delamination and a (90/0/0/90) sublaminates are shown in Fig. 7.2.8. The peak G_{II} component is much smaller than the peak G_I , and would not be expected to play much of a role. Based on G_I one would clearly expect dominant delamination growth to occur transverse to the load direction. This agrees with the experimental observations.

In summary, there are significant qualitative agreements between the observed and predicted behaviors.

7.3 Quantitative Study of IM7/8551-7 Laminates

A variety of measurements and observations were made for IM7/8551-7 laminates with an embedded delamination. As was the case for PEEK, two stacking sequences were used: (0/90/90/0)₆ and (90/0/0/90)₆. The initial delamination was located between the fourth and fifth plies. No edge delamination tests were performed. Because there were no major manufacturing induced artifacts (like the Kapton sticking problem in the PEEK laminates), quantitative comparisons were made between analysis and experiments for postbuckling deformations and initiation of delamination growth. Also, the stability of delamination growth was monitored. A combination of techniques were used to determine the extent and types of damage. These techniques included measurement of deflections, X-ray, ultrasonic C-scans, and sectioning followed by light microscopy.

Figures 7.3.1-7.3.3 show load versus deflection for the six laminate configurations considered (2 stacking sequences and three delamination sizes). The deflection is that in the center of the delaminated region. For each delamination size the agreement between the observed and predicted load versus deflection is fair for the (0/90/90/0) stacking sequence. For the (90/0/0/90) stacking sequence, the agreement is fair for the 30mm delamination. For the 40 and 60mm delaminations, there is a large discrepancy, except at the lower strain levels. This divergence at the larger strains may be due in part to the overlapping of the delamination faces, which occurs in the analysis, but not in reality. The significance of the overlap tends to increase as the ratio of the applied strain to the bifurcation buckling strain increases. This ratio increases with strain for a fixed delamination size and with delamination size for a fixed strain. This may explain the better agreement at lower strains and for smaller delamination sizes.

Figures 7.3.4 and 7.3.5 show the deformed shape of the $y=0$ plane for the two stacking sequences and a 60mm delamination as measured during tests and as predicted from analysis. The strain for the tests was -.0026. The analytical results are for a strain of -.003. This small difference in strain is not important for the comparisons of deformed shape. There is considerable difference in the deformation for the two laminates for the $y=0$ plane. The buckled area is noticeably wider for the (0/90/90/0) laminate than it is for the (90/0/0/90) laminate. The deformation for the $x=0$ plane is not much different for the two laminates. The analysis predicted interpenetration of the delamination faces (since contact constraints were not imposed). The measured and predicted deformed shape agree reasonably well except, of course, where the analysis predicted interpenetration.

Strain-energy release rate distributions were calculated for the six configurations for a range of strains which bracketed the strain at which delamination growth from the Kapton insert occurred. In all cases the G_{III} component was negligible. Figures 7.3.6-7.3.11 show the results of the analysis. There is one figure

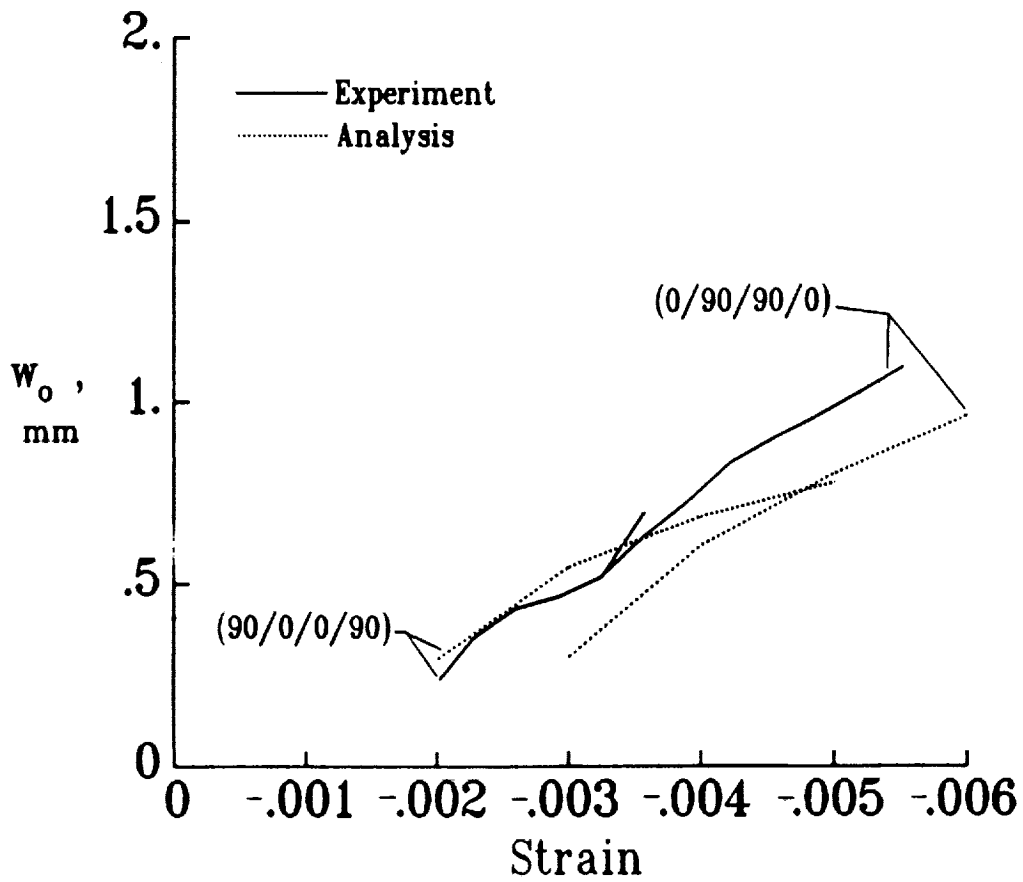


Fig. 7.3.1 Measured and predicted deflection versus ϵ_x for two IM7/8551-7 laminates. Diameter of initial delamination is 30mm.

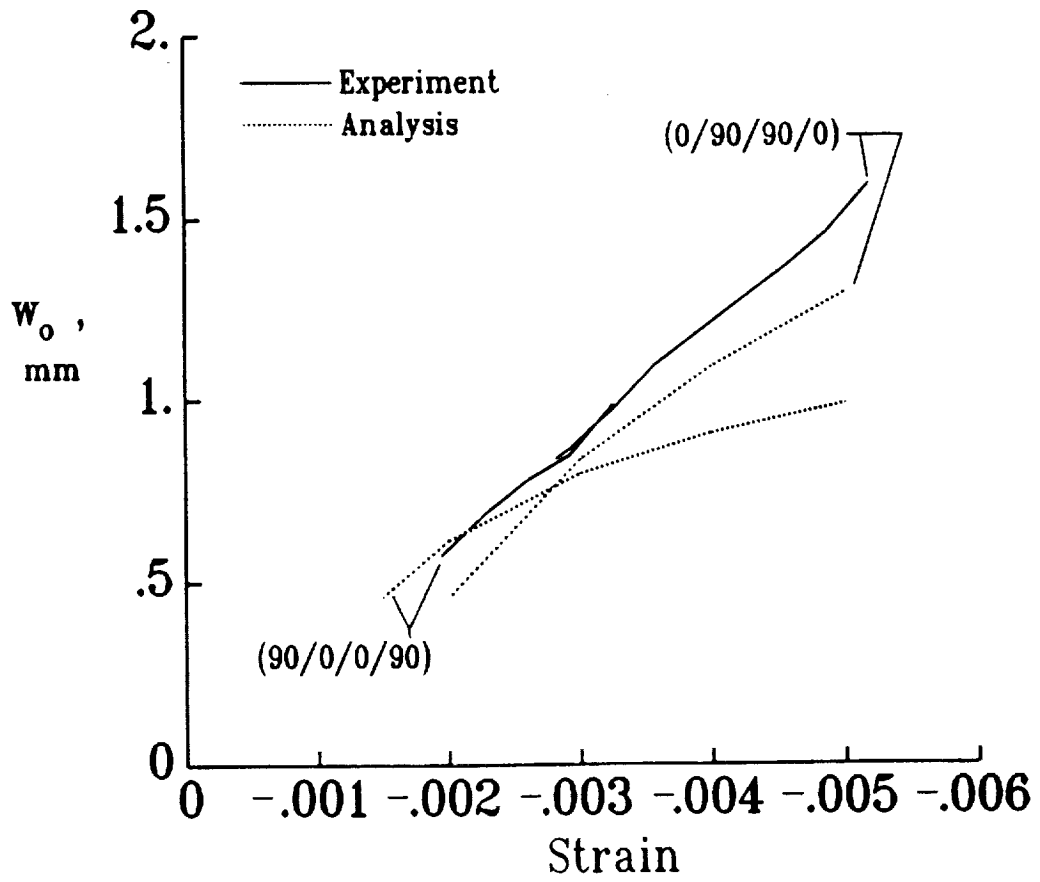


Fig. 7.3.2 Measured and predicted deflection versus ϵ_x for two IM7/8551-7 laminates. Diameter of initial delamination is 40mm.

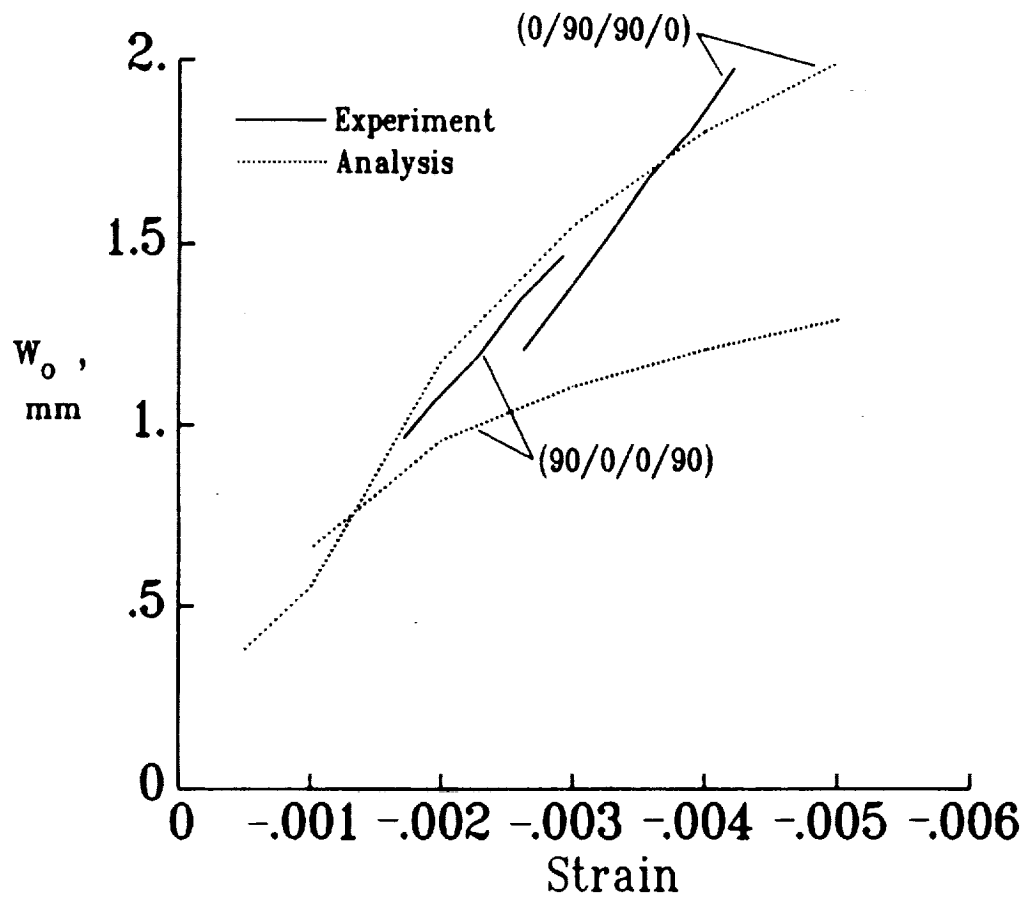


Fig. 7.3.3 Measured and predicted deflection versus ϵ_x for two IM7/8551-7 laminates. Diameter of initial delamination is 60mm.

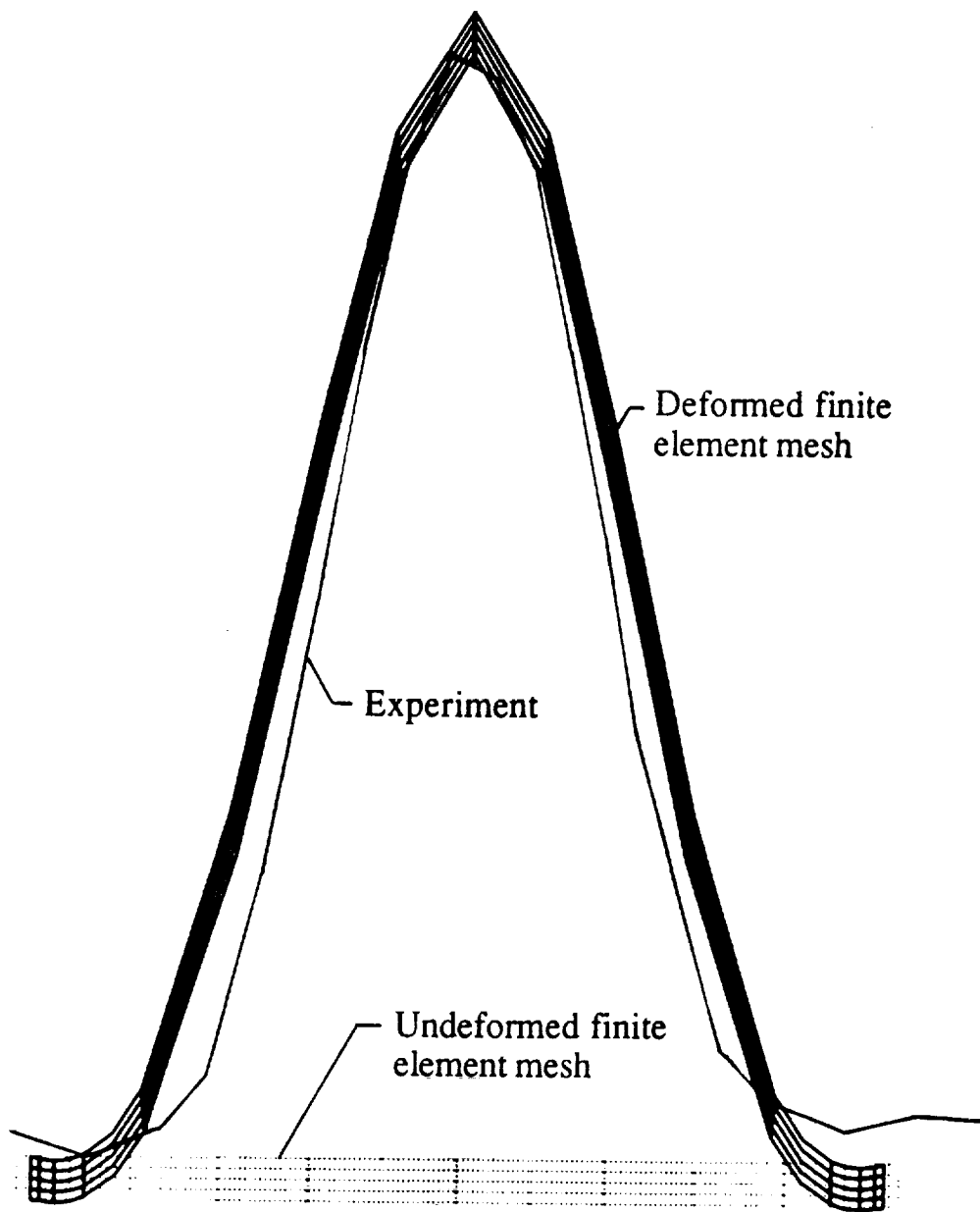


Fig. 7.3.4 Deformation of the $y=0$ plane for a $(0/90/90/0)$ sublaminate. Initial delamination diameter was 60mm.

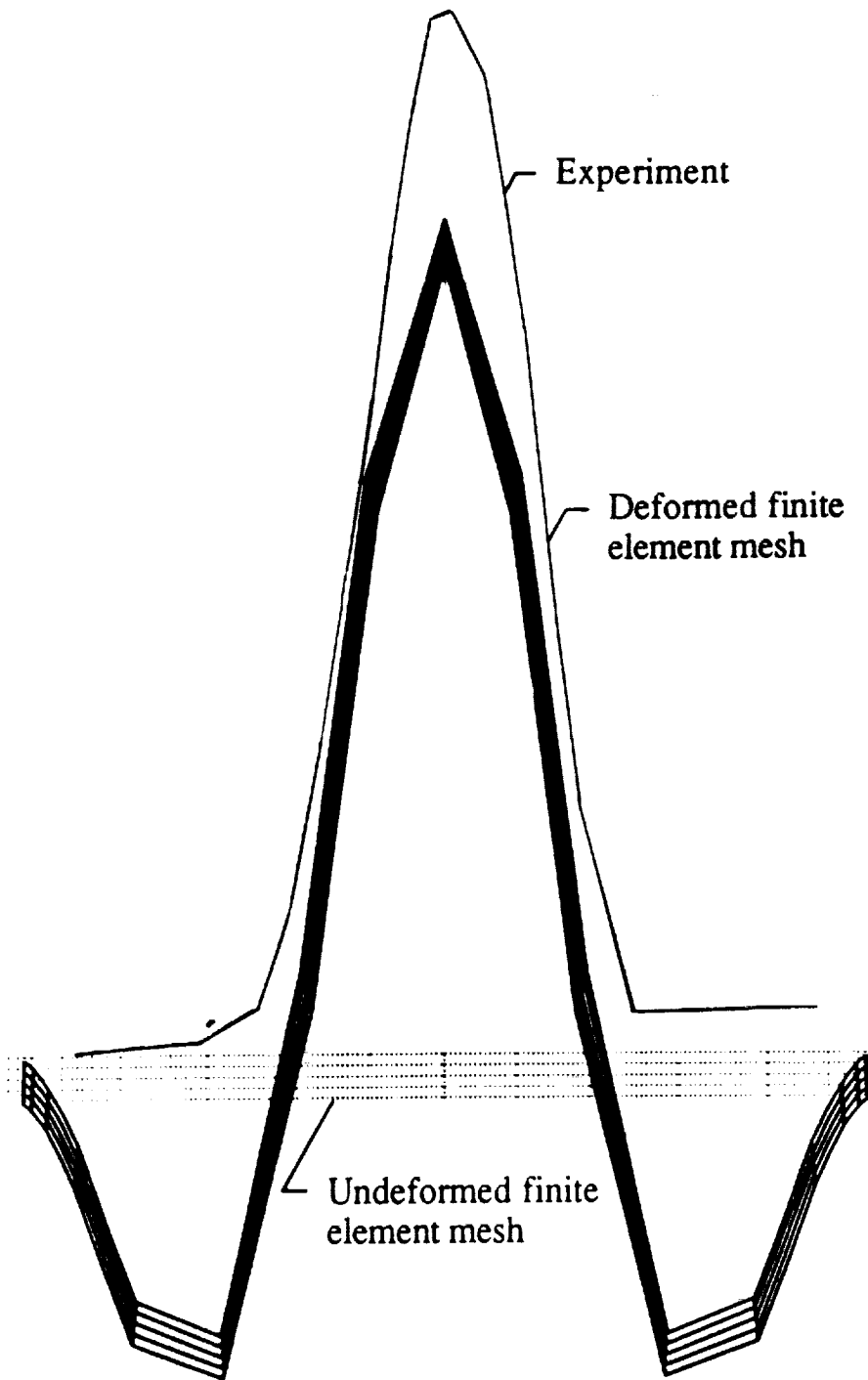


Fig. 7.3.5 Deformation of the $y=0$ plane for a (90/0/0/90) sublaminated. Initial delamination diameter was 60mm.

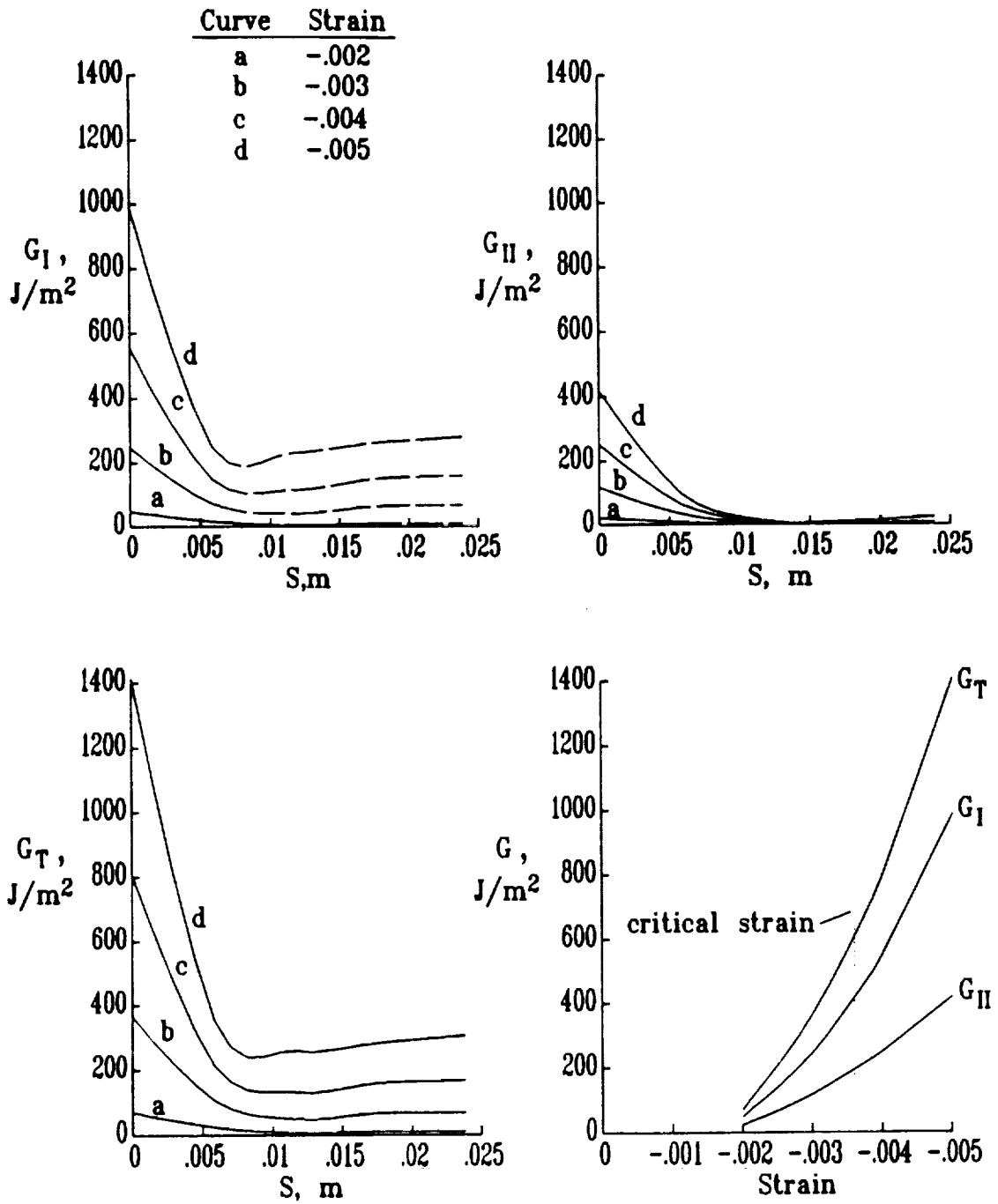


Fig. 7.3.6 Strain-energy release rate distributions and maximum strain-energy release rate versus ϵ_x . The material is IM7/8551-7 and the sublaminates is 30mm in diameter and has a stacking sequence of (90/0/0/90).

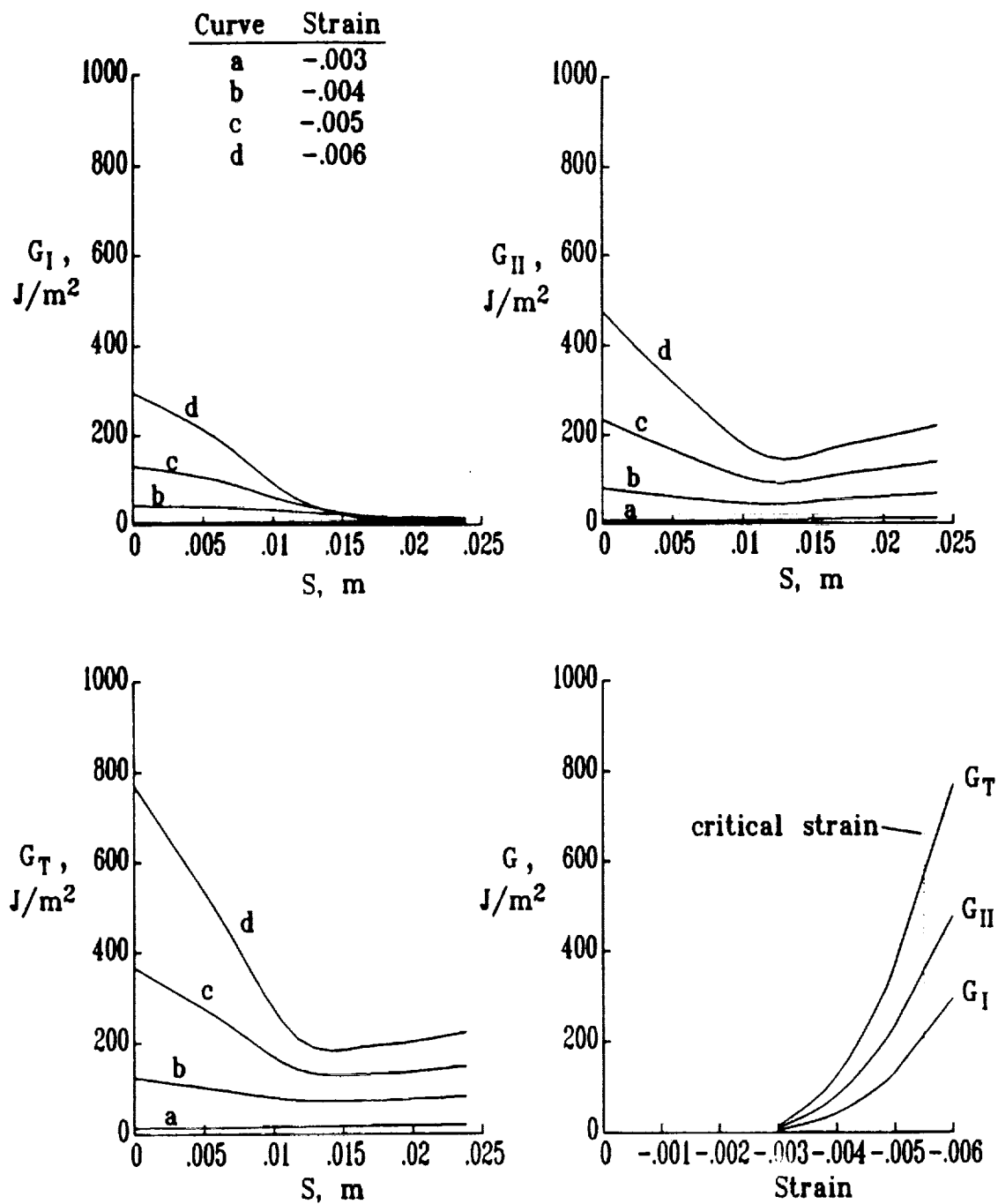


Fig. 7.3.7 Strain-energy release rate distributions and maximum strain-energy release rate versus ϵ_x . The material is IM7/8551-7 and the sublaminates is 30mm in diameter and has a stacking sequence of (0/90/90/0).

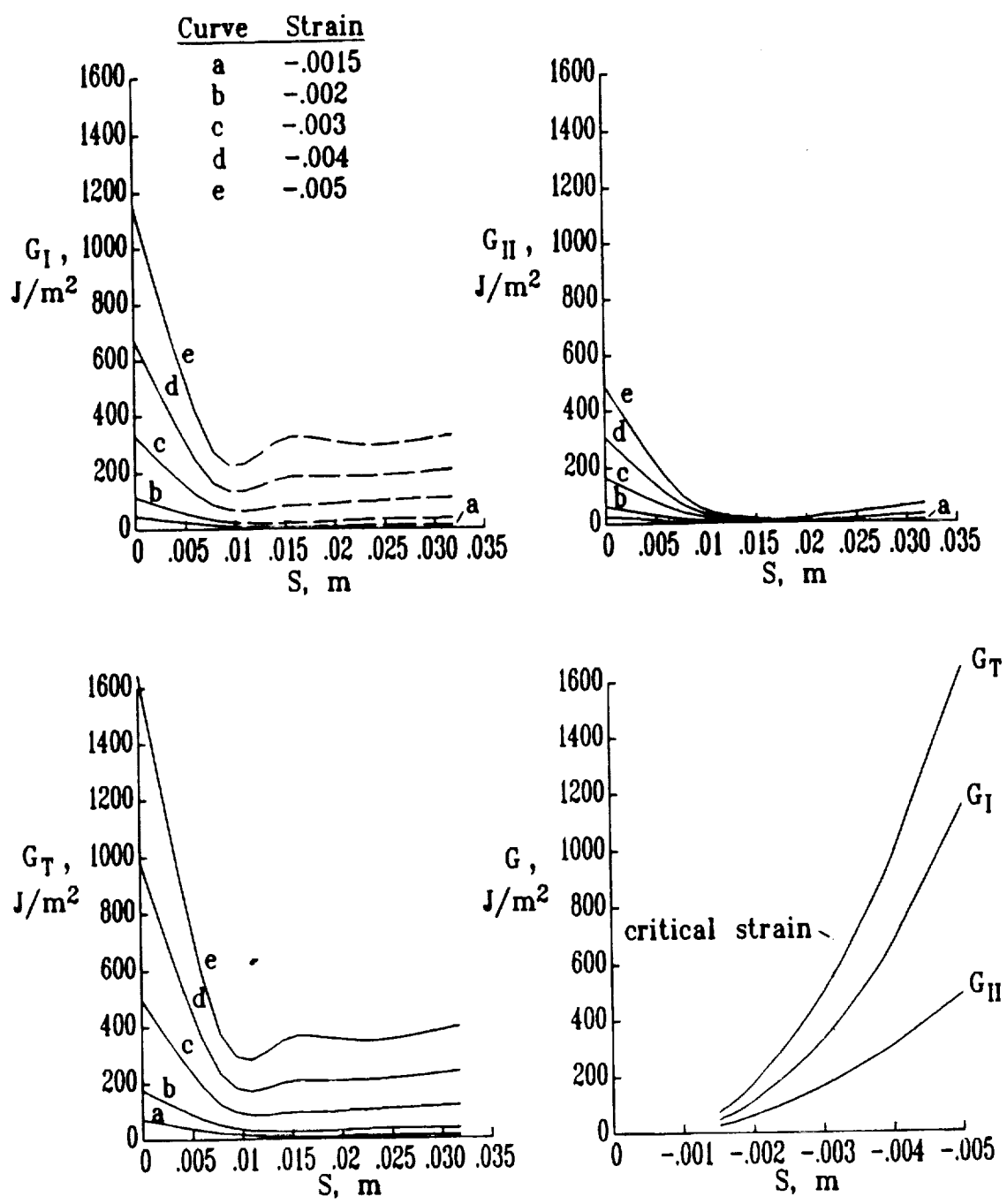


Fig. 7.3.8 Strain-energy release rate distributions and maximum strain-energy release rate versus ϵ_x . The material is IM7/8551-7 and the sublaminates is 40mm in diameter and has a stacking sequence of (90/0/0/90).

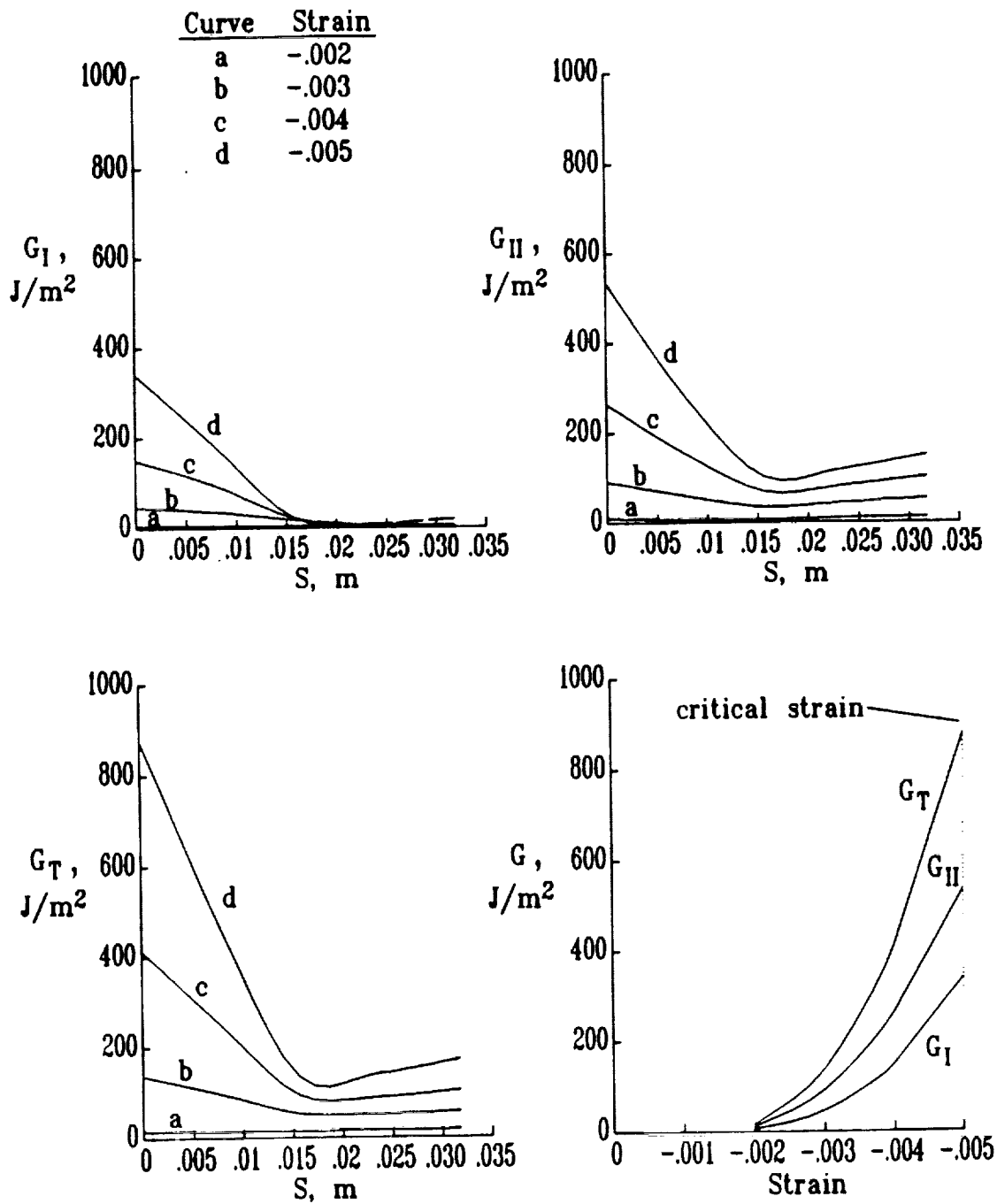


Fig. 7.3.9 Strain-energy release rate distributions and maximum strain-energy release rate versus ϵ_x . The material is IM7/8551-7 and the sublaminates is 40mm in diameter and has a stacking sequence of (0/90/90/0).

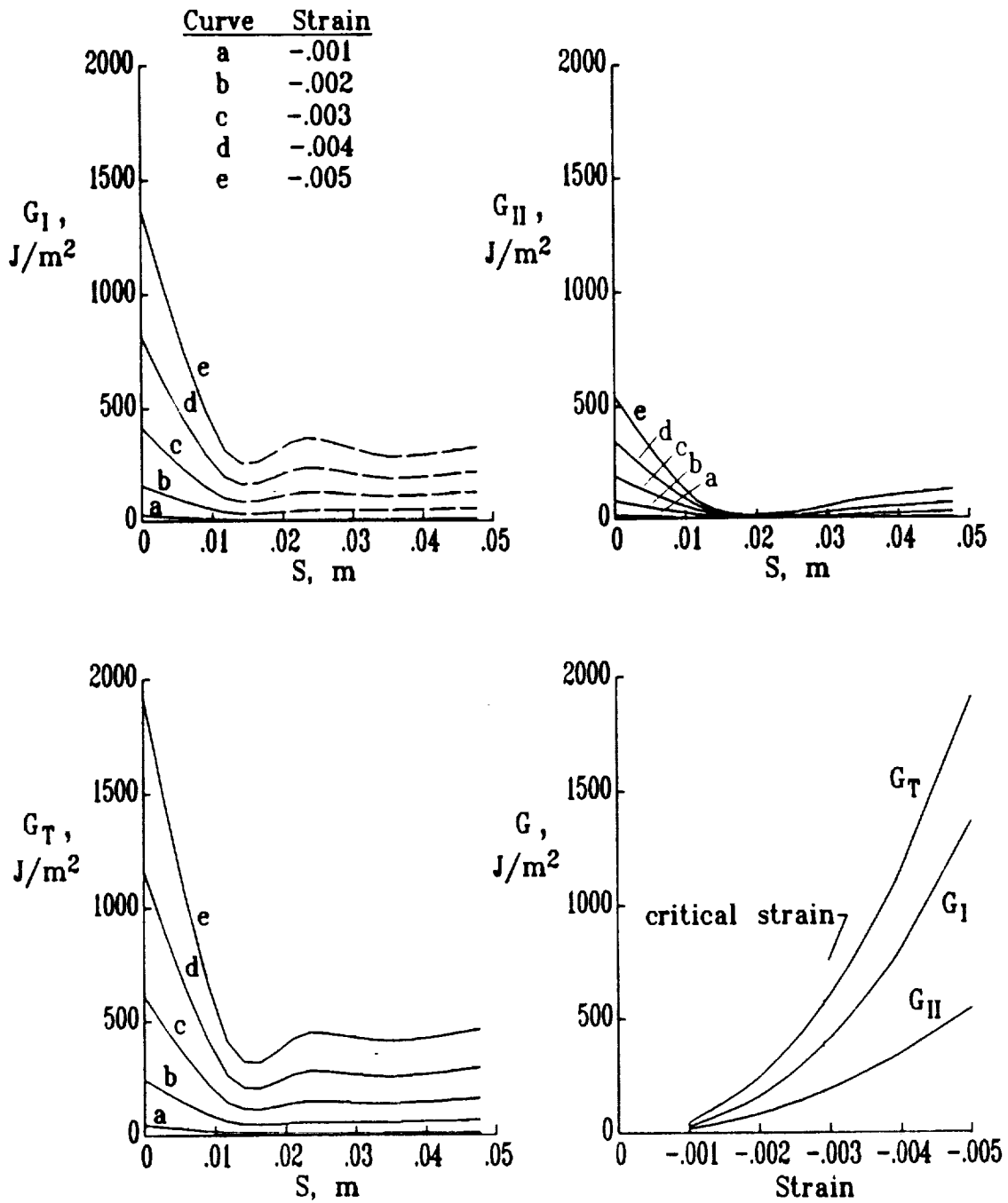


Fig. 7.3.10 Strain-energy release rate distributions and maximum strain-energy release rate versus ϵ_x . The material is IM7/8551-7 and the sublaminates is 60mm in diameter and has a stacking sequence of (90/0/0/90).

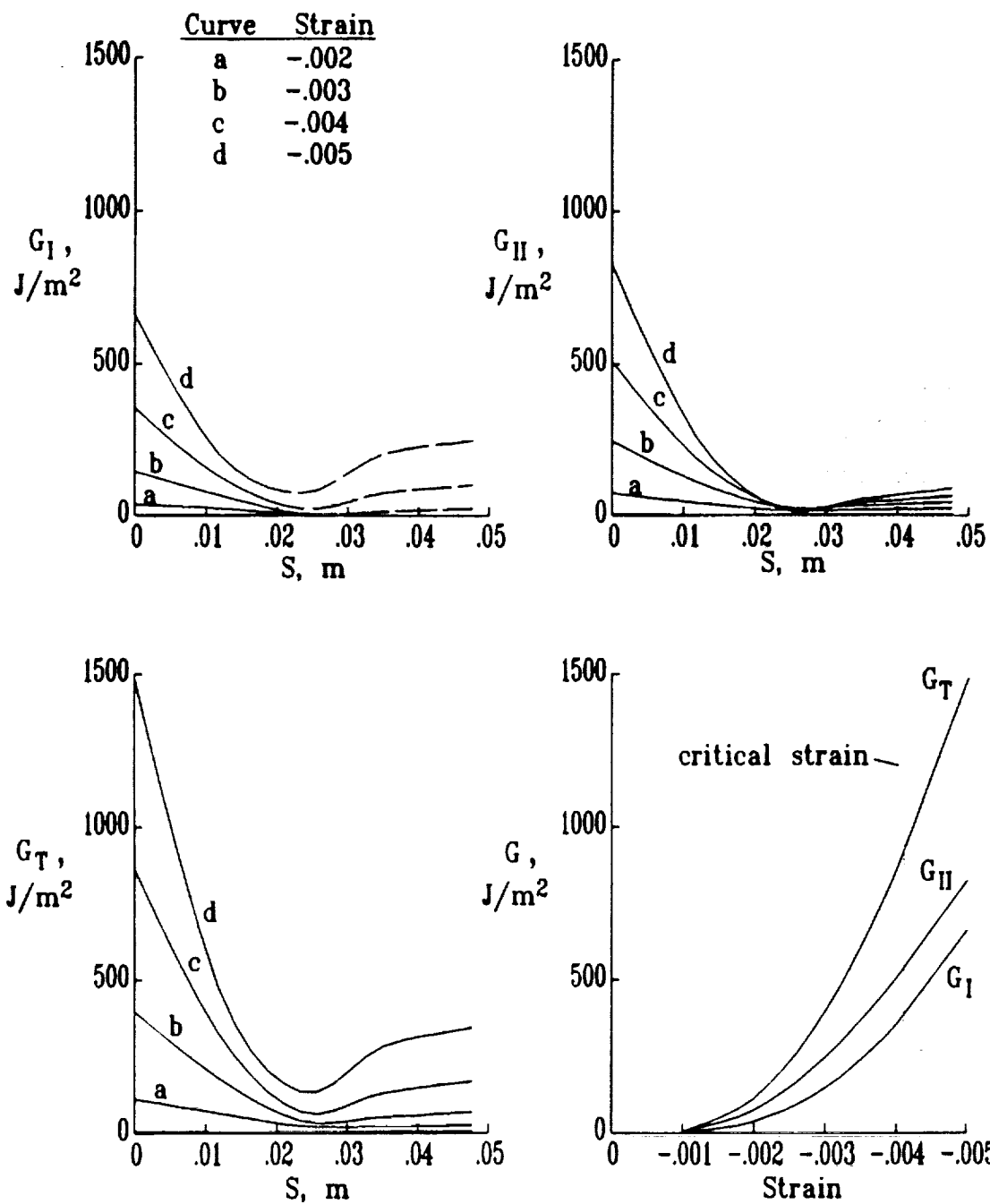


Fig. 7.3.11 Strain-energy release rate distributions and maximum strain-energy release rate versus ϵ_x . The material is IM7/8551-7 and the sublaminates is 60mm in diameter and has a stacking sequence of (0/90/90/0).

for each configuration. Each figure shows the variation of G_I , G_{II} , and G_T along the delamination front. Also shown is the variation of the peak magnitude of G_I , G_{II} , and G_T with applied strain level. In all cases there is a large variation of the strain-energy release rates along the delamination front. The peak magnitudes occurred at $S = 0$ and the magnitudes were small except close to $S = 0$. Obviously, one would expect delamination growth to occur preferentially near $S = 0$, which corresponds to growth transverse to the load direction. During the tests, one could visually determine that the delamination growth was localized near $S = 0$. Figures 7.3.12-7.3.15 show X-rays of several specimens after appreciable delamination growth had occurred. In these particular specimens there was sufficient through-the-thickness damage to permit the dye penetrant to reach the interior. These figures show that the analysis was correct in predicting preferential growth near $S=0$. The X-rays show that significant ply cracking accompanied the growth. Ply cracking occurred both in 0° and 90° plies. The large horizontal cracks in Figs. 7.3.12 and 7.2.14 could be seen on the specimen surface with the naked eye. These cracks formed after delamination growth had occurred. The tests were stopped when the large horizontal cracks formed.

Several specimens were sectioned and polished after testing. Micrographs of these specimens are presented in Figs. 7.3.16-7.3.18. Fig. 7.3.16 shows two cross-sectional views of a 0/90/90/0 sublaminates which had an initial diameter of 40mm. During the test of this specimen, the delamination growth occurred followed (after a few minutes at constant load) by the formation of a horizontal crease in the sublaminates. There was no visible surface damage. Fig. 7.3.16a shows that the crease was a result of fiber microbuckling of the interior surface ply of the sublaminates. Fig. 7.3.16b shows a micrograph taken near the delamination front. Recall that the Kapton implant was located between the fourth and fifth plies. The delamination in Fig.7.3.16b is between the third and fourth plies. the delamination has switched interfaces by way of a matrix crack in the fourth ply. This figure also shows angled matrix cracks in the 90° plies. The angled orientation was typical in all of the specimens examined.



Fig. 7.3.12 Radiograph of IM7/8551-7 laminate with an initial circular embedded delamination of diameter 30mm. The sublaminare is (0/90/90/0).

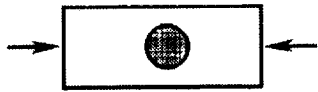
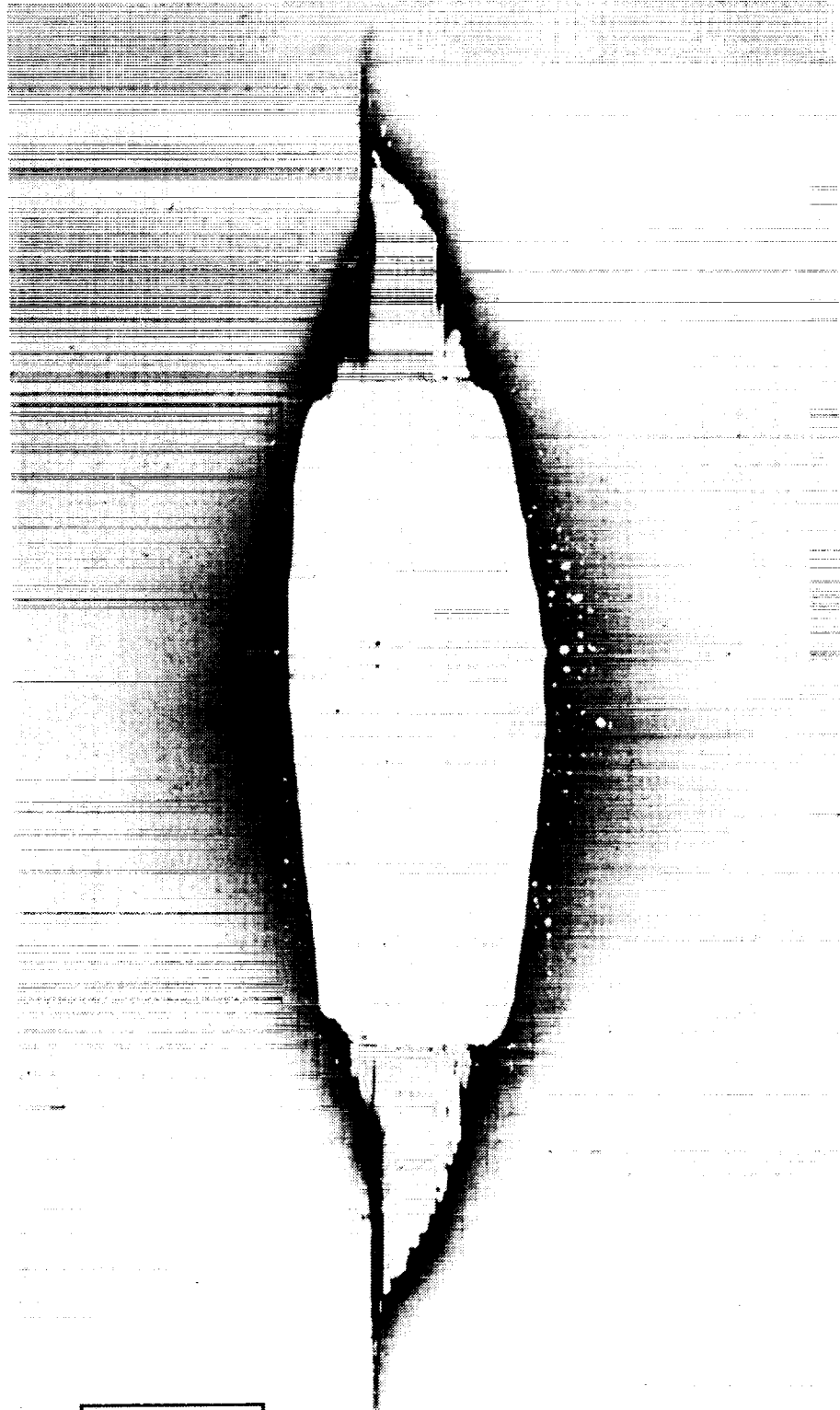


Fig. 7.3.13 Radiograph of IM7/8551-7 laminate with an initial circular embedded delamination of diameter 30mm. The sublaminar is (90/0/0/90).

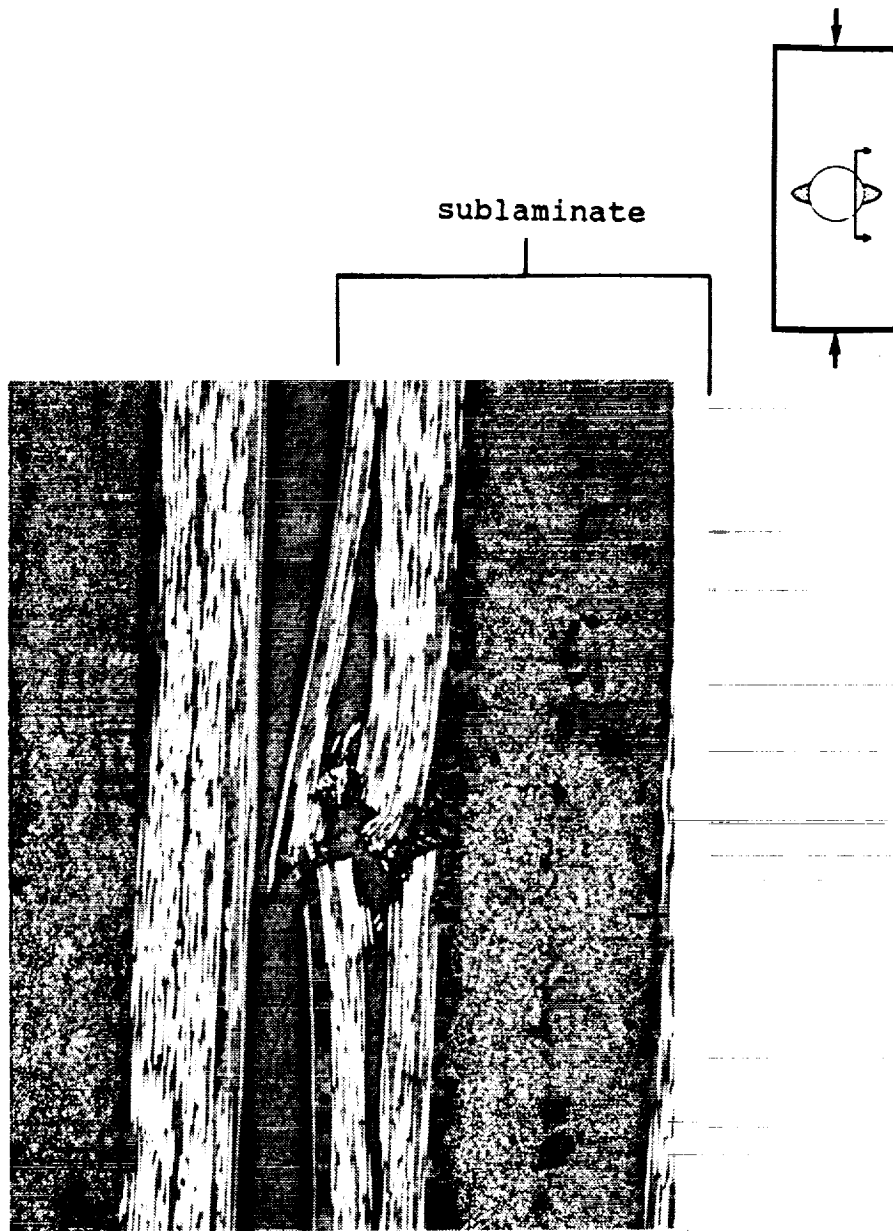
ORIGINAL PAGE IS
OF POOR QUALITY



Fig. 7.3.14 Radiograph of IM7/8551-7 laminate with an initial circular embedded delamination of diameter 60mm. The sublaminare is (0/90/90/0).

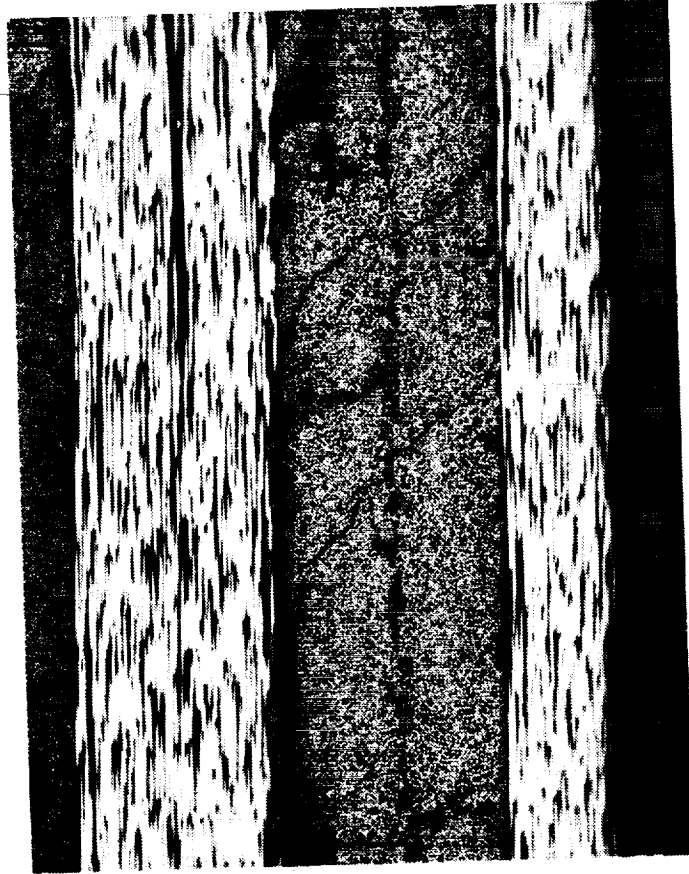
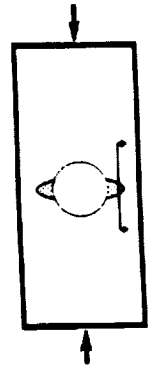


Fig. 7.3.15 Radiograph of IM7/8551-7 laminate with an initial circular embedded delamination of diameter 60mm. The sublaminare is (90/0/0/90).



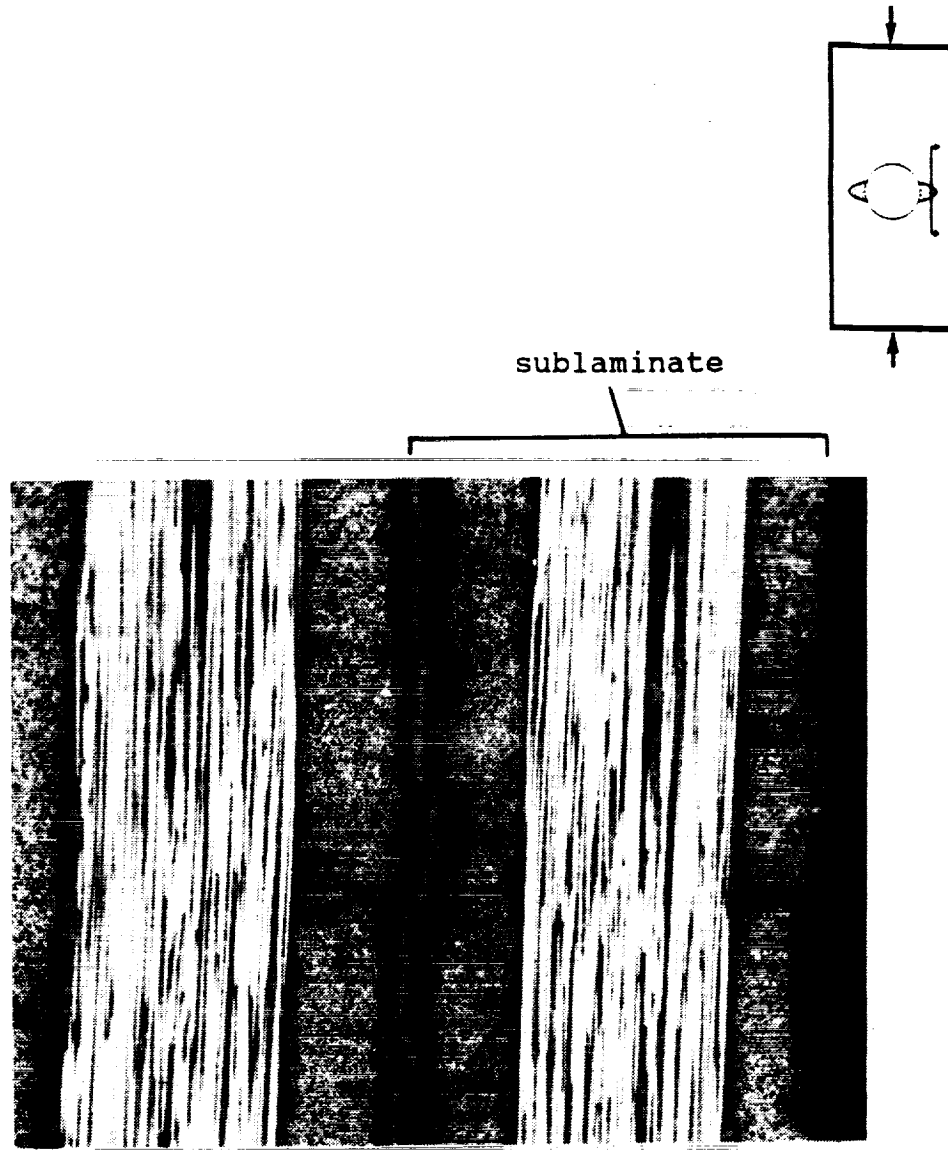
(a) View 1

Fig. 7.3.16 Cross-section of IM7/8551-7 laminate with a (0/90/90/0) sublaminate and an initial delamination diameter of 40mm.



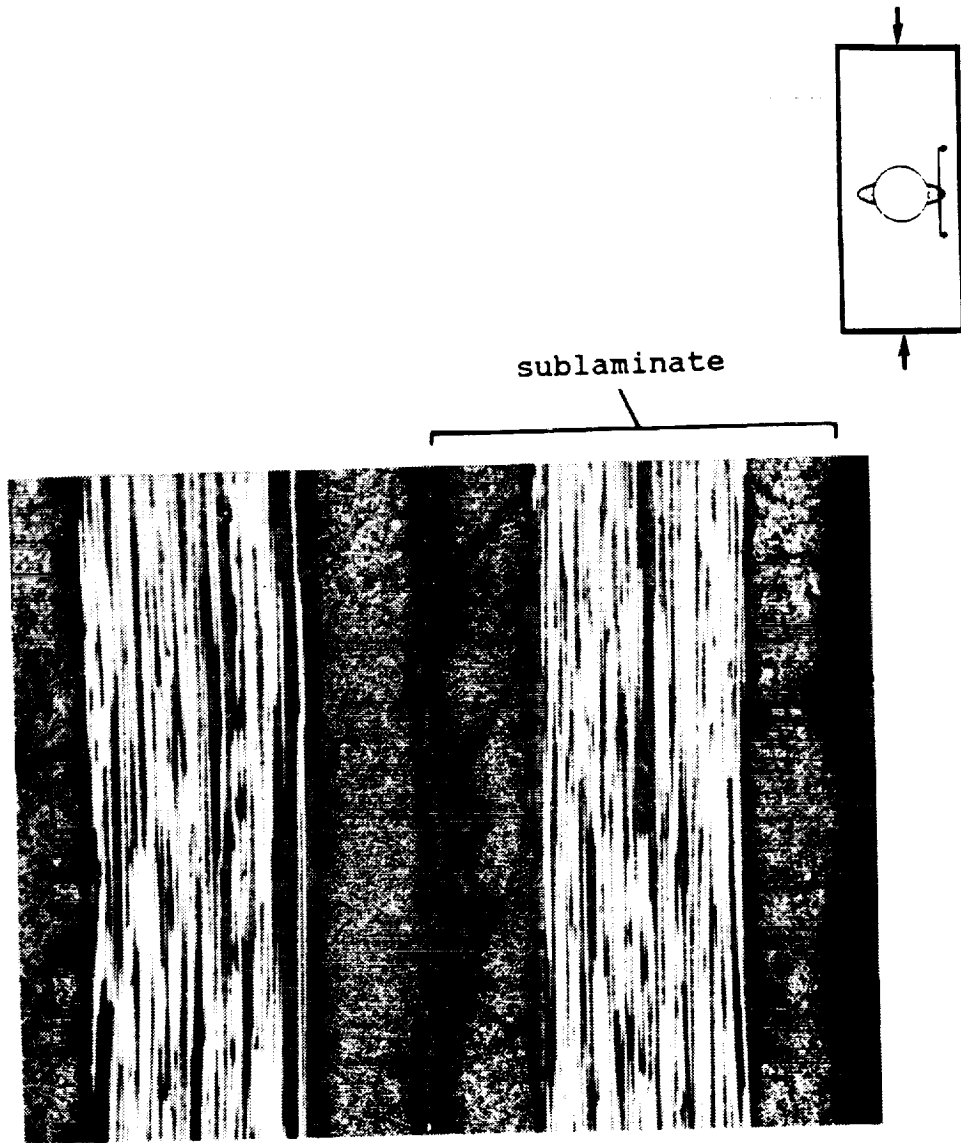
(b) View 2

Fig. 7.3.16, Concluded.



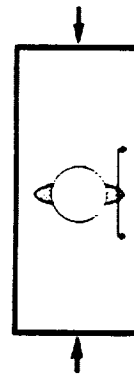
(a) View 1

Fig. 7.3.17 Cross-section of IM7/8551-7 laminate with an (90/0/0/90) sublaminates and an initial delamination diameter of 60mm.



(b) View 2

Fig. 7.3.17 Concluded.



(a) View 1

Fig. 7.3.18 Cross-section of IM7/8551-7 laminate with a (90/0/0/90) sublaminates and an initial delamination diameter of 40mm.



(b) View 2

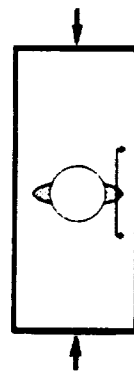


Fig. 7.3.18 Concluded.

Fig. 7.3.17 shows two cross-sections of a 90/0/0/90 sublaminates which had an initial diameter of 60mm. Fig. 7.3.17a shows that even after some growth, the delamination is still at the original interface (i.e. between the fourth and fifth plies). The view in 7.3.17a is of an area near the y-axis. In Fig.7.3.17b the view is of an area offset slightly from the y-axis. There are many ply cracks in this area, but the delamination is still between the fourth and fifth plies.

Fig. 7.3.18 shows a montage of four micrographs of a 90/0/0/90 sublaminates which had an initial delamination diameter of 40mm. In this case the delamination has grown along the interface between the fourth and fifth plies. After some growth, the stresses were such that a crack formed at both ends of the delamination. At one end the crack grew all the way to the surface of the laminate.

The micrographs and the X-rays indicate that even when a configuration starts out fairly simple (in this case a single delamination separating the laminate into two balanced and symmetric laminates), the damage development tends to be complicated. Matrix ply cracking was prevalent in all the tests. The density of the cracks varied with location in the sublaminates. The delamination sometimes switched interfaces, depending on the stacking sequence. In some cases fiber microbuckling occurred.

The strain at which the delamination began to grow was recorded for each configuration. Using these strains and the analytical results in Figs. 7.3.6-7.3.11 one can estimate the peak strain-energy release associated with delamination growth for each specimen. These results are summarized in Fig. 7.3.19. Both G_I and G_{II} are shown. Delamination growth appears to be dominated by G_I . The critical magnitude of G_I based on Fig. 7.3.19 is not much different than the 392-513 J/m^2 reported by the materials manufacturer (ref. 46). When G_{II} was large, the critical G_I tends to be somewhat less.

For the 30mm delamination with a (0/90/90/0) stacking sequence, G_I was quite low. This was probably due to the high strain which would have been

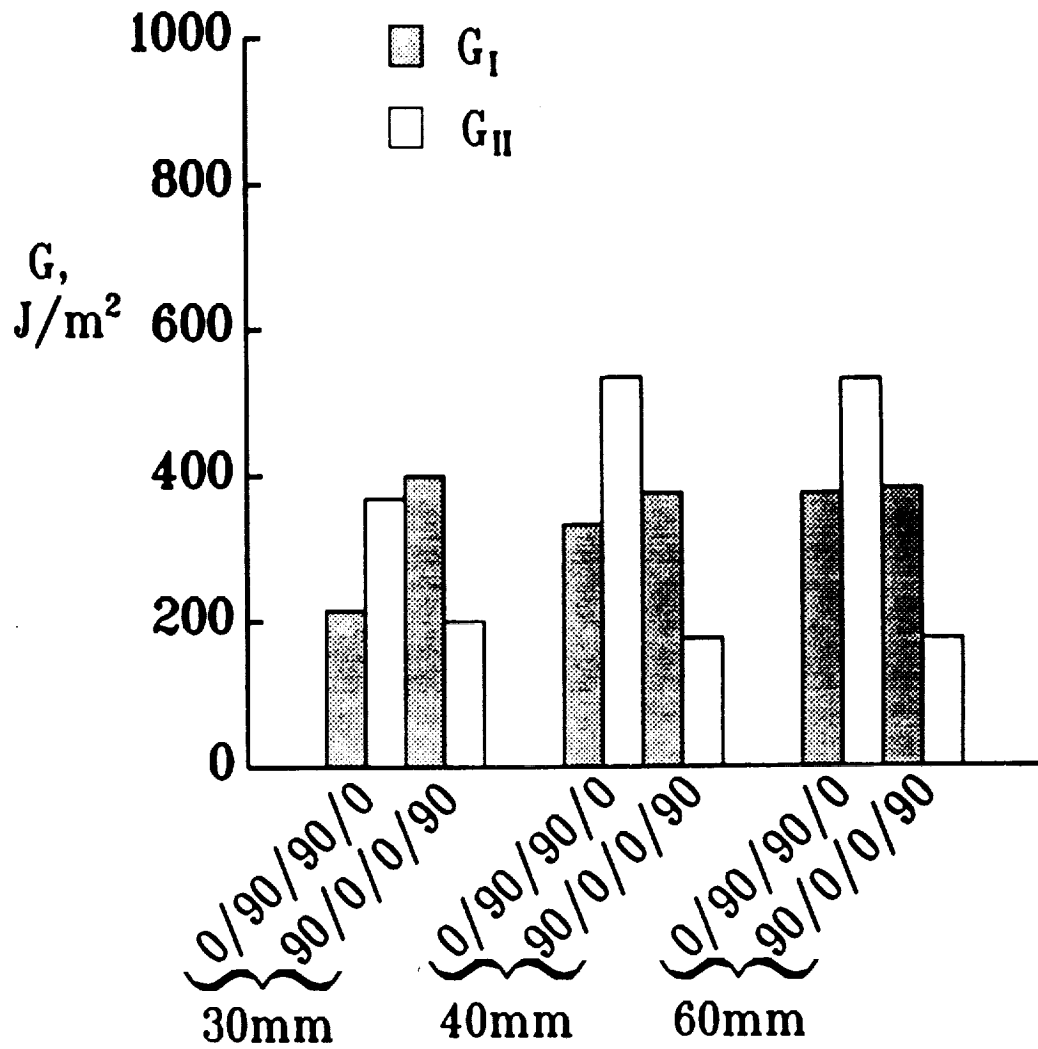


Fig. 7.3.19 Mode I and Mode II strain-energy release rates for delamination growth. Results are shown for two stacking sequences and three delamination sizes.

required to reach a value of G_I of about $400J/m^2$. Fig. 7.3.20 summarizes the strains at which delamination growth began for each configuration. For each delamination size the strain was significantly larger for the (0/90/90/0) stacking sequence. For the 30mm case the strain for growth was -.0055. This nominal strain plus the flexure of the buckled region results in a very high compressive strain in some areas. One might guess that this very high compressive strain could trigger other damage mechanisms which would augment the effect of the postbuckling induced interlaminar stresses. In fact, for both 30mm (0/90/90/0) specimens tested, a horizontal crack formed shortly after delamination growth occurred (see the X-ray in Fig. 7.3.12). This horizontal crack formed when microbuckling occurred on the interior surface of the sublaminates.

The two stacking sequences differed considerably in terms of the stability of delamination growth. The (90/0/0/90) laminate always exhibited at least some slow incremental delamination growth with increased load. The delamination growth in the (0/90/90/0) laminate tended to be abrupt and often the initial growth was quickly followed by formation of a large horizontal crack.

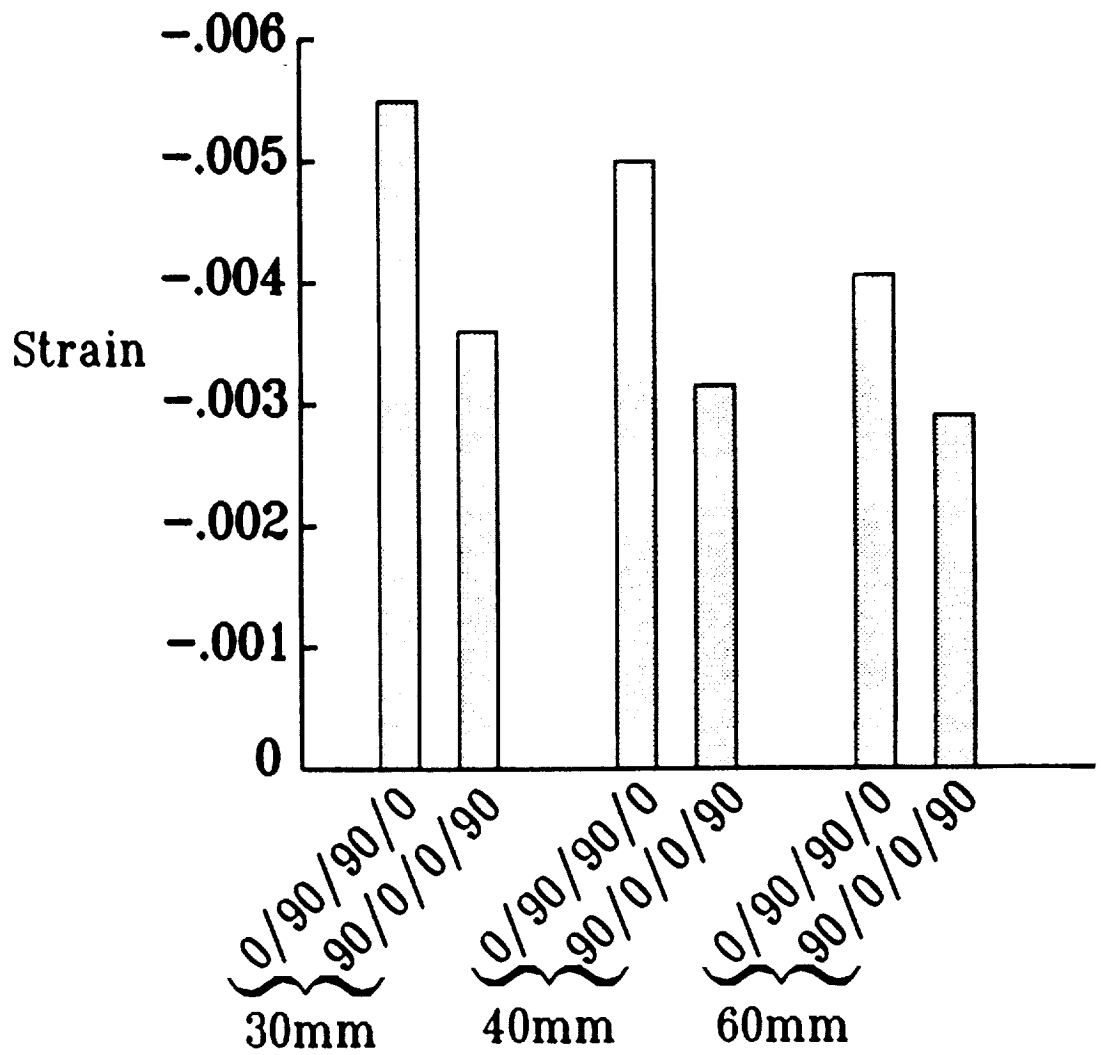


Fig. 7.3.20 Strain at which delamination growth began for IM7/8551-7 laminates with an embedded delamination.

Chapter 8

SUMMARY AND RECOMMENDATIONS

There are many mechanisms which contribute to compression failure of laminated composites. This study has focused on delamination growth driven by local buckling of a delaminated group of plies. This mechanism was referred to as instability-related delamination growth (IRDG). A review of the literature indicated that no detailed analysis had been performed for any three-dimensional configuration which exhibits IRDG. Detailed stress analysis helps identify which material and geometric parameters govern IRDG. Also, without detailed stress analyses it is difficult to determine the accuracy of less expensive approximate analyses.

The goal of this study was to enhance the understanding of IRDG in 3D configurations through a combination of analyses and experiments. There were three tasks in this study: development of a suitable stress analysis program, performance of a parametric analytical study, and performance of a combined experimental and analytical program.

A geometrically nonlinear 3D finite element analysis program, NONLIN3D, was developed to perform the required stress analysis. This program was tailored to exploit the vector processing capability of the CDC VPS32 supercomputer. The program uses a 20-node isoparametric hexahedron element. The program was designed to perform analysis by substructures. This resulted in a large reduction in computational effort, since nonlinear analysis could be restricted easily to just that part of a configuration which needed it. An approximate contact analysis was also implemented. A variety of checks were performed to assure the accuracy of the analysis.

The parametric analytical study was performed on a fictitious material which had the same in-plane stiffnesses as a quasi-isotropic laminate, but had no stacking sequence effects. This material was used so that the effects of strain level and

geometric parameters could be studied without the additional complications due to stacking sequence. Both embedded and edge delaminations were considered. These configurations were found to behave in a complex manner. Some of the observations and accomplishments were:

1. The configurations were definitely mixed mode. In some cases G_I was larger than G_{II} . For other cases the opposite was true.

2. In general, there was a very large variation of the strain-energy release rates along the delamination front. Usually, one would expect initial delamination growth to occur only along a small portion of the front.

3. The locations of maximum G_I and G_{II} depended on the delamination shape and the applied strain.

4. The mode III component was much smaller than G_I and G_{II} .

5. The analysis predicted that for some configurations the sublaminates would overlap the base laminate unless contact constraints were added. Most of the analyses were performed without imposing contact constraints, since the addition of the constraints further complicates an already complicated problem. To determine the errors caused by not including contact constraints, a few strain-energy release rate results were calculated both with and without contact constraints. These results showed that for moderate postbuckling strains, the errors were fairly small.

6. The distribution of total strain-energy release rate can be calculated fairly accurately using plate analysis.

7. An intuitive interpretation of the deformation and load transfer for the embedded delamination was presented. This interpretation explains much of the observed variation of the strain-energy release rates.

The combined experimental and analytical program involved a variety of

configurations. A few preliminary tests were conducted strictly for verifying NONLIN3D. The primary goals of this phase of the study was to determine whether the behaviors predicted by NONLIN3D would occur in actual specimens and to determine if a strain-energy release rate parameter could be used to predict the onset of IRDG.

IRDG was studied for two material systems: AS4/PEEK and IM7/8551-7. Two sublaminates types were considered: (0/90/90/0) and (90/0/0/90). Because of problems in fabricating the PEEK specimens, only qualitative comparisons of analysis and experiments were possible. Quantitative comparisons were made for the IM7/8551-7 material system. Some of the major conclusions were:

1. The shape of the postbuckled sublaminates depended on the stacking sequence. The predicted shapes agreed well with the experimentally measured shapes.
2. The direction of delamination growth depended on stacking sequence for the edge delamination. This behavior was predicted by the analysis.
3. Delamination growth occurred along only a small portion of the delamination front, as predicted by the analysis.
4. Initial delamination growth in the IM7/8551-7 laminates appeared to be governed by the magnitude of G_I .
5. Matrix ply cracking generally accompanied delamination growth. In some cases fiber microbuckling also occurred shortly after delamination growth occurred.

Instability-related delamination growth was defined to be delamination growth caused by buckling of a delaminated group of plies. The tests showed that other damage mechanisms can also become operative when buckling occurs. Explaining the interaction of these various mechanisms with IRDG is beyond the scope of this study. In fact, there is so much that needs to be done to fully understand

IRDG, that it is difficult to make just a few recommendations for future work. The following non-comprehensive comments are offered as general guidelines for future work in the area of instability-related delamination growth.

1. Considerable effort was expended in developing and using NONLIN3D. The 3D analysis is still quite expensive, in spite of the techniques used to reduce the computational effort. These techniques served only to make it possible to make the calculations presented herein. If the synergistic effects of various damage mechanisms are to be studied with any rigor, new approaches must be developed. Hopefully, the results presented will be used to provide direction and insight for developing approximate analyses.

2. A more complete characterization of basic material properties is needed. A full 3D set of material moduli is obviously needed for accurate 3D stress analysis. Also needed is better interlaminar fracture toughness characterization, particularly for mixed mode situations.

3. The effects of the following on IRDG need to be examined for 3D configurations:

- a. unsymmetric sublaminates
- b. global bending
- c. thermal stresses
- d. initial imperfections
- e. multiple delaminations

4. Synergistic effects due to the presence of multiple damage types need considerable experimental investigation.

REFERENCES

1. Kachanov, L. M.: Separation Failure of Composite Materials. *Polymer Mechanics*, vol. 12, 1976, pp. 812-815.
2. Whitcomb, John D. : Analysis of Instability-Related Delamination Growth. *Proceedings of the Sixth Annual Mechanics of Composites review*, AFWAL-TR-81-4001, 1981, pp. 95-100.
3. Whitcomb, John D.: Finite Element Analysis of Instability-Related Delamination Growth. *J. Composite Materials*, Vol. 15, Sept. 1981., pp. 403-426
4. Whitcomb, John D.: Strain-Energy Release Rate Analysis of Cyclic Delamination Growth in Compressively Loaded Laminates. NASA TM-84598, Jan. 1983. Also, in *Effects of Defects in Composite Materials*, ASTM STP 836, American Society for Testing and Materials, 1984, pp.175-193.
5. Whitcomb, John D.: Parametric Analytical Study of Instability-Related Delamination Growth. *Composites Science and Technology*, 25, 1986, pp.19-48.
6. Chai, Herzl; Babcock, Charles D. and Knauss, Wolfgang G.: One Dimensional Modelling of Failure in Laminated Plates by Delamination Buckling. *Int. J. Solids Structures*, Vol. 17, No. 11, 1981, pp. 1069-1083.
7. Wang, S. S.; Zahlan, N. M.; and Suemasu, H.: Compressive Stability of Random Short-Fiber Composites, Part II-Experimental and Analytical Results. *J. Composite Materials*, vol. 19, July 1985, pp. 317-333.
8. Ashizawa, M.: Fast Interlaminar Fracture of a Compressively Loaded Composite Containing a Defect. Presented at the Fifth DOD/NASA Conference on Fibrous Composites in Structural Design, New Orleans, LA, Jan. 1981. (also available as Douglas Paper No. 6994).

9. Simitzes, G. J.; Sallam, S.; and Yin, W. L.: Effect of Delamination of Axially Loaded Homogeneous Laminated Plates. *AIAA Journal*, 1985, pp. 1437-1444.
10. Sallam, S. and Simitzes, G. J.: Delamination Buckling and Growth of Flat, Cross-Ply Laminates. *Composite Structures*, vol. 4, 1985, pp. 361-381.
11. Ramkumar, R. L.: Fatigue Degradation in Compressively Loaded Composite Laminates. NASA CR-165681, April 1981.
12. Ramkumar, R. L.: Performance of a Quantitative Study of Instability-Related Delamination Growth. NASA CR-166046, March 1983.
13. Gillespie, John W. and Pipes, R. Byron: Compressive Strength of Composite Laminates with Interlaminar Defects. *Composite Structures*, Vol. 2, No. 1, 1984, pp. 49-69.
14. Konishi, D. Y. and Johnson, W. R.: Fatigue Effects on Delaminations and Strength Degradation in Graphite/Epoxy Laminates. *Composite Materials: Testing and Design, Fifth Conference, ASTM STP 674*, American Society for Testing and Materials, 1979, pp. 597-619.
15. Chai, H.: The Growth of Impact Damage in Compressively Loaded Laminates. Ph.D. Thesis, California Institute of Technology, March, 1982.
16. Chai, Herzl and Babcock, Charles D.: Two-Dimensional Modelling of Compressive Failure in Delaminated Laminates. *J. Composite Materials*, Vol. 19, Jan. 1985, pp. 67-98.
17. Webster, John D.: Flaw Criticality of Circular Disbond Defects in Compressive Laminates. Center for Composite Materials Report No. 81-03, 1981.
18. Ashton, J. E.; and Whitney, J. M.: *Theory of Laminated Plates*. Technomic, Inc., Stanford, Conn., 1970, pp. 31-34.

19. Shivakumar, K. N. and Whitcomb, J. D.: Buckling of a Sublaminar in a Quasi-Isotropic Composite Laminate. *Journal of Composite Materials*, Vol. 19, Jan. 1985.

20. Whitcomb, J. D. and Shivakumar, K. N.: Strain-Energy Release Analysis of a Laminate With a Postbuckled Delamination. *Fourth International Conference on Numerical Methods in Fracture Mechanics*. Pineridge Press, 1987, pp. 581-605. Also available as NASA TM 89091.

21. Yin, W. L.: Axisymmetric Buckling and Growth of a Circular Delamination in a Compressed Laminate. *International Journal of Solids and Structures*, vol. 21, 1985, pp. 503-514.

22. Fei, Zhizhong and Yin, Wan-Lee: Postbuckling Growth of a Circular Delamination in a Laminate Under Compression and Bending. *Proceedings of SECTAM XII, Vol. II, Callaway Gardens, May 1984*, pp. 130-134.

23. Bottega, W. J. : *The Mechanics of Delamination in Composite Materials*. Ph.D. Dissertation, Yale University, 1984.

24. Rhodes, M. D.; Williams, J. G.; and Starnes, J. H. Jr.: Low-Velocity Impact Damage in Graphite-Fiber Reinforced Epoxy laminates. Paper presented 34th Annual Conference Reinforced Plastics/Composites Institute, The Society of the Plastics Industry, Inc. New Orleans, La., Jan. 29-Feb. 2, 1979.

25. Byers, Bruce A.: Behavior of Damaged Graphite/Epoxy Laminates Under Compression Loading. NASA CR-159293, 1980.

26. Porter, T. R.: Compression and Compression Fatigue Testing of Composite Laminates. NASA CR-168023, 1982.

27. Chai, H.; Knauss, W. G. and Babcock, C. D.: Observation of Damage Growth in Compressively Loaded Laminates. *Experimental Mechanics*, Vol. 23, Sept. 1983, pp. 329-337.

28. Frederick, D. and Chang, T. S.: Continuum Mechanics. Scientific Publishers, Inc., Cambridge, 1972, pp. 79-82.
29. Irons, B. M.: Economical Computer Techniques for Numerically Integrated Finite Elements. Int. J. of Numerical Methods in Engineering, vol. 1, 1969, pp. 201-203.
30. Pawsey, S. F.; and Clough, R. W. : Improved Numerical Integration of Thick Shell Finite Elements. International Journal for Numerical Methods in Engineering, vol. 3, 1971, pp. 275-290.
31. Zienkiewicz, O. C.; Taylor, R. L.; and Too, J. M.: Reduced Integration Technique in General Analysis of Plates and Shells. International Journal for Numerical Methods in Engineering, vol. 3, 1971, pp. 275-290.
32. Gentsch, Wolfgang (editor): Vectorization of Computer Programs with Applications to Computational Fluid Dynamics. Friedr. Vieweg & Sohn Verlagsgesellschaft mbH, Braunschweig, 1984.
33. Howser, L. M. and Tennille, G. M.: VPS-32 MINI MANUAL, Central Scientific Computing Complex Document S-1b. NASA Langley Research Center, 1987, pp. 2.
34. Lambiotte, J.: The Solution of Linear Systems of Equations on a Vector Computer. Ph.D. Dissertation, University of Virginia, 1976.
35. Newman, J. C., JR.: Finite Element Analysis of Crack Propagation - Including the Effects of Crack Closure. Ph.D. Thesis, Virginia Polytechnic Institute and State University, May, 1974.
36. Noor, A. K. and Hartley, S. J.: Evaluation of Element Stiffness Matrices on CDC STAR-100 Computer. Computers and Structures, vol 9, pp. 151-161. 1978.

37. Noor, A. K. and Peters, J. M.: Element Stiffness Computation on CDC CYBER 205 Computer. Communications in Applied Numerical Methods, vol. 2, 1986, pp. 317-328.

38. Bathe, K.: Finite Element Procedures in Engineering Analysis. Prentice-Hall, Inc., Englewood Cliffs, New Jersey, pp.167-169.

39. Weaver, W., Jr.: Computer Programs for Structural Analysis, Van Nostrand, Princeton, New Jersey, 1967.

40. Rybicki, E. F. and Kanninen, M. F.: A Finite Element Calculation of Stress Intensity Factors by a Modified Crack Closure Integral. Engineering Fracture Mechanics, 1977, Vol. 9, pp. 931-938.

41. Wang, S. S. and Choi, I.: The Mechanics of Delamination in Fibre-reinforced Composite Laminates. Part I- Stress Singularities and Solution Structure. Part II- Delamination Behavior and Fracture Mechanics Parameters. NASA CR 172269 and CR 172270, Nov. 1983.

42. Raju, I. S. and Newman, J. C., Jr.: Stress-Intensity Factors for a Wide Range of Semi-Elliptical Surface Cracks in Finite-Thickness Plates. Engineering Fracture Mechanics, Vol. 11, No. 4, p.819.

43. Timoshenko, S. P. and Woinowski-Krieger, S.: Theory of Plates and Shells. McGraw-Hill, New York, 1959, pp. 415-416.

44. Bostaph, G. M. and Elber, W.: A Fracture Mechanics Analysis for Delamination Growth During Impact on Composite Plates. 1983 Advances in Aerospace Structures, Materials, and Dynamics, proceedings of the ASME Winter Annual Meeting, pp. 133-138.

45. Kelkar, A.; Elber, W.; and Raju, I. S.: Large Deflection Behavior of Quasi-Isotropic Laminates Under Low Velocity Impact Type Point Loading. AIAA/ASME/ASCE/AHS 26th Structures, Structural Dynamics, and Materials Conference, 1985. Paper no. AIAA-85-0723.

46. U. S./European Aircraft IM7/8551-7 Qualification Test Results. Hercules Aerospace Products Group publication, 1987.

APPENDIX
SHAPE FUNCTIONS FOR 8- AND 20-NODE ELEMENTS

This appendix gives the shape functions for the 8- and 20-node elements. The node numbering sequence was given earlier in Fig. (2.2.1).

The shape functions for the 8-node element are :

$$\begin{aligned}
 S(1) &= (1 + \delta_1) * (1 - \delta_2) * (1 - \delta_3)/8 \\
 S(2) &= (1 + \delta_1) * (1 + \delta_2) * (1 - \delta_3)/8 \\
 S(3) &= (1 + \delta_1) * (1 + \delta_2) * (1 + \delta_3)/8 \\
 S(4) &= (1 + \delta_1) * (1 - \delta_2) * (1 + \delta_3)/8 \\
 S(5) &= (1 - \delta_1) * (1 - \delta_2) * (1 - \delta_3)/8 \\
 S(6) &= (1 - \delta_1) * (1 + \delta_2) * (1 - \delta_3)/8 \\
 S(7) &= (1 - \delta_1) * (1 + \delta_2) * (1 + \delta_3)/8 \\
 S(8) &= (1 - \delta_1) * (1 - \delta_2) * (1 + \delta_3)/8
 \end{aligned}$$

The shape functions for the 20-node element are :

Corner nodes:

$$\begin{aligned}
 S(1) &= .125 * (1 - \delta_1) * (1 - \delta_2) * (1 - \delta_3) * (-\delta_1 - \delta_2 - \delta_3 - 2) \\
 S(3) &= .125 * (1 - \delta_1) * (1 + \delta_2) * (1 - \delta_3) * (-\delta_1 + \delta_2 - \delta_3 - 2) \\
 S(5) &= .125 * (1 - \delta_1) * (1 + \delta_2) * (1 + \delta_3) * (-\delta_1 + \delta_2 + \delta_3 - 2) \\
 S(7) &= .125 * (1 - \delta_1) * (1 - \delta_2) * (1 + \delta_3) * (-\delta_1 - \delta_2 + \delta_3 - 2) \\
 S(13) &= .125 * (1 + \delta_1) * (1 - \delta_2) * (1 - \delta_3) * (\delta_1 - \delta_2 - \delta_3 - 2) \\
 S(15) &= .125 * (1 + \delta_1) * (1 + \delta_2) * (1 - \delta_3) * (\delta_1 + \delta_2 - \delta_3 - 2) \\
 S(17) &= .125 * (1 + \delta_1) * (1 + \delta_2) * (1 + \delta_3) * (\delta_1 + \delta_2 + \delta_3 - 2) \\
 S(19) &= .125 * (1 + \delta_1) * (1 - \delta_2) * (1 + \delta_3) * (\delta_1 - \delta_2 + \delta_3 - 2)
 \end{aligned}$$

Mid-side nodes on the plane $\delta_1 = 0$:

$$\begin{aligned}
 S(9) &= .25 * (1 - \delta_1 * \delta_1) * (1 - \delta_2) * (1 - \delta_3) \\
 S(10) &= .25 * (1 - \delta_1 * \delta_1) * (1 + \delta_2) * (1 - \delta_3) \\
 S(11) &= .25 * (1 - \delta_1 * \delta_1) * (1 + \delta_2) * (1 + \delta_3) \\
 S(12) &= .25 * (1 - \delta_1 * \delta_1) * (1 - \delta_2) * (1 + \delta_3)
 \end{aligned}$$

Mid-side nodes on the plane $\delta_2 = 0$:

$$\begin{aligned}S(2) &= .25 * (1 - \delta_2 * \delta_2) * (1 - \delta_1) * (1 - \delta_3) \\S(6) &= .25 * (1 - \delta_2 * \delta_2) * (1 - \delta_1) * (1 + \delta_3) \\S(14) &= .25 * (1 - \delta_2 * \delta_2) * (1 + \delta_1) * (1 - \delta_3) \\S(18) &= .25 * (1 - \delta_2 * \delta_2) * (1 + \delta_1) * (1 + \delta_3)\end{aligned}$$

Mid-side nodes on the plane $\delta_3 = 0$:

$$\begin{aligned}S(4) &= .25 * (1 - \delta_3 * \delta_3) * (1 - \delta_1) * (1 + \delta_2) \\S(8) &= .25 * (1 - \delta_3 * \delta_3) * (1 - \delta_1) * (1 - \delta_2) \\S(16) &= .25 * (1 - \delta_3 * \delta_3) * (1 + \delta_1) * (1 + \delta_2) \\S(20) &= .25 * (1 - \delta_3 * \delta_3) * (1 + \delta_1) * (1 - \delta_2)\end{aligned}$$



Report Documentation Page

1. Report No. NASA TM-100655	2. Government Accession No.	3. Recipient's Catalog No.	
4. Title and Subtitle Instability-Related Delamination Growth of Embedded and Edge Delamination	5. Report Date August 1988	6. Performing Organization Code	
	7. Author(s) John D. Whitcomb	8. Performing Organization Report No.	
9. Performing Organization Name and Address National Aeronautics and Space Administration Langley Research Center Hampton, VA 23665-5225	10. Work Unit No. 505-63-01-05	11. Contract or Grant No.	
	12. Sponsoring Agency Name and Address National Aeronautics and Space Administration Washington, DC 20546-0001	13. Type of Report and Period Covered Technical Memorandum	14. Sponsoring Agency Code
15. Supplementary Notes The information presented in this report was offered as a dissertation in partial fulfillment of the requirements for the degree of Doctor of Philosophy, VPI & SU, Blacksburg, Virginia.			
16. Abstract The goal of this research effort was to enhance the understanding of instability-related delamination growth in laminates containing either an embedded or an edge delamination. A three-dimensional geometrically nonlinear finite-element analysis (NONLIN3D) was developed to perform a parametric analytical study of the effects of strain, delamination shape, and delamination size on the distribution of the strain-energy release rate components along the delamination front. Experiments were performed for comparisons of actual and predicted behaviors. The analysis predicted a large variation of G_I and G_{II} along the delamination front. The G_{III} component was always small. The location of maximum G_I and G_{II} depended on the delamination shape and applied strain. In general, the strain-energy release rates were small except in a small region. Hence, delamination growth was expected to occur only a small portion of the delamination front. Experiments corroborated this prediction. The laminate stacking sequence had a large effect on the shape of the deformed region, the direction of delamination growth, and the strain at which delamination growth occurred. These effects were predicted by the analysis. The G_I component appeared to govern initial delamination growth in the IM7/8551-7 laminates.			
17. Key Words (Suggested by Author(s)) Local buckling Compression Delamination Strain-energy release rate Stress analysis	18. Distribution Statement Unclassified - Unlimited Subject Category - 24		
19. Security Classif. (of this report) Unclassified	20. Security Classif. (of this page) Unclassified	21. No. of pages 198	22. Price A09